FACULDADE DE CIÊNCIAS E TECNOLOGIA

DEPARTMENT OF MECHANICAL AND INDUSTRIAL ENGINEERING

ENHANCEMENT OF FUNCTIONALLY GRADED MATERIAL CREATED BY MULTI-FEED WIRE AND ARC ADDITIVE MANUFACTURING USING FULL-FIELD IDENTIFICATION METHOD

FILIPA ALEXANDRA GRIFO CUNHA

Master in Mechanical Engineering

DOCTORATE IN MECHANICAL ENGINEERING

NOVA University Lisbon
October, 2025

FACULDADE DE CIÊNCIAS E TECNOLOGIA

DEPARTMENT OF MECHANICAL AND INDUSTRIAL ENGINEERING

ENHANCEMENT OF FUNCTIONALLY GRADED MATERIAL CREATED BY MULTI-FEED WIRE AND ARC ADDITIVE MANUFACTURING USING FULL-FIELD IDENTIFICATION METHOD

FILIPA ALEXANDRA GRIFO CUNHA

Master in Mechanical Engineering

Adviser: José Manuel Cardoso Xavier
Associate Professor, NOVA FCT

Co-advisers: Telmo Jorge Gomes dos Santos
Full Professor, NOVA FCT

Fabrice Pierron
Full Professor, University of Southampton

Examination Committee

Chair: Vírgilio António Cruz Machado
Full Professor, NOVA FCT

Rapporteurs: António Gil d'Orey de Andrade Campos
Full Professor, Universidade de Aveiro

Carlos Manuel Alves da Silva
Assistant professor, Universidade de Lisboa

Adviser: José Manuel Cardoso Xavier
Associate Professor, NOVA FCT

Members: Valdemar Rebelo Duarte
Assistant Professor, EST IPS

Vírgilio António Cruz Machado
Full Professor, NOVA FCT

Raquel Albuquerque Soares Brás de Almeida
Assistant Professor, NOVA FCT

DOCTORATE IN MECHANICAL ENGINEERING

NOVA University Lisbon
October, 2025

Enhancement of functionally graded material created by multi-feed wire and arc additive manufacturing using full-field identification method

Copyright © Filipa Alexandra Grifo Cunha, NOVA School of Science and Technology, NOVA University Lisbon.
The NOVA School of Science and Technology and the NOVA University Lisbon have the right, perpetual and without geographical boundaries, to file and publish this dissertation through printed copies reproduced on paper or on digital form, or by any other means known or that may be invented, and to disseminate through scientific repositories and admit its copying and distribution for non-commercial, educational or research purposes, as long as credit is given to the author and editor.

This document was created with the (pdf/Xe/Lua)LaTeX processor and the NOVAthesis template (v7.3.9) .

Acknowledgements

I could not have achieved this work alone, therefore I would like to address the following acknowledgments: Firstly, I would like to thank my supervisor, Professor José Xavier, for encouraging me to start my PhD and for his support and guidance throughout these years. Thanks to his vast knowledge, dedication to science and enthusiasm, this entire journey was made easier and more enjoyable. I would like to thank my co-supervisor, Professor Telmo Santos, for always thinking of the best for his students, and for inspiring in me a passion for research. To Professor Fabrice Pierron, my co-supervisor, for giving me the opportunity to spend a year at the University of Southampton, for his enormous wisdom and for encouraging me to look at my work with a more critical eye. To the University of Southampton for providing me with all the learning conditions for a year, and also to the friends I made: Yeajin Lee, Panagiota Tavianatou (Penny), Robert Hamill and Aleksander Marek, for helping me immensely and making me feel at home. I would also like to thank NOVA FCT, DEMI, and Unidemi for creating such an excellent environment for studying and for always supporting me during my PhD. All the shared knowledge, available infrastructure, and spirit of encouraging research were crucial to the development of this work and my personal and professional growth. It is an honour to be part of this institution, where people and science have played a big part in achieving this goal. Thanks to technicians Mr. António Campos and Mr. Paulo Magalhães for all their help in the laboratory. To my colleagues I met during this challenging journey: João Lopes, André Ramalho, Igor Felice, Douglas Serrati, Isaque Brito, Jiajia Shen, and Sam Kokare. To Beatriz Nunes, who joined me at the end of my PhD and gave me the final push I needed to finish. I want to say a big thank you to my parents, Anabela and Paulo, and my sister, Sofia. I am so grateful for all the love, patience and support you have given me. You have always been there for me, especially when I needed it most. To my boyfriend Bernardo, who has always been there for me, I thank you for all your love, understanding and support, which has helped me to overcome every challenge with ease and confidence. This achievement would not have the same meaning without all of you and it would not have been possible to achieve this goal either. To the Foundation for Science and Technology (FCT), I.P., for its financial support through PhD award 2021.06889.BD.

”

“Grandes batalhas só são dadas a grandes guerreiros.”

— Mahatma Gandhi

Abstract

Materials and their importance to society have evolved over time. In today's challenges, material innovation for economic and environmental sustainability has gained prominence. Additive manufacturing (AM) is a promising technology for producing 3D parts. Some AM processes allow for the production of functionally gradient materials (FGMs) in a single step, an advantage over conventional methods. Recently, FGM metal parts have been manufactured by direct arc and wire energy deposition (WAAM) to reduce material costs. Traditional tests are inadequate for evaluating the mechanical properties of FGMs due to their heterogeneity. Therefore, specialized approaches using full-field measurements and advanced inverse methods are required to accurately characterize the unique composition and structure of FGMs.

This thesis presented a numerical analysis and experimental validation of the behaviour of a Cu-CuAl FGM. In the inverse identification, the Virtual Fields Method (VFM) was used to extract material parameters from full-field deformation measurements obtained by Digital Image Correlation (DIC). The FGMs were fabricated by WAAM, using gas tungsten arc welding (GTAW) and inert metal gas (MIG) welding as heat sources. The material parameter identification was carried out based on simulation first, as verification, then on experimental data. A library of Cu-CuAl material compositions was also created to evaluate their properties.

This study evidenced the feasibility of using WAAM in the production of FGMs. The results show that Cu and Al have very different thermal conductivity coefficients and melting temperatures, which contribute to their metallurgical incompatibility. In this way, Cu and CuAl alloys were combined in an FGM which showed better metallurgical compatibility. It can be concluded that preheating the previous layers results in better cohesion between the different FGM materials.

Keywords: Copper · Copper-Aluminium Alloy · Wire and Arc Additive Manufacturing · Functionally Graded Material · Digital Image Correlation · Virtual Field Method.

Resumo

Os materiais e sua importância para a sociedade têm evoluído ao longo do tempo. Nos desafios atuais, a inovação material para a sustentabilidade económica e ambiental tem ganhado destaque. A manufatura aditiva (AM) é uma tecnologia promissora para produzir peças 3D. Alguns processos AM permitem obter materiais com gradiente de funcionalidade (FGMs) numa única etapa, uma vantagem sobre métodos convencionais. Recentemente, peças metálicas FGMs foram fabricadas por deposição direta de energia por arco elétrico e fio (WAAM) para reduzir o custo do material. Os testes tradicionais são inadequados para avaliar as propriedades mecânicas dos FGMs devido à sua heterogeneidade. Assim, são necessárias abordagens especializadas que usem medições de campo completo e métodos inversos avançados para caracterizar com precisão a composição e estrutura únicas dos FGMs.

Esta tese mostrou uma análise numérica e validação experimental do comportamento de um FGM Cu-CuAl. Na identificação inversa, o Método dos Campos Virtuais (VFM) foi utilizado para extrair parâmetros do material a partir de medidas de deformação de campo total obtidas por Correlação Digital de Imagem (DIC). Os FGMs foram produzidos por WAAM, utilizando soldadura com gás inerte de tungstênio (TIG) e gás inerte metálico (MIG) como fontes de calor. A identificação dos parâmetros do material foi realizada primeiro com base na simulação, como verificação, e depois em dados experimentais. Foi também criada uma libraria de composições Cu-CuAl para avaliar as suas propriedades.

Este estudo evidenciou a viabilidade do uso de WAAM na produção de FGMs. Os resultados mostram que Cu e Al possuem coeficientes de condutividade térmica e temperaturas de fusão muito diferentes, o que contribui para sua incompatibilidade metalúrgica. Desta forma, as ligas de Cu e CuAl foram combinadas num FGM que apresentou melhor compatibilidade metalúrgica. Pode-se concluir que o pré-aquecimento das camadas anteriores resulta numa melhor coesão entre os diferentes materiais FGMs.

Palavras-chave: Cobre · Liga Cobre-Alumínio · Deposição directa de energia por arco eléctrico e fio · Materiais com Gradiente de Funcionalidade · Correlação Digital de Imagem · Métodos dos Campos Virtuais.

Contents

List of Figures xii

List of Tables xix

Acronyms xxii

1 Introduction 1
- 1.1 Motivation and background . . . 1
- 1.2 Scientific objectives . . . 4
- 1.3 Structure of thesis . . . 5
- 1.4 Publications . . . 6
  - 1.4.1 Articles on international journals . . . 6
  - 1.4.2 Articles on international conferences and indexed proceedings . . . 6
  - 1.4.3 Conferences . . . 7
  - 1.4.4 Awards . . . 7

2 Literature review 8
- 2.1 Introduction . . . 8
- 2.2 Functionally Graded Materials using Wire and Arc Additive Manufacturing 8
  - 2.2.1 Fe - Al . . . 9
  - 2.2.2 Fe - Ni . . . 10
  - 2.2.3 Ti - Al . . . 11
  - 2.2.4 Ni - Ti . . . 12
  - 2.2.5 Cu - Al . . . 12
  - 2.2.6 Ta - Mo - W . . . 12
  - 2.2.7 HSLA - Cu-Al . . . 13
  - 2.2.8 Inconel 625 - HSLA . . . 13
  - 2.2.9 Ti6Al4V - Inconel 625 . . . 14
  - 2.2.10 Ti6Al4V - SS316L . . . 14
  - 2.2.11 Inconel 625 - stainless steel 316L . . . 15

2.2.12 Stainless steel 308L - Inconel 625 . . . 15
2.2.13 Stainless steel 304L - Inconel 625 . . . 16
2.2.14 Duplex stainless steel - Carbon-manganese steel . . . 16
2.2.15 Low-carb steel - stainless steel 316L . . . 17
2.2.16 Low alloy steel - Austenitic stainless steel . . . 17
2.2.17 Super austenitic stainless steel 904L - Hastelloy C-276 . . . 17
2.2.18 HSLA - Si-Bronze . . . 18
2.2.19 Ni - Cr - Mo . . . 18
2.2.20 Stainless steel 308L - Stainless steel 347 . . . 18
2.2.21 Other materials . . . 19
2.3 Characterisation of Functionally Graded Materials through mechanical tests 19
2.3.1 Microstructure analysis . . . 19
2.3.2 Energy Dispersive X-ray (EDX) analysis . . . 19
2.3.3 Hardness measurements . . . 19
2.3.4 Fractography analysis . . . 20
2.3.5 Corrosion test . . . 20
2.3.6 Phase identification . . . 20
2.3.7 X-ray Computed Tomography (XrayCT) . . . 20
2.3.8 Mechanical tests . . . 20
2.3.9 Inverse mechanical characterisation . . . 21
2.3.10 Mechanical characterisation of functionally graded materials using inverse identification methods . . . 26
2.4 Full-field measurement techniques: Digital Image Correlation . . . 27
2.5 Tensile test with Digital Image Correlation . . . 27
2.6 Material testing 2.0 . . . 29
2.7 Summary . . . 31

3 Theoretical framework **32**
3.1 Introduction . . . 32
3.2 Additive manufacturing . . . 32
3.2.1 Directed Energy Deposition . . . 32
3.2.2 Powder Bed Fusion . . . 33
3.2.3 Vat Photopolymerization . . . 34
3.2.4 Material Jetting . . . 34
3.2.5 Binder Jetting . . . 34
3.2.6 Material Extrusion . . . 34
3.2.7 Sheet Lamination . . . 34
3.3 Functionally Graded Materials . . . 35
3.3.1 Functionally Graded Materials in nature . . . 35
3.3.2 Types of Functionally Graded Materials . . . 36
3.3.3 Methods of manufacturing Functionally Gradient Materials . . . 37

3.3.4 Areas of applications of Functionally Gradient Materials 38
3.3.5 Future research direction 40
3.4 Digital Image Correlation 41
3.4.1 Digital Image Correlation based techniques 41
3.5 The Virtual Fields Method 42
3.5.1 Virtual works principle 42
3.5.2 Case studys of constitutive equations of elastic linear behaviour . 45
3.6 Summary 47

4 Materials and Methods **48**
4.1 Introduction 48
4.2 Materials 48
4.2.1 Copper 48
4.2.2 Aluminium 49
4.2.3 Copper-Aluminium alloy 50
4.3 Parameters and materials selection 51
4.3.1 Pure Copper: MIG and TIG 52
4.3.2 Copper (CuAg): MIG 53
4.3.3 Aluminium alloys: TIG 54
4.3.4 Copper - Aluminium alloy (CuAl9Fe): MIG 57
4.3.5 Pure copper and aluminium gradients: TIG 58
4.3.6 Copper (CuAg) and copper-aluminium (CuAl9Fe) gradients: TIG 58
4.4 Specimen production and preparation 61
4.4.1 Wire and Arc Additive Manufacturing setup 61
4.4.2 Cu-CuAl alloy Functionally Graded Material stepwise production 63
4.4.3 Cu-CuAl alloy Functionally Graded Material continuous production 66
4.4.4 Specimens preparation 67
4.5 Material characterization 67
4.5.1 Hardness measurements 67
4.5.2 Eddy current measurements 70
4.6 Digital image correlation procedure 73
4.6.1 Speckle pattern 73
4.6.2 Case study on the application of Digital Image Correlation and Virtual Fields Method on a 316L stainless steel sample 77
4.7 Conclusion 90

5 Library of material compositions and mechanical properties **91**
5.1 Introduction 91
5.2 Material compositions 91
5.3 DIC procedure 92
5.3.1 100% Cu + 0% CuAl 96

5.3.2 75% Cu + 25% CuAl . . . 100
5.3.3 50% Cu + 50% CuAl . . . 104
5.3.4 25% Cu + 75% CuAl . . . 110
5.3.5 0% Cu + 100% CuAl . . . 115
5.3.6 Material properties . . . 120
5.4 Conclusion . . . 130

6 Cu-CuAl alloy FGM stepwise **131**
6.1 Introduction . . . 131
6.2 Finite element analysis . . . 131
6.3 Tensile tests with Digital Image Correlation . . . 138
6.3.1 Tensile test procedure . . . 138
6.3.2 Digital image correlation method procedure . . . 139
6.3.3 Calibration process . . . 141
6.3.4 Maximum Force . . . 143
6.3.5 Noise evaluation . . . 143
6.3.6 Results . . . 144
6.4 Inverse identification through synthetic data by Virtual fields method . . 147
6.5 Inverse identification through full-field data by Virtual Fields Method . 151
6.5.1 Code Organization and Data Structure . . . 152
6.5.2 Data Location and Reading . . . 153
6.5.3 Region of Interest . . . 153
6.5.4 Virtual Fields . . . 154
6.5.5 Constitutive Law . . . 154
6.5.6 Calculation of Young's Modulus and Poisson's Ratio by VFM . . 154
6.5.7 Frame Processing and Region Separation . . . 155
6.5.8 Computational Robustness and Error Handling . . . 155
6.6 Conclusion . . . 161

7 Cu-CuAl alloy FGM continuous **163**
7.1 Introduction . . . 163
7.2 Finite element analysis . . . 163
7.3 Tensile tests with Digital Image Correlation . . . 168
7.3.1 Tensile test procedure . . . 169
7.3.2 Performance Analysis . . . 169
7.3.3 Digital image correlation (DIC) method procedure . . . 172
7.3.4 Maximum Force . . . 173
7.3.5 Noise evaluation . . . 174
7.3.6 Results . . . 175
7.4 Inverse identification through synthetic data by Virtual Fields Method . 180
7.5 Inverse identification through full-field data by Virtual Fields Method . 181

7.6 Conclusion 187

8 Conclusions and future work **188**
8.1 Summary and conclusions 188
8.2 Innovative aspects 191
8.3 Future research 191
8.4 Future applications 191

Bibliography **193**

List of Figures

1.1 Schematic taskflow of the tasks carried out in the thesis. 6

2.1 Number of publications in Scopus for different full-field optical techniques (units: %). 28
2.2 Number of publications for the different optical techniques. 28

3.1 Schematic diagram of a functionally graded material (a) continuous and (b) stepwise graded structure [217]. 35
3.2 Number of publications in Scopus for functionally graded materials. 36
3.3 Applications of FGMs in different fields (adapted from [1]). 38
3.4 Tensile test with DIC testing system schematic. 41
3.5 Solid shape subject to mechanical load [279]. 44
3.6 Global and fibre coordinate system. 46

4.1 Pure copper wall manufactured by TIG with welding defects. 53
4.2 Pure copper wall manufactured by MIG with welding defects. 53
4.3 Several attempts at Al deposition with different TIG welding parameters. . . 55
4.4 Aluminium alloy 1070 wall manufactured by TIG. 56
4.5 CuAl alloy (CuAl9Fe) wall manufactured by MIG. 57
4.6 90% pure copper and 10% aluminium 1070 alloy wall by TIG with 2 wires. . 58
4.7 MIG WAAM setup. 61
4.8 Torch. 62
4.9 TIG WAAM setup. 64
4.10 Schematic drawing of a Cu-CuAl alloy functional graded material stepwise. 65
4.11 Additive manufacturing wall. 65
4.12 Scheme of FGM Cu-CuAL stepwise. 65
4.13 Schematic drawing of a Cu-CuAl alloy functional graded material continuous. 66
4.14 Scheme of FGM Cu-CuAl continuous. 66
4.15 Additive manufacturing wall that has already been machined. 67
4.16 Additive manufacturing wall after the specimen has been cut. 67

4.17 Hardness setup. 68
4.18 Hardness measurements taken from the substrate to the last deposited layer of the FGM crossection of the Cu-CuAl sample without preheating. 69
4.19 Hardness measurements taken from the substrate to the last deposited layer of the FGM crossection of the Cu-CuAl sample with preheating. 70
4.20 Hardness measurements taken from the substrate to the last deposited layer of the FGM crossection of the Cu-CuAl sample with one layer of 50% CuAg and 50% CuAl in the middle. 71
4.21 Eddy currents setup. 71
4.22 Eddy currents profiles of the Cu-CuAl sample without preheating. 72
4.23 Eddy currents profiles of the Cu-CuAl alloy FGM stepwise. 72
4.24 Eddy currents profiles of the Cu-CuAl alloy FGM continuous. 73
4.25 (a) 3D-printed positioning tool, (b) speckled master mould in the 3Dprinted alignment jig, (c) final stamp. 74
4.26 Stamp application defects: (a) excess paint on the edges, (b) empty areas between stamps, (c) overlapping. 75
4.27 Airbrush system components schematic. 76
4.28 Airbrush schematic [296]. 76
4.29 Image captured at the beginning of the test showing the speckle pattern produced by airbrush. 76
4.30 Tensile test specimen dimension in mm. 77
4.31 Calibration plate used in the test calibration process. 80
4.32 Standard deviation versus number of images in calibration [297]. 81
4.33 Calibration results of the 316L Stainless steel samples. 82
4.34 Maximum force until failure for the 4 specimens tested of 316L stainless steel. 82
4.35 Gray level histogram for each pixel. 83
4.36 Region of interest (ROI). 84
4.37 Global strain fields for specimen in the xx direction, ε_{xx}, for 316L stainless steel: (a) 0KN, (b) 13.5KN, (c) 17KN, (d) 19KN, (e) 21KN and (f) 23KN. . . . 85
4.38 Global strain fields for specimen in the xy direction, ε_{xy}, for 316L stainless steel: (a) 0KN, (b) 17KN, (c) 18KN, (d) 19.5KN, (e) 21.6KN and (f) 23.5KN. . 86
4.39 Stress and strain curve for different Hardening Laws for each specimen. . . 87
4.40 Uni-axial stress and strain curve with (a) uniform and (b) total sensitivity virtual works. 88
4.41 Parameter evolution (Yield stress) with (a) uniform and (b) total sensitivity virtual works. 88
4.42 External and internal virtual work with (a) uniform and (b) total sensitivity. 89
4.43 Stress space identification with (a) uniform and (b) total sensitivity virtual works. 89
4.44 VFM type with (a) uniform and (b) total sensitivity. 89

5.1 Geometry and dimensions of material composition samples [mm]. 92
5.2 Tensile test with DIC setup. 93
5.3 Performance analysis of the signal as a function of the virtual strain gauge in pixels. 94
5.4 Performance analysis of the signal as a function of the virtual strain gauge in pixels. 94
5.5 WAAM wall made of 100% Cu. 96
5.6 Hardness measurements taken from the substrate to the last deposited layer of the FGM crossection of the 100% Cu sample. 97
5.7 Strain-stress curves for all the 100% Cu + 0% CuAl specimens. 97
5.8 Global strain fields in the xx direction, ε_{xx}, for the 100% Cu + 0% CuAl specimen under increasing tensile loads: (a) 869 N, (b) 1347 N, (c) 1587 N, (d) 1753 N, (e) 1790 N, (f) 1408 N. 98
5.9 Global strain fields in the yy direction, ε_{yy}, for the 100% Cu + 0% CuAl specimen under increasing tensile loads: (a) 869 N, (b) 1347 N, (c) 1587 N, (d) 1753 N, (e) 1790 N, (f) 1408 N. 99
5.10 Global strain fields in the xy direction, ε_{xy}, for the 100% Cu + 0% CuAl specimen under increasing tensile loads: (a) 869 N, (b) 1347 N, (c) 1587 N, (d) 1753 N, (e) 1790 N, (f) 1408 N. 100
5.11 WAAM wall made of 75% Cu + 25% CuAl. 101
5.12 Hardness measurements taken from the substrate to the last deposited layer of the FGM crossection of the 75% Cu + 25% CuAl sample. 102
5.13 Strain-stress curves for all the 75% Cu + 25% CuAl specimens. 102
5.14 Global strain fields in the xx direction, ε_{xx}, for the 75%Cu–25%CuAl specimen under increasing tensile loads: (a) 971 N, (b) 1402 N, (c) 1838 N, (d) 2175 N, (e) 2240 N, (f) 1574 N. 103
5.15 Global strain fields in the yy direction, ε_{yy}, for the 75%Cu–25%CuAl specimen under increasing tensile loads: (a) 971 N, (b) 1402 N, (c) 1838 N, (d) 2175 N, (e) 2240 N, (f) 1574 N. 104
5.16 Global strain fields in the xy direction, ε_{xy}, for the 75%Cu–25%CuAl specimen under increasing tensile loads: (a) 971 N, (b) 1402 N, (c) 1838 N, (d) 2175 N, (e) 2240 N, (f) 1574 N. 105
5.17 WAAM wall made of 50% Cu + 50% CuAl. 105
5.18 Hardness measurements taken from the substrate to the last deposited layer of the FGM crossection of the 50% Cu + 50% CuAl sample. 106
5.19 Strain-stress curves for all the 50% Cu + 50% CuAl specimens. 107
5.20 Global strain fields in the xx direction, ε_{xx}, for the 50% Cu + 50% CuAl specimen under increasing tensile loads: (a) 981 N, (b) 1787 N, (c) 2293 N, (d) 2579 N, (e) 2693 N, (f) 2153 N.. 108

5.21 Global strain fields in the yy direction, ε_{yy}, for the 50% Cu + 50% CuAl specimen under increasing tensile loads: (a) 981 N, (b) 1787 N, (c) 2293 N, (d) 2579 N, (e) 2693 N, (f) 2153 N. 109
5.22 Global strain fields in the xy direction, ε_{xy}, for the 50% Cu + 50% CuAl specimen under increasing tensile loads: (a) 981 N, (b) 1787 N, (c) 2293 N, (d) 2579 N, (e) 2693 N, (f) 2153 N. 110
5.23 WAAM wall made of 25% Cu + 75% CuAl. 110
5.24 Hardness measurements taken from the substrate to the last deposited layer of the FGM crossection of the 25% Cu + 75% CuAl sample. 111
5.25 Strain-stress curves for all the 25% Cu + 75% CuAl specimens. 112
5.26 Global strain fields in the xx direction, ε_{xx}, for the 25% Cu + 75% CuAl specimen under increasing tensile loads: (a) 1114 N, (b) 1951 N, (c) 2549 N, (d) 3053 N, (e) 3188 N, (f) 1974 N. 113
5.27 Global strain fields in the yy direction, ε_{yy}, for the 25% Cu + 75% CuAl specimen under increasing tensile loads: (a) 1114 N, (b) 1951 N, (c) 2549 N, (d) 3053 N, (e) 3188 N, (f) 1974 N. 114
5.28 Global strain fields in the xy direction, ε_{xy}, for the 25% Cu + 75% CuAl specimen under increasing tensile loads: (a) 1114 N, (b) 1951 N, (c) 2549 N, (d) 3053 N, (e) 3188 N, (f) 1974 N. 115
5.29 WAAM wall made of 100% CuAl. 115
5.30 Hardness measurements taken from the substrate to the last deposited layer of the FGM crossection of the CuAl sample. 117
5.31 Strain-stress curves for all the 0% Cu + 100% CuAl specimens. 117
5.32 Global strain fields in the xx direction, ε_{xx}, for the 0% Cu + 100% CuAl specimen under increasing tensile loads: (a) 1444 N, (b) 2970 N, (c) 4009 N, (d) 4769 N, (e) 5031 N, (f) 4531 N. 118
5.33 Global strain fields in the yy direction, ε_{yy}, for the 0% Cu + 100% CuAl specimen under increasing tensile loads: (a) 1444 N, (b) 2970 N, (c) 4009 N, (d) 4769 N, (e) 5031 N, (f) 4531 N. 119
5.34 Global strain fields in the xy direction, ε_{xy}, for the 0% Cu + 100% CuAl specimen under increasing tensile loads: (a) 1444 N, (b) 2970 N, (c) 4009 N, (d) 4769 N, (e) 5031 N, (f) 4531 N. 120
5.35 Hardness measurements taken from the substrate to the last deposited layer of the crossection of all material compositions. 122
5.36 Eddy currents measurements taken from the substrate to the last deposited layer of the crossection of all material compositions. 123
5.37 Load-displacement curves for all the material compositions specimens. . . . 124
5.38 Graph of the ultimate tensile strength [MPa], σ_u, of all material compositions. 125
5.39 Graph of the Yield Strength [MPa], σ_y, of all material compositions. 126
5.40 Stress-Strain curve of a 100% Cu specimen (specimen 2). 126
5.41 E determination from elastic analysis of a 100% Cu specimen (specimen 2). 127

5.42 ν determination from elastic analysis of a 100% Cu specimen (specimen 2). . 128
5.43 Comparison of E for different copper percentages. 129
5.44 Comparison of ν for different copper percentages. 130

6.1 Distribution of the parameters E, ν, Y_s and E_t for the distribution zone of the Cu-CuAl alloy FGM stepwise without preheating (Transition zone equal to 3 mm). 132
6.2 Cu-CuAl alloy FGM stepwise (transition zone equal to 3 mm) scheme for attributing the two materials to the defined areas: 1 (blue)- Copper and 2(purple)-CuAl alloy. 133
6.3 Meshing of Cu-CuAl alloy FGM stepwise (transition zone equal to 3 mm) specimen used for the Ansys model. 134
6.4 Schematic of tensile test. 134
6.5 Cu-CuAl alloy FGM stepwise (transition zone equal to 3 mm) specimen DOF Solution: X-Component of displacement on nodal solution in ANSYS. 135
6.6 Cu-CuAl alloy FGM stepwise (transition zone equal to 3 mm) specimen DOF Solution: Y-Component of displacement on nodal solution in ANSYS. 135
6.7 Contour plot of distribution of X-component of stress for Cu-CuAl alloy FGM stepwise (transition zone equal to 3 mm) specimen. 136
6.8 Contour plot of distribution of Y-component of stress for Cu-CuAl alloy FGM stepwise (transition zone equal to 3 mm) specimen. 136
6.9 Contour plot of distribution of X-component of elastic strain for Cu-CuAl alloy FGM stepwise (transition zone equal to 3 mm) specimen. 137
6.10 Contour plot of distribution of Y-component of elastic strain for Cu-CuAl alloy FGM stepwise (transition zone equal to 3 mm) specimen. 137
6.11 Cu-CuAl alloy FGM stepwise specimen. 138
6.12 Experimental setup for stereo-DIC test on Cu-CuAl alloy FGM stepwise specimen. 139
6.13 Calibration results of FGM samples. 142
6.14 Maximum force until failure for the 4 specimens tested of FGM. 143
6.15 Gray level histogram for each pixel. 144
6.16 Global strain fields for specimen in the xx direction, ε_{xx}, for pretest Cu-CuAl alloy FGM stepwise specimen: (a) 0KN, (b) 3KN, (c) 4KN and (d) 5KN. . . . 145
6.17 Global strain fields for specimen in the yy direction, ε_{yy}, for pretest Cu-CuAl alloy FGM stepwise specimen: (a) 0KN, (b) 4KN, (c) 4.5KN and (d) 5KN. . . 145
6.18 Global strain fields for specimen in the xy direction, ε_{xy}, for pretest Cu-CuAl alloy FGM stepwise specimen: (a) 0KN, (b) 4KN, (c) 4.5KN and (d) 5KN. . . 146
6.19 Global strain fields for specimen in the xx direction, ε_{xx}, for pretest Cu-CuAl alloy FGM stepwise specimen: (a) 0KN, (b) 1KN, (c) 2KN, (d) 2.5KN, (e) 3.5KN and (f) 4KN. 147

6.20 Global strain fields for specimen in the yy direction, ε_{yy}, for pretest Cu-CuAl alloy FGM stepwise specimen: (a) 0KN, (b) 5.6KN, (c) 6.7KN, (d) 7KN, (e) 7.7KN and (f) 8.2KN. 148
6.21 Global strain fields for specimen in the xy direction, ε_{xy}, for pretest Cu-CuAl alloy FGM stepwise specimen: (a) 0KN, (b) 5.5KN, (c) 6KN, (d) 7KN, (e) 7.6KN and (f) 8.2KN. 149
6.22 FE Nodes and Element Centroids. 150
6.23 Regular grid data with FE Nodes and Element Centroids. 150
6.24 Identified Boundary Nodes. 151
6.25 Regular grid data, FE Nodes and Boundary. 151
6.26 Regular grid data without nan values. 152
6.27 Regular grid data without nan values. 152
6.28 Engineering stress-strain curve for the Cu-CuAl alloy FGM stepwise specimens. 157
6.29 DIC stress-strain curve for the Cu-CuAl alloy FGM stepwise specimens. . . 158
6.30 Comparison between stress strain curves for Cu-CuAl FGM stepwise specimen 1. 158
6.31 Comparison of ν from FEA, engineering and DIC values. 160
6.32 Comparison of E from FEA, engineering and DIC values. 161

7.1 Cu-CuAl alloy FGM continuous (transition zone equal to 7 mm) scheme for attributing the two FGM materials to the defined areas: 1 (blue)- Copper and 2(purple)- CuAl alloy. 164
7.2 Meshing of Cu-CuAl alloy FGM continuous (transition zone equal to 7 mm) specimen used for the Ansys model. 165
7.3 Cu-CuAl alloy FGM continuous (transition zone equal to 7 mm) specimen DOF Solution: X-Component of displacement on nodal solution in ANSYS. 166
7.4 Cu-CuAl alloy FGM continuous (transition zone equal to 7 mm) specimen DOF Solution: Y-Component of displacement on nodal solution in ANSYS. 166
7.5 Contour plot of distribution of X-component of stress for Cu-CuAl alloy FGM continuous (transition zone equal to 7 mm) specimen. 167
7.6 Contour plot of distribution of Y-component of stress for Cu-CuAl alloy FGM continuous (transition zone equal to 7 mm) specimen. 167
7.7 Contour plot of distribution of X-component of elastic strain for Cu-CuAl alloy FGM continuous (transition zone equal to 7 mm) specimen. 168
7.8 Contour plot of distribution of Y-component of elastic strain for Cu-CuAl alloy FGM continuous (transition zone equal to 7 mm) specimen. 168
7.9 Cu-CuAl alloy FGM continuous specimen. 169
7.10 Experimental setup for DIC test on Cu-CuAl alloy FGM continuous specimen. 170
7.11 Graphic performance analysis of the strain component signal (E_{xx}). 171
7.12 Graphic performance analysis of the signal in relation to virtual strain gauge (pixels). 171

7.13 Maximum force until failure for the 5 specimens tested of FGM. 174
7.14 Gray level histogram for each pixel. 175
7.15 Global strain fields for specimen in the xx direction, ε_{xx}, for Cu-CuAl alloy FGM continuous specimen: (a) 0KN, (b) 3.3KN, (c) 4.2KN, (d) 5.5KN, (e) 6.7KN and (f) 8KN. 177
7.16 Global strain fields for specimen in the yy direction, ε_{yy}, for Cu-CuAl alloy FGM continuous specimen: (a) 0KN, (b) 3.2KN, (c) 4.2KN, (d) 6.5KN, (e) 8KN and (f) 8.2KN. 178
7.17 Global strain fields for specimen in the xy direction, ε_{xy}, for Cu-CuAl alloy FGM specimen: (a) 0KN, (b) 4.2KN, (c) 5.5KN, (d) 7.5KN, (e) 7.8KN and (f) 8.2KN. 179
7.18 Engineering stress-strain curve for the Cu-CuAl alloy FGM continuous specimens. 182
7.19 DIC stress-strain curve for the Cu-CuAl alloy FGM continuous specimens. . 183
7.20 Comparison between stress strain curves for Cu-CuAl FGM continuous specimen 3. 184
7.21 Comparison of ν from FEA, engineering and DIC values. 185
7.22 Comparison of E from FEA, engineering and DIC values. 186

List of Tables

2.1 Summary of FGM production using the WAAM process. 9
2.2 Summary of characterisation techniques for Functionally Graded Materials (FGMs). 21
2.3 Summary of materials, processes, tests, and objectives reported in the characterisation of metallic Additive Manufacturing (AM) using Direct Energy Deposition (DED) processes. 22
2.4 Summary of studies on the mechanical characterisation of gradient-based metallic materials, including welded joints and FGM, using inverse methods such as Virtual Fields Method (VFM) and Finite Element Model Updating (FEMU) in combination with full-field measurements. 24
2.5 Summary of studies applying DIC in tensile testing 30
2.6 Differences between MT1.0 and MT2.0 [190]. 30

3.1 Summary of methods of manufacturing FGMs. 37

4.1 Mechanical, electrical, and thermal properties of a copper (CuAg) [287]. . . 49
4.2 Mechanical, electrical, and thermal properties of a copper–aluminium alloy (CuAl9Fe) [293, 294]. 51
4.3 Chemical composition of the wire feedstocks used in this work (wt.%): . . . 51
4.4 TIG welding parameters for the pure copper layers. 52
4.5 MIG welding parameters for the pure copper layers. 53
4.6 MIG welding parameters for the CuAg layers. 54
4.7 TIG welding parameters for the aluminium alloy 5087 layers. 55
4.8 TIG welding parameters for the aluminium alloy 1070 layers. 56
4.9 MIG welding parameters for the Copper-Aluminium layers. 57
4.10 TIG welding parameters for different gradients of pure copper and aluminum 1070 alloy layers. 59
4.11 TIG welding parameters for the 100% copper (CuAg) layers. 59
4.12 TIG welding parameters for the 50% coppper (CuAg) and 50% copper-aluminium (CuAl9Fe) layers. 59

4.13 Examples of materials deposited by WAAM in TIG and MIG. 60
4.14 Stereo-DIC settings for the tensile test of 316L stainless steel specimens. . . . 78
4.15 DIC parameters for tests on 316L stainless steel specimens. 79

5.1 Number of samples of the different material compositions created in the material library. 91
5.2 2D DIC settings for the tensile test of Cu. 95
5.3 DIC parameters for tests on Cu and CuAl samples. 95
5.4 Process parameters for the deposition of 100% Cu layers using GMAW in WAAM. 96
5.5 Process parameters for the deposition of 75% Cu + 25% CuAl layers using GMAW in WAAM. 101
5.6 Process parameters for the deposition of 50% Cu + 50% CuAl layers using GMAW in WAAM. 106
5.7 Process parameters for the deposition of 25% Cu + 75% CuAl layers using GMAW in WAAM. 111
5.8 Process parameters for the deposition of 100% CuAl layers using GMAW in WAAM. 116
5.9 Process parameters for different Cu–CuAl compositions in WAAM fabrication. 121
5.10 Summary of maximum load, displacement at fracture, and average hardness for different Cu–CuAl compositions. 124
5.11 Measured Poisson's ratio and Young's modulus for each specimen. 128

6.1 Stereo-DIC settings for the tensile test of FGM specimens stepwise. 139
6.2 DIC parameters for the tensile test of FGM specimens stepwise. 140
6.3 Mean and median of Poisson coefficient for Cu-CuAl alloy FGMs stepwise specimens through finite element analysis. 153
6.4 Mean of Young's module for Cu-CuAl alloy FGMs stepwise specimens through finite element analysis. 153
6.5 Mean and median of Poisson coefficient for Cu-CuAl alloy FGMs stepwise specimens through engineering data. 156
6.6 Summary of tensile test engineering parameters and Young's modulus for the three Cu-CuAl alloy FGM stepwise specimens. 157
6.7 Mean of Poisson coefficient for Cu-CuAl alloy FGMs stepwise specimens through DIC data. 159
6.8 Mean and median of Young Modulus for Cu-CuAl alloy FGMs stepwise specimens through DIC data. 159

7.1 2D-DIC settings for the tensile test of FGM specimens continuous. 170
7.2 DIC parameters for the tensile test of FGM specimens continuous. 173
7.3 Mean and median of Poisson coefficient for Cu-CuAl alloy FGMs continuous specimens through finite element analysis. 180

7.4 Mean of Young's module for Cu-CuAl alloy FGMs continuous specimens through finite element analysis. 180
7.5 Mean and median of Poisson coefficient for Cu-CuAl alloy FGMs continuous specimens through engineering data. 181
7.6 Summary of tensile test engineering parameters and Young's modulus for the three Cu-CuAl alloy FGM continuous specimens. 182
7.7 Mean of Poisson coefficient for Cu-CuAl alloy FGMs continuous specimens through DIC data. 184
7.8 Mean and median of Young Modulus for Cu-CuAl alloy FGMs continuous specimens through DIC data. 185

Acronyms

AM Additive Manufacturing *(pp. xix, 1, 2, 4, 5, 11, 21–23, 25, 32, 49, 52, 56, 64, 67)*

BAMS Bimetallic Additively Manufactured Structures *(pp. 15, 17)*

CAD Computer-Aided Design *(p. 1)*

DED Direct Energy Deposition *(pp. xix, 21, 22, 32)*
DIC Digital Image Correlation *(pp. 3–5, 22, 23, 25, 27–31, 41, 42, 48, 67, 78, 79, 84)*
DLD Direct Laser Deposition *(p. 33)*
DMD Direct Metal Deposition *(p. 32)*
DMLS Direct Metal Laser Sintering *(p. 34)*
DVC Digital Volume Correlation *(p. 41)*

EDX Energy Dispersive X-ray *(pp. viii, 8, 16, 17, 19, 21)*
EMS Electromagnetic Stirring *(pp. 13, 14)*
EVFM Eigenfunction Virtual Fields Method *(p. 4)*

FE Finite Element *(p. 26)*
FEM Finite Element Method *(pp. 2, 25)*
FEMU Finite Element Model Updating *(pp. xix, 22–25)*
FFOT Full-Field Optical Technique *(pp. 3, 27)*
FGM Functionally Graded Material *(pp. xix, 1, 2, 4, 5, 8–27, 35–37, 39, 40, 48, 51, 57, 59, 63–66, 69, 70, 72, 77, 90)*
FOV Field of View *(pp. 77, 83, 141)*
FSW Friction Stir Welding *(p. 24)*

GMAW Gas Metal Arc Welding *(pp. 52, 64)*
GTAW Gas Tungsten Arc Welding *(pp. 9, 11, 12, 52, 55)*

HSLA High Strength Low Alloy *(pp. 13, 14, 18)*

IHT In-situ Heat Treatment *(p. 14)*

LENS Laser Engineered Net Shaping *(p. 33)*
LMD Laser Metal Deposition *(pp. 11, 16, 33)*

MIG Metal Inert Gas *(pp. 52, 53, 57, 59, 61, 64)*

OTS Optimized Transition Strategy *(p. 14)*

PBF Powder Bed Fusion *(p. 33)*

ROI Region of Interest *(p. 83)*

SEM Scanning Electron Microscope *(pp. 14, 17)*
SLM Selective Laser Melting *(p. 34)*
SLS Selective Laser Sintering *(pp. 33, 34)*

T-WAAM Twin-Wire and Arc Additive Manufacturing *(pp. 11, 13, 59)*
TIG Tungsten Inert Gas *(pp. 52, 53, 59, 61, 63)*

VFM Virtual Fields Method *(pp. xix, 4, 5, 22–26, 84)*

WAAM Wire and Arc Additive Manufacturing *(pp. 2, 4, 5, 8–22, 25, 33, 48, 50, 61, 63, 64, 66, 90)*
WFS Wire Feed Speed *(p. 52)*

XrayCT X-ray Computed Tomography *(pp. viii, 16, 19–21)*
XRD X-ray Diffractometer *(pp. 12–14, 17, 20, 21)*

1

Introduction

1.1 Motivation and background

The materials have been the guide to some areas of the world where your progress is essential for the development of those areas [1]. Understanding the evolution and manufacture of materials has been fundamental to the development of society [2]. Nowadays scientists and engineers recognize the importance of materials innovation for economic and environmental reasons [3]. The development of new materials allows for the advancement of civilization as it enables human beings to do things they could not do before [4]. Composite materials are the most advanced form of materials that are made from two or more constituents in order to take advantage of the chemical and physical properties of each material [5].

Engineering is constantly looking for inspiration in nature in an attempt to answer questions and solve engineering problems [6]. FGM is one of those cases where engineering sought inspiration from nature, bones [7], teeth [8], wood [9] and bamboo [10]. Nature is a great source of inspiration for the design and manufacture of materials or their components. Natural or biological materials tend to show great heterogeneity in their compositions. Nature provides a huge diversity of living organisms favourable to produce gradients in materials considering the numerous chemical, structural and geometric variations that can be shaped [11].

Additive manufacturing (AM), also known as 3D printing, is the process of creating a part by joining material, typically by adding news layers over a substrate, in order to obtain a final product from data in a computer-aided design (Computer-Aided Design (CAD)) model [12]. The AM technology has gained enormous industrial and research interest in recent years, due to its potential for manufacturing complex single-stage components [13]. In the last decade, this technology has come to be seen as a process for manufacturing functional parts for a wide range of polymers and metallic materials. However, as AM has typically a low production rate, it is more suitable for manufacturing specific and complex parts than mass production. It is a technique successfully applied across different areas, from biomedical [14] to electric motors [15] to aerospace industries [16]. Another

technological advantage is the ability to produce parts with an almost final shape, thus reducing production time and costs [17]. Nevertheless, products obtained by AM still require further development on open issues regarding internal defects due to printing errors and residual and thermal stresses [18, 19]. This quality uncertainty can create parts wastage, increase parts delivery time and prevent AM implementation in industries that require high performance components with quality assurance. Some of the AM processes allow the production of FGM parts. AM technology allows the production of FGM components in a single step, which is an advantage over other manufacturing methods [20]. More recently, researchers have focused on studying FGM production through Wire and Arc Additive Manufacturing (WAAM) with the aim of looking for manufacturing method that will reduce material cost [21]. The WAAM twin-wire process has already been successfully applied with various material combinations, such as Fe-Al [22], Fe-Ni [23], Ti-Al [21], Ni-Ti [24], Cu-Al [25], duplex stainless steel-carbon manganese steel [26] and inconel625-stainless steel [27].

The FGMs were created with the main objective of overcoming limitations exposed by conventional materials. These types of materials provide opportunities to combine two or more mechanical properties into a single material. The FGM concept was acquired from nature to be used in solving engineering problems [20]. FGMs are not recent in nature [3].

In the paradigm of Industry 4.0, a tight integration of AM processes has been established regarding new classes of advanced materials. Examples of advanced materials are, for instance, FGM and hybrid material parts, that can have an outstanding mechanical behaviour regarding homogeneous standard engineering counterparts. The hypothesis may be formulated on the light of a biological perceptive. Consistent progress of AM technology will yield the synthesis of materials with specific-oriented structure and functionality. This approach claims an unprecedented potential in which materials can evolve into the bio-inspired paradigm of heterogeneity and gradient mechanical properties [11]. The design of advanced materials exhibiting exceptional characteristics can now be properly tackled by AM processes towards application-driven engineering solutions. This vision shares the same paradigm as the patient-specific healthcare systems and medical devices. Besides, this new generation of high-value materials will contribute to environmental and sustainability challenges by the rational use of resources and energy.

With the computational development that has taken place, the scientific community has made a huge development in the Finite Element Method (FEM) and its companions. These technologies allow to obtain the field of distribution of displacements, strains and stresses in different engineering structures. However, these methodologies may not present the most real or accurate results, requiring experimental tests to be carried out. In numerical models it is common to make assumptions about the constitutive parameters of the material. Since the constitutive equations of a material that describe its response when subjected to a request can only be determined with experimental tests. With the classic approach to the characterization of the materials, several experimental tests would be necessary to determine all the constitutive parameters of a material[28].

Around the 1980s they were developed by the mechanical engineering community: the full-field measurement techniques. These techniques provide the displacement, acceleration and deformation distribution fields with just a single experimental test [29]. One of the full-field measurement techniques that has been developed was the digital image correlation [30]. In the onset of the so-called digital revolution, image-based technologies have been emerging. This progress has allowed the development of full-field optical techniques Full-Field Optical Technique (FFOT)s for experimental continuum mechanics [31, 32]. Intrinsically, these methods are in contrast with counterpart devices by providing contactless and full-field data. According to the physical phenomenon involved in the image formation, these methods can be divided into two main categories: white-light (*e.g.*, digital image correlation Digital Image Correlation (DIC), grid method, projection moiré) and interferometric (*e.g.*, moiré interferometry, electronic speckle pattern interferometry, speckle shearography) techniques [33, 34]. On the one hand, white-light techniques rely on the analysis of the light intensity variation of a geometrical pattern describing the material deformation. This type of techniques can be sorted regarding the characteristic pattern as random, period or feature-based. On the other hand, the interferometric techniques are based on the phenomenon of interference of light waves. These techniques use a monochromatic and coherent light source (e.g., a laser) to illuminate the material surface. Considering the way light interacts with this surface, these methods can be sorted into diffused light (speckle) and diffracted light (grating) interferometric techniques. The selection of a given optical technique is dependent on the application itself. Nevertheless, some guidelines may be defined considering the cost, the simplicity of implementation, the performances (spatial and temporal resolutions, accuracy), the kinematic quantity to be measured (*e.g.*, displacement, strain, curvature), the expected range of deformation, the sensitivity to vibrations and the size of the region of interest (from nano to structural scales). The impact of FFOTs in providing kinematic measurements across a whole region of interest, has brought novel insights into different applied scientific areas. Among others, one may underline the measurement of gradient fields [35–37], fracture cracking evaluation [38–42], image-based approaches of high-strain rate dynamical behaviour of materials [43–47], numerical modelling validation from image-based measurements [48–50], and inverse material parameter identification from heterogeneous tests [51–54]. Advanced monitoring techniques have also been applied with the AM process in order to enhance the technology.

In mechanical dynamics, two main problems can be identified: the direct and inverse problems. Inverse methods for material design utilize computational techniques and algorithms to create or find materials with desired properties. These methods reverse-engineer the desired material properties, identifying the composition and structure of the material that can achieve those properties [55]. The development of simulation methods and computational resources has led to the advancement of methodologies, providing fresh insights into the formation of specific structures in materials and their correlation with other properties of significance. Inverse methods, which are crucial to

scientific discovery and problem-solving, are highly interdisciplinary, bringing together contributions from mathematics, physics, computer science and engineering [56]. Data from full-field measurement techniques can be further processed by inverse computation techniques such as The VFM [28]. The VFM has been increasingly studied or used for the materials characterization. The technique allows the characterization of materials through a single experimental test unlike the conventional techniques. This methodology allows a great flexibility in the design of mechanical tests and take advantage of heterogeneous displacement/strain fields do material parameters [57]. Subramanian [58] in his study presented a variant of the VFM named the Eigenfunction Virtual Fields Method (EVFM) where the virtual fields are based on eigenfuntions of measured strain fields. Nayakanti [59] in his work applied the EVFM in order to successfully determine the problem of determining the linear elastic properties of a FGM.

1.2 Scientific objectives

The main objective of this project is to mechanically characterise the Cu-CuAl FGM produced by wire and arc additive manufacturing.

There are the main objectives:

- Carried out a literature review on the inverse characterisation of heterogeneous materials, materials produced by additive manufacturing and FGMs produced by WAAM. A review of how full-field measurement techniques can be used to perform in-situ monitoring for various applications has also been carried out. DIC in particular is then mentioned, along with all its possible applications. A review is also given of all the material combinations ever produced for a FGM using WAAM;

- One of the main objectives of this research is the production of FGMs with a combination of copper and aluminium materials by the AM WAAM process;

- Another objective is to carry out a non-destructive evaluation with the aim of inspecting and mapping the heterogeneities of FGM using techniques such as eddy currents, hardness measurements, electrical conductivity measurements and macroscopic and microscopic morphology;

- A full field measurement technique (DIC) was used to characterise the mechanical behaviour of the manufactured FGM. This technique was applied in an experimental tensile test using in situ stereo DIC;

- The virtual field method is then used as a full-field inverse identification method to determine the elastic material properties of the FGM produced by WAAM.

1.3 Structure of thesis

This thesis is structured as follows:

Chapter 2 presents a detailed literature review, starting with an overview of FGMs by the WAAM process and their different combinations of materials. An overview of the characterisation of these FGMs is then given. The chapter continues with a section dedicated to the inverse identification of different types of materials, such as heterogeneous materials, AM materials and FGMs, using different inverse techniques. It ends by summarizing the full-field measurement techniques. DIC and its applications are then discussed in more detail. The chapter closes with a brief summary of a new paradigm in mechanical testing of materials, the material testing 2.0.

Chapter 3 contains the theory on which this work is based. First, additive manufacturing and its various processes are described. FGMs, their types, manufacturing methods and applications are then presented. Next, digital image correlation is described as a full-field measurement technique. Finally, the virtual field method is introduced as a reverse identification method.

Chapter 4 begins with a description of the materials used in this work. The WAAM setup is then described. The parameters and selection of materials for the fabrication of FGMs are detailed. Next, the fabrication of the Cu-CuAl alloys is explained. Then, the preparation of the specimens for the application of the speckle pattern is described. Subsequently, a material characterisation of the FGMs produced by hardness measurements, electrical conductivity measurements, eddy currents and macroscopic and microscopic morphology. The chapter concludes with an explanation of the DIC procedure and a case study of the application of DIC in a tensile test with 316L stainless steel.

This Chapter 5 presents the library of material compositions and mechanical properties through various depositions of Cu and CuAl with various percentages of each material.

Chapter 6 shows the post processing of Cu-CuAl alloy FGM stepwise. A finite element analysis is performed. Tensile tests are performed with DIC. At the end, the samples are characterized by identifying the spatial variability of material parameters of FGMs by VFM using synthetic images and full-field data.

Chapter 7 shows the post processing of Cu-CuAl alloy FGM continuous. A finite element analysis is performed. Tensile tests are performed with DIC. At the end, the samples are characterized by identifying the spatial variability of material parameters of FGMs by VFM using synthetic images and full-field data.

Chapter 8 provides an overview of the research outlined in this thesis. It includes a discussion of the methodology employed and the resultant experimental findings. Further, it outlines the constraints of this work and proposes recommendations for future applications.

Figure 1.1 shows the workflow of the thesis structure, highlighting the tasks carried out in each chapter.

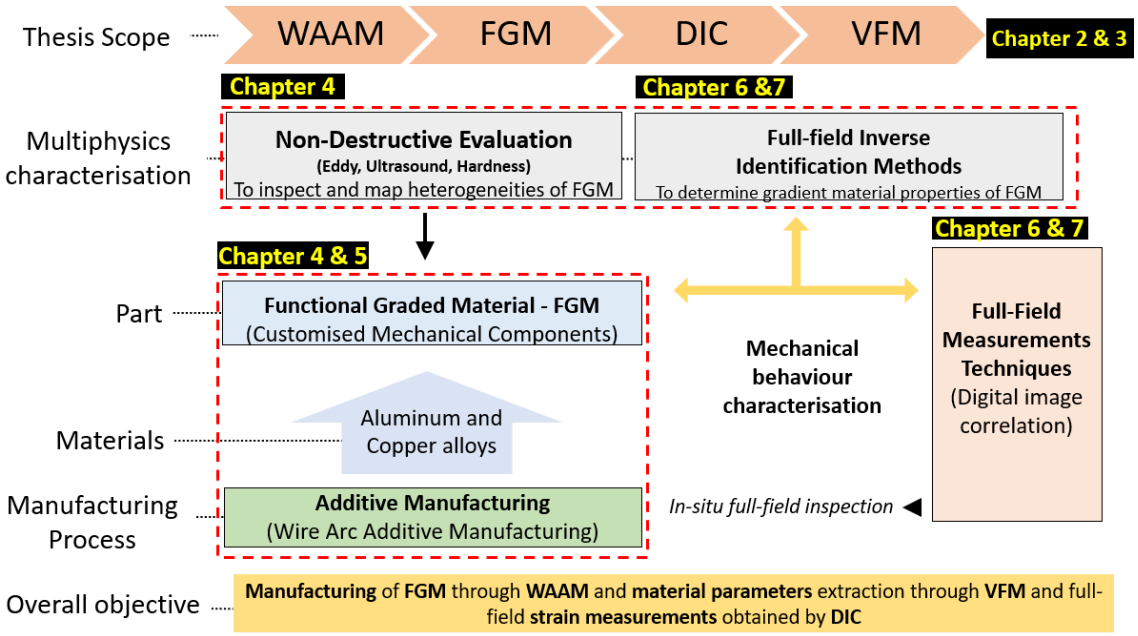

Figure 1.1: Schematic taskflow of the tasks carried out in the thesis.

1.4 Publications

1.4.1 Articles on international journals

- Cunha, Filipa G.; Santos, Telmo G.; Xavier, José. "In Situ Monitoring of Additive Manufacturing Using Digital Image Correlation: A Review". Materials 14 6 (2021): 1511. DOI: 10.3390/ma14061511

- Silva, R.F.; Coelho, P.G.; Gustavo, C.V.; Almeida, C.J.; Farias, F.W.C.; Duarte, V.R.; Xavier, J.; Esteves, M.B.; Conde, F.M.; Cunha, F.G.; et al. Functionally Graded Materials and Structures: Unified Approach by Optimal Design, Metal Additive Manufacturing, and Image-Based Characterization. Materials 2024, 17, 4545. https://doi.org/10.3390/ma17184545

- Cunha, Filipa G.; Santos, Telmo G.; Xavier, José. "Functionally Graded Materials by Wire and Arc Additive Manufacturing: Processing Approaches, Applications, and Mechanical Characterisation – A Systematic Review". Materials, in review.

- Cunha, Filipa G.; Nunes, Beatriz; Santos, Telmo G.; Xavier, José. "A Library of Mechanical Properties of Cu-CuAl Alloys Produced by Wire and Arc Additive Manufacturing". Manufacturing and Materials Processing, 2026, 10(1), 42. https://doi.org/10.3390/jmmp10010042

1.4.2 Articles on international conferences and indexed proceedings

- Cunha, Filipa G.; Santos, Telmo G.; Xavier, José. "In situ monitoring of wire and arc additive manufacturing by digital image correlation: a case study". Procedia

Structural Integrity 37 (2022) 33–40. DOI: 10.1016/j.prostr.2022.01.056

1.4.3 Conferences

- iDICs 2024: PhotoMechanics - International DIC Society 2024 Conference (Paper accepted). Paper that will be presented: “Understanding the behaviour of a Cu-CuAl functionally graded alloy using DIC”. Authors: Filipa G. Cunha, Telmo G. Santos, José Xavier, Fabrice Pierron. 29 to 31 Out 2024 at Université Clermont Auvergne, Fr.

- BSSM 2023: The 17th International Conference on Advances in Experimental Mechanics. Paper presentation entitled: “Mapping the elasto-plastic properties of a Cu-CuAl functionally-graded alloy using the Virtual Fields Method”. Authors: Filipa G. Cunha, Telmo G. Santos, José Xavier, Fabrice Pierron. 30 Aug to 1 Sep 2023 at University of Glasgow, UK.

- BSSM 2022: The 16th International Conference on Advances in Experimental Mechanics. Paper presentation entitled: "Fabrication of copper-aluminium FGMs through Wire and arc additive manufacturing". Authors: Filipa G. Cunha, Valdemar R. Duarte, Telmo G. Santos, José Xavier, Fabrice Pierron. 6 to 8 Sep 2022 at University of Oxford, UK.

- ICSI 2021: The 4th International Conference on Structural Integrity. Paper presentation entitled: "In situ monitoring of wire and arc additive manufacturing by digital image correlation: a case study". Authors: Filipa G. Cunha, Telmo G. Santos, José Xavier. 30 Aug to 1 Sep 2021 at Funchal, Madeira, Portugal.

- ICSI 2019: The 3rd International Conference on Structural Integrity. Paper presentation entitled: "Identification of high strain rate behaviour of wood based on an image-based inertial impact test". Authors: F. Cunha, L. Fletcher, J. Xavier, F. Pierron. 2 to 5 September 2019 at Funchal, Madeira, Portugal.

1.4.4 Awards

- 2022 Young Stress Analyst Competition - YSA 2022 Runners up: In 2022 YSA took place alongside the BSSM’s 16th International Conference on Advances in Experimental Mechanics on 7th September 2022 at St Anne’s College, University of Oxford, Oxford, UK. The YSA has been generously sponsored for many years by our Corporate Member Airbus UK who provide the prize money and funds for the YSA finalists to attend the Annual Conference free of charge. Work presented: “On material identification of Pinus pinaster Ait. at high strain rate loading by the image-based inertial impact test”

2

Literature review

2.1 Introduction

This chapter presents a summary of the literature reviewed on this work. The review begins with an overview of all the materials already used to produce FGMs by WAAM, as well as the functional gradients achieved and their applications. This is followed by a summary of the various mechanical tests already used to characterise FGMs, such as X-ray computed tomography, tensile testing, microstructural analysis, EDX, hardness measurements, fractographic analysis, corrosion testing and phase identification. This is followed by a brief review of inverse methods used in the characterisation of heterogeneous materials, additive manufacturing materials and functionally graded materials. A summary of digital image correlation in tensile testing for the identification of the mechanical behaviour of different materials was then presented. The chapter concludes with a description of Material Testing 2.0, which explains this methodology and some of the techniques involved, such as full-field measurement techniques and inverse identification techniques. All the knowledge gained from the bibliographic review served as a source of knowledge and inspiration for the work developed in the remaining chapters of the thesis.

2.2 Functionally Graded Materials using Wire and Arc Additive Manufacturing

The WAAM process is a technology that combines an electric arc as a heat source with a thread used as feedstock. This technique is becoming increasingly popular due to its advantages, such as higher deposition rates and the ability to produce more distinctive parts in less time [60].

Over time, studies have shown that the twin-wire WAAM process has been successfully used to manufacture various binary system alloys, including materials such as Fe-Al [22, 61], Ti-Al [21, 62, 63], Ni-Ti [24, 64], Cu-Al [65], and Fe-Ni [23]. Table 2.1 shows a summary of the materials used to produce FGM, the functional gradients created, examples of

applications of these FGM and their respective references. Sorted by the based-material combination, these studies will be further reviewed in the following.

Table 2.1: Summary of FGM production using the WAAM process.

Materials	Functional gradient	Examples of industrial application	References
Fe—Al	Al gradient 15 to 55 at (%)	Applications requiring high-damage resistance	[22, 61]
Fe—Ni	20 to 50% of Ni	Aeronautical and maritime industries	[23, 66, 67]
Ti—Al	20 to 50% of Al	Aerospace and automotive	[21, 62, 63]
Ni—Ti	50% of Ni and 50% of Ti	Automotive, aerospace, robotic, and biomedical	[24, 64]
Cu—Al	0.9 o.d. 99.9 copper wire and 0.9 o.d. 1080 grade aluminum wire	Shipbuilding industries	[65]
Ta—Mo—W	100% Ta 0% Mo to 0% Ta 100% Mo to 0% Mo 100% W	High temperature applications	[68]
HSLA—Cu-Al	25 layers of HSLA steel and 20 layers of Cu-Al alloy	Applications that require high thermal/electrical conductivity, wear resistance with excellent mechanical properties	[27]
Inconel 625—HSLA	100% Inconel 625 0% HSLA to 0% Inconel 625 100% HSLA	Applications on special environments with harsh running condition, pressurized water reactor re-action system and connecting parts of pipe and safe side	[69–72]
Ti6Al4V—Inconel 625	100% Ti6Al4V 0% Inconel 625 to 0% Ti6Al4V 100% Inconel 625	Applicarions in extreme environments, including aerospace engineering, nuclear power generation, sensor, biomedical implants, vice optoelectronic, and absorption systems	[73]
Ti6Al4V— SS316L	5at.% Fe to 65at.%Fe	Applications that require an excellent corrosion resistance, high strength-to-weight ratio and low cost	[74]
Inconel 625—SS316L	11 layers of SS316L and 8 layers of Inconel 625	Aerospace, power generation, petrochemical, chemical and marine applications	[75–78]
SS308L—Inconel 625	100% SS308L 0% Inconel 625 to 100% Inconel 625 0% SS308 or The gradient is made along the layer deposition	-	[79–82]
Inconel 625—SS304L	75% SS304L 25% Inconel 625 to 25% SS304L 75% IN62	-	[83]
DSS — CMS	Half of the wall is duplex stainless steel and the other half is carbon manganese steel	Marine risers	[26, 84]
Low-carb steel—SS316L	Half of the wall is SS316L and the other half is Inconel 625	Bimetallic structures	[85]
LAS—ASS	Layers of each material deposited interspersed	-	[86]
SS904L—Hastelloy C-276	2 layers of SS904L followed by 22 layers of Hastelloy C-276	Harsh environments such as oil and gas industries and nuclear power plants for manufacturing steam generator, reformers	[87]
Inconel 825—SS316L	20 layers of Inconel 825 and 20 layers of SS316L	Environments that require corrison-resistant alloys	[88, 89]
TA1—Inconel 625	100% TA1 and 0% Inconel 625 to 100% Inconel 625 and 0% TA1	Extreme environment conditions	[90]
HSLA – Si-Bronze	100% HSLA and 0% Si-Bronze to 100% Si-Bronze and 0% HSLA	-	[91]
Ni – Cr – Mo	10 layers with different % Ni, Cr and Mo	Defense, aerospace, and nuclear applications	[92]
Stainless steel 308L – Stainless steel 347	100% SS308L and 0% SS347 to 100% SS347 and 0% SS308L	Replacing current components or innovating new ones for applications in pipelines, pressure vessels, and power plants.	[93]

HSLA: High Strength Low Alloy; SS316L: Stainless-steel 316L; 308L: Stainless steel 308L; 304L: Stainless steel 304L; ; DSS: Duplex stainless steel; CMS: Carbon-manganese steel; LAS: Low alloy steel; ASS: Austenitic stainless steel; SS904L: Super austenitic stainless steel;

2.2.1 Fe - Al

Shen et al. [22] conducted a study to assess the feasibility of manufacturing Fe-FeAl FGMs using the WAAM process. In the WAAM system, a Gas Tungsten Arc Welding (GTAW) power source and a tungsten torch were employed. Pure argon served as the inert gas in this study. Two wire feeders were employed to construct the specimens. The aluminium

(Al) composition exhibited an increased gradient from 15 to 55 atomic per cent (at.%), while the iron (Fe) composition remained nearly constant throughout the process. After the specimen manufacturing process, material tests were conducted to characterise the material, including hardness testing and analysing the chemical composition gradient of the material. Fe-Al intermetallic material was selected for this study due to its favourable characteristics, such as high damage resistance, excellent oxidation, and corrosion resistance. Thus, Fe-FeAl FGMs are expected to exhibit similar characteristics. The results of this study indicated that the designed chemical composition could be enhanced by adjusting the ratio of the wire feed from iron and aluminium wires.

Fe3Al-based iron aluminide has been investigated for its outstanding oxidation and sulfidation resistance properties. Consequently, this material can withstand high temperatures, presenting a low density and a low production cost. These attributes render it promising for manufacturing alloy steels in components used for fossil fuel energy systems requiring high thermal and corrosion resistance. Similar to the preceding work, Shen et al. [61] employed the WAAM technique to produce an aluminium alloy. However, this study presents a more detailed examination of Fe3Al-based iron aluminide, elucidating its morphology, chemical composition, and mechanical characteristics. Particular emphasis is placed on the anisotropy resulting from the manufacturing process. Through characterising the microhardness and chemical composition of the manufactured material, it can be concluded that the properties are homogeneous throughout the manufactured wall. However, the tensile properties differ significantly in the longitudinal and normal directions due to epitaxial growth. The results of this study underscore the efficacy of the WAAM process in producing Fe_3Al-based iron aluminide components.

2.2.2 Fe - Ni

The combination of FeNi materials has garnered significant interest due to their favourable physical properties, including high magnetic permeability, low values of magnetic anisotropy, a small coefficient of expansion, and unique elastic properties [66]. Shen et al. [66] produced the Fe_3Ni-FeNi material using WAAM process. This research also aimed to characterise the Fe-Fe_3Ni phase transformation process using a high-intensity neutron diffraction instrument. The results of this characterisation provided a new perspective on the phase evolution in the FGMs Fe-Fe_3Ni. Following the manufacture of the FGMs, a characterisation of the microstructure and composition obtained in the process was also conducted using optical and electron microscopes.

Shen et al. [67] fabricated an alloy of fcc-FeNi using WAAM. To characterise the evolution of the thermal lattice of FeNi, neutron diffraction was directed onto the sample fabricated in situ during a heat treatment process. According to the neutron diffraction results performed on the fabricated sample, detecting an anisotropic evolution of the fcc-FeNi network was possible, indicating the presence of a FeNi superstructure in the FGMs material manufactured by the WAAM process. This study demonstrated the reliability of

the Twin-Wire and Arc Additive Manufacturing (T-WAAM) technique in manufacturing structures with Fe-Ni materials.

Shen et al. [23] present a study on the manufacture of Fe_3Ni-FeNi FGMs fabricated by the twin-wire WAAM process. Fe-Ni binary alloys exhibit attractive characteristics in aerospace applications due to the small coefficient of thermal expansion of Fe_3Ni and the favourable elevated temperature corrosion resistance of FeNi. Thus, Fe_3Ni-FeNi FGMs have been considered promising materials in the aerospace industry. The gradient of this FGMs design was achieved by varying the Ni content from 20 to 50%.

2.2.3 Ti - Al

Wang et al. [21] studied the TiAl FGMs production through the use of the double-WAAM method. TiAl alloys have several engineering applications such as aerospace and automotive due to their material properties, high heat resistance, high thermal conductivity and low density. The objective was also to investigate the material properties as the variation of microstructure and mechanical properties. The specimen composition gradient is created from pure Ti to Ti 50 to% Al. Pure titanium wire with a 1.0 mm in diameter and a 1080 pure aluminium with a 0.9 mm in diameter are controlled by their individual wire feeding speeds. The angle of each nozzle with the substrate is 30. The angle between the two nozzles is 60 in order to maintain stability between the molten pool. The WAAM system use GTAW torch and power source, with an argon inert gas mechanism. Previous studies have shown that TiAl FGMs had been successfully manufactured using direct Laser Metal Deposition (LMD). However, WAAM has been the main choice of manufacturing method to produce TiAl FGMs. WAAM has less process time due to high deposition rates and lower waste material when compared to powder-based AM processes. The results of this study show that the functionality gradient has been successfully applied to TiAl alloys.

Ma et al. [62] and Ma et al. [63] carried out two studies on the production of $\gamma-$TiAl through the WAAM process. In the soldering process, separate pure Ti and Al wires were combined. The proportions were chosen so that a $\gamma-$TiAl alloy is produced. For this twin-wire WAAM approach it is crucial to understand how process parameters influence the microstructure and properties of materials. Studying these parameters is important to produce FGMs successfully, repeatable and with quality. One of the objectives of these investigations is to determine the effect of the interpass temperature (temperature of the material in the weld area immediately before the next layer is produced). Alloys $\gamma-$TiAl are thermally very sensitive and have very variable cooling rates. These characteristics can have a big difference in the structural properties of the manufactured material. The interpass temperature is considered one of the main parameters that must be optimised to obtain a better final product.

2.2.4 Ni - Ti

Zeng et al. [24] employed the WAAM process to fabricate NiTi FGMs using a Ni-rich Ni-based wire. The obtained FGMs were predominantly austenitic at room temperature, as confirmed through various techniques, including microscopy, differential scanning calorimetry, and high-energy synchrotron X-ray Diffractometer (XRD). Additionally, the mechanical properties of the specimens were evaluated through tensile-to-fracture and superelastic cycling tests. Notably, this study was the first to report superelastic behaviour in NiTi produced via WAAM under tensile testing conditions, demonstrating the potential of WAAM for fabricating NiTi FGMs. The findings suggest new avenues for creating complex geometries using NiTi shape memory alloys.

Yu et al. [64] demonstrate that WAAM is a promising technique for manufacturing NiTi shape memory alloys, capable of producing parts with large dimensions and high geometric complexity. The FGMs produced comprised approximately five layers of NiTi alloy deposited via WAAM. This study thoroughly investigated and compared the macroscopic morphology, microstructure evolution, phase transformation, and mechanical properties of the fabricated FGMs wall. The results indicate that the WAAM process is an innovative methodology for manufacturing NiTi shape memory alloys. The inherent thermal gradient during the deposition process introduces heterogeneity in characteristics such as microstructure, phase transformation behaviour, and mechanical properties. Future research should focus on refining this process to manufacture structures with increased complexity, greater precision in geometries, and enhanced mechanical properties.

2.2.5 Cu - Al

Dong et al. [65] explored the manufacturing process of Cu-Al alloys using the twin-wire WAAM process, which is highly relevant to the shipbuilding industry due to the alloys' exceptional wear and corrosion resistance. Traditionally, these alloys have been produced via powder metallurgy. However, in this instance, the GTAW method was employed as the heat source within WAAM to create FGMs. The materials were shielded in an argon-inert atmosphere during production to ensure the purity of the copper and aluminium raw materials. Intermetallic phases such as CuAl2 and Cu9Al4 were identified throughout the manufacturing process. The gradation in the FGMs was achieved using a copper wire of 0.9 o.d. 99.9 grade and an aluminium wire of 0.9 o.d. 1080 grade, thus establishing a material gradient.

2.2.6 Ta - Mo - W

In their study, Marinelli et al. [68] successfully fabricated a structure incorporating two FGMs using distinct refractory metals—molybdenum and tungsten—deposited onto a tantalum substrate. Following the layer deposition, comprehensive tests were conducted to assess the microstructure, hardness, and chemical composition of the samples. A notable

observation was the presence of a dense network of cracks at the tantalum-molybdenum interface, primarily attributed to the mismatch in thermal expansion coefficients between the two metals. Additionally, a marked transition in microstructural evolution was observed with the deposition of tungsten layers atop the molybdenum base. This was linked to the rapid solidification of the melt pool, resulting in heterogeneous solidification across the materials. In the initial FGM layers bridging molybdenum and tungsten, notable variations in composition and hardness were detected, arising from differences in the melting points of the materials and the swift solidification process of the FGM layers. Notably, no cracking was observed between the molybdenum and tungsten layers, attributed to their similar thermal expansion coefficients. The study highlights potential applications for FGMs made from these refractory materials in high-performance components such as turbine blades, rocket nozzles, and nuclear reactor parts.

2.2.7 HSLA - Cu-Al

Rodrigues et al. [27] developed a FGMs composed of a copper alloy and a High Strength Low Alloy (HSLA) through the process of T-WAAM. Copper and steel materials are of major importance to a myriad of industries due to the potential to combine high thermal and electrical conductivity with wear resistance and excellent mechanical properties. However, integrating copper with steel presents several challenges due to mismatch in thermal expansion coefficients, melting temperatures and crystal structures. Following the production of the FGMs, their microstructure and mechanical properties were analysed using optical microscopy, scanning electron microscopy, and high-energy synchrotron XRD. This investigation revealed a smooth gradient in hardness and electrical conductivity along the height of the FGMs sample. The mechanical properties indicated that the FGMs exhibited a tensile strength of 690 MPa and an elongation of 16.6%.

2.2.8 Inconel 625 - HSLA

The manufacturing of FGMs specimens by combining Inconel 625 and HSLA using a WAAM system was recently studied [69–72]. The FGMs was created through a functional gradient from 100% Inconel 625 with 0% HSLA to 0% Inconel 625 with 100% HSLA. The combination of these two materials can be beneficially used in specialised environments with harsh operating conditions, such as pressurised water reactor system, as well as in the connecting parts of pipes and safety-critical areas. The first challenge addressed aimed to produce FGMs specimens of Inconel 625 and HSLA steel using the WAAM process in conjunction with synchronous Electromagnetic Stirring (EMS) [71]. It was concluded that the synchronous EMS technology allowed a refinement of the microstructure with reducing primary dendrite spacing by 22.6% and enabled an increase in tensile strength from 512 MPa to 563 MPa. In a second study, the WAAM technique was combined with EMS to manufacture Inconel 625-HSLA steel FGMs [70]. The effects of EMS on the produced FGMs were then analysed, focusing on microstructures, precipitations,

mechanical properties, and corrosion resistance. The use of EMS proved effective in optimising the formability of FGMs samples, demonstrating that this technique enabled a significant refined the microstructure of the FGMs. Moreover, the study demonstrated that EMS not only increased the tensile strength and microhardness of the FGMs but also optimised their corrosion behaviour. In Zhang et al. [72] an Optimized Transition Strategy (OTS) was developed to modify the Inconel 625-HSLA steel FGMs manufactured by WAAM with the aim of eliminating the poor performances graded region. In this study, the microstructures, precipitation and mechanical properties were investigated in room temperature and $700^{\circ}C$. Finally, in the study by Zhang et al. [69], FGMs of Inconel 625-HSLA steel were manufactured with In-situ Heat Treatment (IHT) performed during the WAAM process to enhance performance. The effect of IHT on the FGMs was evaluated by analysing their microstructures, precipitates, and mechanical properties. It can be concluded that there was an improvement in tensile strength along with building direction from 512 ± 15 MPa to 602 ± 10 MPa.

2.2.9 Ti6Al4V - Inconel 625

In the study by Han et al. [73], the dual-WAAM technology was applied to produce a FGMs with Ti6Al4V to Inconel 625. The functional gradient in this FGMs was achieved through 100% Ti6Al4V with 0% Inconel 625 to 0% Ti6Al4V with 100% Inconel 625. In this study, the average ultimate compression strength and strain of vertical samples were 1390.25 MPa and 10.96%. Ti6Al4V and Inconel 625 materials, when combined as FGMs, can be applied in extreme environments, including aerospace engineering, nuclear power generation, sensors, biomedical implants, optoelectronic devices, and absorption systems.

2.2.10 Ti6Al4V - SS316L

Chen et al. [74] used Ti6Al4V and stainless-steel 316L (SS316L) wires through a double-WAAM process. This FGM was designed by varying the Fe from 5 at.% to 65 at.%. In this study, surface cracks developed when the atomic fraction of Fe reached a percentage of 50 at.%, attributed to the formation of Fe_2Ti phase. The fracture extended to layers with 35 at.% Fe. The microstucture of the FGMs produced was then studied using an optical microscope and a Scanning Electron Microscope (SEM). To investigate the phase composition of the produced material an XRD was used. With this material characterisation, it was possible to conclude that the maximum microhardness of the FGMs produced was 945 HV0.2 when the FGMs had a content of 60 at.% Fe. These two materials have some engineering applications in environments that require an excellent corrosion resistance, high strength-to-weight ratio and low cost.

2.2.11 Inconel 625 - stainless steel 316L

Ahsan et al. [75] manufactured a Bimetallic Additively Manufactured Structures (BAMS) by combining Inconel 635 and austenitic stainless steel 316L (SS316 L) through the WAAM process. After the part was manufactured, electron microscopy and elemental mapping were used to characterise the two materials in the manufactured part. Extensive analyses were carried out to characterise the phenomena of interfacial crystallographic growth and elemental diffusion. This analysis revealed that at the crystalline interface, the grains were elongated in one direction. To assess the mechanical properties of the fabricated material, microhardness and tensile tests were performed, along with a study of the fracture surface. The hardness values ranged from 220 to 240 HV for both materials. The tensile test results indicated that the material had a tensile strength of 600 MPa and an elongation of 40%. This study demonstrated the potential of manufacturing FGMs with the combination of Inconel 635 and austenitic stainless steel (SS316 L) through the WAAM process. Inconel 625 and austenitic stainless steel are two materials widely used in bimetallic structures applied to the aerospace, energy, petrochemical, chemical and marine industries.

The study Yu et al. [78] investigates how different composition gradients affect the microstructure and mechanical properties of FGMs made from 316L stainless steel and Inconel 625. Using dual wire plasma arc additive manufacturing, the researchers produced FGMs with different compositional transitions. They discovered that certain compositional regions, particularly those containing approximately 20 wt% Inconel 625, exhibited grain boundary cracking and reduced mechanical properties. By adjusting the composition gradient to exclude these problematic regions, the study achieved FGMs with improved microhardness and tensile strength and identified an optimum composition at 50 wt% Inconel 625. This optimisation strategy effectively improves the overall performance of FGMs by eliminating areas prone to defects and poor mechanical properties.

2.2.12 Stainless steel 308L - Inconel 625

Stainless steel 308 L and Inconel 625 can be used as base material for the production of FGMs through the WAAM processs with the a functionality gradient [79–82]. The combination of these two materials seems to be appropriate since nickel-based alloy reveals high strength and an excellent high-temperature performance, although stainless steel has good corrosion resistance and low cost. Li et al. [79] detailed the creation of a functional gradient during layer deposition, where the composition transitioned from 100% Stainless steel 308L at the base layers, through a gradient between the two materials in the middle, to 100% Inconel 625 at the end, resulting in FGMs with a compositional transition aligned with the direction of the torch travel. The manufactured FGMs was analysed for its chemical composition, microstructure, phases, and mechanical properties. In Li et al. [82], the focus shifted to the analysis of crack formation during the deposition of FGMs made of Inconel 625 and Stainless steel 308L. This research investigated the type, location, causes, initiation, and propagation of these cracks. Optimisation measures

were also studied in order to eliminate the cracks. Li et al. [80] identified that there was a weakening of the WAAM layers in the range of 10% to 50% of Inconel 625 with a reinforcement of a local Nb alloy in order to improve the strengthening of the matrix solution. After the addition of this Nb alloy, the tensile strength increased from 385 MPa to 510 MPa and the elongation increased from 8.3% to 16.9%. In [81], two wire-feeding strategies were identified that impact the modelling, microstructure, and mechanical properties of FGMs prepared by WAAM, with the aim of improving the manufacturing process of 308L stainless steel-Inconel 625 FGMs.

2.2.13 Stainless steel 304L - Inconel 625

Yoo, Lee, and Kim [83] produced Inconel 625–Stainless steel 304L FGMs using WAAM to evaluate the feasibility of the process with these two materials. Bimetallic structures, is often prone to defects due to abrupt changes in microstructure and properties between dissimilar metals. This study showed that this FGMs can be improved using a combined LMD and the WAAM process. This FGMs was produced with a functional gradient ranging from 75% Stainless steel 304L and 25% Inconel 625 to 25% Stainless steel 304L and 75% Inconel 625. The article explored the microstructure, tensile properties at room temperature, and microhardness of the material. The microhardness of the LMD–WAAM samples increased with higher Inconel 625 content. The fracture patterns differed between the LMD–WAAM and WAAM samples, with the former showing fractures near the interface between different Inconel 625 content layers, while the latter fractured near the Stainless steel 304L interface. The LMD–WAAM samples demonstrated an 8% higher tensile strength compared to those fabricated using only the WAAM process, with tensile strength being inversely proportional to the laser power used during fabrication.

2.2.14 Duplex stainless steel - Carbon-manganese steel

Marine risers are cylindrical conduits designed to facilitate the transportation of crude oil and gas from the wellhead to offshore facilities. These structures are subjected to corrosion from harsh environmental conditions on the outside, and to oxidation caused by the crude oil and gas on the inside. Chandrasekaran, Hari, and Amirthalingam [26] explored the development of FGMs, specifically for marine risers and manufactured by the WAAM process. The FGMs developed for marine risers were achieved by integrating duplex stainless steel on the inside of the cylindrical conduit with carbon-manganese steel on the outside. In FGMs produced by WAAM, it is common to observe material diffusion between the different layers, resulting in a coalescence zone where the two materials merge.

Following the production of the FGMs, a series of experimental tests were conducted to characterise the material. XrayCT was employed to detect any defects that occurred during the manufacturing process. Tensile tests were performed to obtain the stress-strain curve, while a detailed microstructure analysis was carried out on the FGMs. EDX analysis was

used to identify the elemental composition of the sample. Additionally, a micro-hardness test was conducted to determine the Vickers hardness values, and fractography was employed to analyse the fracture characteristics of the sample. Finally, a corrosion test was carried out to assess the corrosion resistance of the two constituent materials.

2.2.15 Low-carb steel - stainless steel 316L

Ahsan et al. [85] conducted an investigation where an additively fabricated BAMS was developed with low carbon steel (LCS) and stainless steel 316L (SS316L) using the WAAM process. WAAM technology enables the creation of FGMs by building BAMS structures layer by layer. After fabrication, the material underwent heat treatment within a temperature range of 800 °C to 1100 °C. Following heat treatment, the failure site of the FGMs shifted from low carbon steel to stainless steel. To analyse the microstructural and mechanical properties of the manufactured material, several tests were conducted: SEM, EDX spectroscopy, and the Vickers hardness test.

2.2.16 Low alloy steel - Austenitic stainless steel

In this study Ayan and Kahraman [86] a low alloy steel and austenitic stainless steel FGMs was manufactured by WAAM technology. The functional gradient was produced in an intercalary way, the first 3 layers were fabricated with low alloy steel, and the other layers continued in order as 4th layer austenitic stainless steel, 5 layers low alloy steel, 6 layers austenitic stainless steel. In this way, a large number of interfaces were generated. After manufacture, the FGMs was mechanically characterised according to hardness, tensile, and fatigue tests. It was concluded through XRD analysis that the FGMs regions are predominantly ferritic. In the hardness analysis, the FGMs showed different hardness for each layer produced. The highest hardness value was reached in the low alloy steel layers. Finally, it can be concluded that the FGMs structures with these two materials have strong mechanical properties when produced by WAAM.

2.2.17 Super austenitic stainless steel 904L - Hastelloy C-276

Rajesh Kannan et al. [87] investigated the manufacture of the FGMs of super austenitic stainless steel SS904L and Hastelloy C-276 using WAAMs technology. These FGMs are potentially applicable in harsh environments, such as in the oil and gas industries and nuclear power plants, where they could be used in the manufacturing of steam generators and reformers. The FGMs were produced by depositing 22 layers of SS904L, followed by 22 layers of Hastelloy C-276. This study specifically evaluated the fatigue behaviour and microstructure of the fabricated FGMs. Tensile tests revealed a yield strength of 311 MPa and a tensile strength of 681 MPa. Fatigue testing showed the material had a fatigue resistance of 156 MPa after enduring 2×10^6 cycles. The failure was initiated and

occurred in the weaker SS904L region due to the varying microstructural characteristics along the build direction.

2.2.18 HSLA - Si-Bronze

The study El-Husseiny et al. [91] explores the creation of FGMs by sequentially depositing HSLA steel and silicon bronze (Si-Bronze) using WAAM. The primary focus of the research is to understand the microstructural evolution, with particular attention to the fusion zone between these dissimilar alloys, and to assess their mechanical properties.The findings indicate a high level of structural integrity in the fabricated bimetallic walls.An analysis was conducted on a 9 mm interface for microstructural changes, elemental distribution, and microhardness along the build direction. The microhardness profiles revealed a gradual transition through the diffusion zone without the presence of intermetallic compounds. Tensile tests demonstrated that fractures occurred in the Si-Bronze region, as anticipated, and bending tests indicated good ductility at the joint between the two alloys. Direct shear tests indicated a shear strength comparable to that of HSLA steel, thus confirming the feasibility of using WAAM technology to fabricate HSLA steel/Si-Bronze FGMs.

2.2.19 Ni - Cr - Mo

The study Singh, Singh, and Gupta [92] examines the development of Ni-Cr-Mo-based FGMs using the WAAM technique. The investigation focuses on the effects of compositional variations and post-deposition friction stir processing on the metallurgical and mechanical properties of the FGMs. The as-deposited samples exhibited a combination of dendritic and columnar grains, while the post-processed samples showed refined, recrystallized grains. Furthermore, microhardness measurements revealed a gradual increase from 147 to 335 HV from the bottom to the top of the samples in both conditions, attributed to the presence of CrNi3 and MoNi4 precipitates. Tensile tests also indicated a continuous increase in strength from the bottom to the top of the samples under both conditions.

2.2.20 Stainless steel 308L - Stainless steel 347

The study [93] investigates the fabrication of stainless steel 347/308L components using the Wire and Arc Additive Manufacturing (WAAM) technique. The research focuses on analysing the resulting microstructure and mechanical properties of the fabricated materials. Furthermore, the mechanical properties, including tensile strength and elongation, are comparable to those of conventionally manufactured 308L stainless steel, thereby suggesting that the WAAM process is a viable method for producing these materials for industrial applications.

2.2.21 Other materials

Reisgen, Sharma, and Oster [94] explored the potential for generating structures with chemical gradients by varying the wire feed speeds in a multi-wire WAAM process. In this study, three combinations of two materials were produced, each with different chemical compositions. The chemical elements involved in these combinations included C, Mn, Si, S, P, Ni, Cr, Nb and Mo. The gradient was achieved through a linear transition where the composition of each material varied from 0% to 100%. To produce a FGM with two materials, the process required two wires set at an angle of 30° between them and an angle of 20° between the wire and the workpiece surface. The results of this study demonstrated that it is possible to alter the chemical composition of the molten pool by adjusting the wire feed speeds during the manufacturing process.

2.3 Characterisation of Functionally Graded Materials through mechanical tests

Following the manufacture of FGMs, it is essential to characterise the structured material. A variety of techniques have been employed for this purpose, including microstructural analysis, EDX analysis, hardness measurements, fractography, corrosion testing, phase identification, XrayCT, and mechanical testing.

2.3.1 Microstructure analysis

Microstructural analysis is an important method for the characterisation and evaluation of products and materials. This type of analysis enables the determination of parameters such as grain size, coating thickness, porosity, and pore structure. Numerous studies in the literature have used microstructural analysis to characterise FGMs [26, 75, 85].

2.3.2 EDX analysis

EDX analysis is an analytical technique employed for elemental analysis or chemical characterisation of samples. This method involves the interaction between an excitation source, typically X-rays, and the sample. Several studies in the literature have utilised EDX analysis for the characterisation of FGMs materials [26, 63, 68].

2.3.3 Hardness measurements

Hardness is a material property that describes its resistance to plastic deformation. Various methods exist for measuring hardness, typically by assessing the depth or area of an indentation made by an indenter of a specific shape, under a given force, and over a set time period. The three standard test methods for determining material hardness are Brinell, Vickers, and Rockwell. Considerable interest has been shown in measuring the hardness of FGMs, given the varied compositions these materials can possess [95–97].

2.3.4 Fractography analysis

Fractography is a method used to study the failure and fracture surfaces of materials. Analysing the characteristics of fracture surfaces can help identify the causes of material or component failure. This technique has been employed to characterise FGMs produced by WAAM, as documented in several studies [26, 85].

2.3.5 Corrosion test

Corrosion tests are employed to study the release of components into solution as materials degrade. Various test methods exist to assess material performance in specific environments over a projected service life. Numerous studies have explored the corrosion behaviour of manufactured FGMs [64, 98], including those produced by WAAM as detailed in [26].

2.3.6 Phase identification

Phase identification, one of the most important applications of XRD, is used to analyse the phase evolution of materials involved in the production of FGMs. Several studies have employed this technique to characterise FGMs manufactured by WAAM [22, 24, 61, 63–67].

2.3.7 XrayCT

XrayCT is a non-destructive technique that provides detailed information about the internal structure of materials, from metre to nanometre scales. By leveraging the penetrating power of X-rays, this method captures a series of two-dimensional images, which can then be reconstructed into cross-sections of the material under analysis. This process also enables three-dimensional greyscale analysis, known as a tomogram. One of the main advantages of XrayCT is its non-destructive nature, meaning the material or component does not need to be damaged for characterisation [99]. This technique has been widely used in the literature for the characterisation of FGMs [100, 101].

2.3.8 Mechanical tests

Mechanical tests are carried out to characterise material properties that describe the constitutive equations for the material. These tests provide critical information on the stiffness, strength and ductility of materials under different loading conditions. In a classical tensile mechanical test, key mechanical properties measured include ultimate tensile strength, breaking strength, maximum elongation, and reduction in area. From these measurements, mechanical parameters such as Young's modulus and Poisson's ratio can be determined [102]. While tensile testing is commonly used for isotropic materials, it has also been employed to characterise FGMs [22, 27, 61, 64].

As outlined in Table 2.2, the following techniques have been identified in the literature review for the purpose of characterising FGMs.

Table 2.2: Summary of characterisation techniques for FGMs.

Technique	Purpose	Parameters analysed	References
Microstructure	Internal structure analysis	Grain size, coating thickness, porosity	[26, 75, 85]
EDX	Elemental analysis	Chemical composition, present elements	[26, 63, 68]
Hardness	Resistance to plastic deformation	Brinell, Vickers, Rockwell hardness	[95–97]
Fractography	Fracture surface analysis	Failure modes, crack propagation	[26, 85]
Corrosion Testing	Degradation assessment	Performance in corrosive environments	[26, 64, 98]
Phase Identification (XRD)	Crystalline phase analysis	Phase identification, crystalline composition	[22, 24, 61, 63–67]
XrayCT	Non-destructive 3D imaging	Internal structure, phase distributio	[99–101]
Mechanical Testing	Mechanical properties evaluation	Strength, ductility, Young's modulus, Poisson's ratio	[22, 27, 61, 64]

EDX: Energy-dispersive X-ray; X-ray CT: X-ray Computed Tomography.

2.3.9 Inverse mechanical characterisation

The identification of constitutive parameters can typically be carried out through two primary methodologies,. On the one hand, mechanical tests are employed to characterise relevant material properties, based on loading and geometry configurations that yield homogeneous and simple kinematic deformation fields, thereby allowing to closed-form solutions that relate the parameters to the measurements. On the other hand, advances in full-field deformation techniques have paved the way for a new approach, which conversely exploits heterogeneous stress and strain distributions across the region of interest to achieve material characterisation [53, 103]. A key feature of this approach is its high flexibility in the design of new mechanical tests, enabling multiparameter material identification within a single test configuration [52, 104, 105].

2.3.9.1 Characterisation of metallic additive manufacturing materials: classical approach

The mechanical characterisation of metallic materials produced by AM, notably by DED processes such as WAAM, has typically been carried out using classical mechanical tests. The primary objective of these studies is the manufacturing process itself; therefore, conventional mechanical characterisation is generally performed on homogeneous specimens that are representative of the functional volume of the parts.

Recent research on DED-based AM has increasingly focused on the mechanical, metallurgical, and functional performance of the manufactured parts, as summarised in

Table 2.3. The most studied materials include steel alloys (*e.g.* 316L, ER70S-6 and carbon steel), titanium alloys (*e.g.* Ti-6Al-4V), aluminium alloys (*e.g.* Al-5Mg, 5356) and nickel- and cobalt- based superalloys [86, 106–108]. For that general purpose, the commonly methodologies applied to AM metals include tensile testing, hardness measurements, detailed microstructural analysis via optical and electron microscopy, corrosion testing, impact testing and fractography [86, 108–111]. The types of specimens employed vary from specimens extracted in different orientations (vertical and horizontal), FGMs, bimetallic or multilayer specimens, as well as parts with geometries optimised [112–114]. A number of studies have also analysed the effects of post-production heat treatment and process parameters, including deposition speed, interlayer cooling time and the use of recycled powders, on the microstructure and mechanical performance of materials [109, 115, 116]. The results obtained demonstrate significant mechanical anisotropy, thereby reinforcing the importance of process control and the implementation of heat treatments in order to enhance the final properties of the material.

Table 2.3: Summary of materials, processes, tests, and objectives reported in the characterisation of metallic AM using DED processes.

Material	Process	Specimen type	Methods	Objective	References
Dissimilar steels, bronze, bimetallic	WAAM	Multilayer and bimetallic specimens	Tensile test, hardness, microstructure	Analysis of interfaces, functional gradients and transition zones	[86, 107, 117]
Structural steels, carbon steels	WAAM	Vertical and oriented test specimens	Tensile test, hardness, microstructure	Optimisation of parameters and effects of heat treatment	[109, 112, 113]
Titanium and Ti-Nb alloys	DED (Laser)	Multilayer and gradient samples	Tensile test, hardness, microstructure	Influence of recycling, functional gradients and interfaces	[108, 114, 116]
Ni and Co–Cr superalloys	Hot-wire TIG and DED	Post-treated specimens	Tensile test, hardness, fractography	Optimisation of post-heat treatment and mechanical evaluation	[110, 118]
Aluminium alloys, bronze alloys	WAAM	Oriented and multilayer specimens	Tensile test, hardness, fractography	Study of anisotropy, porosity and multidirectional properties	[111, 115, 119]
316 stainless steel with tungsten	DED (Laser)	Modified surface layers	Tensile test, corrosion, microstructure	Improvement in corrosion resistance and mechanical properties	[120]

2.3.9.2 Characterisation of metallic additive manufacturing materials: full-field approach

Significant advances have been achieved in the mechanical characterisation of metallic materials through the integration of full-field experimental techniques with inverse identification strategies. This paradigm shift combines full-field measurements, notably DIC, with advanced inverse approaches such as the VFM [121–123] and FEMU [124–126], providing a concise and more robust characterisation of the material parameters governing elasto-plastic constitutive behaviour. These methodologies have been shown to enable the extraction of high-fidelity constitutive parameters from non-standard tests, including

those involving geometric complexity, material heterogeneity, or weld-affected zones [127, 128].

These techniques have been applied to a range of metallic materials, including aluminium alloys [129], high-strength steels [130], and welded structures [128], where anisotropy [131], strain-rate effects and damage evolution are prevalent. Inverse approaches have been shown to facilitate the identification of flow curves and the calibration of sophisticated constitutive models, including Hill, Barlat and GTN models, which frequently incorporate strain-rate sensitivity and shear-driven mechanisms [132–134].

The experimental setups extend beyond uniaxial testing [135], encompassing biaxial configurations [136], notched specimens [124], and custom-designed weld zone tests [137]. It is imperative that tests are conducted at varying orientations and strain rates for the purpose of calibrating diretionally sensitive or rate-dependent models [135, 138, 139].

The VFM is favoured for its computational efficiency and direct use of equilibrium equations with full-field data, especially from DIC [137, 140]. Meanwhile, FEMU provides flexibility and is well-suited for the identification of complex or non-linear constitutive behaviours through iterative optimisation [141, 142]. It has been demonstrated that both approaches are robust even under non homogeneous deformation fields, a phenomenon that is commonly observed in miniaturised or welded specimens [121, 143].

Recent studies have harnessed machine learning in combination with data from FEMU/VFM methodologies applied to heterogeneous tests, achieving enhanced resilience to experimental noise and significantly faster convergence in parameter identification [144, 145]. The compatibility of VFM and FEMU with numerical models and imaging tools positions them as core enablers of hybrid digital twins in material science [104].

2.3.9.3 Characterisation of gradient-based metallic materials: full-field approach

Recent studies have highlighted the increasing importance of inverse methods based on full-field measurements for the mechanical characterisation of gradient-based metallic materials, particularly in welded joints and FGMs produced by AM. These materials are inherently heterogeneous due to phase transitions or compositional gradients, making conventional testing unsuitable for capturing their behaviour. In response, a new generation of experimental approaches has emerged, shifting the focus from traditional standardised tests towards integrated strategies that combine full-field measurements with computational inversion techniques to extract rich, spatially distributed information about material behaviour [103].

Table 2.4 summarises studied that apply inverse identification methods, such as VFM and FEMU, to welded joints, FGMs, and other heterogeneous metallic systems. These examples highlight how full-field measurements, often supported by DIC, have been employed to identify spatially varying constitutive parameters under diverse configurations. Reported applications include the evaluation of microstructural anisotropy [131], the influence of thermal gradients [146], and the characterisation of local heterogeneities

[147]. Beyond providing richer constitutive descriptions, these methodologies also reduce the number of required independent tests, limit testing time, and mitigate variability in experimental campaigns [148].

Table 2.4: Summary of studies on the mechanical characterisation of gradient-based metallic materials, including welded joints and FGM, using inverse methods such as VFM and FEMU in combination with full-field measurements.

Material	**Mechanical test**	**Inverse method**	**Objective**	**Reference**
Aluminum welded joint	Tensile test	FEMU	Identification of strength variation in HAZ	[128]
FSW joint – AA6061-T6	Tensile test FEM + DIC	VFM	Identification of local yield stress	[149]
2024-T3 aluminum (FSW)	Tensile test	VFM	Identification of elastic and plastic properties	[147]
Ti–6Al–4V (EBW)	Tensile test with DIC	VFM	Identification of elastic and plastic properties	[150]
FSW Aluminum 2024-T3	Tensile test + DIC	VFM	Identification of local properties	[151]
Composite with FBG sensors	Delamination (monotonic and fatigue)	FEMU	Analysis of delamination using FBG and numerical inversion	[152]
Multi-steel spot weld (DP600 and mild steel)	Not specified	FEMU	Modelling and identification of connector behaviour	[153]
Ductile adhesive	Tensile test at low temperatures	FEMU	Modelling adhesive behaviour under low temperature	[154]
Various metals and polymers	Not applicable	FEMU	Review of inverse identification in crash and impact engineering	[155]
Ductile adhesive	Tensile test at –40°C	FEMU	Identification of constitutive properties under thermal loading	[156]
2 mm thick Al-Mg alloy laser-welded	Tensile test + DIC	VFM	Identification of local elasto-plastic properties	[157]
2.5 mm thick aluminum alloy laser-welded	Tensile test + DIC + FEM	VFM	Identification of elasto-plastic parameters with kinematic hardening	[123]
Not specified	Not specified	FEMU	Structural source identification	[158]
FSW Aluminum alloy (Al-Cu)	Simulated tensile test	FEMU	Simulation of damage and fracture using GTN inverse fitting	[148]

In the context of welded metals, Kim et al. [143] used VFM to identify the local yield stress variation across the weld line in Friction Stir Welding (FSW) joints [143]. Similarly, Sutton et al. (2008) and [150] compared VFM with the Uniform Stress Method, showing that VFM captures local elastic and plastic properties with greater fidelity [147, 150]. Shahmirzaloo et al. [151] employed DIC in conjunction with the VFM to map local stress–strain curves across different zones of friction-stir-welded Al2024 joints—revealing that the advancing side of the thermo-mechanically affected zone exhibits significantly

lower Young's modulus and yield strength compared to the base metal. Similarly, Jiang et al. [157] combined DIC measurements with VFM to identify an elasto-plastic damage-coupled constitutive model of laser-welded aluminium alloy, extracting spatially resolved strain fields near the weld region. Nazemi et al. [128] applied FEMU to quantify property gradients in the heat-affected zone (HAZ), demonstrating the robustness of the approach when full-field data is noisy or incomplete. Studies by Cognard et al. [154, 156] and Markiewicz et al. [155] extended the use of these techniques to hybrid and adhesive joints, assessing performance under mechanical and environmental conditions.

In the context of welded materials, Nayakanti and Subramanian [128] utilised the FEM to characterise the heterogeneous mechanical behaviour of the heat-affected zone (HAZ) in aluminium joints. In a similar vein, Stutz et al. [152] employed FEM in conjunction with FBG sensors to investigate delamination in composite structures. These approaches have the potential to be adapted for the analysis of transition zones in metallic components. In the case of FGMs, Lezgy-Nazargah [159], demonstrated the ability of FEMU to reconstruct spatial constitutive distributions from full-field displacement data acquired via DIC. These works confirm FEMU's potential in addressing complex property gradients in functionally graded structures.

When it comes to FGMs, inverse methods are essential for understanding materials with intentionally designed spatial property gradients. Nayakanti et al. [59] introduced the eigenfunction VFM, applying it to a uniaxially loaded FGM plate with an exponential Young's modulus variation. The study successfully demonstrated that spatially varying elastic parameters can be identified with high accuracy using virtual fields derived from the material's deformation eigenmodes. Other works examined AM-produced FGMs made of metals like Ti-Al, Fe-Ni, Ni-Ti, or Cu-Al, frequently manufactured via WAAM. These studies—such as those by Zeng et al. (2020) and Yu et al. (2022)—used DIC in tandem with FEMor FEMU to evaluate phase transformation, hardness evolution, and property transitions within multilayer metallic structures [24, 78]. Complex architectures, such as Ta-Mo-W and Inconel-steel FGMs, have also been studied, particularly in high-temperature or corrosion-resistant applications [68, 69].

Nayakanti et al. [59] studied the material properties of FGMs proposing the eigenfunction VFM. In this study, a plate with a circular hole was considered, submitted to uni-axial tension. FGMs was produced with an exponential variation of Young's modulus. To perform this exponential variation, 50 layers of 0.4 mm were made in the piece. Eigenfunction is a variant of VFM that uses the eigenfunctions of the strain fields measured as virtual fields [160–162]. This strain fields were generated by a finite-element (FE) solution for a plate with circular hole made by FGMs. This study showed the success of using the eigenfunction VFM to determine the material properties of a FGMs linear elastic. These material properties showed results very close to the real values. The method involves analysing the link between measured data and virtual fields created from the FGM's eigenfunctions. The eigenfunctions indicate the basic deformation modes in the material, from which virtual fields are constructed to compare with experimental measurements,

facilitating the extraction of elastic constants. The advantages of eigenfunction VFM are emphasized in the paper, including their usefulness in dealing with complex and inhomogeneous materials such as FGMs, and their ability to account for variations in material properties across space. The paper showcases a versatile application of the method on various FGMs structures in materials science and engineering, where comprehension of mechanical behaviour is crucial. It also establishes the Eigenfunction VFM as a promising technique for characterising elastic constants of functionally graded materials. The paper presents a computational method for characterising the elastic constants of FGMs that can provide insights into their mechanical properties, aiding researchers and engineers in designing FGMs for specific applications. This valuable contribution to the field of materials science and engineering enhances the understanding and design of FGMs. Researchers and professionals with an interest in FGMs and their mechanical behaviour may find the eigenfunction VFM outlined in this paper to be a valuable resource for their research.

2.3.10 Mechanical characterisation of functionally graded materials using inverse identification methods

Identifying the mechanical properties in FGMs inversely can be a complicated and computational process, especially for FGMs with intricate property gradients. Nevertheless, it is an essential step to create FGMs with customised mechanical properties in specific applications of aerospace, materials science and structural engineering.

Nayakanti et al. [59] studied the material properties of FGMs using eigenfunction virtual fields method. The Eigenfunction Virtual Fields Method, a computational technique for determining the elastic properties of FGMs. In this study, a plate with a circular hole was considered, submitted to uni-axial tension. FGMs was produced with an exponential variation of Young's modulus. To perform this exponential variation, 50 layers of 0.4 mm were made in the piece. Eigenfunction is a variant of virtual fields method that uses the eigenfunctions of the strain fields measured as virtual fields [58]. This strain fields were generated by a Finite Element (FE) solution for a plate with circular hole made by FGMs. This study showed the success of using the eigenfunction virtual fields method to determine the material properties of a FGMs linear elastic. These material properties showed results very close to the real values. The method involves analysing the link between measured data and virtual fields created from the FGMs's eigenfunctions. The eigenfunctions indicate the basic deformation modes in the material, from which virtual fields are constructed to compare with experimental measurements, facilitating the extraction of elastic constants. The advantages of Eigenfunction Virtual Fields Method are emphasized in the paper, including their usefulness in dealing with complex and inhomogeneous materials such as FGMs, and their ability to account for variations in material properties across space. The paper showcases a versatile application of the method on various FGMs structures in materials science and engineering, where comprehension of mechanical behaviour is crucial. It also establishes the Eigenfunction Virtual Fields

Method as a promising technique for characterising elastic constants of functionally graded materials. The paper presents a computational method for characterising the elastic constants of FGMs that can provide insights into their mechanical properties, aiding researchers and engineers in designing FGMs for specific applications. This valuable contribution to the field of materials science and engineering enhances the understanding and design of FGMs. Researchers and professionals with an interest in FGMs and their mechanical behaviour may find the Eigenfunction Virtual Fields Method outlined in this paper to be a valuable resource for their research.

2.4 Full-field measurement techniques: Digital Image Correlation

Several FFOTs are currently available providing full-field deformation measurements across a whole region of interest, for different purposes. They can be applied over a spectrum of different magnifications, from micro to structural scales of observation. For the purpose of this review, by in situ it is understood monitoring that are taking place during a physical event. Hence, a research question can be raised concerning what optical techniques will be most suitable or have been already applied for in situ monitoring and for what specific purpose.

A survey of published research on the topic and oriented review was carried out to answer this question. The SciVerse Scopus database was used to collect relevant publications using predefined searching keywords referring both to a given optical technique and in situ measurement. This strategy was adopted for the sake of reproducibility in defining the scientific methodology. A search for title, abstract and keywords was performed assuming DIC, grid method, electronic speckle pattern interferometry (ESPI) and moiré interferometry. Other optical techniques were not found relevant for the analysis. Figure 2.1 shows, in percentage, the amount of publications fulfilling such criteria. Generically, it can be concluded that DIC is the most used optical technique for measurements.

Furthermore, Figure 2.2 shows the evolution over time, since the year of 1990, of the number of publications crossing the searching keywords of the specific FFOT and in situ measurement. As it can be reinforced, there has been an increasing interest on DIC, particular in recent year, when compared to other counterpart FFOTs. Therefore, in the following, only the DIC technique will be actually addressed.

2.5 Tensile test with Digital Image Correlation

Tensile testing, when combined with DIC, has been extensively applied in the study of different classes of materials, thus enabling the comprehension of deformation, damage, and fracture phenomena at multiple scales.

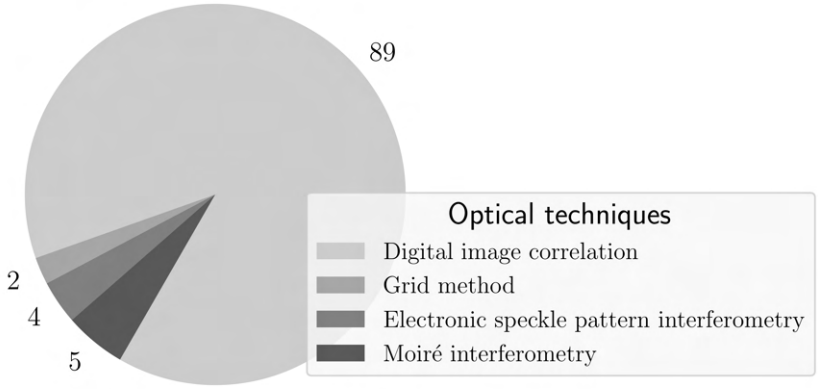

Figure 2.1: Number of publications in Scopus for different full-field optical techniques (units: %).

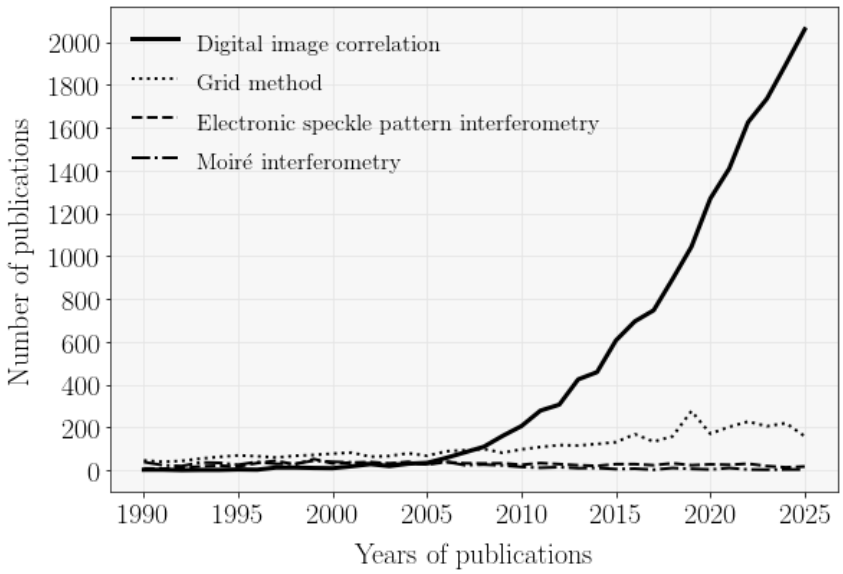

Figure 2.2: Number of publications for the different optical techniques.

Aluminum and alloys: A number of studies have applied tensile and DIC to aluminium alloys, both in welded joints and in structural alloys. For instance, Ahn et al. [163] investigated the effect of welding speed on AA2024-T3, while Li et al. [164] analysed how Fe content affects damage mechanisms in A319 aluminium. Other works highlight the behaviour of aluminium alloys under specific conditions, such as hydrogen environments [165], composite joining processes [166] and anisotropic behaviour in alloys produced by laser powder fusion [167–169]. These studies demonstrate the importance of DIC for characterising deformation heterogeneities, anisotropic ductility, and failure mechanisms in aluminium alloys.

Steels and Ferrous Alloys: The combined use of tensile and DIC is also common in high-strength steels and stainless steels. Kasvayee et al. [170, 171] studied the distribution

of strain and location of cracks in ductile irons. In contrast, Janeiro et al. [172] and Ren et al. [173] analysed the deformation-induced martensitic transformation and the effect of grain morphology in high-strength steels. More recent work has examined the role of non-metallic inclusions and the influence of mesoscopic segregation in advanced steels. Similarly, Kim et al. [174] used DIC in conjunction with in-situ EBSD to understand deformation in multiphase steels. These results confirm the relevance of DIC in analysing local heterogeneities and hardening mechanisms.

Titanium and Ti-based Alloys: The focus of this study is titanium and titanium-based alloys. In their seminal contributions, Gao et al. [175], Ling et al. [176], Shen et al.[177], Shi et al. [178], Statnik et al. [179], and Wang et al. [180] have explored the deformation heterogeneity and plastic anisotropy of titanium alloys manufactured by additive or hybrid methods. The present studies highlight the effectiveness of DIC in identifying stress concentrations and fracture phenomena in advanced alloys produced by additive manufacturing or laser repair.

Composites and Structured Materials: In the field of composite and polymeric materials, Djouda et al. [181] and Hamouche et al. [182] analysed structures produced by additive manufacturing and reinforced composites, while Moutrille et al. [183] studied composite/aluminium adhesive joints. Salem et al. [184] focused on dissimilar welding interfaces in stainless steels, while Sun et al. [185] evaluated aluminium matrix composites reinforced with Ti2AlC. The presented illustrations elucidate the versatility of DIC in quantifying deformations within heterogeneous systems and critical interfaces.

Functional Materials and Biomaterials: A number of other studies have addressed a variety of applications: Luo et al. [186] investigated volumetric variations in lithium-ion batteries. Kalnaus et al. [187] studied polymeric separators for Li-ion batteries, while Bretelle et al. [188] analysed biological tissues (porcine skin) under tension. These cases illustrate how DIC transcends the conventional boundaries of metallurgy, extending its application to the domains of functional and biomaterials.

The articles under consideration highlight the importance of employing DIC in tensile tests for gaining insights into the behavior of materials, thereby contributing to the progression of materials science and engineering. Table 2.5 summarizes studies on ductility tests in welded joints, highlighting failure mechanisms, analysis methods and the influence of processes such as GTAW and laser on various materials.

2.6 Material testing 2.0

The application of camera-based full-field measurement techniques in mechanical testing of materials has resulted in the requirement for more sophisticated test setups. This approach is commonly known as 'Material testing 2.0'. Consequently, there has been an increase in more advanced and comprehensive experimental tests [189]. It is essential to distinguish between MT1.0 and MT2.0.

Table 2.5: Summary of studies applying DIC in tensile testing

Material / System	Focus of the study	Key findings	References
Aluminum AA2024-T3 (laser welding)	Effect of welding speed on weld joints	Welding speed influences mechanical properties and deformation patterns	[163]
A319 Al (varying Fe content)	Effect of Fe content on damage mechanisms	Higher Fe promotes different failure mechanisms	[164]
Al-Si (LPBF)	Anisotropic ductility in additively manufactured alloy	Anisotropy linked to microstructure induced by AM process	[167]
Multiphase steels	Strain-induced martensitic transformation, strain localization	DIC quantifies heterogeneities and crack initiation mechanisms	[172–174]
Ductile irons	Strain distribution, crack formation and FEM correlation	FEM–DIC shows consistency; failure governed by strain localization	[170, 171]
Titanium alloys (WAAM, DED, hybrid)	Heterogeneous deformation, plastic anisotropy, stress concentration	DIC highlights non-uniform strain and stress concentration effects	[175–180]
Composites / Polymers (AM, reinforced, joints)	Polymeric structures, adhesive joints, dissimilar welds	DIC captures strain in heterogeneous regions and critical interfaces	[181–185]
Functional materials (Li-ion batteries)	Separators and volume change during cycling	DIC effective in complex strain fields in polymers and electrodes	[186, 187]
Biological tissues (porcine skin)	Effect of sample preservation on mechanical response	DIC enables evaluation of stress softening and permanent set	[188]

Table 2.6: Differences between MT1.0 and MT2.0 [190].

	Advantages	Drawbacks
MT1.0	Simple to exploit Test standards available Inexpensive	Poor in contents Sensitive to boundary conditions Limited applicability
MT2.0	Very rich in contents (fewer tests needed) Less sensitive to boundary conditions Allows to test stress interactions Wide design space Possibility to test specimens "as manufactured"	Complex to exploit More expensive to set up No test standards available

Table 2.6 illustrates the differences between MT1.0 and MT2.0. MT2.0 enables the use of full-field measurements such as DIC due to its ability to handle more complex geometries and loads [190]. Full-field measurements are used to determine mechanical parameters of materials through inverse identification techniques, the two main methods are FEMU [191] and VFM [28]. MT2.0 has several applications for different types of materials, including composite materials [192], metals [193], metallic welds [157], polymers and elastomers

[194], wood [195], and brittle materials [196]. Various test configurations and methodologies make it possible to identify mechanical properties such as orthotropic stiffness, viscoelasticity, viscoplasticity, and high strain rate properties. The MT2.0 methodology has various applications and challenges in material characterization [197]. Quantifying uncertainty when using MT2.0 is challenging due to difficulties in recording and processing test images for reverse identification. Designing optimal test setups is crucial for MT2.0 as it significantly impacts measurement accuracy. Efforts have been made to standardize MT2.0 test methods, although standardization of DIC appears to be unattainable. It can be concluded that MT2.0 heavily relies on full-field kinematic measurements and inverse identification, which are now mature enough to be integrated into new mechanical test methods [198]. Furthermore, while some applications of MT2.0 are becoming standardized, further research is required for heterogeneous materials. It is noted that the design of optimal MT2.0 test configurations remains an area that requires more research, with an emphasis on directing more efforts towards this aspect. The scientific community should conduct pre-standardization research to aid in the development of new MT2.0 test methods that can enhance the efficiency of mechanical testing of materials [190].

2.7 Summary

A summary of all the materials and material combinations already used to produce FGMs using WAAM has been described in this chapter. Several mechanical tests used to characterise FGMs have also been described. Inverse methods have already been applied to heterogeneous materials, additive manufacturing materials and functionally graded materials to characterise materials. Several DIC studies coupled with tensile testing are presented. Material Testing 2.0 is described as a methodology that improves the understanding of experimental testing and enables the use of more complex geometries and loads.

3

Theoretical framework

3.1 Introduction

This chapter introduces some of the theoretical methods that will be used throughout this thesis. The chapter begins with a description of the different AM processes. It then focuses on FGMs, their types, fabrication methods, application areas and future research directions. Next, the full-field measurement technique DIC is explained. Finally, the virtual field method is described as an inverse method.

3.2 Additive manufacturing

In AM, several distinct processes has been developed and are currently available on the market. Based on the fundamental parts and functionality of the equipment, these processes can be grouped into seven distinct categories [199]: (i) directed energy deposition; (ii) powder bed fusion; (iii) vat photopolymerization; (iv) material jetting; (v) binder jetting; (vi) material extrusion; (vii) sheet lamination. In the following, the principal characteristics of each process are described and reviewed.

3.2.1 Directed Energy Deposition

DED technologies require a concentrated energy source and a flow of raw materials, crossing over a common focal zone. Typically, these processes have the presence of an inert shielding gas. The density of energy generated at a specific point melts the raw material in and around that place, giving rise to the formation of melt pools [200]. This procedure can be seen in the video [201].

3.2.1.1 Direct Metal Deposition

The technology of Direct Metal Deposition (DMD) can also be termed by the laser manufacturing process (LMP) or metal shaping laser (MSL). This technology is aided by laser and allows the manufacture of materials by layered deposition, through a melting

sequence, with powder solidification through the laser beam. This process also allows for other applications such as surface treatment (coating) or repair of parts [11, 202].

3.2.1.2 3D Laser Cladding

Laser cladding is a powder injection technology using a laser source. This technology allows the manufacture, repair of pears, coating and rapid metal prototyping. In this process, a laser beam melts the powder particles, forming a thin layer of substrate. A wide variety of deposition materials can be used [203].

3.2.1.3 Direct Laser Deposition

Direct Laser Deposition (DLD) can also be termed by LMD or Laser Engineered Net Shaping (LENS) is based on a laser for the manufacture of functional metal parts. This process is carried out by simultaneously supplying metallic powder and laser energy focused on an area. A relatively high power laser is used to create a melt pool on the substrate, using an inert atmosphere, the powder being injected simultaneously [204]. One of the biggest problems of this process is the residual stresses due to the heating and cooling of the part during its manufacture [205].

3.2.1.4 Wire and Arc Additive Manufacturing

The WAAM process is defined as a combination of an electric arc used as a heat source and a wire applied as a raw material. The WAAM technique is currently being adopted by industry due to its advantages, higher deposition rates and manufacturing of larger parts in less time [60].

3.2.2 Powder Bed Fusion

In Powder Bed Fusion (PBF) technology, a source of energy, such as the laser or the electron beam, is used to digitize each layer of the powder already spread in order to selectively melt the material, thus forming the piece. This consists of an inert atmosphere or partial vacuum process in order to provide protection to the molten metal. In this technology, several parts can be built simultaneously so that the construction chamber can be fully used [206]. This procedure can be seen in the video [207].

3.2.2.1 Selective Laser Sintering

The Selective Laser Sintering (SLS) process uses a poser source to sinter powder to produce pieces of powder materials using one or more lasers that selectively sinter surface particles, that is, layer by layer. This technology is carried out in a closed chamber [206].

3.2.2.2 Selective Laser Melting

Selective Laser Melting (SLM) also known as Direct Metal Laser Sintering (DMLS) is similar to the SLS process. The complete melting of the powder bed particles occurs using one or more lasers [206, 208].

3.2.3 Vat Photopolymerization

Is defined by the liquid photopolymer in a vat that is cured selectively by light activated polymerization. This light is usually the UV radiation from lasers or lamps. The raw material for this process is in a liquid or pasty format [199]. This procedure can be seen in the video [209].

3.2.4 Material Jetting

Material jetting is one of the fastest and most accurate AM technologies. This technology is defined as a process in which droplets of construction material are selectively deposited. These droplets can be a liquid photoplomer or a fused wax, and are solidified through a radiation light source by chemical reaction [210]. This procedure can be seen in the video [211]

3.2.5 Binder Jetting

Is characterised by the selective deposition of a liquid bonding agent in order to join powder materials. Powders, powder mixtures and a liquid bonding agent are the raw materials for this technology. These raw materials are connected through a chemical bond or thermal reaction, thus forming the metallic, ceramic or polymeric part [199]. This procedure can be seen in the video [212].

3.2.6 Material Extrusion

Material extrusion is the most popular, well-known and popular technology of all AM processes. The material used in the process is selectively distributed through a nozzle or orifice until the piece is obtained. The material used is a filament or paste, which is usually thermoplastic or structural ceramics [213]. This procedure can be seen in the video [214].

3.2.7 Sheet Lamination

Sheet lamination uses sheets of material, which are glued together to form an object. These sheets can be made of different materials, such as metal, polymers or powdered ceramic material held together by a binder. The sheets of material are bonded through a thermal reaction or a chemical reaction bond, using ultrasound [215]. This procedure can be seen in the video [216].

3.3 Functionally Graded Materials

FGM is an advanced engineering material where its composition and structure can be changed gradually in order to modify the properties of the material [217]. The term FGM where first proposed in the early 1980s for engineering application because some researchers in Japan had a problem in a space plane project that need a composite material to support high temperature difference [218]. The schematic of a functionally graded conventional material is shown in the figure 3.1. There can be two ways to obtain a gradient, continuous or discontinuous. In figure 3.1 (a) the gradient is achieved through the gradual change with the position of the microstructure and the composition of the material. While in figure 3.1 (b) the gradient is achieved in a stepwise manner.

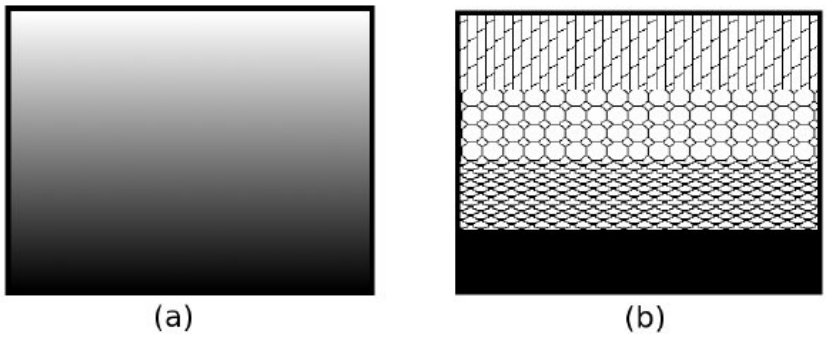

Figure 3.1: Schematic diagram of a functionally graded material (a) continuous and (b) stepwise graded structure [217].

Since the 80s, the interest in commercializing and researching FGM has increased in the scientific community due to the possibility of creating different gradients and to be able to optimize the properties of materials [219]. To prove these considerations, a study was carried out using a SciVerse Scopus database to join all the works published over the years. A keyword used in this research was 'functionally graded material' and a search was performed for the title, abstract and keywords. Figure 3.2 shows the evolution over time, since the year of 1988, of the number of publications. This research shows the growing increase in the number of publications about FGMs over the last few years. In this investigation, it is concluded that there are about 13237 publications on FGM from the late 1980s to the present. On the topic of FGMs, China (3588 publications) leads with the largest number of contributions made to the knowledge of this area, followed by the United States of America (1818 publications) and then Iran (1773 publications).

3.3.1 Functionally Graded Materials in nature

The engineering structures were primarily built from natural materials such as stone, wood and clay. Then, engineering focused on synthetic materials from natural inorganic materials. Thus, metallurgy came to dominate materials engineering. The era of plastics came to develop the characterization of materials through microscopes. This advance

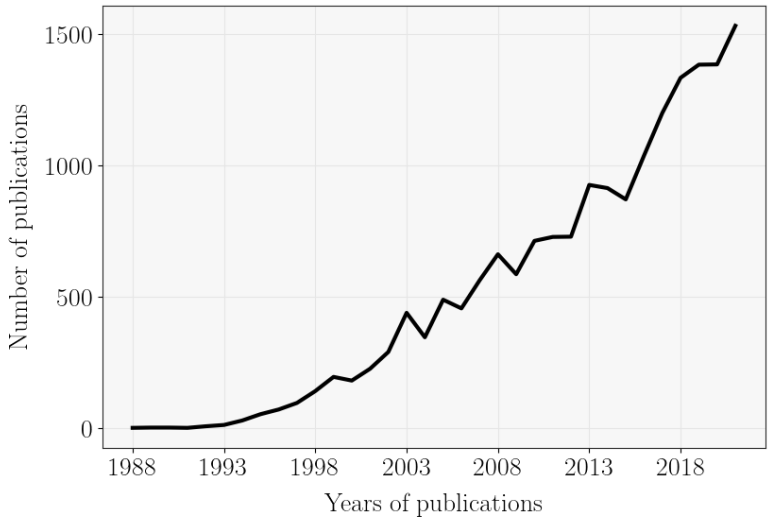

Figure 3.2: Number of publications in Scopus for functionally graded materials.

made possible the existence of more studies on the characterization of the microstructure of materials, which allows the development of new theories about the behaviour of materials. Researchers have gone back to the past for inspiration from nature to the design of natural composite materials [9]. Biological materials served as inspiration for this new class of materials that emerged and which causes a huge interest in mechanics and materials communities, the FGM) [220]. With the latest advances in materials development over the past few decades researchers have provided new opportunities to engineer materials using FGM. In nature, from insect wings to bamboo, signs can be found that the FGMs were selected through the unique coupling between material and stress distribution [221, 222]. With the arrival of new materials and manufacturing processes, it is possible to develop engineered materials with tailored functionally graded structures [223].

3.3.2 Types of Functionally Graded Materials

Materials can change composition, microstructure or porosity across its volume so in that way there are three types of FGM: Chemical Composition Gradient Functionally Gradient Materials, Porosity Gradient Functionally Gradient Materials and Microstructure Gradient Functionally Gradient Materials [218].

3.3.2.1 Chemical composition gradient of Functionally Gradient Materials

In this type of FGMs, the chemical composition varies gradually in the spatial direction. This process can be carried out with a single or multiphase material [224].

Table 3.1: Summary of methods of manufacturing FGMs.

Category	Methods	References
Gas based methods	Chemical vapour deposition	[226]
	Physical vapor deposition	[227]
	Thermal spray	[228]
	Surface reaction process	[229]
Liquid phase methods	Centrifugal casting	[230, 231]
	Combustion	[232]
	Tape casting	[233]
	Slip casting	[234]
	Gel-casting	[235]
	Electrophoretic deposition	[236]
	Chemical solution deposition	[235]
	Laser deposition	[237, 238]
	Directional solidification	[239]
	Sedimentation	[240]
	Electrochemical gradation	[241]
Solid phase methods	Spark plasma sintering	[242]
	Powder metallurgy	[243, 244]

3.3.2.2 Porosity gradient of Functionally Gradient Materials

The porosity gradient FGMs are materials whose gradient pores is achieved by changing the spatial position over the entire volume. The porosity dimension and geometry are modelled in order to achieve certain specifications and properties in the FGM. There can be two types of gradation in the porosity gradient FGM: gradation in pores density and gradation in pores size [224].

3.3.2.3 Microstructure gradient of Functionally Gradient Materials

Microstructure gradient FGM is another type of FGM. In this type of FGM, the microstructure is gradually altered to produce a different microstructure in order to achieve certain properties of the material. Although there are other methods to produce microstructure gradient FGM, the solidification process is a technique in which the surface of the material is tempered, that is, developing surface properties of the material [1]. Controlled heat treatment is another process to achieve the microstructure gradient FGM [224].

3.3.3 Methods of manufacturing Functionally Gradient Materials

Manufacturing techniques can play an important role in the design of FGMs as well as in their properties [225]. There are different approaches to obtain a compositional gradient in the composition of the material, which includes gas based, liquid phase and solid phase methods [3]. Table 3.1 summarizes the manufacturing methods of FGMs by category.

3.3.3.1 Gas based methods

Gas based methods include chemical vapor deposition [226], physical vapour deposition [227], thermal spray [228] and surface reaction process [229].

3.3.3.2 Liquid phase methods

Liquid phase methods include centrifugal casting [230, 231], combustion [232], tape casting [233], slip casting [234], gel-casting [245], electrophoretic deposition [236], chemical solution deposition [235], laser deposition [237, 238], directional solidification [239], sedimentation [240] and electrochemical gradation [241].

3.3.3.3 Solid phase methods

Solid phase methods include spark plasma sintering [242] and powder metallurgy [243, 244].

3.3.4 Areas of applications of Functionally Gradient Materials

Nowadays FGMs show a large variety of applications such as aerospace, automobile, biomedical, defence, electrical/electronic, energy, marine and opto-electronics. This range of applications can be expanded in the future when the production costs of this type of materials are reduced [1].

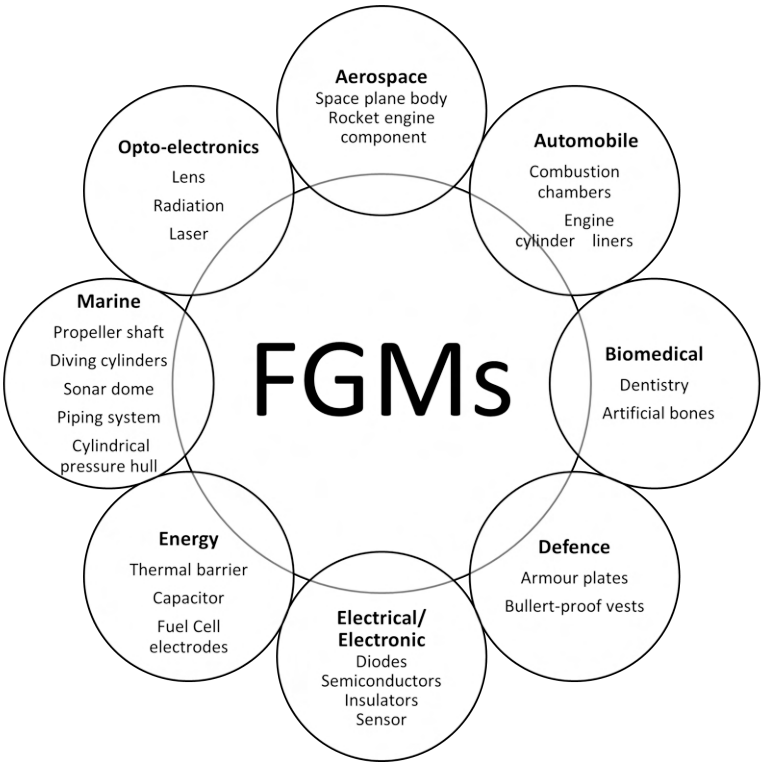

Figure 3.3: Applications of FGMs in different fields (adapted from [1]).

3.3.4.1 Aerospace

FGMs were primarily designed for a space application [217]. FGMs can withstand very high thermal gradients, which makes them suitable for aerospace structures [246]. In this way, most of the aerospace components and structures are nowadays produced through FGMs [247]. Some of the aerospace components where FGMs can be found include rocket engine components, spacecraft truss structure, heat exchange panels and some space structures like reflectors, solar panels, camera housing, turbine wheels, turbine blade coatings, nose caps and space shuttles [20].

3.3.4.2 Automobile

The use of FGMs for applications in the automobile industry is still limited due to the high cost of production of this type of materials. However, these materials are being used in components where their production by FGMs justifies the high manufacturing cost. FGMs are present in the following automobile components: engine cylinder liners for diesel engine pistons, leaf springs, spark plugs, combustion chambers, drive shafts, shock absorbers, flywheels and racing car brakes [20].

3.3.4.3 Biomedical

In nature it is possible to find FGMs, mainly in the human body, bones and teeth are two examples [247]. However, these are among the most replaced parts of the human body. In this way, biocompatible FGMs are used to replace these components of the human body. FGMs are also used in the biomedical industry in implants due to their porous properties being similar to the parts to be replaced [248].

3.3.4.4 Defence

Some FGMs have penetration resistance properties, preventing crack propagation. This property is very attractive to the defence industry [248]. FGMs are used in th defence industry in some applications such as bullet-proof vests and armour plates [247]. However, they can also be applied to vehicles in order to make them bulletproof [20].

3.3.4.5 Electrical/electronic

FGMs are also used in applications in the electrical and electronics industries. We can see FGMs in diodes, semiconductors, insulators and sensor production. In microelectronics there are components that are made of nano FGMs [20].

3.3.4.6 Energy

The energy industry is constantly looking for new and different graded materials in order to improve the efficiency of some of its components. These are some of the applications

of FGMs in the energy industry: the inner wall of nuclear reactors, the thermo-electric converter for energy conversion, the solar panel, the solar cells, the tubes and pressure vessels. The graded electrode are used for the production of solid oxide fuel and the piezo-electric FGMs are used for the ultrasonic transducer, the dielectric, the fuel cell, the turbine blade coatings and the thermal barrier coatings [20].

3.3.4.7 Marine

In the marine industry it is also possible to find several FGMs components. The applications in the marine industry are: propeller shaft, diving cylinders, sonar dome, composite piping system and cylindrical pressure hull [20].

3.3.4.8 Opto-electronics

FGMs can also be found in the opto-electronics industry. In this industry FGMs can be applied in optical fibre materials, lens, lasers, highly efficient photo dectectors, solar cells, tunable photodetector, magnetic storage media and production of semiconductors [248].

3.3.5 Future research direction

Since the conception of the FGMs, research work has been carried out by distinguished researchers in this area in order to improve the manufacture of FGMs. The characterization of FGMs has also been part of studies carried out by a large number of researchers. There has been considerable progress in the investigation of FGMs since their discovery, however much remains to be investigated. FGMs are seen as excellent advanced engineering materials with great potential to revolutionize the manufacturing industry in the twenty-first century. Additive manufacturing offers great advantages in the production of FGM, however there is still room for improvement. One of the possible improvements for the future is the development of a predictive model to help control the AM process. The performance of some FGM production techniques needs improvement [249]. The improvement of production techniques should follow the direction of reducing manufacturing costs [250]. Future research needs to consider the needs of the industry, particularly in FGM applications. The material characterization of FGM through non-destructive methods is one of the suggestions for future improvements. New geometries, gradation and combinations of FGM properties are also a point of investigation for researchers [251]. FGM is a promising engineering material for many possible applications. However, there are some research needs to be met [217]. Research needs appear to be numerous and diverse, but the benefits and potential of FGMs justify these efforts in their research [1]. FGMs are being developed more and more in an optimized way in order to take advantage of the best performance of the materials [9]. The reproducibility of FGM is important for their mass production in industry, however it is still difficult to determine the gradient, the dilution effect during fabrication, as well as the cost of manufacturing the composition of the material gradient [252].

3.4 Digital Image Correlation

3.4.1 Digital Image Correlation based techniques

The desktop computer is connected to a MatchID trigger box, which is a customized hardware used to synchronize the two cameras with precise time triggering and provide analog output for experimental feedback, such as force cell and displacements. Additionally, the MatchID trigger box is connected to the two cameras and the electromechanical test machine. The Figure 3.4 shown a schematic of the Tensile test with DIC test system.

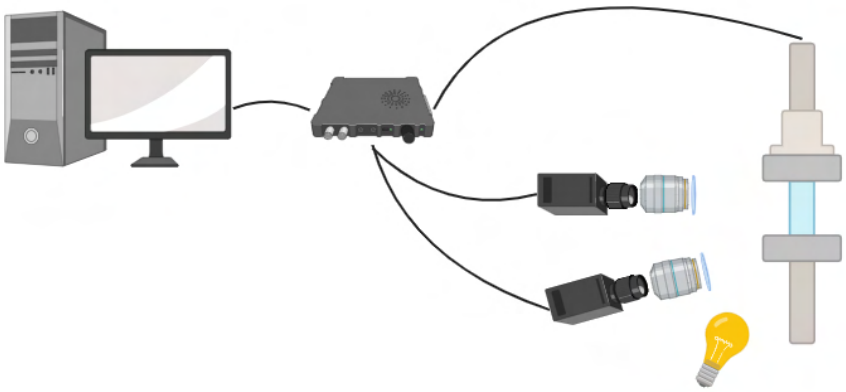

Figure 3.4: Tensile test with DIC testing system schematic.

Several references in the literature can be pointed concerned with the DIC technique and principle [253]. Generically, three different optical configurations can be proposed known as 2D DIC, 3D DIC (stereovision), and Digital Volume Correlation (DVC). A survey on the 2D DIC version can be found in [254], which covers the main principle and methodology to obtain displacement and strain fields from image correlation. Detailed discussions are given concerning measurement accuracy from both experimental conditions and algorithm details. Measures to achieve high accuracy deformation measurements are also recommended. This review was recently updated covering historical achievements, recent advances and open question for further developments [255]. These articles are rather theoretical and therefore no practical code implementation is given. A recent paper in [256] aimed to overcome this gap, discussing code implementation in a scripting language for 2D DIC. An overview of the principle and applications of the stereovision set-up for experimental mechanics, which employees two cameras to measure 3D displacement and strain fields on any 3D object, is presented in [257]. Finally, a review of DVD can be found in [258], in which achievements, challenges, sources of measurement bias and uncertainties were analysed and *ex-situ* and in situ experiments discussed.

The 2D/3D DIC technique provides full-field, contactless displacements of a target object by correlating images recorded before and after the application of a given deformation. The subset-based correlation method is typically implemented in most available codes, although other approaches have been proposed such as the (global) finite element-based

DIC [259] and the Fourier-based DIC [260]. There are several commercial software available in the market including Correlated Solutions [261], GOM Correlate [262], MatchID [263], LaVision [264], Eikosim [265]. Open-source codes have been also developed such as Ncorr[266], DICe [267], μDIC [268], multiDIC [269], pyxel [270], py2DIC [271], UFreckles [272] and YADICS [273]. In the subset-based approach, the reference (or undeformed) image is typically divided into subsets with may overlap by a step size. These are basic parameters that will influence the spatial resolution and accuracy of the measurements. Therefore, their selection typically requires a convergence study, in a compromise between correlation (small subsets) and interpolation (large subsets) errors [37, 274, 275]. Several mathematical correlation criteria have been proposed for estimating the displacement field in the subset matching algorithm approach [254]. It has been shown that the zero-normalized sum of squared differences (ZNSSD) is a robust algorithm since it take into account both offset and linear scale variations of light intensity. The correlation criterion is solved with regard to deformation parameter which will defined the mapping function. An iterative algorithm, such as Newton-Raphson or Levenberg-Marquardt, can then be used for finding the optimal set of deformation parameters for the correlation coefficient.

DIC provides displacements at a large set of discrete data points across a surface of interest. However, strain fields are usually required in the mechanical analysis. Therefore, a robust (with regard to noise) numerical differentiation algorithm is needed to reconstruct the strain fields from measured displacements. Typically, this is achieved by means of function approximation, which can be locally or globally defined. In the local approach, a point-wise least square fitting strategy can be implemented [254, 276]. The regularisation parameters in this case is the size of the strain window, which need to be selected by compromise between filtering and representativeness.

3.5 The Virtual Fields Method

3.5.1 Virtual works principle

The Virtual Fields Method is based on the principle of virtual works, according to the expression:

$$-\int_{V_m} \sigma : \varepsilon^* \mathrm{d}V + \int_{\partial V_m} \vec{T}.\vec{u}^* \mathrm{d}S = \int_{V_m} \rho \vec{a}.\vec{u}^* \mathrm{d}V \tag{3.1}$$

where σ is the Cauchy stress tensor, $\vec{T}$ is the Cauchy stress vector acting on the boundary surface ∂V_m, $\vec{u}^*$ is a vector function defined as the field of virtual displacements, ε^* the virtual strain tensor, ρ the density of the material, $\vec{a}$ the acceleration vector given by the second order derivative of the displacement vector ($\vec{a} = \partial^2\vec{u}/\partial t^2$). The operator "." stands for the scalar product of vectors, while ":" stands for the scalar product of arrays. This equation is verified for any cinematically admissible virtual field [277] and expresses the global dynamical equilibrium of a given solid [278].

Subsequently, some simplifying hypotheses were proposed, such as:

- the density, thickness, and stiffness remain constant throughout the space;
- the kinematic fields are uniform in the direction of sample thickness;
- the sample is in plane stress state.

Under these circumstances, the principle of virtual works (equation 3.1) acquires the following form:

$$-\int_S \sigma : \varepsilon^* \mathrm{d}S + \int_{\partial l} \vec{T}.\vec{u}^* \mathrm{d}l = \rho \int_S \vec{a}.\vec{u}^* \mathrm{d}S \tag{3.2}$$

In this equation, S represents the surface of the region of interest, l the boundaries. It is then necessary to replace the stress tensor with a constitutive model of the material, the most common being the isotropic or orthotropic elastic linear [44].

Two methods are used to introduce this principle. The first method is more generic as it corresponds to the weak form of equilibrium equations. The second method involves calculating the work done by a load when a virtual offset is applied to a solid.

3.5.1.1 Method 1: From Local Equilibrium Equations to the Virtual Work Principle

The equation presented is based on equilibrium equations that are valid at any point in the domain being considered. These equations can be multiplied by an arbitrary function, denoted by g_i, where $i = 1...3$. The resulting products yield three equations that can be added to give the final equation:

$$\int_V \sigma_{ij,j} g_i \mathrm{d}V + \int_V b_i g_i \mathrm{d}V = \int_V \rho a_i g_i \mathrm{d}V \tag{3.3}$$

Next, a piecewise integration is performed to eliminate the stress divergence present in the first integral, as demonstrated below:

$$\int_V (\sigma_{ij} g_i)_{,j} \, \mathrm{d}V - \int_V \sigma_{ij} g_{i,j} \, \mathrm{d}V + \int_V b_i g_i \mathrm{d}V = \int_V \rho a_i g_i \mathrm{d}V \tag{3.4}$$

Afterwards, several integrations are performed, resulting in the following equation:

$$-\int_V \sigma_{ij} g_{i,j}^{sym} \mathrm{d}V + \int_S T_i g_i \mathrm{d}S + \int_V b_i g_i \mathrm{d}V = \int_V a_i g_i \mathrm{d}V \tag{3.5}$$

Equation efE:4.11 represents the weak form of the equilibrium equations. This name is used because the required order of continuity to obtain an acceptable solution is lower due to the smaller order of the derivatives. If S is divided into multiple subsurfaces, S will be replaced by S_f, where the load is applied. The equation can then be described as follows:

$$-\int_V \sigma_{ij} g_{i,j}^{sym} \mathrm{d}V + \int_{S_f} T_i g_i \mathrm{d}S + \int_V b_i g_i \mathrm{d}V = \int_V \rho a_i g_i \mathrm{d}V \tag{3.6}$$

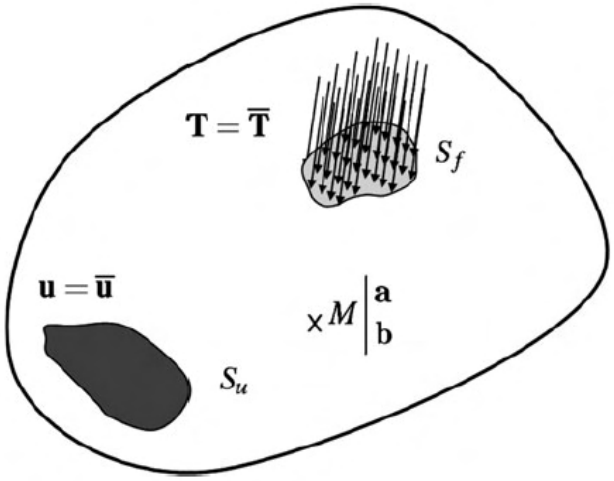

Figure 3.5: Solid shape subject to mechanical load [279].

3.5.1.2 Method 2: Principle of Virtues through Charge

It is now considered a second method for introducing the principle of virtual work. Consider the body shown in Figure 3.5, which is subjected to applied forces, T, at its limit, S_f, and volumetric forces, b, acting on its mass, V. The body may have various configurations that satisfy the displacement boundary conditions due to a certain distribution of acceleration. These configurations cause a displacement distribution in relation to the actual location of the body points. This displacement is referred to as the virtual offset, denoted by u^*:

The virtual offset is different from the actual offset, u, that occurs when the load is applied. Actual displacement is measured relative to the initial setting, defined when the body is at rest. Virtual displacement is considered relative to the actual location of the body points once the load has been applied. The virtual work performed by the load when the body is subject to a virtual displacement is now taken into account. Since virtual work is defined as the work performed by the load in the field of virtual displacement, the following equation is defined:

$$W^* = \int_S \mathbf{T} \cdot \mathbf{u}^* \mathrm{d}S + \int_V \mathbf{b} \cdot \mathbf{u}^* \mathrm{d}V - \int_V \rho \mathbf{a} \cdot \mathbf{u}^* \mathrm{d}V \quad \forall \mathbf{u}^* KA \tag{3.7}$$

After several integrations it is possible to obtain the equation that leads to the principle of virtual work:

$$\int_V \sigma : \varepsilon^* \mathrm{d}V + \int_V \mathbf{T} \cdot \mathbf{u}^* \mathrm{d}V + \int_V \mathbf{b} \cdot \mathbf{u}^* \mathrm{d}V = \int_V \rho \mathbf{a} \cdot \mathbf{u}^* \mathrm{d}V \quad \forall u^* KA \tag{3.8}$$

The following definitions are generally presented:

$$\begin{cases} W^*_{int} = \int_V \sigma : \varepsilon^* \mathrm{d}V & \text{Internal virtual work} \\ W^*_{ext} = \int_V \bar{T} \cdot u^* \mathrm{d}S + \int_V b \cdot u^* \mathrm{d}V & \text{External virtual work} \\ W^*_{acc} = \int_V \rho a \cdot u^* \mathrm{d}V & \text{Virtual work done by the acceleration} \end{cases} \tag{3.9}$$

Thus, equation 3.8 can be described as follows [279]:

$$W^*_{int} + W^*_{ext} = W^*_{acc} \quad \forall u^* KA \tag{3.10}$$

Two different methods were demonstrated for introducing the principle of virtual works: a mathematical method and a physical method.

3.5.2 Case studys of constitutive equations of elastic linear behaviour

3.5.2.1 Orthotropic behaviour

Given the plane stress state, in indexed notation the stress tensor (σ) and the strain tensor (ε) can be denoted by [279]:

$$\sigma : \begin{bmatrix} \sigma_x \\ \sigma_y \\ \sigma_s \end{bmatrix} \quad \varepsilon : \begin{bmatrix} \varepsilon_x \\ \varepsilon_y \\ \varepsilon_s \end{bmatrix} \tag{3.11}$$

Optical field techniques allow measurements to be made on the external surface of the specimen, so it is necessary to ensure that the external surface response is representative of the volume. In this way, thin plates are used which are subjected to a flat state of stress. The stress field is related to the deformation field by the constitutive equations. The relationship between stress and linear deformation of a thin plate of orthotropic material subjected to a plane stress state according to Hooke's law can be expressed by:

$$\begin{bmatrix} \sigma_x \\ \sigma_y \\ \sigma_s \end{bmatrix} = \begin{bmatrix} Q_{xx} & Q_{xy} & 0 \\ Q_{xy} & Q_{yy} & 0 \\ 0 & 0 & Q_{ss} \end{bmatrix} \begin{bmatrix} \varepsilon_x \\ \varepsilon_y \\ \varepsilon_s \end{bmatrix} \tag{3.12}$$

where Q_{ij} are the stiffness matrix components in the material coordinate system, σ_i, $(i = x, y, s)$ are the stress tensor components and ε_i are the strain tensor components. In the case of constitutive models for orthotropic materials, a global coordinate system is defined. Figure 3.6 shows the global and local coordinate systems, where $x - y$ is the global coordinate axis system and θ is the angle between the two coordinate systems. The local coordinate system is also defined as the axis system that represents the fibre orientation of the material:

For a material with isotropic elastic linear behaviour the equation 3.11 is simplified to:

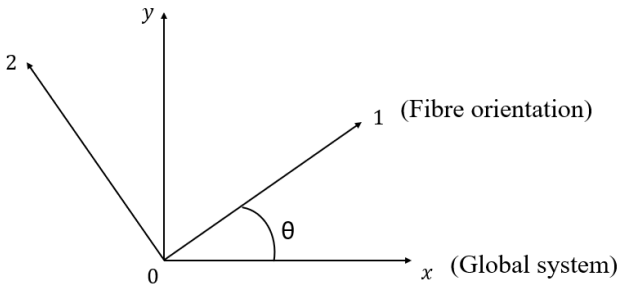

Figure 3.6: Global and fibre coordinate system.

$$\begin{bmatrix} \sigma_x \\ \sigma_y \\ \sigma_s \end{bmatrix} = \begin{bmatrix} Q_{xx} & Q_{xy} & 0 \\ Q_{xy} & Q_{xx} & 0 \\ 0 & 0 & \dfrac{Q_{xx} - Q_{xy}}{2} \end{bmatrix} \begin{bmatrix} \varepsilon_x \\ \varepsilon_y \\ \varepsilon_s \end{bmatrix} \tag{3.13}$$

on what,

$$\begin{cases} Q_{xx} = Q_{yy} \\ Q_{xy} = Q_{yx} \\ Q_{ss} = \dfrac{Q_{xx} - Q_{xy}}{2} \end{cases} \tag{3.14}$$

The constitutive equations for isotropic materials require only two independent parameters, Q_{xx} and Q_{xy}, which can be expressed as a function of Young's modulus (E) and Poisson's ratio (u) using the following expressions:

$$\begin{cases} \nu = Q_{xy}/Q_{xx} \\ E = Q_{xx}(1 - \nu^2) \end{cases} \tag{3.15}$$

Substituting the constitutive law described earlier in the principle of virtual work (equation 3.1) gives the following equation:

$$\begin{aligned} Q_{xx} \int_S (\varepsilon_x \varepsilon_x^* + \varepsilon_y \varepsilon_y^* + \frac{1}{2}\varepsilon_S \varepsilon_S^*) \mathrm{d}S + Q_{xy} \int_S (\varepsilon_x \varepsilon_y^* + \varepsilon_y \varepsilon_x^* - \frac{1}{2}\varepsilon_S \varepsilon_S^*) \mathrm{d}S \\ = \int_{\partial S} T_i u_i^* \mathrm{d}L - \int_S \rho a_i u_i^* \mathrm{d}S;\ i \in (x, y) \end{aligned} \tag{3.16}$$

The constitutive equations for orthotropic materials depend on four independent parameters: Q_{xx}, Q_{xy}, Q_{yy}, and Q_{ss}. The relationship between stress and strain in the global coordinate system is expressed as follows:

$$\begin{bmatrix} \sigma_x \\ \sigma_y \\ \sigma_s \end{bmatrix} = \begin{bmatrix} Q_{xx} & Q_{xy} & Q_{xz} \\ Q_{xy} & Q_{yy} & Q_{yz} \\ Q_{xz} & Q_{yz} & Q_{ss} \end{bmatrix} \begin{bmatrix} \varepsilon_x \\ \varepsilon_y \\ \varepsilon_s \end{bmatrix} \tag{3.17}$$

By substituting the components of the stiffness with equivalent expressions as a function of Young's modulus and Poisson's ratio in equation efE:4.23, it can be obtain the following expression:

$$\begin{bmatrix} \sigma_x \\ \sigma_y \\ \sigma_s \end{bmatrix} = \begin{bmatrix} \frac{E_x}{1-\nu_{xy}\nu_{yx}} & \frac{-\nu_{yx}E_x}{1-\nu_{xy}\nu_{yx}} & 0 \\ \frac{-\nu_{xy}E_y}{1-\nu_{xy}\nu_{yx}} & \frac{E_y}{1-\nu_{xy}\nu_{yx}} & 0 \\ 0 & 0 & G_{xy} \end{bmatrix} \begin{bmatrix} \varepsilon_x \\ \varepsilon_y \\ \varepsilon_s \end{bmatrix} \tag{3.18}$$

Thus, the four stiffness components relate to Young's modulus and Poisson's ratio through the following mathematical equations:

$$\begin{cases} E_x = Q_{xx} - \dfrac{Q_{xy}^2}{Q_{yy}} \\ E_y = Q_{yy} - \dfrac{Q_{xy}^2}{Q_{xx}} \\ \nu_{xy} = \dfrac{Q_{xy}}{Q_{yy}} \\ G_{xy} = Q_{SS} \end{cases} \tag{3.19}$$

Poisson's ratio can also be related to Young's modulus with the following expression [280]:

$$\nu_{yx} = \nu_{xy}\frac{E_y}{E_x} \tag{3.20}$$

The aim is to determine the stiffness components, such as Q_{xx}, Q_{xy}, Q_{yy} and Q_{ss}, which are related to E and ν and are required for the possible identification of the stress-strain curve of the material under study [44].

3.6 Summary

This chapter is notable for the theoretical presentation of the methods used in the following chapters. The different additive manufacturing processes are described in detail. Next, the FGMs as a whole are described. The DIC technique is then described in detail as a full-field measurement technique. Finally, the chapter concludes with a detailed discussion.

4

Materials and Methods

4.1 Introduction

The chapter begins with an explanation of the materials studied (copper, aluminium and copper-aluminium alloy) and used in the fabrication of the specimens. In the following section, an exposition is provided of the welding parameters that were utilised, in conjunction with a detailed discussion of the materials that were selected, with the objective of achieving the optimal combination of materials for the fabrication of the FGM specimens. Subsequently, the WAAM configuration is presented. The following discussion present a detailed explanation of the fabrication of the Cu-CuAl alloy FGM. The subsequent description provides comprehensive insight into the specimen preparation process, encompassing the machining of the AM wall and the cleaning of the surface. In the material characterisation section, the FGM specimens were characterised by two tests: hardness characterisation and eddy current measurements. The DIC section provides a detailed exposition of the methodology employed in the application of the speckle pattern to the specimens, along with a comprehensive account of the experimental tests conducted on 316L stainless steel. These tests were designed to verify the geometry of the specimens, the DIC setup, and all associated parameters.

4.2 Materials

4.2.1 Copper

Copper is a reddish-brown metal caused by impurities and oxides. At standard temperature and pressure, it is solid and has a metallic sheen, as well as being ductile and malleable. Copper can be recycled, but oxidizes when in contact with oxygen and/or water. Copper and copper alloys have widespread usage in industries due to their excellent physical and chemical properties. These properties include high thermal conductivity (400 W/(m K)), electrical conductivity (58 106 S/m), and corrosion resistance [281]. Nevertheless, impurities can significantly impact their physical properties. The use of pure copper material can prevent the influence of impurities, thereby guaranteeing more stable physical and

chemical properties [282]. Pure copper is extensively used in the aerospace, automotive, and electrical sectors due to its high thermal and electrical conductivity, as well as its machinability [283]. Electrolytic copper, also known as pure copper, is among the most commonly used metals worldwide. The metal's purity is determined by the copper content, which is 99.9% in this case. Pure copper is a key material for heat exchangers and radiators as it has high thermal conductivity. The manufacturing and electrical industries have grown rapidly in recent years, resulting in an increasing demand for more complex structures and geometry [284]. Unfortunately, traditional production methods are unable to handle the processing of complex geometries. AM technology offers a solution for producing intricate parts. Significant research is focused on the AM of pure copper due to its superior chemical and physical properties [285]. Pure copper is extensively used in several fields such as electrical power, heat dissipation, decoration, piping and others due to its remarkable properties such as electrical conductivity, corrosion resistance, thermal conductivity, and toughness. Certain copper alloy materials possess favourable electrical and thermal conductivity properties, along with relatively high strength, making them commonly used components in creating combustion chamber parts for electronic, aviation, and aerospace engines. Nowadays, the industry is faced with the difficulty of reducing weight and dealing with structural complexity. Fortunately, the integration of additive manufacturing offers a convincing resolution to these difficulties [286]. The mechanical, electrical, and thermal properties of copper are demonstrated in Table 4.1.

Table 4.1: Mechanical, electrical, and thermal properties of a copper (CuAg) [287].

Mechanical Properties	
Hardness, Vickers	50
Ultimate tensile strength [MPa]	210
Yield strength [MPa]	33.3
Elongation at break [%]	60
Elastic modulus [GPa]	110
Poisson's ratio	0.343
Electrical Properties	
Electrical resistivity [$\Omega.m$]	1.70×10^{-5}
Thermal Properties	
Melting point [$^{\circ}C$]	1083.2

4.2.2 Aluminium

Aluminium alloys are attractive due to their exceptional mechanical properties and low density, resulting in sturdy, lightweight parts [288]. The exceptional qualities of aluminium - excellent corrosion resistance, high strength-to-weight ratio, and the capacity to form alloys with various metals and non-metals - render it perhaps the most cost-effective and

appealing metallurgy, with numerous utilities in transport, power, machinery, consumer electronics, construction, packaging, and containers, among others. Welding aluminium has always posed problems due to various material properties, including its high coefficient of thermal expansion, formation of a tenacious oxide film, and tendency to form porosity, despite its widespread use [289]. High-strength aluminium alloys are extensively utilised in fabricating structural components within the aerospace sector. The alloys are chosen for their excellent strength-to-weight and stiffness-to-weight ratios, along with their good machinability. However, the intricate geometry of numerous aerospace components can present manufacturing obstacles when conventional subtractive manufacturing methods are employed [290]. The use of WAAM process for aluminium alloys is limited by a lack of understanding. The main issues in aluminium WAAM include cracks, surface oxidation and porosity. Aluminium alloys are extensively utilized in diverse industrial sectors including aerospace, shipbuilding, train building, and automotive industries attributable to their lightweight and superior resistance to corrosion. Various aluminum alloys are used besides ultrapure aluminium (Al), with key alloying elements being copper, silicon, magnesium, zinc and manganese [291]. However, when used in WAAM, these alloys present significant challenges because of the high levels of porosity caused by aluminium oxides and high heat transfer during the process. If the oxides are not melted in the molten pool, they become trapped and lead to a reduction in mechanical properties [292].

4.2.3 Copper-Aluminium alloy

Copper alloys are metallic alloys in which copper is the main component. These materials possess exceptional resistance to corrosion. Cu-Al series alloys are commonly utilized in fossil fuel pipelines as well as specific parts of shipbuilding coatings, including propellers, valves, and layered plates, because of their exceptional corrosion and wear resistance. The Al element, which serves as a solid solution element in Cu-Al alloy, aides mainly in enhancing the formation of double strain and positioning density during the twinning deformation process. This results in a more refined grain size and optimised properties, including improved hardness and yield strength (YS) for the Cu-Al alloy. Previous research on Cu-Al alloys has primarily focused on improving material strength by optimising crystal structures through the use of microalloying elements such as Ni, Zr, Cr, and Ag. Various plastic deformation processes, including cold rolling, equal channel angular pressing, and high-pressure twisting, can considerably enhance the strength and hardness of alloys. This is achieved by refining grains, generating twins in materials with low failure energy stacking [65]. The mechanical, electrical, and thermal properties of copper–aluminum are demonstrated in Table 4.2.

Table 4.2: Mechanical, electrical, and thermal properties of a copper–aluminium alloy (CuAl9Fe) [293, 294].

Mechanical Properties		
Hardness, Vickers	137	
Ultimate tensile strength [MPa]	552	to586
Yield strength [MPa]	269	to293
Elongation at break [%]	28	
Elastic modulus [GPa]	117	
Poisson's ratio	0.34	
Electrical Properties		
Electrical resistivity [$\Omega.m$]	1.30×10^{-5}	
Thermal Properties		
Melting point [°C]	1040	

4.3 Parameters and materials selection

In order to produce a high-quality welding result, it is crucial to establish various parameters, including the welding type, current, voltage, travel speed, wire feed speed, and shielding gas. In selecting materials for the fabrication of FGMs, it is imperative to consider the properties of both materials, their metallurgical compatibility, the application environment, and the weldability of each material. In order to reach the two final FGM materials, a long journey was undertaken and several studies of welding parameters and materials were carried out. The analysis revealed the presence of four wires, the chemical compositions of which are delineated in Table 4.3.

Table 4.3: Chemical composition of the wire feedstocks used in this work (wt.%):

Material	Cu	Al	Fe	Ag	Mn	Ni	Si	Mg	Zn	Ti	Cr	Zr
Pure Copper	99,9											
Copper (Dt-CuAg)	>99,5			1,0								
Aluminium (ER1070)	0,004	99,7	0,25		0,03		0,2	0,03	0,04	0,03		
Aluminium (ER5087)		Rest			0,8			5,0		0,12	0,08	0,15
Copper Aluminium alloy (DT-CuAl9Fe)	Rest	8,5	0,8		0,5	0,5						

4.3.1 Pure Copper: MIG and TIG

The initial material subjected to analysis was pure copper. Electrolytic copper, otherwise referred to as pure copper, is one of the most widely utilised metals on the global scale. The purity of the material is directly proportional to the percentage of copper in its composition, which in this case reaches 99.9%. The wire utilised in this experiment had a diameter of 1 mm. The optimal distance between the torch and the substrate is 13 mm. The time between layers was defined as the time required for the temperature of the last deposited layer to fall below 100°C. The wire parameters have been the subject of study using GTAW and Gas Metal Arc Welding (GMAW) welding processes, also known as Tungsten Inert Gas (TIG) and Metal Inert Gas (MIG), respectively. Due to its status as an excellent conductor of energy, copper absorbs practically all of the energy from the welding process, resulting in increased heating of the layers during the deposition process. Consequently, it is imperative to allow the final layer to cool prior to the deposition of the subsequent layer. The deposition of the copper layers was accomplished through the implementation of TIG welding, employing a travel speed ranging from 260 to 280 mm/min and a wire feed speed ranging from 3 to 3.5 m/min. The parameters were modified in accordance with the deposition of the layers. The current employed was 120 A, and argon was utilised as the shielding gas, with a flow rate ranging from 15 to 20 l/min. The concluding parameters for this material are delineated in Table 4.4.

Table 4.4: TIG welding parameters for the pure copper layers.

Process	GTAW
Travel speed	260 to 280 mm/min
Wire feed speed	From 3 m/min to 3,5 m/min
Current	120 A
Shielding gas	Pure Ar
Shielding gas flow rate	15 -20 l/min

Various challenges can lead to wall defects when welding copper. Porosity, for example, is a common issue caused by gases present in the welding area or inadequate flow. Although the surface was cleaned between layers to prevent this defect, it was insufficient. Figure 4.1 shows a copper wall with several pores. Another noticeable defect in the part is the lack of penetration or insufficient fusion. This is usually caused by a low welding current or inadequate preparation of the base material. To address this, the welding current can be adjusted.

The wire feed speed for copper layers deposited by MIG was different for the various layers of the AM wall. For the first and second layers, the Wire Feed Speed (WFS) was 3.5 m/min. For the third to sixth layers, it was 3 m/min. For the seventh and final layers, it was 2.8 m/min. A larger WFS was used in the first layers than in the last layers. A higher feed rate could be used in the first layers because the cohesion between the layers was excellent, as these layers still had traces of the steel substrate. The WFS had to be decreased for the final layers because a slower feed rate allows for greater cohesion between the

Figure 4.1: Pure copper wall manufactured by TIG with welding defects.

layers, resulting in a better appearance and greater precision.

A mixture of argon (Ar) and carbon dioxide (CO2) was used as a shielding gas to minimise oxide formation, which is common in copper welding. This shielding gas also ensured good arc stability, penetration and deposition rates. A single-pass deposition strategy with a return movement was employed. The torch initiates the arc and moves in a y pattern while extruding the necessary materials. Once the end of the layer is reached, the arc ceases and the torch ascends in the z direction before returning to the starting point. The final parameters obtained for this material are described in Table 4.5.

Table 4.5: MIG welding parameters for the pure copper layers.

Process	GMAW
Travel speed	320 mm/min
Wire feed speed	From 2,8 m/min to 3,5 m/min
Voltage	19-20 V
Shielding gas	Ar and CO2
Shielding gas flow rate	15 -20 l/min

Figure 4.2 displays a pure copper wall produced using the MIG welding process. This wall has fewer defects than one produced using TIG, which indicates that the MIG process is more stable. The layers have a better appearance and are more cohesive with fewer defects.

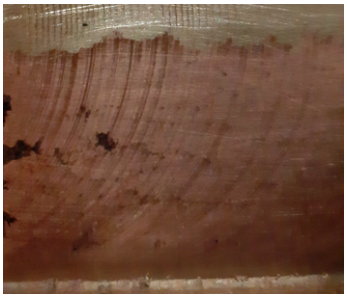

Figure 4.2: Pure copper wall manufactured by MIG with welding defects.

4.3.2 Copper (CuAg): MIG

The deposition of pure copper wire presented a significant challenge, given the absence of electrolytic copper in welding coils with diameters ranging from 1 to 1.2 mm. It has

been established that the diameter of electrolytic copper wire available in electrical cables ranges from 1 to 1.2 mm. The utilisation of copper wire that does not conform to the coil form becomes unfeasible due to incompatibility. In view of the aforementioned welding defects in the pure copper, and for the reasons previously stated, the decision was taken to utilise CuAg copper wire, which contains 1% silver and the remainder copper. This wire is the coil that most closely resembles electrolytic copper. The material was examined using the gas metal arc welding process. The fabrication process was characterised by a consistent feed rate of 450 mm/min for all layers. The wire feed speed was set at 5 m/min for all layers. The shielding gas used in this experiment was pure argon. The utilisation of argon in the context of copper welding has been demonstrated to impede oxidation, enhance arc stability, and mitigate the formation of slag. The welding parameters used for the CuAg layers are described in the table 4.6.

Table 4.6: MIG welding parameters for the CuAg layers.

Process	GMAW
Travel speed	450 mm/min
Wire feed speed	5 m/min
Voltage	19-20 V
Shielding gas	Pure Ar
Shielding gas flow rate	15 -20 l/min

In contradistinction to the deposition of pure copper, the welding seams of this CuAg wire exhibit a significantly superior visual appearance. The material displays an absence of pores and exhibits optimal penetration and cohesion between layers. The parameters established a suitable width and height for the bead, thereby enabling the deposition of layers of copper.

4.3.3 Aluminium alloys: TIG

The second material to be studied is aluminium. The process of aluminium deposition by welding can present certain challenges. Aluminium is a material surrounded by a layer of refractory oxide, which does not rupture under direct current (DC) in the TIG process, making welding impossible. Consequently, the utilisation of alternating current (AC) is imperative. This study focuses on two aluminium alloys: 5087 and 1070. The 5087 series is distinguished by its manganese composition, while the 1070 series is widely regarded as being composed exclusively of aluminium, with a purity of 99.7%. The present study involved the execution of multiple deposition welding beads, with various parameters employed to attain the desired quality of the bead. The objective of the present study was to ascertain the most effective parameters for achieving high-quality welding beads. As illustrated in Figure 4.3, the study highlights the challenges associated with the analysis of welding beads exhibiting varying parameters. The deposition of these two alloys was performed on an aluminium substrate.

Figure 4.3: Several attempts at Al deposition with different TIG welding parameters.

The initial focus of the study was Alloy 5087. It was observed that the initial layer deposited exhibited an optimal weld bead appearance. However, subsequent layers did not visually demonstrate a satisfactory weld bead, with the formation of balls of material that were ejected to the sides rather than a continuous deposition of material. Nevertheless, the most optimal parameters utilised in this deposition process correspond to the parameters delineated in Table 4.7.

The GTAW process was utilised as the welding method. The initial layer was operated at a travel speed of 260 mm/min and a wire feed speed of 3.5 m/min. For the subsequent layers, the travel speed was increased to 280 mm/min and the wire feed speed was decreased to 3 m/min. This modification was implemented with the objective of minimising defects and enhancing penetration in the subsequent layers. The weld pool and weld metal deposition rate were found to be more precisely controlled by reducing the wire feed speed. The welding process was conducted using an alternating current (AC) with a magnitude of 150 A. The selection of pure argon as the shielding gas was made on the basis of its ability to protect the deposition zone against the influence of atmospheric oxygen and nitrogen, which can cause oxidation. Argon (Ar) has been shown to create an inert environment around the welding arc, thereby preventing the formation of oxides on the aluminium during the welding process.

Table 4.7: TIG welding parameters for the aluminium alloy 5087 layers.

Process	GTAW
Travel speed	260 to 280 mm/min
Wire feed speed	3 to 3,5 m/min
Current	150 A
Shielding gas	Pure Ar
Shielding gas flow rate	15 -20 l/min

An alternative alloy was selected in order to ascertain whether it would provide a superior deposition option, given that the 5087 series did not yield satisfactory deposition results. As with alloy 5087, gas tungsten arc welding was utilised as the welding process.

The initial layer was welded utilising a travel speed of 260 mm/min and a wire feed speed of 3.5 m/min. For the second layer, the travel speed was increased to 280 mm/min, while the wire feed speed was reduced to 3 m/min. The subsequent layers were then welded using a travel speed of 300 mm/min and a wire feed speed of 2.8 m/min. Table 4.8 shows the welding parameters used to deposit aluminium alloy 1070.

Table 4.8: TIG welding parameters for the aluminium alloy 1070 layers.

Process	GTAW
Travel speed	260 to 300 mm/min
Wire feed speed	2,8 a 3,5 m/min
Current	150 A
Shielding gas	Pure Ar
Shielding gas flow rate	15 -20 l/min

Subsequent to the establishment of the optimal welding parameters for alloy 1070, an AMwall was produced. The dimensions of the produced wall were as follows: 130mm length, 25mm height, and 10mm thickness. The optimal thickness for an AM wall is approximately 5mm, a thickness that allows for machining while maintaining approximately 1-2mm of specimen thickness. The production of walls with a thickness greater than 5mm can lead to the unnecessary consumption of materials. However, the wall's appearance deviates from the intended design due to deformations at its extremities. As illustrated in Figure 4.4, an aluminium AM wall is presented.

Figure 4.4: Aluminium alloy 1070 wall manufactured by TIG.

The objective of the study was to establish a FGMthrough the investigation of the cohesion between copper and aluminium layers in an aluminium wall. The previously deposited aluminium layers were reused and CuAg layers were added on top. However, the study found no cohesion between the two materials. Furthermore, upon contact between the copper (CuAg) wire and aluminium in the melting pool, the formation of material balls occurs, which are subsequently expelled outwards. The underlying cause of this phenomenon can be attributed to various factors, including the presence of excess filler material, the utilisation of high travel speeds, the employment of low welding currents, the use of inadequate shielding gases, the substandard preparation of the previously deposited material, or the presence of unfavourable welding conditions. In an effort to optimise the welding seam, a number of welding parameters were modified, but regrettably, this approach did not yield the desired results. Furthermore, layers of aluminium were deposited on top of previously deposited layers of CuAg. The layers

appeared to be cohesive, but cracks and lack of penetration were observed. Despite the endeavour to ameliorate the defects in question by means of modifying the welding parameters of the two materials, this attempt was unsuccessful.

4.3.4 Copper - Aluminium alloy (CuAl9Fe): MIG

Given the apparent incompatibility of aluminium with CuAg as FGM, an alternative wire was investigated. The choice of copper aluminium alloy (CuAl9Fe) was determined by its elevated copper content, which has been demonstrated to enhance the cohesion between the two materials. This wire is also an aluminium alloy, with an aluminium content of 9%. The gas metal arc welding process was utilised to deposit the CuAl alloy layers, with a constant travel speed of 300 mm/min being maintained throughout the deposition process. The wire feed speed was set at 4 m/min for the initial layer and 3.8 m/min for the subsequent layers. The elevated wire feed speed during the initial layer facilitated enhanced penetration between the final layer of CuAg and the initial layer of CuAl9Fe, thereby promoting improved cohesion between the two materials. An electrical potential of 19-20 V was applied, and pure argon was used as a shielding gas in the welding process. The interpass temperature was maintained at a level below 100°C, with a duration of approximately 2 minutes between each layer. The parameters of the CuAl layers are described in table 4.9.

Table 4.9: MIG welding parameters for the Copper-Aluminium layers.

Process	GMAW
Travel speed	300 mm/min
Wire feed speed	From 3,8 m/min to 4 m/min
Voltage	19-20 V
Shielding gas	Pure Ar
Shielding gas flow rate	15 -20 l/min

Following the production of a FGM consisting of CuAg and CuAl9Fe, it was determined that the bond between the two materials was weak and the transition zone was abrupt. In order to consolidate the bond, it was necessary to preheat the CuAg layers to a temperature of between 400 and 500°C prior to the deposition of the CuAl9Fe layers. The preliminary heating process resulted in a more substantial transition zone between the two materials, exhibiting a more uniform gradient. As illustrated in Section 4.5, the differences between samples with and without preheating are evident. As illustrated in Figure 4.5, the figure displays the layered structure of the MIG deposited CuAl9Fe material.

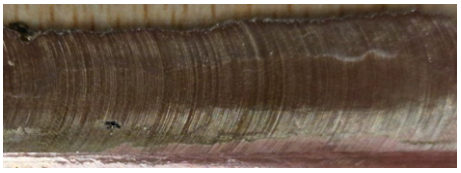

Figure 4.5: CuAl alloy (CuAl9Fe) wall manufactured by MIG.

4.3.5 Pure copper and aluminium gradients: TIG

Following an experimental process involving the analysis of various wires composed of diverse materials, the objective was to integrate two wires in order to generate a layer of material. The initial attempt to combine two wires involved the utilisation of pure copper wire and aluminium liga 1070 wire. The mixture comprised 90% pure copper and 10% 1070 aluminium alloy. This weld blend exhibited encouraging outcomes when only a limited number of layers were deposited. It has been demonstrated that, upon the attempt to deposit a quantity exceeding two or three layers, the layers begin to manifest defects and arc instability. As illustrated in Figure 4.6, the deposition of multiple layers of two wires is demonstrated: The substance under consideration consists of 90% pure copper and 10% 1070 aluminium alloy.

Figure 4.6: 90% pure copper and 10% aluminium 1070 alloy wall by TIG with 2 wires.

The parameters for the various layers were distinct, with an increase in the number of layers resulting in a decrease in wire feed speed and an increase in travel speed to achieve enhanced penetration. For the initial layer, a feed rate of 260 mm/min and a wire speed of 3.5 m/min were utilised. In the subsequent layers, a feed rate of 280 mm/min and a wire feed speed of 3 m/min were utilised. The utilisation of alternating current was imperative during the process of depositing aluminium wire. The current value (A) was found to vary according to the material used. For layers of 100% aluminium, the current employed was 150 A. To deposit 100% copper by TIG, a current of 120 A was utilised. The deposition of 90% copper and 10% aluminium was achieved by utilising an electric current of 115 A. The utilisation of an electrical current of 110 A was observed in the experiment, with the composition of the substance being 80% copper and 20% aluminium. A current of 105 A was employed for the layers comprising 60% copper and 40% aluminium. The layers comprising 80% copper and 20% aluminium alloy 1070 demonstrated some adhesion to the preceding layers, while the layers consisting of 60% copper and 40% aluminium alloy 1070 exhibited no adhesion to the previous layers. As illustrated in Table 4.10, the parameters employed for the deposition of layers exhibiting varying gradients of pure copper and aluminium alloy are delineated.

4.3.6 Copper (CuAg) and copper-aluminium (CuAl9Fe) gradients: TIG

In order to establish a library of material compositions for varying percentages of Cu and CuAl, as outlined in Chapter 5, it was imperative to conduct a comprehensive study of the

Table 4.10: TIG welding parameters for different gradients of pure copper and aluminum 1070 alloy layers.

Process	GTAW
Travel speed	260 to 280 mm/min
Wire feed speed	From 3 m/min to 3,5 m/min
Current	110 to 150 A
Shielding gas	Pure Ar
Shielding gas flow rate	15 -20 l/min

welding parameters in T-WAAM. In order to utilise the T-WAAM method, it is necessary to employ the TIG welding process. Para o TIG, os parametros das camadas de 100% copper (CuAg) estão mostradas na Table 4.11.The parameters of the 100% copper (CuAg) layers are delineated in Table 4.11.

Table 4.11: TIG welding parameters for the 100% copper (CuAg) layers.

Process	GTAW
Travel speed	130 mm/min
Wire feed speed	1 m/min
Current	135 A
Shielding gas	Pure Ar
Shielding gas flow rate	15 l/min

Table 4.12: TIG welding parameters for the 50% coppper (CuAg) and 50% copper-aluminium (CuAl9Fe) layers.

Process	GTAW
Travel speed	110 mm/min
Wire feed speed	2 m/min
Current	170 A
Shielding gas	Pure Ar
Shielding gas flow rate	15 l/min

The previous subsections describe studies of various materials and two welding processes: TIG and MIG. Firstly, the study focused on pure copper material, which was deposited using TIG and MIG. Next, CuAg was studied with MIG, which provided the best surface finish and no defects for the copper layers. Subsequently, aluminum alloys were studied with TIG and alternating current, but as it did not yield the best results, CuAl9Fe was analyzed with MIG. Finally, the study analyzed the different gradients with copper and aluminum. Table 4.13 summarises the two welding processes used in this study, as well as the materials and types of walls constructed.

The two materials selected for utilisation in the fabrication of FGMs were copper (CuAg) and copper-aluminium (CuAl9Fe). The parameters employed in the FGMs conducted in this study were those delineated in Table 4.6 and Table 4.9. Young's modulus is a material property that quantifies the stiffness of a material, the extent to which it resists elastic deformation when subjected to an external load. As demonstrated in the literature

Table 4.13: Examples of materials deposited by WAAM in TIG and MIG.

TIG		**MIG**	
5087 alloy and 1070 alloy			
Pure Copper		Pure Copper	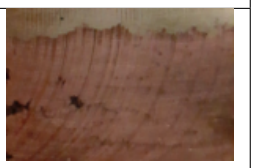
		Dt-CuAg	
Copper and aluminium gradients			
		DT-CuAl9Fe	

review, the Young's modulus of Cu has been determined to be 110 GPa, while the Young's modulus of the CuAl alloy has been measured to be 117 GPa. It is evident that the Cu alloy, characterised by a lower Young's modulus value, will demonstrate a reduced resistance to loading. Yield stress is defined as the limit at which a material begins to deform plastically. As demonstrated in the relevant literature, the yield stress value of Cu is found to be the lowest, with a value of approximately 33 MPa, in comparison to the yield stress value of the CuAl alloy, which is approximately 269 MPa. Consequently, the Cu material should be the first to deform plastically, as it has a lower yield stress than the CuAl alloy, since the this is more resistant.

4.4 Specimen production and preparation

4.4.1 Wire and Arc Additive Manufacturing setup

To study the chosen materials and select the parameters, two welding processes were used, TIG and MIG. The setups for the two welding processes are similar. The MIG WAAM setup with the various components described previously is shown in Figure 4.7 and figure 4.8.

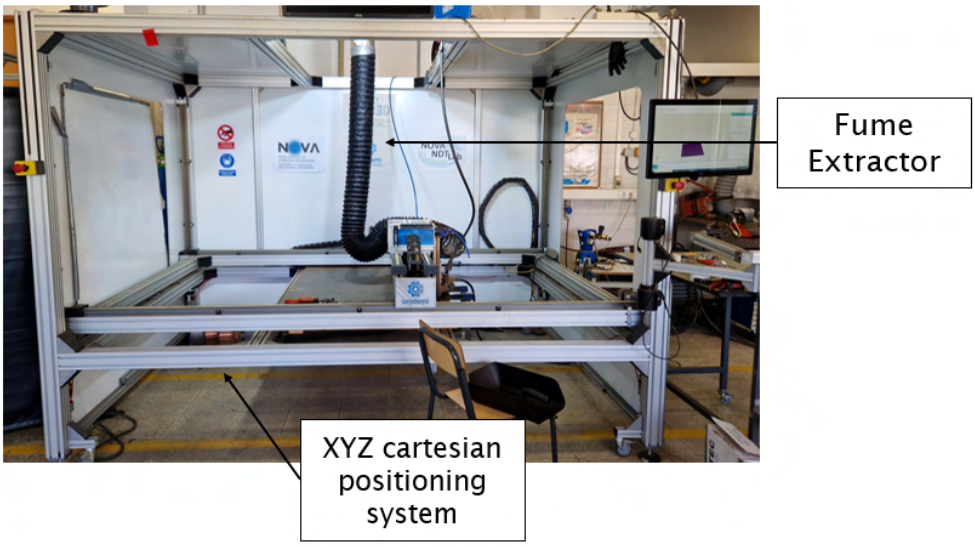

Figure 4.7: MIG WAAM setup.

The manufacturing of parts using the MIG WAAM process involves a setup that includes the following components:

- The GMAW power source is a crucial component. For this task, a Oerlikon CITOWAVE III 420 welding machine was utilize;
- A 3-axis moving table frame made of 80 x 80 mm Bosch Rexroth aluminium profiles is required to function as a 3D printer. The profiles provide a rigid structure to support the weight of the components and the forces caused by their movement. This moving table enables the production of parts with various geometries;
- The 3-axis guide includes 57STH56 NEMA-23 bipolar stepper motors, which are controlled by TB-6600 drivers. The board utilized for this purpose is the Arduino Mega 2560;
- To guide the welding wire, a welding torch was used;
- An essential component of the system is the Unicraft MV300P exhaust fan;
- The negative output of the power source was connected to a 25 mm^2 copper cable, which runs through the cable trays to the moving head, providing electrical energy

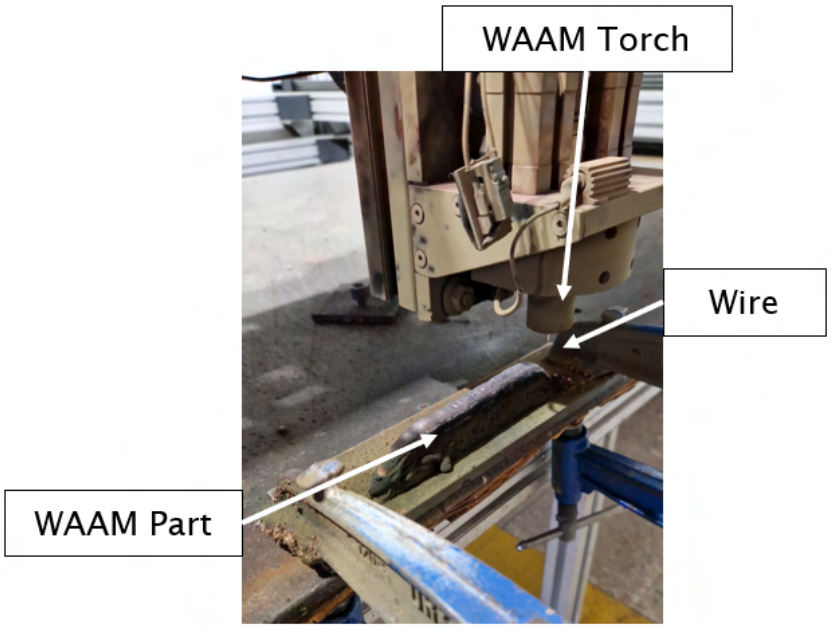

Figure 4.8: Torch.

to the connected torches. Additionally, a power cable was attached to the positive pole of the welding machine's power source, connecting to the equipment's steel substrate. To modify the polarity, simply adjust the cable connections at the welding machine's power supply;

- To supply the torch with shielding gas, a flexible tube is routed through the cable trays from the moving head to the solenoid valve inside the welding machine. This ensures that activating the welding trigger automatically triggers the supply of shielding gas;

- The G-Code programming language was used with the repetitive-host software to control the movement in the x, y, and z directions. The following G-Code was used to create the layers:

  - Incremental coordinates were used for movement in XYZ and extruder operation;

  - The welding machine was safely shut down;

  - The appropriate feed rate was selected;

  - The welding process was initiated;

  - The arc initiation and melting bath temperature rise are delayed by 2000 ms;

  - The welding position is optimised by elevating it by 1.5mm;

  - Wire feeding and movement along the Y-axis begins;

- Welding is concluded upon completion;

- The Z-axis is raised by 2 mm while simultaneously retracting the wire by 15 mm, returning to the initial position.

The production of parts using the TIG WAAM process involves a set-up consisting of the following components:

- The GTAW power source is a very important feature. For this purpose, a Oerlikon CITOTIG 315 AC/DC welding machine;
- To function as a 3D printer, a 3-axis moving table frame made from 80 x 80 mm Bosch Rexroth aluminium profiles is required. The profiles create a rigid structure to support the weight of the parts and the forces caused by their movement. This moving table allows parts with different geometries to be produced;
- The 3-axis guide contains 57STH56 NEMA-23 bipolar stepper motors controlled by TB-6600 drivers. The board used is the Arduino Mega 2560;
- A welding torch was used to guide the welding wire;
- The Unicraft MV300P exhaust fan is an essential part of the system;
- The negative output of the power source was attached In addition, a power cable was attached to the positive pole of the welding machine's power source and connected to the equipment's steel substrate. To change the polarity, simply adjust the cable connections on the machine's power supply;
- To supply the torch with shielding gas, a flexible tube is guided through the cable trays from the moving head to the solenoid valve inside the welding machine. This guarantees that when the welding trigger is activated, the shielding gas supply is automatically activated;
- The G-code programming language was utilized with the Repetitive Host software to control movement in the x, y and z directions. The G-code used in the TIG welding process was similar to that of the MIG process.

Figure 4.9 shows the TIG WAAM setup with the various components described above.

4.4.2 Cu-CuAl alloy Functionally Graded Material stepwise production

After studying various materials, investigating welding parameters and analyzing the best combinations of materials, the FGM that would be produced was defined. The wires used to manufacture the multimaterial metal part were DT-CuAg (copper) and ERCuAl-A2 (Cu-Al alloy). The deposition parameters of these two wires, copper and Cu-Al alloy, are

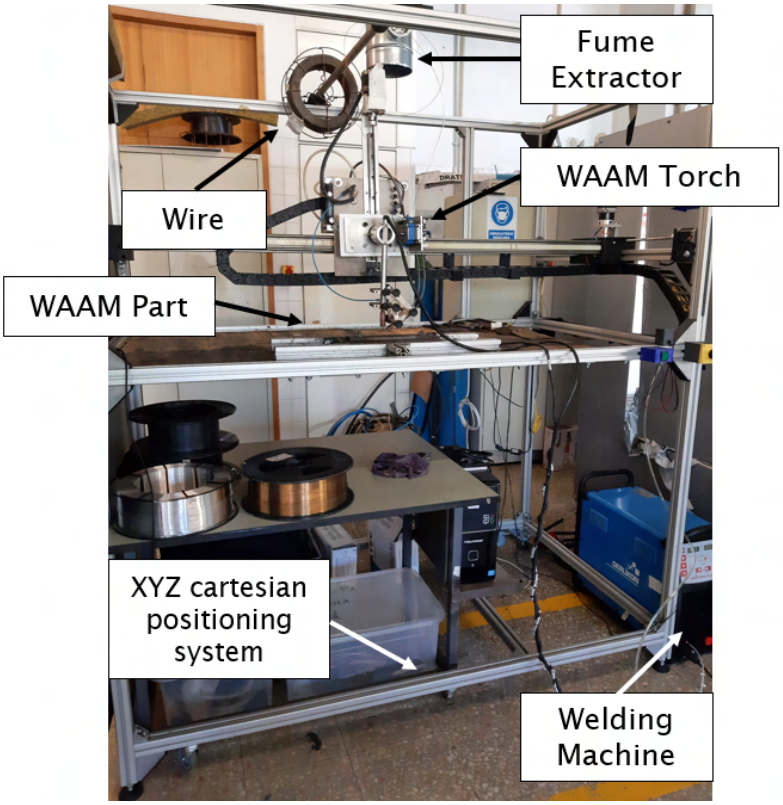

Figure 4.9: TIG WAAM setup.

described in Table 4.6 and Table 4.9 respectively. The substrate used was mild steel, with dimensions of 180mm in length, 50mm in width, and 8mm in thickness. Prior to layer deposition, the substrate was thoroughly cleaned to eliminate any potential contaminants that may compromise the weld quality, prevent inclusion of residues or particles, and avoid corrosion by removing any oxide layers. After cleaning the surface, the copper wire was deposited, followed by the CuAL alloy wire. The FGM walls were produced with 15 layers of Copper and 8 layers of CuAl.During the production of this wall, a greater number of copper layers were deposited compared to copper-aluminum alloy. The purpose of this was to ensure that the copper layers analyzed would not be affected by the metal substrate after the wall is separated and machined.

Between the copper layers and the CuAl layers, the copper layers are preheated to 400-500ºC, to provide greater cohesion between the two materials. An interpass temperature of 100-150°C was maintained and monitored using a pyrometer. This temperature range produces a more stable and consistently formed deposit with reduced ripple [295]. An FGM was made using the GMAW power source through the MIG process. The manufactured walls were simple walls 120 mm long and 50 mm high. The process parameters used are detailed in table 4.6. The wall shown in Figure 4.11 is an AM WAAM wall with the specifications described above.

The wall exhibits high-quality union between the copper layers and the substrate, as well as between the copper layers and the CuAl alloy layers. All deposited layers on this

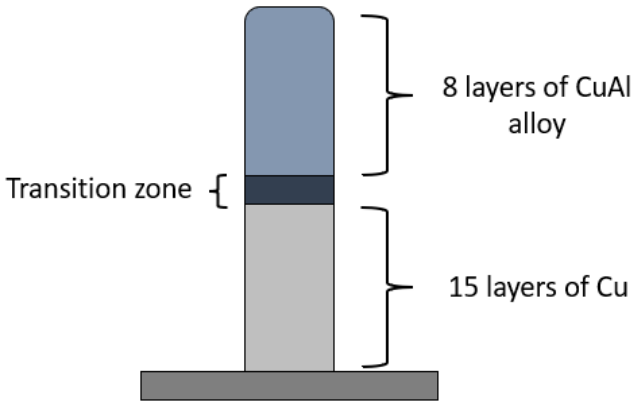

Figure 4.10: Schematic drawing of a Cu-CuAl alloy functional graded material stepwise.

Figure 4.11: Additive manufacturing wall.

wall are defect-free, indicating the appropriateness of the parameters used. The copper layers experienced some melting due to heating at 400-500ºC. Maintaining the geometric precision of the piece proved to be a challenge. During the deposition of the layers, the wall thickness increased, posing challenges to maintaining precise dimensions, tolerances, and movement of the positioning axes. In the end, the FGM specimens with a stepwise functional gradient have the structure shown in Figure 4.12.

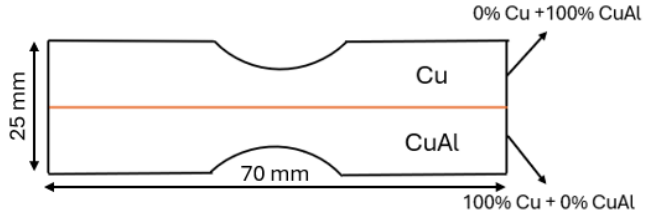

Figure 4.12: Scheme of FGM Cu-CuAL stepwise.

4.4.3 Cu-CuAl alloy Functionally Graded Material continuous production

In this section, several walls will be produced using WAAM in order to produce an FGM with DT-CuAG (copper) and ERCuAl-A2 (Cu-Al alloy) wires, with the structure shown in Figure 4.13. As illustrated in Figure 4.13, the schematic representation of a FGM derived from the Cu–CuAl system is presented. The component under scrutiny consists of a foundation of copper layers, over which a transition zone is said to develop until reaching the upper region, which is composed of CuAl-rich layers. At the centre of the transition zone, an intermediate composition of 50% Cu + 50% CuAl is represented, thus illustrating the progressive change between phases. This configuration of FGM design facilitates the optimisation of the material's overall performance, thereby reducing abrupt discontinuities between distinct layers and mitigating stress concentrations.

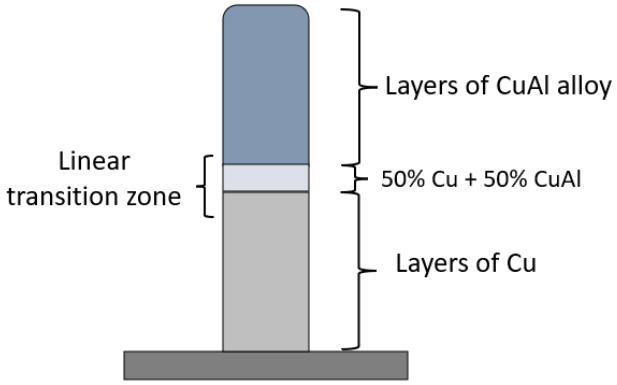

Figure 4.13: Schematic drawing of a Cu-CuAl alloy functional graded material continuous.

As Figure 4.14 illustrates schematically, the tensile specimen of Cu–CuAl exhibits a continuous functional gradient. The material under scrutiny exhibits a progressive composition transition, from 100% Cu at one end to 100% CuAl at the other, passing through an intermediate zone of 50% Cu + 50% CuAl. This configuration facilitates the examination of the impact of gradual composition variation on the mechanical properties of the specimen.

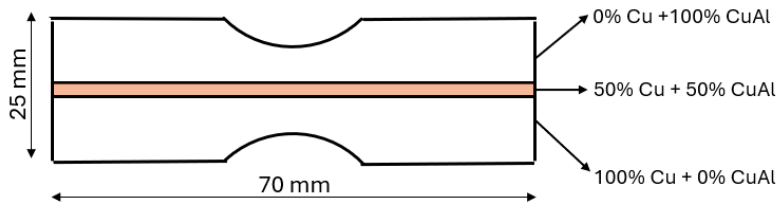

Figure 4.14: Scheme of FGM Cu-CuAl continuous.

4.4.4 Specimens preparation

Sample preparation involves several steps. The first step is to grind the AM wall, remove excess layers and remove the substrate, as illustrated in figure 4.15. A milling cutter was used to create two flat surfaces.

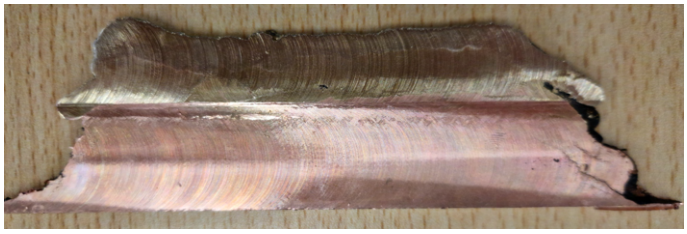

Figure 4.15: Additive manufacturing wall that has already been machined.

The next step is to cut the geometry of the specimen using water jet cutting, as shown in figure 4.16 Waterjet cutting is a variant of hydrodemolition, which involves cutting materials with water under extreme pressure and combining this pressure with the incorporation of an abrasive material such as carborundum, corundum or silica.

Figure 4.16: Additive manufacturing wall after the specimen has been cut.

The next step will be to apply the speckle pattern to perform the DIC tests. First you need to sand the specimen with a sandpaper. Then, possible residues are removed with acetone. The surface is then cleaned with IPA (Isopropyl Alcohol) to ensure that it is ready for painting.

To obtain the best analytical results for microstructure, Vickers hardness or eddy current, specimens are often mounted in an resin epoxy mold and polished to a mirror finish. The resin mount is often precisely sectioned to expose critical areas of interest within the specimen. This process ensures that a flat, oxide-free layer is exposed for accurate imaging and chemical analysis. To achieve the correct mix ratio of 2:1 by volume, simply measure out two parts resin to 1 part hardener (epoxy) before mixing the components.

4.5 Material characterization

4.5.1 Hardness measurements

The Vickers indentation test is an established procedure for assessing material hardness. The experiment is uncomplicated to perform, requires minimal sample material, and is

least destructive, which allows for multiple repetitions. This technique is recognized to be one of the most dependable and fundamental methods of material testing, thus, making it commonly adopted. The Vickers Hardness (HV) is calculated by optically measuring the diagonal lengths of the indent left by the indenter.

The dimensions of the diamond-shaped indentation were measured along both axes in millimetres and then averaged to determine dimension d. The sample's hardness was then determined based on a calibration for various kilogram loads (F). The hardness (HV) is expressed by the following equations:

$$HV = 1,8544 * \frac{F}{d^2} \tag{4.1}$$

$$d = \frac{d_1 + d_2}{2} \tag{4.2}$$

To measure hardness, a Mitutoyo HM-112 Hardness Testing Machine was employed. To perform the three hardness measurement profiles, the setup in Figure 4.17 was used.

Figure 4.17: Hardness setup.

A load of 0.5 kgf was applied across the entire height of the sample for a duration of 10 seconds. The measurements were taken in steps of 0.5mm, starting from the substrate to the last deposited layers for all the samples.

In this subsection, three samples were analysed to determine their microhardness profiles: Cu-CuAl without preheating with functionally graded stepwise, Cu-CuAl with preheating with functionally graded stepwise and Cu-CuAl with functionally graded continuous.

Figure 4.18 illustrates the microhardness profiles of the Cu-CuAl sample without preheating. A total of 136 observations were conducted across the sample. The 3 zones of different materials are clearly visible in the graph. The first section corresponds to the copper layers (from 0 to 24 mm). The last section corresponds to the copper-aluminum alloy layers (27 to 60 mm). From the measured hardenesses it can be concluded that the transition zone from the copper layers to the copper-aluminum alloy layers is 3 mm. The

average hardness of the Cu layers is 52 HV (height < 24 mm). The CuAl layers have an average hardness of 166 HV (height > 27 mm).

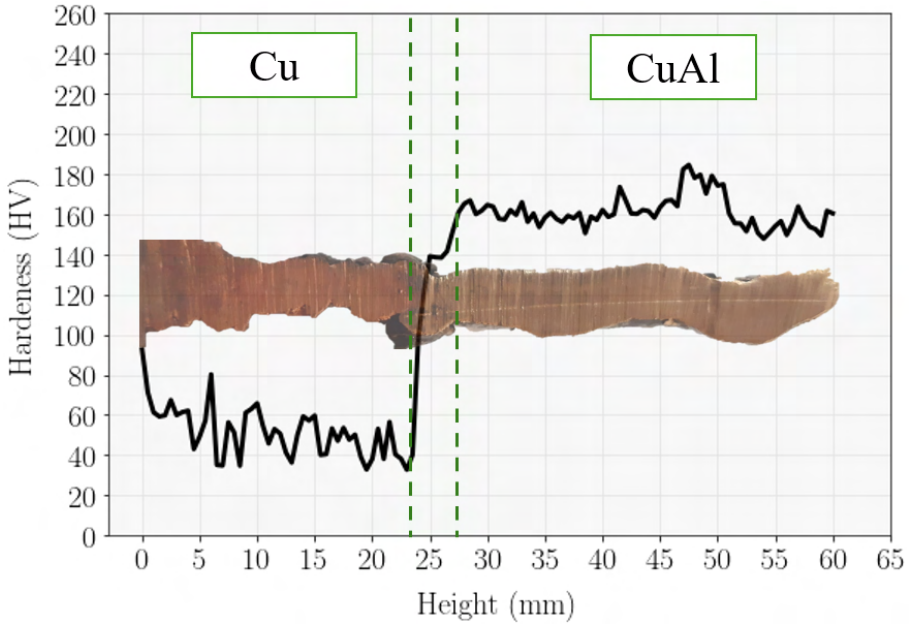

Figure 4.18: Hardness measurements taken from the substrate to the last deposited layer of the FGM crossection of the Cu-CuAl sample without preheating.

Figure 4.19 illustrates the microhardness profiles of the Cu-CuAl sample with preheating. 78 observations were conducted across the sample. The 3 zones of different materials are clearly visible in the graph. The first section corresponds to the copper layers (from 0 to 22 mm). The last section corresponds to the copper-aluminum alloy layers (26 to 35 mm). From the measured hardenesses it can be concluded that the transition zone from the copper layers to the copper-aluminum alloy layers is 4 mm. The average hardness of the Cu layers is 45 HV (height < 22 mm). The CuAl layers have an average hardness of 157 HV (height > 26 mm).

Figure 4.20 illustrates the microhardness profiles of the Cu-CuAl sample with preheating. 90 observations were conducted across the sample. The 3 zones of different materials are clearly visible in the graph. The first section corresponds to the copper layers (from 0 to 23 mm). The last section corresponds to the copper-aluminum alloy layers (30 to 45 mm). From the measured hardenesses it can be concluded that the transition zone from the copper layers to the copper-aluminum alloy layers is 7 mm. The average hardness of the Cu layers is 56 HV (height < 22 mm). The CuAl layers have an average hardness of 153 HV (height > 30 mm).

Through these hardness measurement profiles, it is possible to conclude that preheating the adjacent layers before depositing the layers of the following material causes the FGM transition zone to increase slightly. The deposition of an intermediate layer of 50% Cu and 50% CuAl between layers of the two materials results in a larger FGM transition zone.

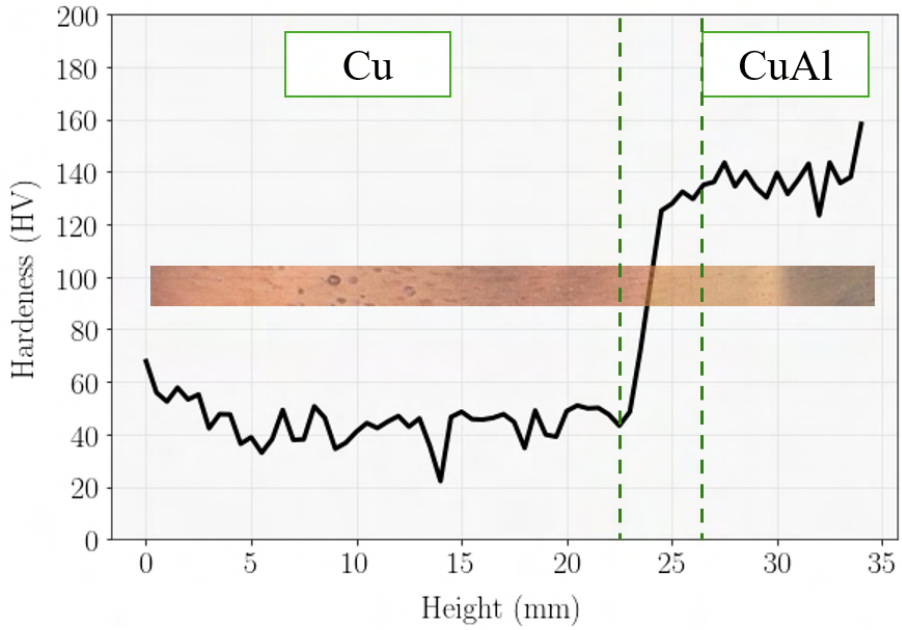

Figure 4.19: Hardness measurements taken from the substrate to the last deposited layer of the FGM crossection of the Cu-CuAl sample with preheating.

4.5.2 Eddy current measurements

In this subsection, several electrical conductivity measurements will be carried out on Cu-CuAl alloy FGM stepwise and Cu-CuAl alloy FGM continuous specimens.

Eddy current measurements were conducted in order to evaluate the homogeneity of microstructures and the variations in the treated materials. An Olympus absolute helical shielded EC probe with a straight axis surface, featuring a range of 1 to 6 MHz, was utilized. An Olympus Nortec 500C impedance measuring device was also employed. In Figure 4.21 it is possible to observe the setup used for the eddy current measurements.

Results were obtained on a vertical axis at the centre of the cross section at a sampling rate of 1 MHz. In all samples, the test frequency was set to 1MHz while the angle was fixed at 268º to ensure alignment of the electrical conductivity variation with the imaginary axis. The gain was adjusted individually for each material to optimize the output signal. Calibration equations were determined by performing measurements on standard materials having electrical conductivity comparable to that of the specimens under examination to convert the output signal into %IACS.

The relative eddy current signal along the scanned region is presented in Figure 4.22 for the Cu-CuAl alloy FGM stepwise without preheating. The x-axis represents the sample length, defined as the distance from the top of the sample down to the substrate. The y-axis corresponds to the relative eddy current signal, i.e., the intensity of the currents induced in the material during the measurement. A clear transition is evident between the Cu base material and the CuAl alloy, as indicated by the two dashed vertical lines at approximately 9–10 mm. In the Cu region, the normalized response remains relatively stable around unity, while a pronounced decrease is detected once the probe crosses into

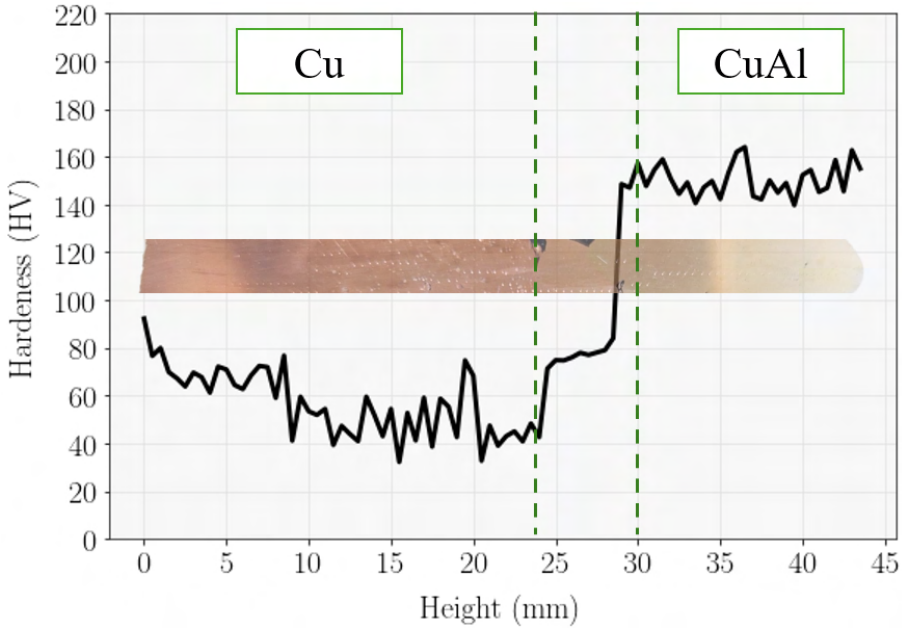

Figure 4.20: Hardness measurements taken from the substrate to the last deposited layer of the FGM crossection of the Cu-CuAl sample with one layer of 50% CuAg and 50% CuAl in the middle.

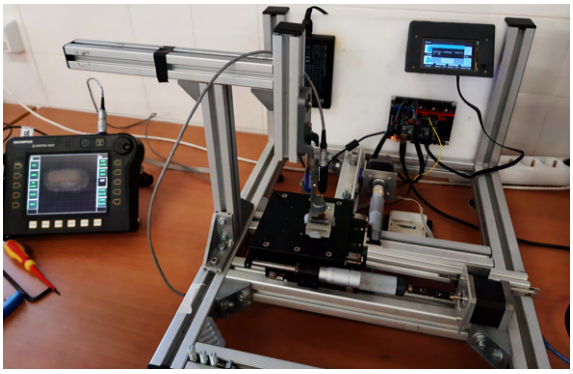

Figure 4.21: Eddy currents setup.

the CuAl side. This decline is indicative of the reduced electrical conductivity exhibited by the alloy in comparison to copper, thereby validating the efficacy of the eddy current technique in differentiating between various materials. The overlaid optical image of the cross-section further illustrates the Cu/CuAl boundary, enabling a direct correlation between the relative signal and the actual joint morphology.

As illustrated in Figure 4.23, the relative eddy current response has been measured across the Cu/CuAl interface of the Cu-CuAl alloy FGM stepwise with preheating. In this instance, the signal displays a significant increase at approximately 8–9 mm, as indicated by the dashed vertical lines. The Cu region displays a lower and relatively stable response, while a sharp rise is observed as the probe enters the CuAl alloy side, where the signal stabilises at higher values. This is due to the difference in electrical conductivity between pure copper and the CuAl alloy, leading to distinct eddy current intensities in each region.

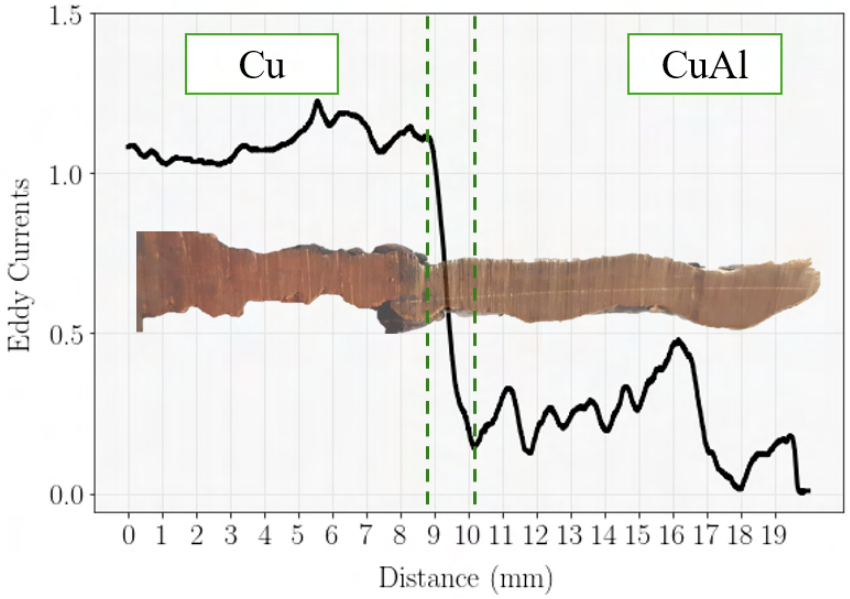

Figure 4.22: Eddy currents profiles of the Cu-CuAl sample without preheating.

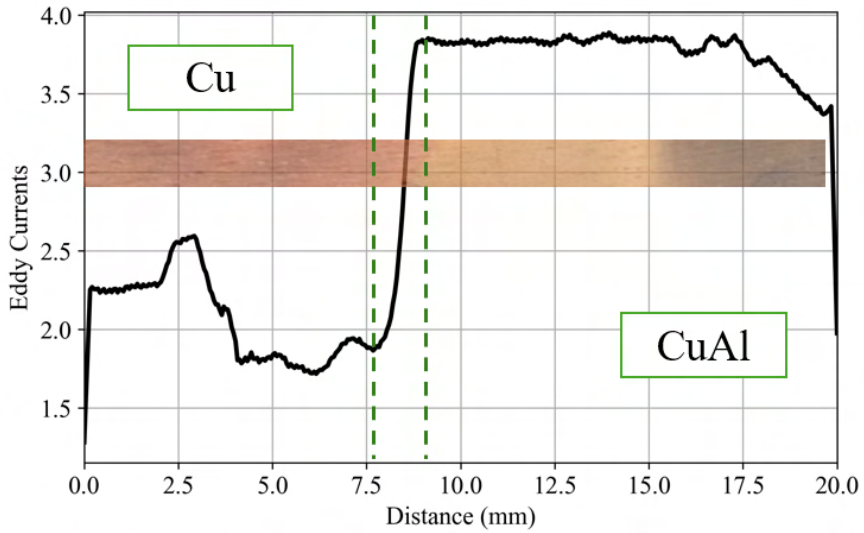

Figure 4.23: Eddy currents profiles of the Cu-CuAl alloy FGM stepwise.

The overlaid optical image of the cross-section allows for direct comparison between the physical joint and the measured signal, thus confirming the effectiveness of the technique in detecting the transition between dissimilar materials.

The Figure 4.24 illustrates the relative eddy current response of the Cu-CuAl alloy FGM continuous. These figures present the relative eddy current signals obtained across the Cu/CuAl interface for different scanning conditions. In all cases, a distinct transition between the two materials can be identified, demarcated by the dashed vertical lines. For copper, the response remains relatively stable at lower values, while upon entering the CuAl alloy, the signal exhibits a sharp increase and stabilises at a higher level. This

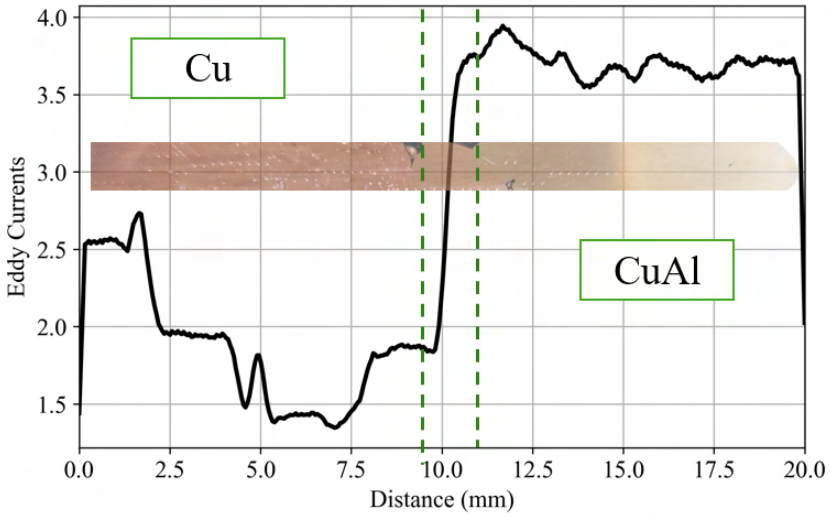

Figure 4.24: Eddy currents profiles of the Cu-CuAl alloy FGM continuous.

behaviour is indicative of the disparities in electrical conductivity between copper and the CuAl alloy, thereby substantiating the sensitivity of the eddy current technique to material heterogeneities. The overlaid optical images of the cross-sections provide a direct visual correlation between the experimental signal and the physical joint morphology, thereby highlighting the capability of this approach to detect and localise material transitions with a high degree of precision.

4.6 Digital image correlation procedure

4.6.1 Speckle pattern

In order to conduct full-field measurements, it is imperative to apply a speckle pattern to the sample being studied. The three most conventional techniques for applying the speckle pattern are via a spray can, airbrush, or stamp.

4.6.1.1 Stamp

First, it was decided to utilize the stamp technique. To capture 3-5 pixels per speckle on a 25 mm wide sample, a pixel size ranging from 41.7 to 69.4 microns is necessary. The application of speckle pattern using stamps is accomplished via Microcontact printing. This technique facilitates the formation of self-assembled monolayers (SAMs) of ink on a substrate's surface using relief patterns on a master stamp made of polydimethylsiloxane (PDMS) or Urethane rubber. The method shares similarities with nanotransfer printing (nTP) since it achieves conformal contact. PDMS, which is a silicone polymer with many applications, is frequently used to create the master stamps.

The production of a silicone stamp involves a set of consecutive steps. Firstly, a speckled master mold composed of silicon is created using the photolithography process at the

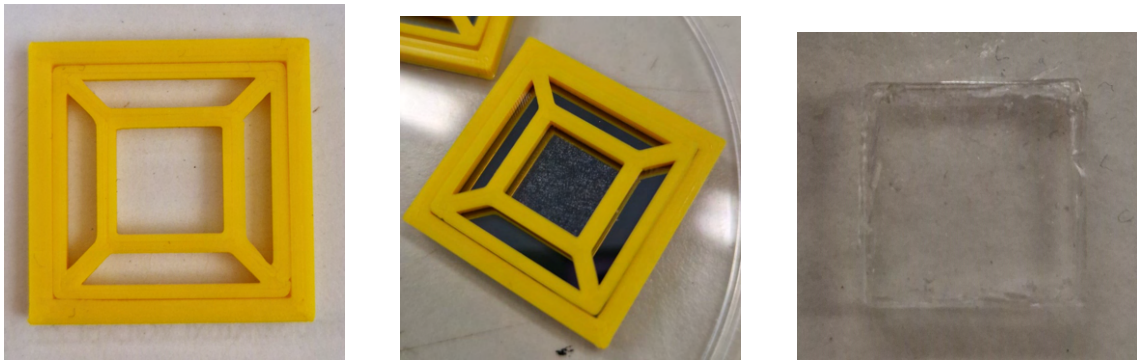

(a) (b) (c)

Figure 4.25: (a) 3D-printed positioning tool, (b) speckled master mould in the 3Dprinted alignment jig, (c) final stamp.

lithography facility located at the University of Southampton. Following this, a silicone elastomer and a silicone elastomer curing agent are mixed together in a ratio of 10:1 for several minutes. The resulting mixture is then placed in a vacuum pump for a duration of 30 minutes until no bubbles are discernible in the PDMS mixture. Next, the mottled silicon master will be positioned in a 3D-printed aligning jig. PDMS solution will be poured into the mould, exceeding its capacity.

Whilst this technique has numerous advantages, including the ability to utilize a PDMS stamp repeatedly, as well as being a straightforward application process that can produce a wide range of pattern types and varying speckle sizes, it does have two notable shortcomings. Firstly, there is a challenge in achieving reproducibility due to the fact that the master can only be used once, and secondly, it can be difficult to apply the same standard uniformly and equally to all samples. The final mixture undergoes degassing to prevent any bubbles from forming in the PDMS mould upon its readiness. To ensure that the PDMS mould has two level surfaces, the liquid mixture is concealed under a microscope glass slide. Subsequently, the PDMS mould is kept in a fume hood for 48 hours for it to cure. Once cured, a stable pdms stamp is created by extracting it from the 3D-printed positioning tool. The PDMS stamp replicates the inverse pattern of the master mold. In other words, the raised areas of the stamp correspond with the recessed areas of the master mold. This stamp was employed to transfer ink onto the test piece, creating a speckled pattern.

The process of applying a stamp to a specimen involves the following steps: Next, apply the stamp to the specimen and press down evenly across the entire surface. Firstly, apply ink onto a smooth and clean surface, such as a microscope slide. Next, apply the stamp to the specimen and press down evenly across the entire surface. After a short waiting period, press the stamp onto the inked surface and maintain pressure for a few more seconds. Next, apply the stamp to the specimen and press down evenly across the entire surface. Lastly, clean the stamp with acetone and reuse as necessary.

Stamping the test piece poses certain challenges. Additionally, the stamp dimensions

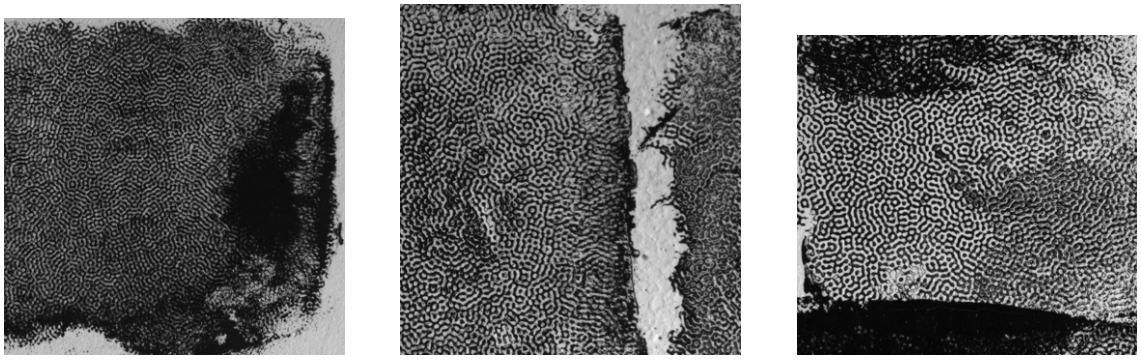

(a) (b) (c)

Figure 4.26: Stamp application defects: (a) excess paint on the edges, (b) empty areas between stamps, (c) overlapping.

are 10X10 mm whereas the field of view of the test piece has dimensions of 57X30 mm, necessitating the need to apply the stamp 18 number of times. Initially, using stamps with very small speckle sizes was problematic as it hindered the creation of a recognizable pattern. This requires the application of multiple stamps in close proximity, which may result in empty spaces or overlap. Additionally, the pressure applied to the stamp may be uneven, leading to a non-uniform pattern. Given the microscopic nature of the pattern, even slight inconsistencies in pressure are sufficient to create an uneven pattern across the entire surface. Given the microscopic nature of the pattern, even slight inconsistencies in pressure are sufficient to create an uneven pattern across the entire surface.

4.6.1.2 Airbrush

Due to complications associated with utilizing the stamp method to execute the pattern, the approach of using an airbrush was employed. While the spray can method is practical and easy to apply, it is challenging to maintain control over the speckle size making it unsuitable for the study.

The Airbrush speckle pattern technique was utilized on all examples. Abbreviations of technical terms will be explained at first use. The system employed was a Gravity feed airbrush, wherein the paint moves down to the nozzle due to gravity and the pressurized air "pushes" the paint out. An air compressor connected to the airbrush nozzle is necessary to pressurise the air. A schematic of the components and operation of the airbrush system is shown in Figure 4.27.

To apply the speckle pattern, first connect the airbrush to the compressor with a cable. Then about 10 drops of black paint were put into the gun and 1 or 2 drops of airbrush flow improver were added. Everything was mixed with a brush. A pressure of 50 psi was maintained throughout the application. After use, the pipe was washed with water and an airbrush cleaner. The airbrush must always be used parallel to the pattern application surface. A schematic of the airbrush nozzle and its components is shown in Figure 4.28.

One challenge with airbrushing is that the speckles are uniform in size, resulting in

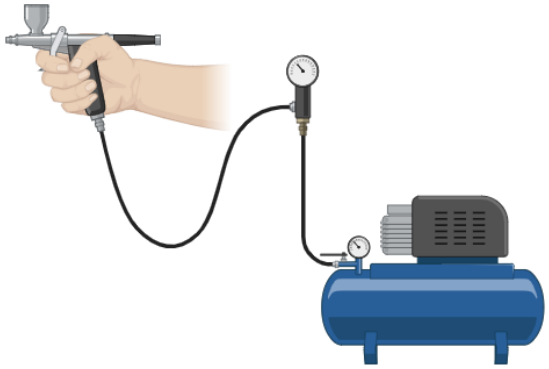

Figure 4.27: Airbrush system components schematic.

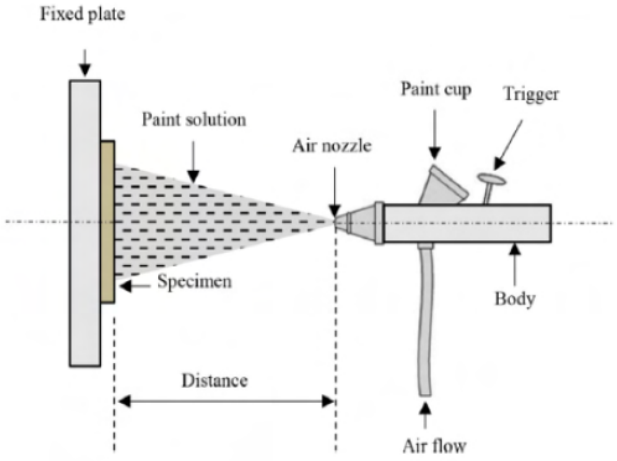

Figure 4.28: Airbrush schematic [296].

an unwanted aliasing effect. An effective solution is utilizing an airbrush flow improver to mix with paint. This allows for the paint to adjust in thickness, leading to speckles of varying sizes. The image in Figure 4.29 displays a specimen with a speckle pattern applied using an airbrush.

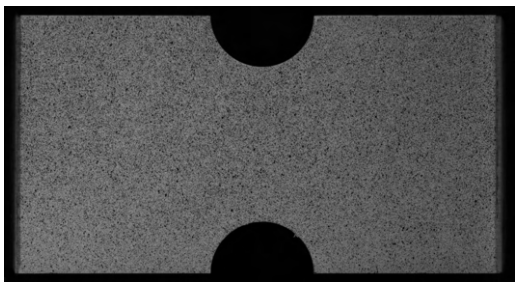

Figure 4.29: Image captured at the beginning of the test showing the speckle pattern produced by airbrush.

The speckle pattern should be random to prevent any predictable interference with

correlation accuracy. The speckle density of the pattern should be uniform, despite its randomness. Additionally, there should be a high contrast between the light and dark areas of the speckle pattern to ensure image correlation identification. The provided pattern highlights a potential issue, namely the aliasing effect.

4.6.1.3 Spray

In experimental tests conducted with continuous FGM specimens, the speckle pattern was applied by means of spray paint, thereby ensuring rapid and even distribution of the pattern across the surface. The selection of this procedure was made on the basis that it is the most suitable option for the geometry and continuity of the composition transition exhibited by the specimens in question. Conversely, for the stepwise FGM specimens, the airbrush technique was employed, a method that affords greater local control over the pattern deposition and is adequate for the characterization of the discrete layers. The application of the speckle pattern using spray paint began with the cleaning of the surface of the specimen. Subsequently, an additional layer of white paint was applied and permitted to dry. This process was repeated on three occasions. The application of the speckle pattern was completed with the addition of a layer of black paint. This technique demands a high level of control over the spray cap of the device, thus allowing for the formation of dots of different sizes.

4.6.2 Case study on the application of Digital Image Correlation and Virtual Fields Method on a 316L stainless steel sample

Four samples of 316L stainless steel were tested to validate the geometry decided in Chapter 6. These experimental tests aimed to identify the challenges and errors that require improvement. The dimensions of these samples were as follows:

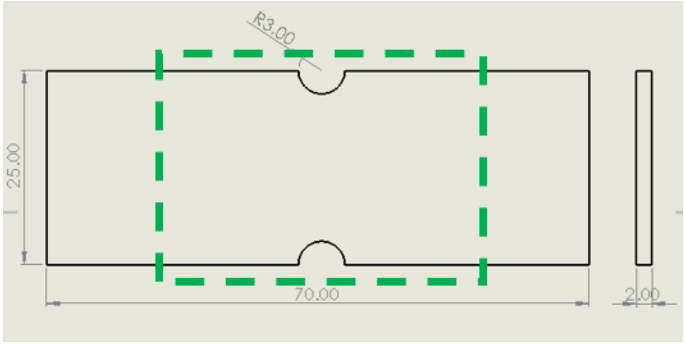

Figure 4.30: Tensile test specimen dimension in mm.

The Field of View (FOV) of this study is represented by the green dashed area and has dimensions of 57X30 mm.

4.6.2.1 Tensile test procedure

The experiment was conducted using an Instron 5569 electromechanical test machine with a 50 kN load cell. The specimens were vertically aligned and secured in the grips, and subjected to a displacement rate of 1.5 mm/min during the tensile test. Two cameras captured images using stereo-DIC, one aligned with the specimen and the other at an angle. Stereo-DIC has the advantage of measuring out-of-plane movement. For the tests, two Blackfly 8.9MPx cameras were used to provide sufficient spatial resolution. The cameras were rotated to maximize spatial resolution on the sample. The cameras were equipped with 105mm lenses (Sigma 105mm f/2.8 EX DG Macro Lens, Sigma Corporation, Aizu, Japan) and a sensor array. Two polarisers were placed on both lenses to filter the light, and two LED lights were used to illuminate the samples. The experimental setup is shown in Figure 6.12.

Table 4.14 presents the main characteristics employed in the stereo-DIC tensile tests of 316L stainless steel specimens.

Table 4.14: Stereo-DIC settings for the tensile test of 316L stainless steel specimens.

DIC setting	Specification
Electromechanical test machine	Instron 5569
CMOS Cameras	Blackfly 8.9MPx
Lens	Sigma 105mm f/2.8 EX DG Macro Lens
Stereo angle	19,76 °
Patterning technique	Airbrush
DIC technique	Stereo correlation
DIC software	MatchID, version 2024.1

4.6.2.2 Digital image correlation (DIC) method procedure

During the tensile test, a DIC system was used to measure surface deformations in the analyzed samples. This system requires specialized DIC software for capturing and analyzing images of samples during tensile testing. The software uses algorithms to track pixel patterns and calculate surface deformations as these patterns change over time. Additionally, high-resolution, high-frame-rate cameras are necessary to capture detailed images of samples during testing. This study employs a stereo system comprising two cameras that cover the sample surface. Adequate lighting is necessary to ensure sufficient contrast in the captured images for analysis by the DIC software. The speckle pattern is also crucial in the DIC system, requiring a high-contrast pattern on the sample that is visible to the cameras and remains undistorted during testing. These markings will be visible to the cameras as reference points for the DIC software to calculate deformations. The process of applying the speckle pattern has been previously described in Section 4.6.1. It is crucial to have an appropriate experimental setup where the cameras capture the entire surface of the sample and the lights illuminate it without creating any shadow areas

during the tensile test. Table 4.15 displays the default DIC parameters used in the analysis of 316L stainless steel samples.

Table 4.15: DIC parameters for tests on 316L stainless steel specimens.

DIC Parameter	Specification
General DIC Settings	
Technique Used	2D Digital Image Correlation
Camera Resolution	16bit, 5320 × 4600 pixels
Pixel to mm conversion	0.004
Average Speckle Size	11 pixels
Subset Size	41 pixels
Step Size	2 pixels
Shape Function	Quadratic
Interpolation Function	Bicubic Spline
Correlation Criterion	ZNSSD
Prefiltering	Gaussian (Kernel size = 5)
Strain Settings	
Strain Window	55 data points
Virtual Strain Gauge (VSG)	149 pixels
Strain Interpolation Function	Bilinear Quadrilateral (Q4)
Strain Tensor	Hencky

After performing the calibration, around 20 still images were captured. The DIC technique requires a static reference image for comparison with subsequent images to calculate displacements and deformations of the test. As with most experimental techniques, DIC is susceptible to experimental noise, which affects the accuracy of the results. As with many experimental techniques, DIC is vulnerable to experimental noise, also known as random error, which can impact the precision of the technique. The primary source of this noise is the camera acquisition process, which introduces random variations in the gray level values of the captured images. This noise propagates through the DIC process and affects the measured coordinates and all derived quantities. The random nature of image acquisition noise can be reduced by averaging multiple images. This is a simple process for the reference DIC image, which usually involves the test sample under no load conditions. Multiple 'static' images of the test sample can be captured and averaged to produce an approximately 'noiseless' reference image. However, generating a similar 'noiseless' deformed image(s) is a challenging task. It is important to exercise caution regarding the effects, such as creep. In the 4 samples, an aperture of 16 was used in both cameras. An illumination intensity of 40-50% was defined in the lamp used. The same exposure time of 33000 μs was used for all of the tests. The images were taken at 0.5 Hz because the camera's high spatial resolution does not provide much temporal resolution.

4.6.2.3 Calibration process

To evaluate the specimen geometry through captured images, the system setup required calibration. This involved determining the image parameters of each camera, as well as their relative position and orientation in relation to one another. The camera calibration exercise must be repeated whenever a camera is moved or when any of the settings are changed, such as focus or aperture. Calibration involves capturing images of the calibration target from various viewing perspectives. The calibration target should be of a similar size to the sample being studied and placed in the same position as the sample. During calibration, multiple images of the calibration target must be captured at the sample position with different angles and tilt directions. Camera calibration is the process of estimating the parameters between a lens and an image sensor of an imaging camera. The aim of stereo-DIC calibration is to establish the intrinsic camera parameters, such as image scale, focal length, image center, and lens distortions, as well as the extrinsic parameters of the stereo-DIC system, including stereo-angle, distance between cameras, and distance from cameras to the object. These parameters are used to correct lens distortion, measure the size of an object, or determine the location of the camera in the scene. The calibration process consisted of the following steps:

- The first step was to select a calibration target of an appropriate size, equal to or slightly smaller than the sample FOV.
- The next step is to create a working space in which to perform the calibration. This space must be large enough for the calibration target to be held, rotated, tilted and translated if necessary. In this case, a 9X12 2.50mm calibration target was used.
- The subsequent stage involves adjusting the lighting. It is imperative to ensure that there is a uniform contrast across the entire calibration target, without any glare in any of the directions or angles used by the calibration target. These conditions must be identical in both cameras for the stereo DIC. The calibration target used in the calibration process for the four DIC tests is shown in Figure 4.31.

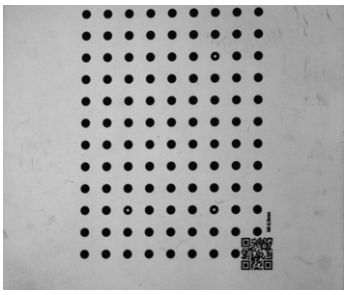

Figure 4.31: Calibration plate used in the test calibration process.

- Image acquisition is performed to ensure well-extracted resources throughout the optical system. The number of calibration images required or recommended depends

on the calibration target and the DIC software. The most appropriate value for the number of images-error ratio is 150-200 images. However, it is more important to have high-quality images than a large number of images. Figure 4.32 demonstrates an improvement in the standard deviation of both pixels and millimetres when more calibration images are used in the parameter estimation process.

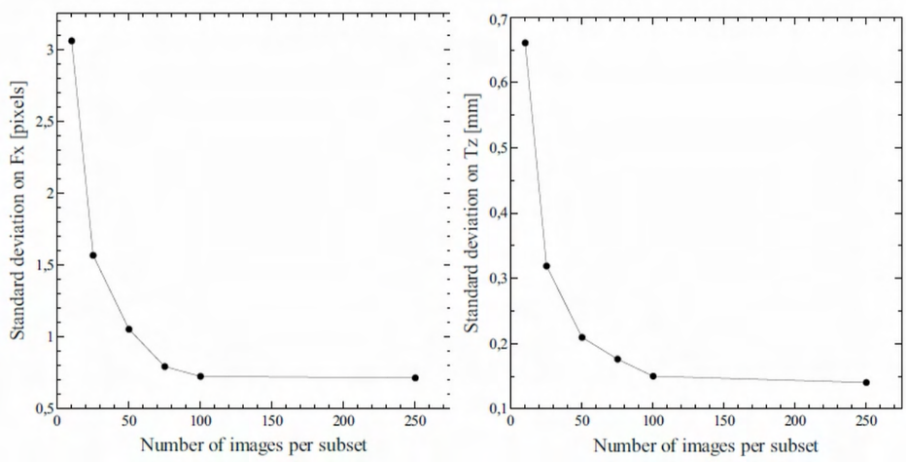

Figure 4.32: Standard deviation versus number of images in calibration [297].

- It is then necessary to extract all the points in all the images. To validate the imposed settings, it is necessary to perform point detection for a single image by image processing. For the point detection, a minimum required number of points of 80 and a black and white threshold of 40 were used.

- The next step is to review the calibration results. After that, check the rejected images to see if there was an obvious reason for the failure. It is important to verify whether the remaining accepted images still fill the working field of view of the optical system. Finally, ensure that the features extracted from the accepted images are correct.

- Finally, the review calibration parameters. The values of the calibration parameters should be compared with the corresponding physical values. This includes parameters such as the image center, lens focal length, angles, and distance between two cameras. The results are shown in Figure 4.33.

The cameras have intrinsic properties that are determined, including F_x, the focal length in the x direction, F_y, the focal length in the y direction, C_x, the main point x coordinate, C_y, the main point y coordinate, and K_1, the first-order radial distortion in the case of radial/tangential distortion model. The stereo system's extrinsic parameters include θ, the stereo-angle around the x-axis; ϕ, the stereo angle around the y-axis; ϕ, the stereo angle around the z-axis; T_x [mm], the camera distance in the x-direction; T_y [mm], the camera distance in the y-direction; and T_z [mm], the camera distance in the z-direction.

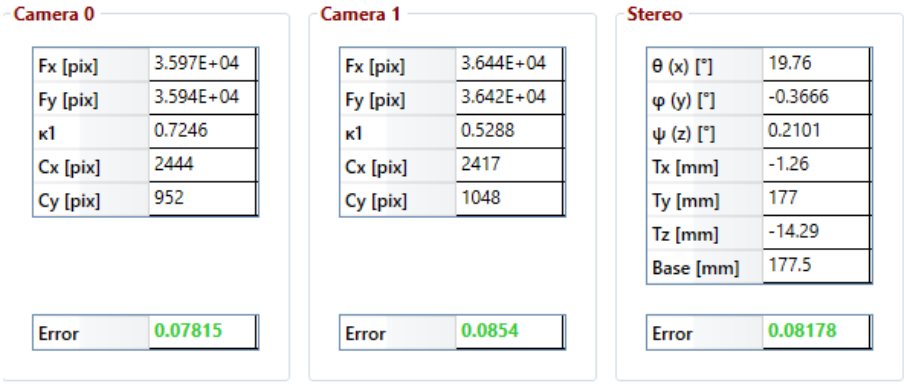

Figure 4.33: Calibration results of the 316L Stainless steel samples.

4.6.2.4 Maximum Force

Four samples, including a pre-test sample and three samples made of the same material and geometry, were tested until failure. The maximum forces of the four specimens were very similar despite the different compositions of the two materials. Figure 4.34 illustrates the varying maximum forces of the four samples.

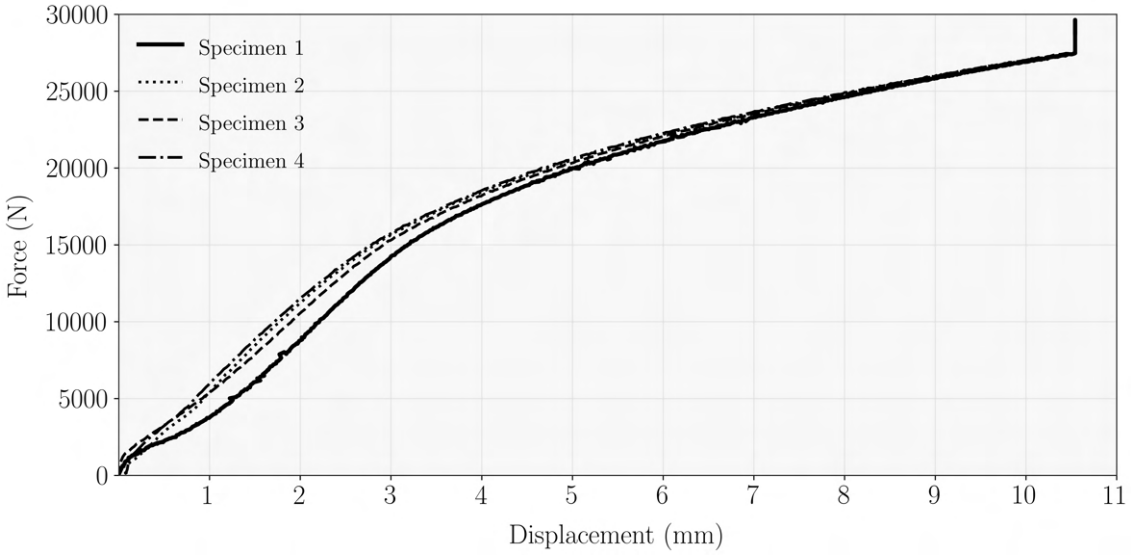

Figure 4.34: Maximum force until failure for the 4 specimens tested of 316L stainless steel.

This graph shows the displacement in mm against the required force in N. This graph shows that the behaviour curves of the 4 specimens tested are similar. The 4 specimens behave identically because their geometry and material are the same.

4.6.2.5 Noise evaluation

Before performing the DIC tensile test, it is necessary to check the quality of the captured images and evaluate the noise levels. 20 still images were taken before the start of the test, then these images were averaged to compensate for the noise, the static noise for each

camera was calculated using MatchID [1]. Before performing the DIC test, it is important to check the quality of the captured images and evaluate their noise levels. The noise was found to be 0.01387 of the dynamic range for the sample-aligned camera. The average spot size of each sample was calculated using MatchID. The smallest spot size achieved with an airbrush was approximately 6,8 pixels. The standard deviation of the selected DIC field variable gives the noise floor of the field variable. Figure 4.35 shows the grayscale histogram for each pixel.

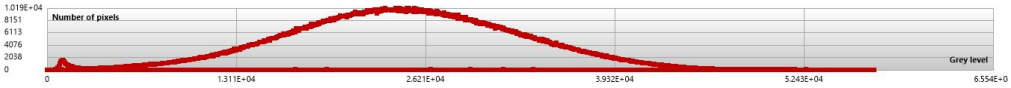

Figure 4.35: Gray level histogram for each pixel.

The histogram should cover all ranges of pixel intensities present in the image and display good contrast with different pixel intensities clearly distinguishable. Saturation at the extremes of the histogram should be avoided. An excessive concentration of pixels at one or both ends of the histogram may indicate loss of information in areas of extremely high or extremely low brightness in the image. Upon analysis of the histogram, it can be concluded that this is a well-balanced and representative distribution of intensities among the image pixels.

4.6.2.6 Results

In these results, the 4 specimens had similar behavior, as shown in Figure 4.34, so only the results of one of the tested specimens will be shown. To perform the analysis, it is necessary to define the Region of Interest (ROI). Since the area furthest away from the notches has similar behaviour, we do not need to analyse the entire FOV. The Figure 4.36 displays the region of interest that was analysed in this study.

In this image, the sample has been rotated to the left. This means that in this image, loading is occurring to the left side.

After defining the ROI, the settings for calculating strains and stresses were established. The results for several variables were obtained by correlating strains and stresses. However, the most significant variables for studying these samples are the displacements and associated strains and stresses, which are more relevant in the x direction.

The displacements in the x direction show results within expectations. The displacements occur according to the loading during the tensile test.

The displacements in the vertical direction are not significant, as they did not show significant strain values. This conclusion supports the statement made earlier that since

[1]The author would like to acknowledge the parallel support from the project "Fluid-Structure Interaction for Functional Assessment of Ascending Aortic Aneurysms: A Biomechanical-Based Approach Toward Clinical Practice" (DOI: 10.54499/PTDC/EMD-EMD/1230/2021), funded by the Foundation for Science and Technology (FCT). The author gratefully acknowledges this project for providing access to the latest version of the MatchID digital image correlation software, which was essential for the full-field measurements and inverse identification procedures presented in this thesis.

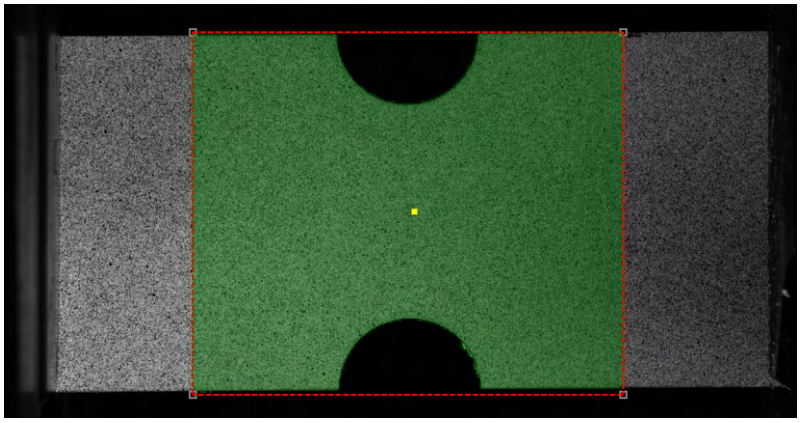

Figure 4.36: Region of interest (ROI).

the loading direction is horizontal, the displacements in the vertical direction are not significant.

The experimental tests were coupled to 3D stereo DIC, allowing for the determination of displacements in the z direction. The displacements in the z-direction are not very relevant, as they are practically nonexistent. It is evident that there is no movement in the z-direction, therefore the z-component is negligible.

Figure 4.37 displays the global strain in the xx direction. The maps demonstrate a uniform distribution of strains due to the specimen's uniform geometry and homogeneous material. Additionally, the maps indicate that the specimen will fail in the area of greatest deformation, which is the region between the notches. The frames chosen were chosen because they show the evolution over the time of application of the loading. These were chosen with two principles in mind: showing the evolution of the test in a uniformly distributed manner over time and showing when there is any change in strains in any area of the specimen.

The global strain fields in the yy direction did not show significant strain values. ε_{yy} was not so relevant, since the specimen is homogeneous and loading occurs in the x direction.

Figure 4.38 displays the global strain maps in the xy direction. The maps indicate a slight rotation of the specimen in the notch area, which may be due to a small misalignment of the tensile machine grips.

After analysing the results of the specimen deformations in the DIC tensile test, they are then analysed using inverse identification by VFM.

4.6.2.7 Inverse identification of 316L Stainless steel by VFM

In this study, VFM is used as a technique to solve the inverse problem, i.e. to identify the constitutive parameters of the model using data from the tensile DIC tests. The VFM module of the MatchID software was used to perform this identification.

The practical workflow for this analysis was as follows:

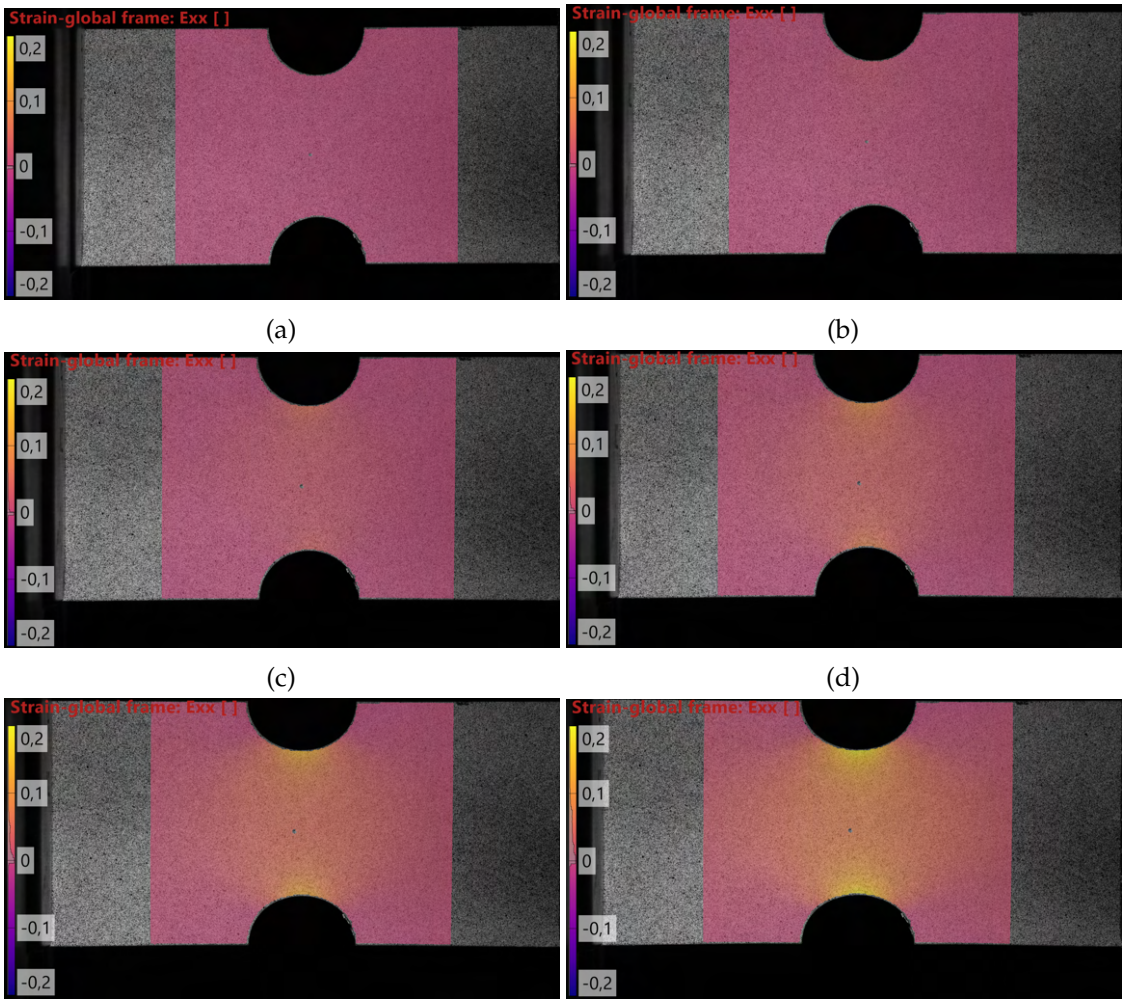

Figure 4.37: Global strain fields for specimen in the xx direction, ε_{xx}, for 316L stainless steel: (a) 0KN, (b) 13.5KN, (c) 17KN, (d) 19KN, (e) 21KN and (f) 23KN.

- The VFM module in MatchID stero was used in this analysis.
- The boundary conditions of the model were then defined. A horizontal force was considered on one of the surfaces and a clamping force was applied to the other surface.
- The force data was defined by the force data from the tensile test performed using a .csv file created in MatchID Stereo.
- The next step is to assign a material orientation. However, in this study the material was considered to be isotropic, so it was not necessary to assign a material orientation.
- It was necessary to specify the material model to be identified. Here is the time for the study where the material properties are set. In this model an elastoplastic material model has been defined. First the elastic properties are defined and then the plastic parameters are defined. In the elastic properties the type was defined as isotropic,

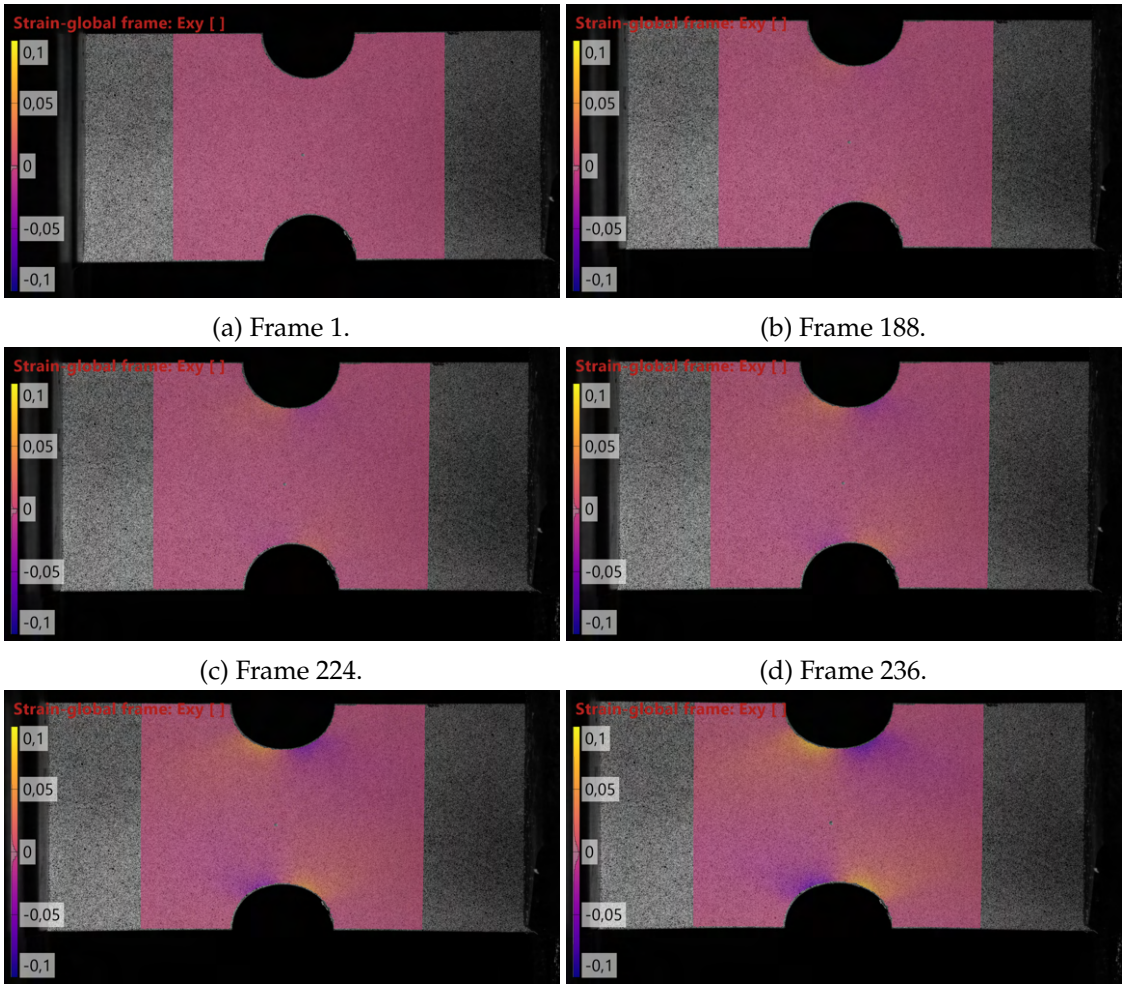

(a) Frame 1. (b) Frame 188.

(c) Frame 224. (d) Frame 236.

(e) Frame 276. (f) Frame 296.

Figure 4.38: Global strain fields for specimen in the xy direction, ε_{xy}, for 316L stainless steel: (a) 0KN, (b) 17KN, (c) 18KN, (d) 19.5KN, (e) 21.6KN and (f) 23.5KN.

the Young's modulus parameters (210GPa) and the Poisson's coefficient (0.33). The plasticity parameters were then defined. The Von Mises-Newton-Raphson yield criterion was chosen first. By applying plasticity theory (Von Mises criterion) with numerical techniques (Newton-Raphson method) to predict plastic behaviour in materials. A hardening law was also defined to describe how the yield surface changes under plastic deformation. Three possible hardening laws were considered: Linear, Swift and Ludwik.

- Define the specimen geometry with thickness.
- Optimise VFM settings. In this box, you can define the type of virtual works to be used (uniform or total sensitivity), as well as changing the orientation of the pattern or the number of elements that make up the mesh.

Four specimens were tested in the DIC tensile test and the results were processed in

the MatchID software using the VFM module. The Von Mises-Newton-Raphson yield criterion was selected for all four specimens, and three hardening laws were applied: Linear, Swift, and Ludwik. Figure 4.39 displays the four graphs of the tested specimens. Each graph displays the stress and strain curve for the specimen in question under the three hardening rules. The four graphs exhibit three curves with very similar behaviour.

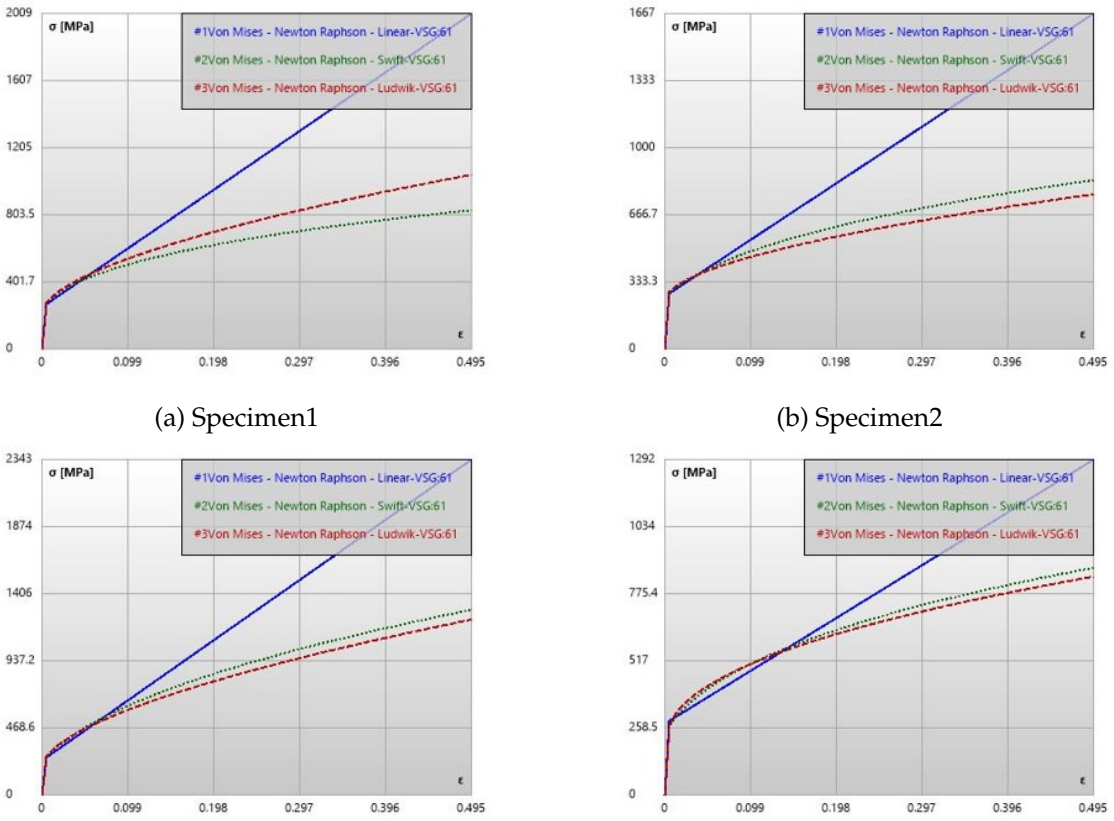

(a) Specimen1

(b) Specimen2

(c) Specimen3

(d) Specimen4

Figure 4.39: Stress and strain curve for different Hardening Laws for each specimen.

For nonlinear models, virtual fields can be used either uniform or with total sensitivity. While total sensitivity fields outperform uniform fields, they are generally slower due to the need to determine new fields based on mesh area and time step. Figure 4.40 shows the uniaxial stress and strain curves for uniform virtual works (a) and total sensitivity virtual works (b).

For models that cannot be directly determined, an iterative process is applied. The default number of iterations is 50, or the iterative procedure will stop automatically if value convergence is reached, even if fewer iterations than the maximum were used. The yield stress value for each of the 50 iterations is presented in Figure 4.41.

As the energy of a system must be conserved, all externally applied work must be balanced by the work done internally through strain energy. Thus, the external virtual work must be equal to the internal virtual work, assuming all energy in the system is in the form of work and strain energy. Figure 4.42 illustrates the identity between external

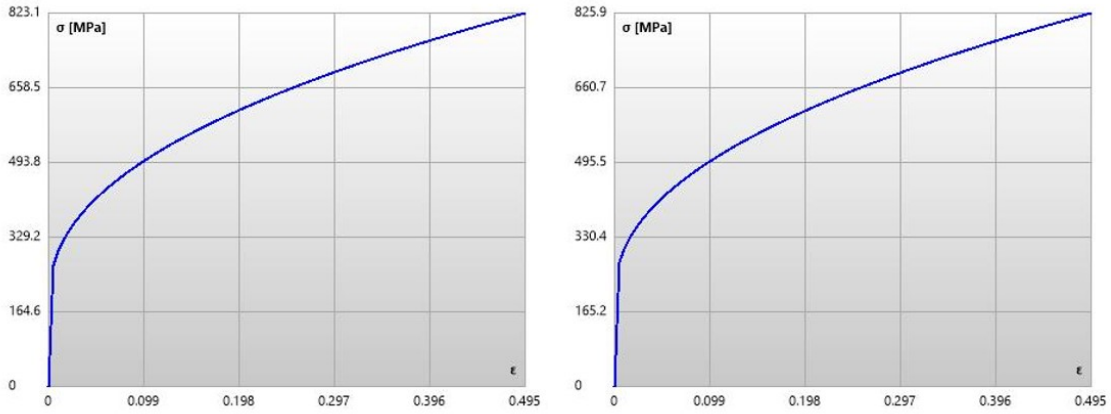

(a) (b)

Figure 4.40: Uni-axial stress and strain curve with (a) uniform and (b) total sensitivity virtual works.

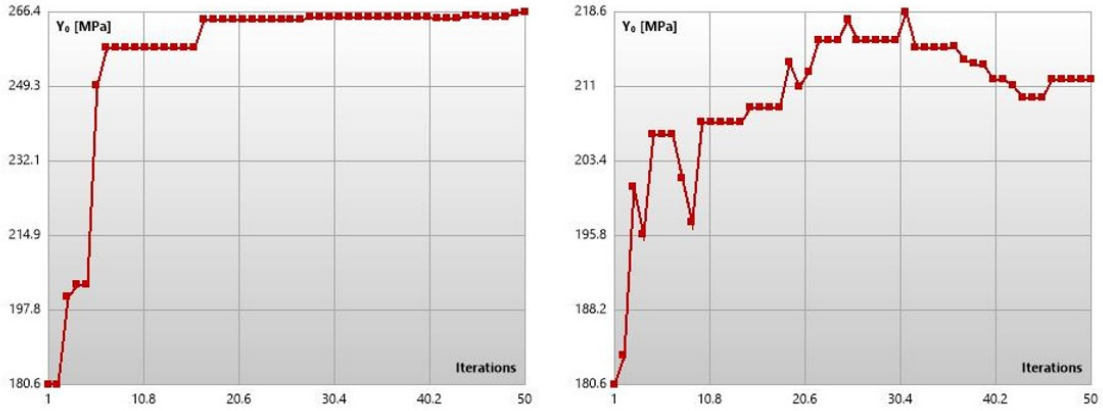

(a) (b)

Figure 4.41: Parameter evolution (Yield stress) with (a) uniform and (b) total sensitivity virtual works.

and internal work, as expected.

Figure 4.43 shows the stress space identification for the uniform virtual works (a) and the total sensitivity virtual works (b). In this plot, the material frame stresses can be presented per time step or over all time steps, normalised to the equivalent stress or not. As an alternative, invariants or principal stresses can be examined. In the case of plasticity, the initial yield surface is displayed based on the identified material parameters. It should be noted that this 2D projection in the material frame requires a certain shear contribution. The default value for the shear contribution is zero, but it can be updated to one, which represents pure shear conditions.

Figure 4.44 displays the parameters identified in this analysis. Yo represents the yield stress in MPa, K represents the hardening value, and the residual value is the difference between the external virtual work and the internal virtual work. By default, 50 iterations

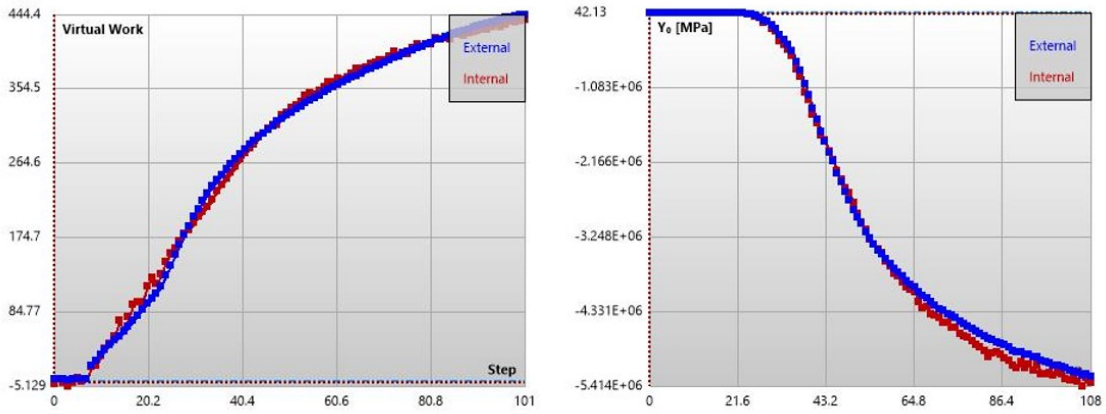

(a) (b)

Figure 4.42: External and internal virtual work with (a) uniform and (b) total sensitivity.

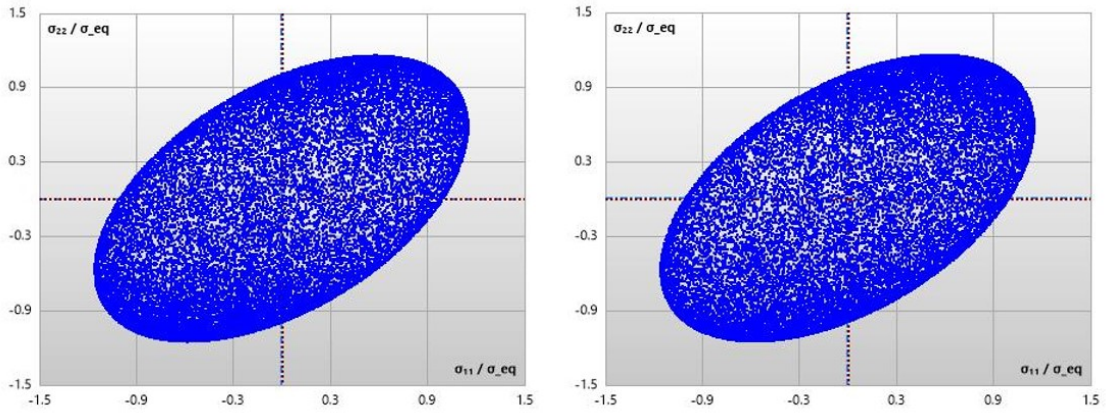

(a) (b)

Figure 4.43: Stress space identification with (a) uniform and (b) total sensitivity virtual works.

were performed in each analysis.

Y₀ [MPa]	K [MPa]	n	Residual	Iterations
196.9	862.8	0.4546	64.72	50

(a)

Y₀ [MPa]	K [MPa]	n	Residual	Iterations
211.7	856.6	0.4718	0.02891	50

(b)

Figure 4.44: VFM type with (a) uniform and (b) total sensitivity.

The yield stress of 316L stainless steel usually ranges from 170 to 310 megapascals (MPa), dependent on factors such as the specific grade, heat treatment and manufacturing process. This steel grade is widely used in various industries due to its excellent corrosion resistance, high strength and versatility. However, to obtain precise information regarding the yield stress of a particular batch or product, it is recommended to refer to the manufacturer's specifications or consult materials engineering references. Based on the graph in Figure 4.44, the values obtained for both virtual work types were similar and fall within

the typical range for 316L stainless steel.

4.7 Conclusion

This chapter begins by showing that pure aluminium is ultimately not a good material to deposit by WAAM. Next, the welding parameters used for the deposition of each material and the choice of copper and copper-aluminium alloys for the production of FGMs are shown. It then shows how the two types of FGMs (stepwise and continuous) were produced. In the stepwise FGM there was an abrupt variation between the two materials (100% Cu and 0% CuAl to 0% Cu and 100% CuAl), while the continuous FGM showed a more gradual variation in the composition of the two materials. The material characteristic shows two non-destructive measurements for the two types of specimens and their conclusions. It can be posited that the preheating of adjacent layers prior to the deposition of subsequent layers can result in a slight increment in the FGM transition zone.

The findings of the eddy currents analysis are outlined in the following conclusions: eddy current measurements exhibited distinct transitions between the Cu and CuAl regions in all samples examined; eddy currents is higher and more stable in the Cu region, but it drops abruptly upon passing to the CuAl zone due to the lower conductivity of this alloy; the technique was found to be effective in distinguishing materials and locating the interface, with a strong correlation between the measured signal profile and the actual joint morphology observed in the optical images. The chapter ends with a description of the DIC procedure and a case study of the geometry to be used, the speckle pattern application process and the tensile test on 316L stainless steel.

5

Library of material compositions and mechanical properties

5.1 Introduction

This chapter describe the library of material compositions and mechanical properties. In the material composition and mechanical properties library section, a collection of different Cu and CuAl alloy compositions is created. The mechanical properties are then determined for each composition. The samples of different compositions were characterised by hardening measurements, electrical conductivity measurements and tensile tests using DIC. The material compositions studied were: 100% Cu + 0% CuA, 75% Cu + 25% CuAl, 50% Cu + 50% CuAl, 25% Cu + 75% CuAl and 0% Cu + 100% CuAl.

5.2 Material compositions

In this section, a material library will be created with a collection of different compositions of Cu and CuAl alloy. For each composition, the mechanical properties will be determined. It is important to note that each combination involves a distinct mixture of materials, as such, it is not possible to identify identical welding parameters across all the various combinations presented. The composition of the materials under investigation and the number of samples tested for each composition are presented in Table 5.1.

Table 5.1: Number of samples of the different material compositions created in the material library.

Volume fractions (%)	Cu	Al	Samples
100% Cu + 0% CuAl	99%	-	4
75% Cu + 25% CuAl	96,88%	1,83 %	3
50% Cu + 50% CuAl	94,52 %	4 %	3
25% Cu + 75% CuAl	91,7 %	6,5 %	3
0% Cu + 100% CuAl	89,7%	8,5 %	4

For all material compositions, three samples were prepared, with the exception of those containing 100% Cu and 100% CuAl, for which four samples were prepared to serve as a preliminary test. The purpose of the pretest sample is to evaluate the test conditions prior to the execution of all subsequent tests. The process of producing and characterising this library of various material compositions comprised several steps. Initially, the walls were produced using the AM WAAM process. Two distinct welding processes were employed in this study: in the case of the 100% samples of a single material, the GMAW process was employed. Conversely, for the combination of two materials, the GTAW process was utilised. Following the production of all the WAAM walls required for the library, one extremity was removed with the intention of affixing it in resin for the purpose of conducting hardness and eddy current measurements. The subsequent WAAM wall was then subjected to machining using a CNC machine, with the objective of preparing the sample with the geometry shown below. As illustrated in Figure 5.1, the geometry and dimensions of the material composition samples, measured in millimetres, are presented. These samples were utilised in the tensile testing of the samples, employing the DIC method. These dimensions are in accordance with DIN EN ISO 6892-1: Tensile tests on metals.

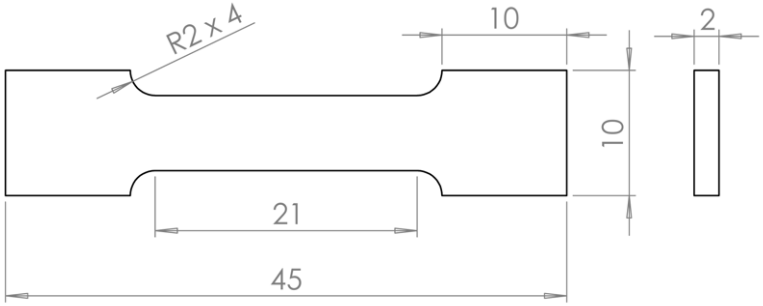

Figure 5.1: Geometry and dimensions of material composition samples [mm].

Initially, the hardness measurements of each specimen was measured. This was followed by the measurement of eddy currents, and finally, tensile tests were conducted in combination with the DIC. The following subsections present the findings from this study for each material composition, with a concluding general analysis of the characterisation.

5.3 DIC procedure

The specimens were produced using the WAAM process. The fabrication of composite materials was accomplished through the utilisation of the GTAW technique, a method that facilitates the concurrent employment of wire feedstocks. The experimental setup comprised a welding power supply, a WAAM torch, shielding gas, a fume extractor, and wire. The configuration of the DIC apparatus for the various material components can be observed in Figure 5.2. The assembly of a 3-axis movable table was undertaken, employing $80x80$ mm Bosch Rexroth aluminium profiles. The implementation of bipolar stepper

motors was instrumental in facilitating precise positioning. The movement in the x, y, and z directions was controlled via G-code programming in conjunction with repetitive host software. The welding operations were executed using an Oerlikon CITOTIG 315 AC/DC machine. Mild steel substrates, each measuring 250 mm in length, 50 mm in width, and 8 mm in thickness, were utilised subsequent to cleaning and preparation. Two types of wire feedstock were selected for the different material compositions: DT-CuAg (copper) with a diameter of 1.2 mm and ERCuAl-A2 (copper-aluminium alloy) with a diameter of 1 mm.

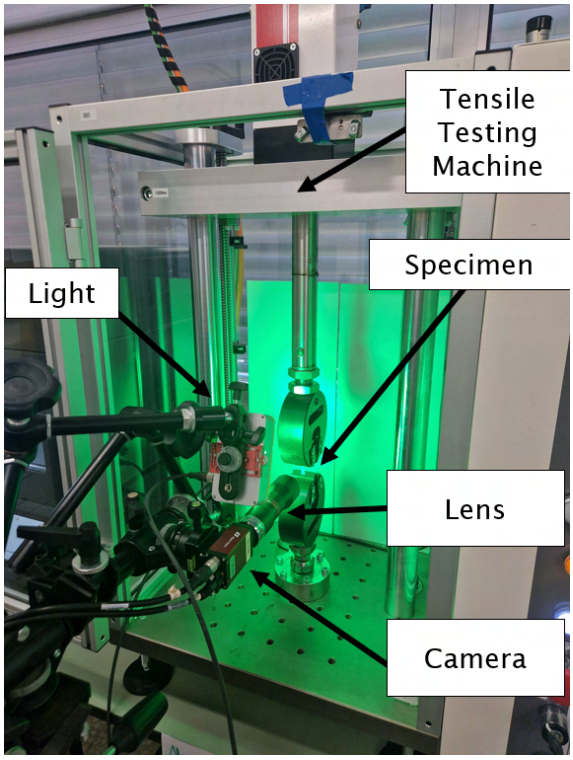

Figure 5.2: Tensile test with DIC setup.

As presented in Figure 5.3, a distribution map of the strain component Exx over an analysed area is demonstrated, employing a 91 VSG, with a colour scale denoting varying strain values. This approach is employed to evaluate the local behaviour of the strain in the analysed sample. The specimen was selected on the basis of the presence of significant deformations at a specific point.

Figure 5.4 shows a graph with error bars. This graph shows how the strain component Exx changes as a function of the VSG in pixels for the selected point [1265]. The horizontal axis of the graph shows the VSG values, and the vertical axis shows the Exx values. The coloured bars show different ways to process data: The colours red, blue, green, and purple in the legend at the top right show the different types of functions. You can see how each method responds to the VSG variation, with means and standard deviations shown in the distribution of points for each configuration.

The PA target settings that were used for the present analysis were as follows:

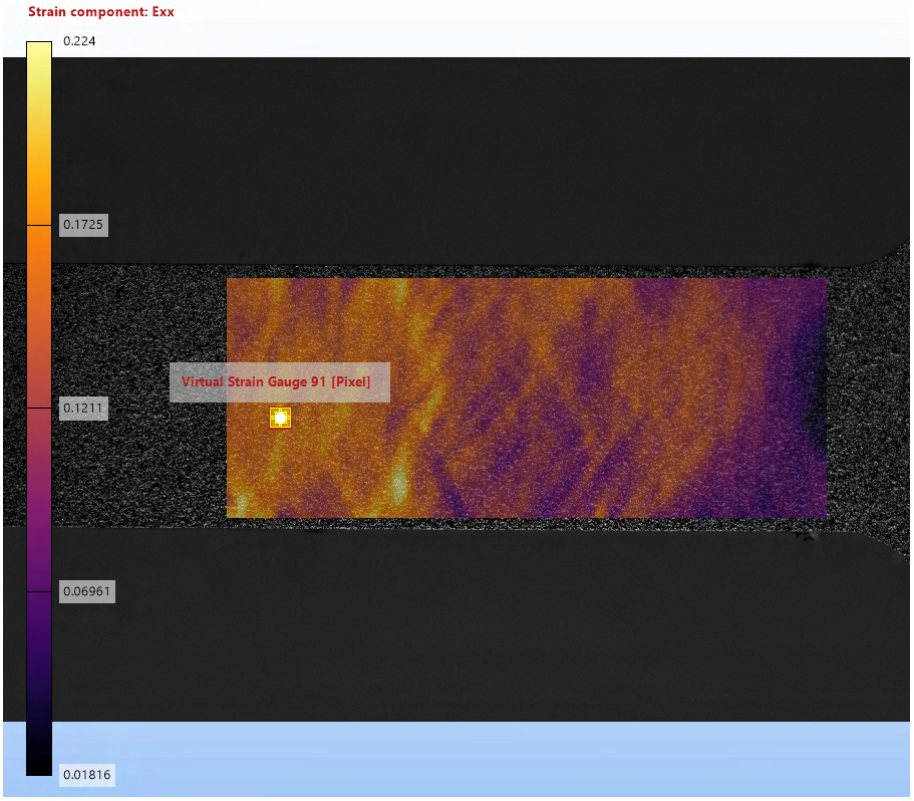

Figure 5.3: Performance analysis of the signal as a function of the virtual strain gauge in pixels.

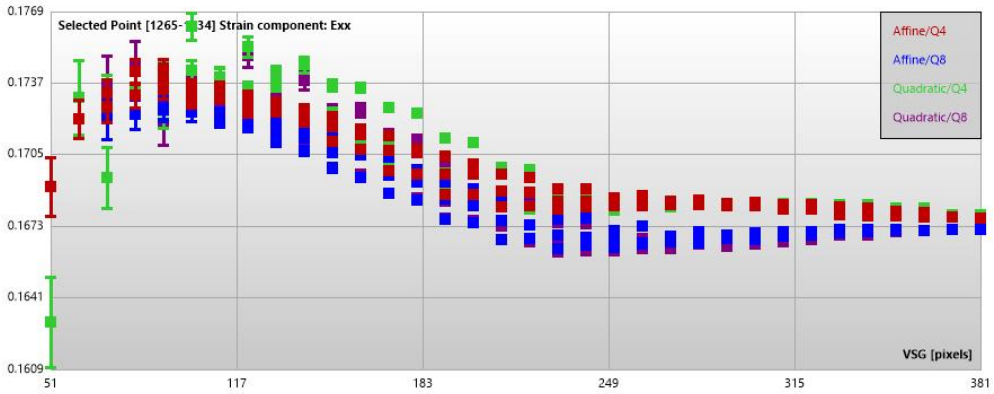

Figure 5.4: Performance analysis of the signal as a function of the virtual strain gauge in pixels.

- Subset size: 51
- Step size: 10
- Shape function: affline
- Strain window: 5
- Polynomial order: bilinear Q4

- Tensor: Green-Lagrange
- Virtual strain gauge: 91

After looking at all the available data, it was decided that the VSG under analysis would have to be between 51 and 183 pixels. This range was chosen to match the point where the signal changed the most, as shown in Figure 5.4. After the VSG of 183, the analysis zone increases a lot, which leads to too much signal smoothing. Q8 has lost more correlation points than Q4. This is because Q8 has a higher polynomial order. Increases in both spatial resolution and VSG have been shown to result in a decrease in signal, leading to a process of smoothing. Table 5.2 and Table 5.3 show the key experimental conditions employed in the DIC analysis of tensile tests conducted on copper and CuAl alloy samples.

Table 5.2: 2D DIC settings for the tensile test of Cu.

DIC setting	**Specification**
Electromechanical test machine	STEP Lab 10 kN
Camera	Manta G-1236
Lens	DTCM111-26-AL, FOV 26 mm Telecentric lens
Patterning technique	Airbrush
DIC technique	2D DIC
DIC software	MatchID, version 2025.2

Table 5.3: DIC parameters for tests on Cu and CuAl samples.

DIC Parameter	**Specification**
General DIC Settings	
Technique Used	2D Digital Image Correlation
Camera Resolution	16-bit, 4112 × 3008 pixels
Pixel to mm conversion	0.00487
Average Speckle Size	8 pixels
Subset Size	51 pixels
Step Size	10 pixels
Shape Function	Affine
Interpolation Function	Bicubic Spline
Correlation Criterion	ZNSSD
Prefiltering	Gaussian (Kernel size = 5)
Strain Settings	
Strain Window	5 data points
Virtual Strain Gauge (VSG)	91 pixels
Strain Interpolation Function	Bilinear Quadrilateral (Q4)
Strain Tensor	Green-Lagrange

5.3.1 100% Cu + 0% CuAl

This subsection examines the composition of 100% Cu + 0% CuAl. The wall was deposited with one wire of CuAg. Twenty-seven layers were deposited on the wall shown in Figure 5.5.

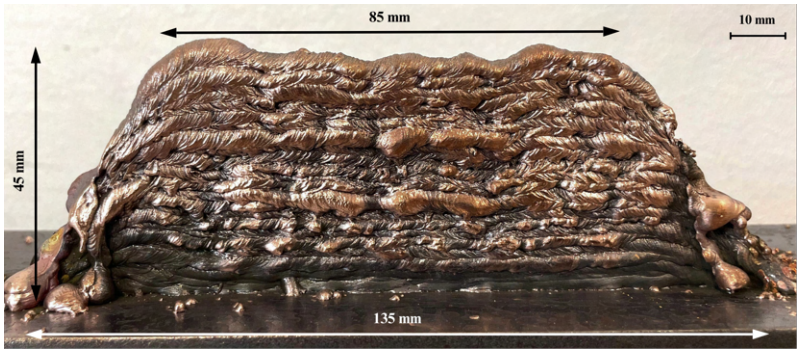

Figure 5.5: WAAM wall made of 100% Cu.

Subsequently, four samples of this wall were prepared for mechanical characterisation. Table 5.4 presents the welding parameters for the material composition of 100% Cu. The GMAW welding process was used. The travel speed and wire feed speeds were both set to 450 mm/min and 500 mm/min, respectively, for all layers. Arcal 37 was used at a flow rate of 15–20 l/min. The process voltage was set to between 19 and 20 V, and the interpass temperature was set to between 80 and 100°C.

Table 5.4: Process parameters for the deposition of 100% Cu layers using GMAW in WAAM.

Process	GMAW
Travel speed	450 mm/min
Wire feed speed	500 mm/min
Voltage	19-20 V
Shielding gas	Arcal 37
Shielding gas flow rate	15 -20 l/min
Interpass temperature	80-100°C

Figure 5.6 illustrates the microhardness profiles of the 100% Cu samples. The average hardness of the Cu layers is 52 HV. It has been demonstrated that the initial layers (the area in close proximity to the substrate) exhibit higher hardness values compared to the intermediate layers, with a reading of approximately 80 HV. This phenomenon can be attributed to the accelerated solidification process, facilitated by the high thermal conductivity of copper and the extraction of heat by the steel substrate. Consequently, a more refined microstructure is formed, resulting in enhanced hardness. In the subsequent layers, a lower thermal gradient is observed, resulting in a slower rate of solidification. Consequently, a larger grain size is evident, leading to a decrease in hardness to 50-60 HV. These oscillations may be indicative of minor variations in the thermal input or micro-defects in the layers, which can locally influence the hardness measurement. The presence

of a downward hardness profile indicates the existence of microstructural heterogeneity along the vertical axis.

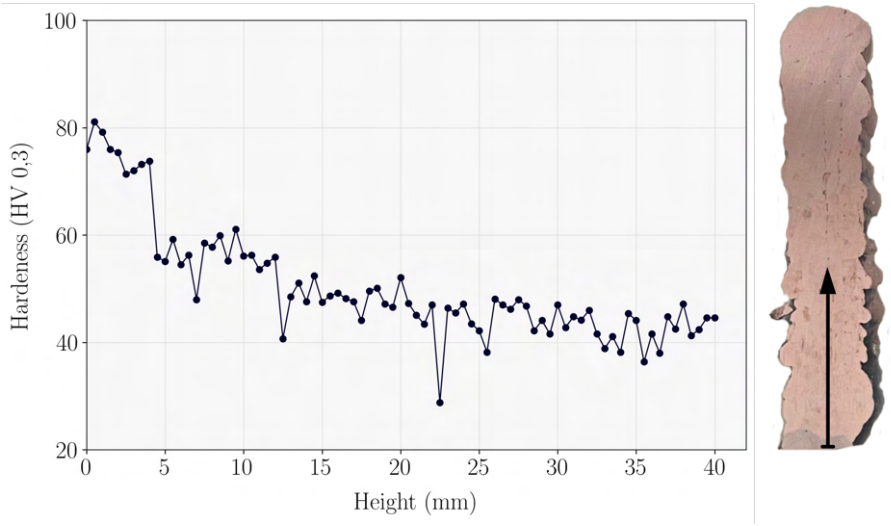

Figure 5.6: Hardness measurements taken from the substrate to the last deposited layer of the FGM crossection of the 100% Cu sample.

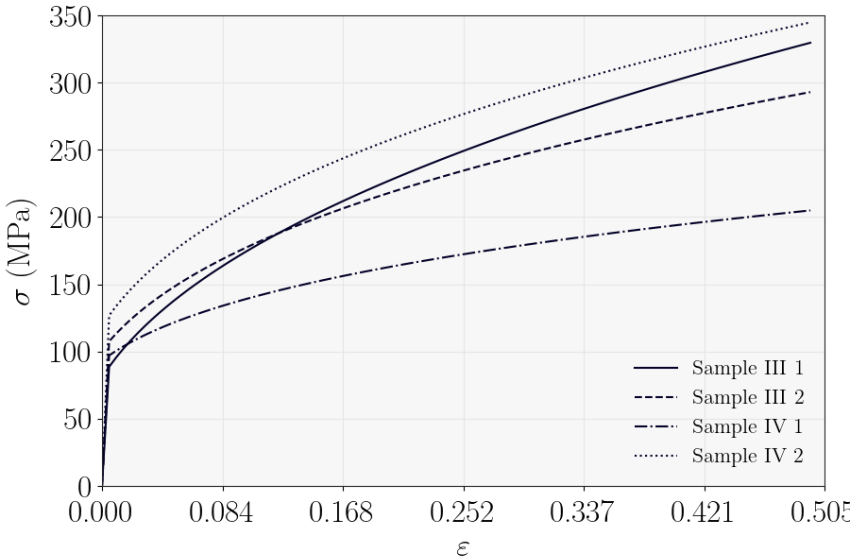

Figure 5.7: Strain-stress curves for all the 100% Cu + 0% CuAl specimens.

As illustrated in Figure 5.7, the stress-strain curves obtained for the 100% Cu material (without the addition of CuAl) are presented. The typical behaviour of ductile materials can be observed, characterised by a sharp increase in stress for small initial strains, followed by a relatively stable hardening region. The samples analysed (III 1, III 2, IV 1 and IV 2) demonstrate a comparable overall trend, despite exhibiting variations in mechanical response. It is evident that the specimens in series IV exhibit slightly higher resistance, while those in series III demonstrate lower values. This observation signifies the impact of the processing conditions on the material's ultimate performance. It is evident that, in

general, these results corroborate the reliability of the mechanical behaviour of pure copper manufactured by WAAM. Nevertheless, they also disclose the presence of dispersion, which is associated with the experimental conditions and the variability between samples. This analysis is fundamental to understanding the reproducibility limits of the process and serves as a reference for direct comparison with Cu-CuAl alloys.

The DIC results for the horizontal displacements in the x direction, $U[mm]$, for the 100% Cu + 0% CuAl specimen. As the load increases, the displacement increases accordingly and becomes relatively uniformly distributed throughout the working cross-section, reflecting the ductile nature of copper. The maximum displacement value recorded was approximately 3 mm, thus demonstrating the material's capacity to withstand substantial deformations prior to fracture. The homogeneous nature of the deformation is also confirmed by the absence of highly localised dislocation zones, which suggests good structural continuity in the WAAM produced sample.

The DIC results for the horizontal displacements in the y direction, $V[mm]$, for the 100%Cu specimen. The maps illustrate the Poisson effect, characterised by relatively minor transverse displacements (maximum of approximately 0.44 mm) and a consistent distribution. It has been demonstrated that these transverse variations become more visible at higher loads. However, these measurements do not indicate significant instabilities.

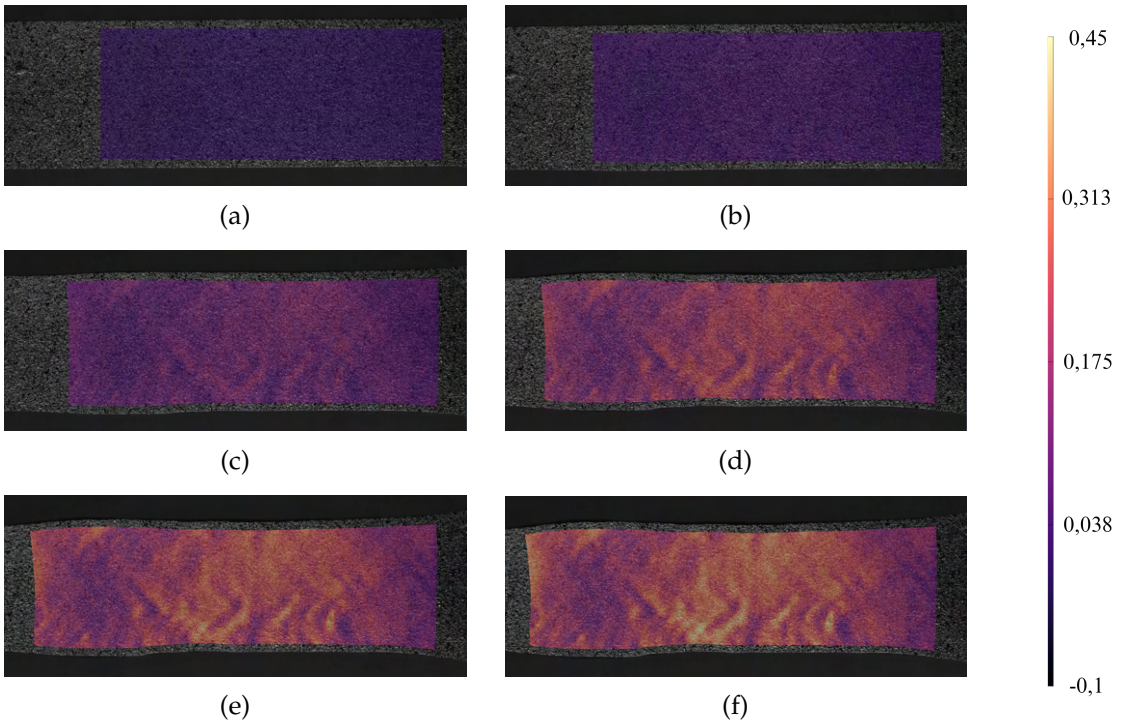

Figure 5.8: Global strain fields in the xx direction, ε_{xx}, for the 100% Cu + 0% CuAl specimen under increasing tensile loads: (a) 869 N, (b) 1347 N, (c) 1587 N, (d) 1753 N, (e) 1790 N, (f) 1408 N.

Figure 5.8 shows the global strain fields in the xx direction, ε_{xx}, for the 100% Cu specimen under increasing tensile loads. In the preliminary stages of the process (a) and

(b), the strain distribution is almost uniform, thereby validating the material's elastic regime. As demonstrated by the intermediate loads (c) and (d), the manifestation of minor heterogeneities becomes evident, although with a relatively diffuse distribution. As the magnitude of the load increases, the strain intensity concomitantly rises. However, the formation of localised shear bands remains evident. The maximum recorded value is approximately 0.45, indicating a substantial degree of deformation prior to rupture. These results confirm the ductile and stable behaviour of pure copper, characterised by distributed elastic deformation and the absence of significant localised strain concentrations. This is in contrast to Cu-Al alloys, where heterogeneity is more pronounced.

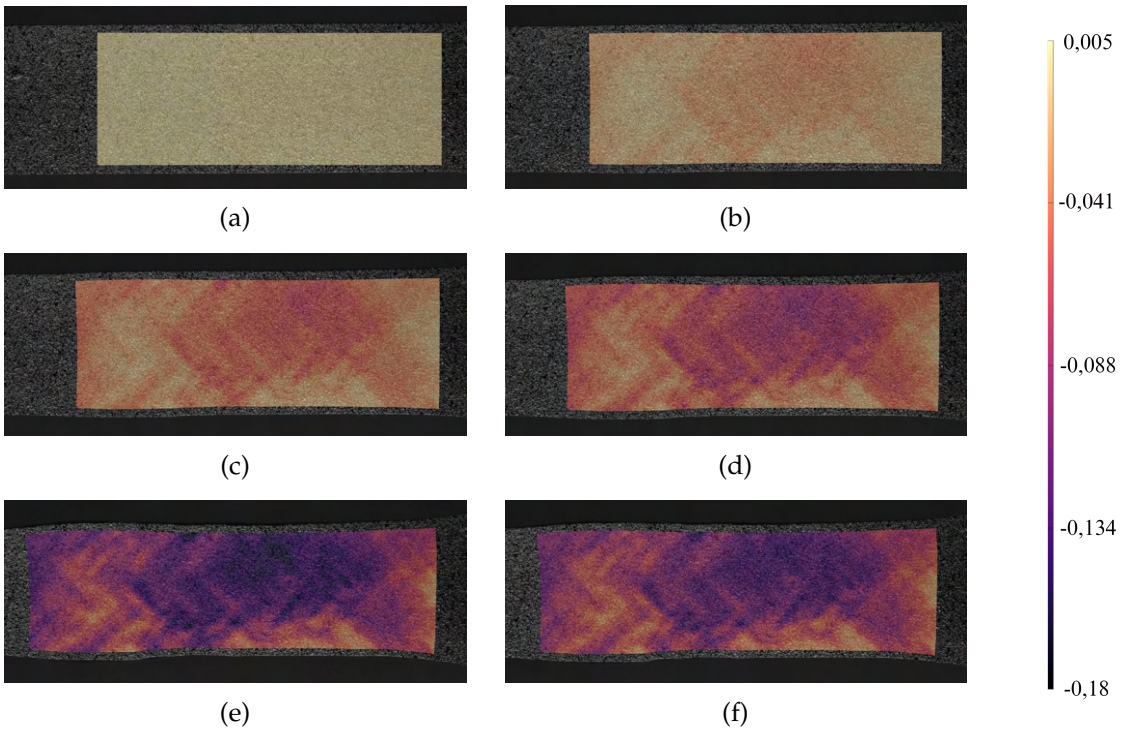

Figure 5.9: Global strain fields in the yy direction, ε_{yy}, for the 100% Cu + 0% CuAl specimen under increasing tensile loads: (a) 869 N, (b) 1347 N, (c) 1587 N, (d) 1753 N, (e) 1790 N, (f) 1408 N.

Figure 5.9 shows the global strain fields in the yy direction, ε_{yy}, for the 100% Cu specimen under increasing tensile loads. In circumstances where loads are minimal ((a) and (b)), the strains experienced are negligible, with values approaching zero. This observation aligns with the initial elastic regime. As the load increases ((c) and (d)), more evident variations associated with the Poisson effect emerge, with alternating regions of contraction and expansion. As the magnitude of the load increases ((f) and (g)), the variations previously mentioned become more pronounced and are distributed in diagonal patterns, reaching values of approximately -0.18. This distribution is consistent with the global distribution of the strain, which does not exhibit any significant local concentration. This outcome serves to substantiate the ductile nature of copper and the structural integrity of the material produced by WAAM.

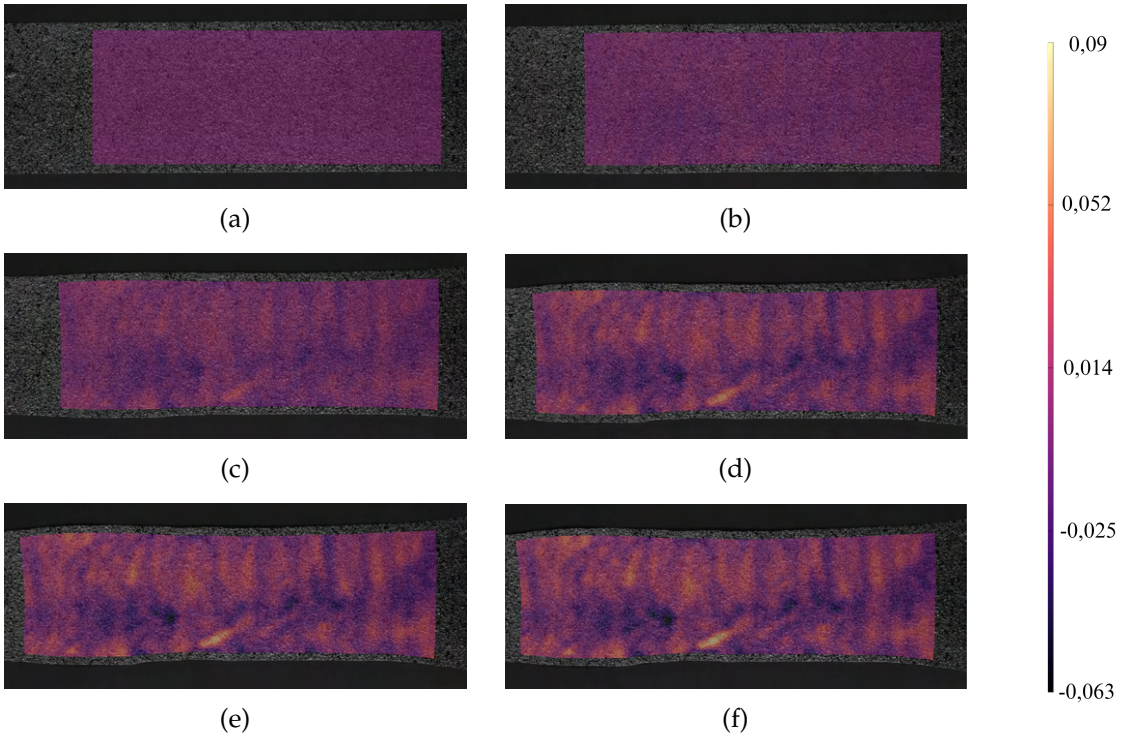

Figure 5.10: Global strain fields in the xy direction, ε_{xy}, for the 100% Cu + 0% CuAl specimen under increasing tensile loads: (a) 869 N, (b) 1347 N, (c) 1587 N, (d) 1753 N, (e) 1790 N, (f) 1408 N.

Figure 5.10 shows the global strain fields in the xy direction, ε_{xy}, for the 100% Cu specimen under increasing tensile loads. In the early phase of the process (a) and (b), shear strains are negligible and uniform, indicative of the elastic regime. As the load increases ((c) and (d)), slight patterns of distributed shear, still of low intensity, emerge. As the load magnitude increases ((f) and (g)), the manifestation of these strains becomes more pronounced, resulting in a wavy distribution that pervades the entire section. This distribution approaches a value of 0.09, indicating a significant degree of variability. Nevertheless, no localised critical concentrations were detected, thereby confirming that the process of plastification occurs in a relatively homogeneous manner. These results serve to reinforce the ductile nature of pure copper, in addition to its capacity to undergo stable deformation during the process of WAAM.

5.3.2 75% Cu + 25% CuAl

This subsection analyses the composition of 75% Cu + 25% CuAl. The deposition of the wall involved two wires, namely CuAg and CuAl9Fe, with a total of nineteen layers deposited on the designated wall, as illustrated in Figure 5.11.

Subsequently, three samples of the wall were prepared for mechanical characterisation. As illustrated in Table 5.5, the welding parameters for the material composition of 75% Cu + 25% CuAl are presented. The GTAW (Gas Tungsten Arc Welding) process was utilised

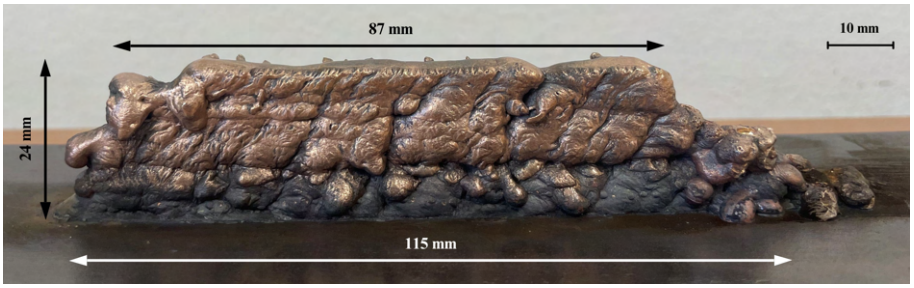

Figure 5.11: WAAM wall made of 75% Cu + 25% CuAl.

in the fabrication of the component. The travel speed and wire feed speeds were both set to 95 mm/min and 712 mm/min, respectively, for all layers. The pure Argon was utilised at a flow rate of 15–20 l/min. The process current was set to a range of 160 A, and the interpass temperature was set to a range of 250-350°C.

Table 5.5: Process parameters for the deposition of 75% Cu + 25% CuAl layers using GMAW in WAAM.

Process	GTAW
Travel speed	95 mm/min
Wire feed speed	712 mm/min
Cu wire feed speed	534 mm/min
CuAl wire feed speed	178 mm/min
Current	160 A
Shielding gas	Pure Ar
Shielding gas flow rate	15 -20 l/min
Interpass temperature	250-350 °C

Figure 5.12 illustrates the microhardness profiles of the 75% Cu + 25% CuAl samples. The average hardness of the 75% Cu + 25% CuAl layers is 79 HV. The variations in the hardness profile are attributable to alterations in the microstructure, consequent to greater or lesser heat dissipation. It can be hypothesised that alterations in hardness values are attributable to changes in the homogeneity of the Cu-CuAl mixture.The hardness values of the 75% Cu + 25% CuAl mixture demonstrate higher values throughout the height in comparison to 100% Cu, indicating that the addition of 25% CuAl enhances the hardness and appears to stabilise the profile across the entire height of the wall.

As illustrated in Figure 5.13, the stress-strain curves corresponding to the samples of the material with a composition of 75% Cu and 25% CuAl are presented. It is evident that the incorporation of 25% aluminium leads to a substantial enhancement in mechanical strength in comparison with pure copper, as evidenced by the more precipitous slope of the curves and the elevated maximum stress values. The three samples tested (Sample V, Sample VI and Sample VII) exhibited variability, particularly with regard to the stresses attained at deformations greater than 0.2. Samples VI and VII exhibited substantially higher strength values, exceeding 500 MPa, while Sample V demonstrated lower values, ranging from 250 to 300 MPa. This dispersion may be associated with microstructural differences

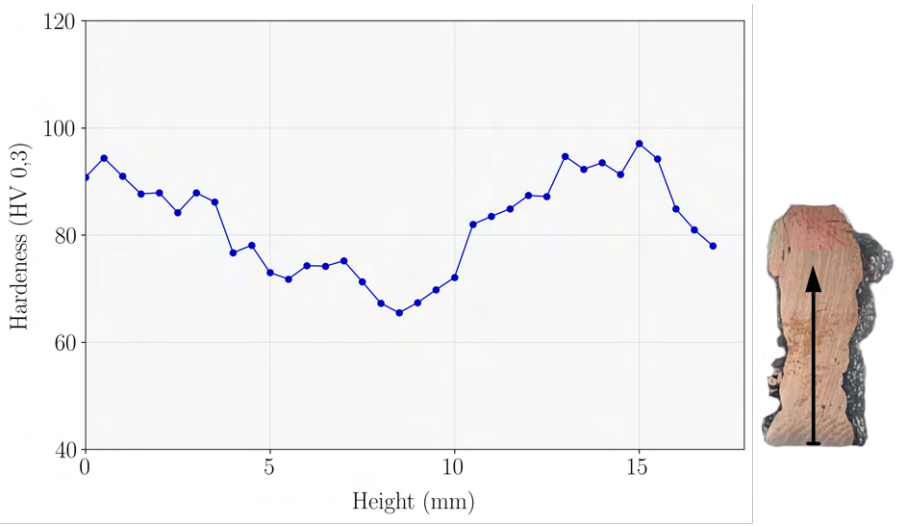

Figure 5.12: Hardness measurements taken from the substrate to the last deposited layer of the FGM crossection of the 75% Cu + 25% CuAl sample.

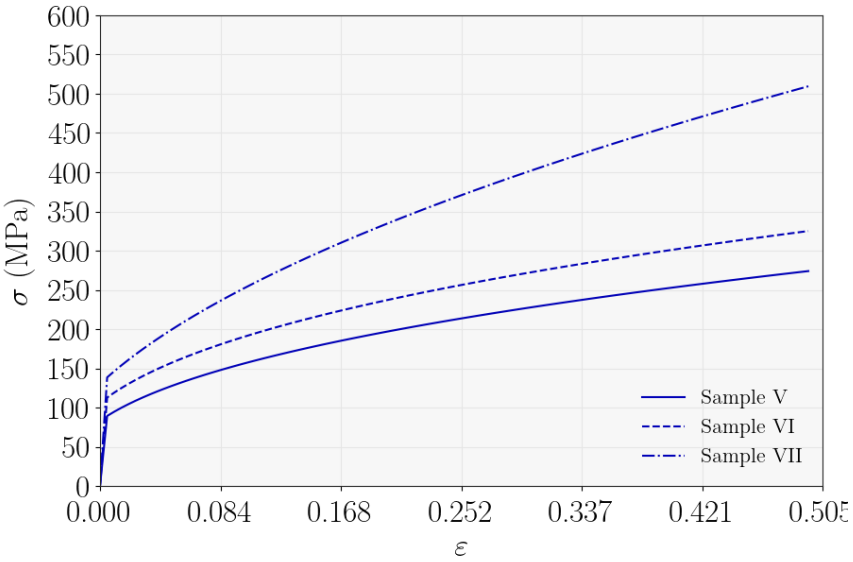

Figure 5.13: Strain-stress curves for all the 75% Cu + 25% CuAl specimens.

or local variations introduced during the WAAM process, revealing the sensitivity of the alloy to the deposition conditions. The outcomes of this study demonstrate that the incorporation of 25% CuAl results in substantial enhancement of mechanical strength when compared with pure copper. However, it is also observed that this addition leads to increased dispersion among the samples. This finding indicates the necessity for optimisation of processing parameters to ensure the reproducibility and consistency of the properties obtained.

The DIC results for the horizontal displacements in the x direction, $U[mm]$, for the 75%Cu + 25%CuAl specimen under different applied loads (from 865 N to 2239 N). The lateral scale indicates that the displacement varies from 0 to 5.72 mm. The images demonstrate that the displacement occurs from right to left, concurrent with the occurrence

of the loading. The displacement profile displays uniform behaviour throughout the cross-section of the specimen, attributable to its homogeneous nature.

The DIC results for the horizontal displacements in the y direction, $V[mm]$, for the 75%Cu + 25%CuAl specimen. The images demonstrate that the displacements remain relatively small, with a maximum amplitude of approximately 0.4 mm. The observed low values thus indicate the horizontal behaviour of the test.

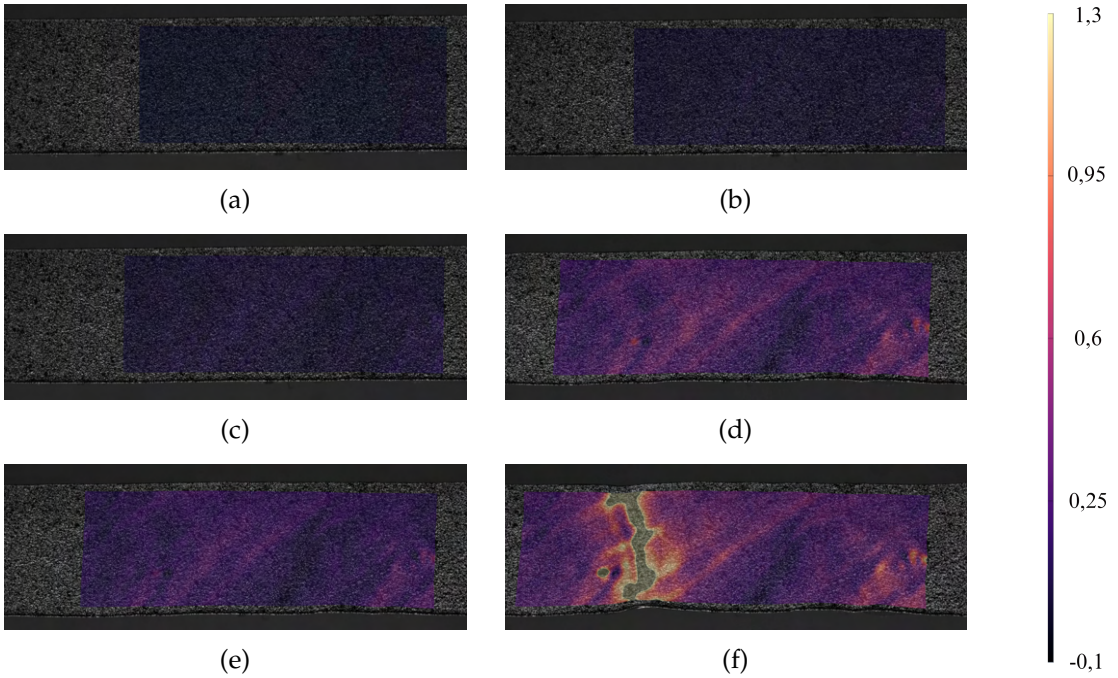

Figure 5.14: Global strain fields in the xx direction, ε_{xx}, for the 75%Cu–25%CuAl specimen under increasing tensile loads: (a) 971 N, (b) 1402 N, (c) 1838 N, (d) 2175 N, (e) 2240 N, (f) 1574 N.

Figure 5.14 shows the global strain fields in the xx direction, ε_{xx}, for the 75% Cu–25% CuAl specimen under increasing tensile loads. For the lowest loads (a) and (b), the strain distribution is almost homogeneous, indicating an elastic response. As the load increases (c), the formation of localised strain bands becomes evident, aligned diagonally across the specimen. This phenomenon signifies the initiation of heterogeneous plastic deformation. At higher loads ((f) and (g)), these strain concentrations intensify and propagate, forming the zones where specimen fracture will occur.

Figure 5.15 shows global strain fields in the yy direction, ε_{yy}, for the 75%Cu + 25%CuAl specimen under increasing tensile loads. For low loads ((a) and (b)), the fields remain close to zero and practically uniform, in accordance with the elastic regime. As the load increases ((c)-(e)), minor non-uniformities emerge, predominantly at the specimen's extremities, signifying the initiation of transverse strain accommodation. At higher loads ((f) and (g)), localised regions of both tensile and compressive strain become evident, reflecting the Poisson effect and heterogeneous plastic flow across the cross-section. Despite the fact that the transverse strain amplitudes are comparatively diminished in comparison to the

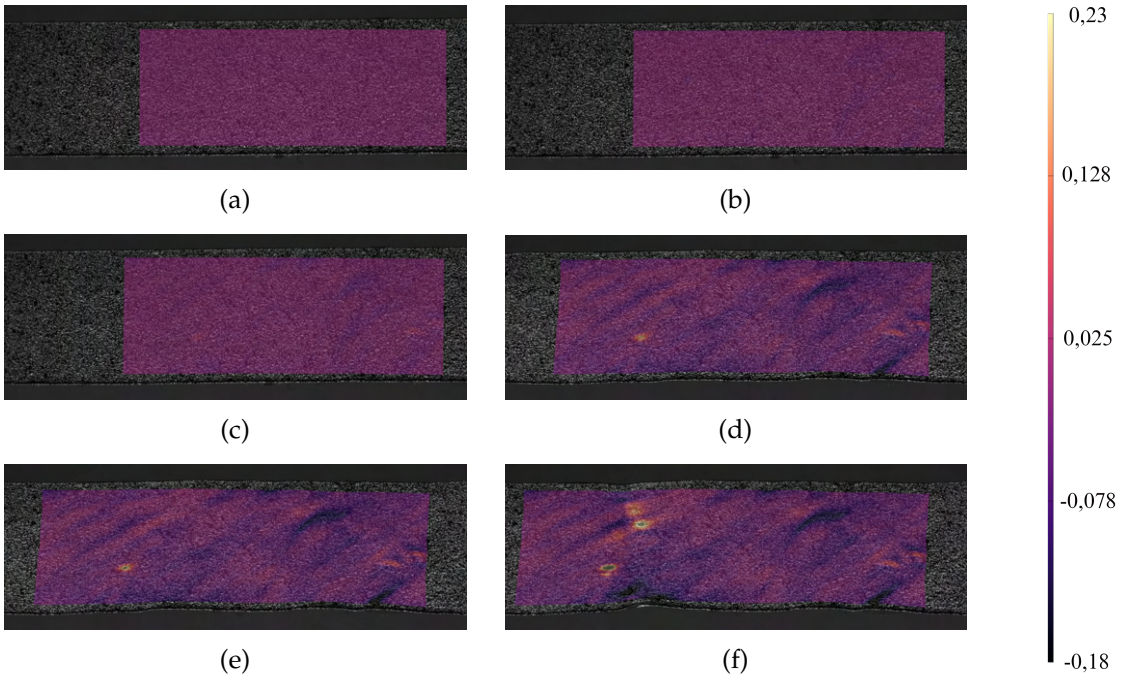

Figure 5.15: Global strain fields in the yy direction, ε_{yy}, for the 75%Cu–25%CuAl specimen under increasing tensile loads: (a) 971 N, (b) 1402 N, (c) 1838 N, (d) 2175 N, (e) 2240 N, (f) 1574 N.

longitudinal ones (maximum of approximately 0.23), their progression is indicative of the emergence of local instabilities and the impact of microstructural gradients in constraining lateral deformation.

Figure 5.16 shows global strain fields in the xy direction, ε_{xy}, for the 75%Cu + 25%CuAl specimen under increasing tensile loads. In the initial stages ((a) and (b)), the deformations remain reduced and homogeneous, compatible with the elastic regime. As of (c), the presence of diagonal patterns of distributed shear becomes evident, which undergo a progressive intensification with increasing load ((d) - (f)). At higher levels (g), the formation of more pronounced shear bands is observed, associated with localized concentrations of deformation, indicating the onset of plastic instabilities. The comparison with pure copper demonstrates that the presence of aluminium promotes greater heterogeneity in the distribution of ε_{xy}. This is indicative of a more pronounced hardening and a less uniform deformation mechanism.

5.3.3 50% Cu + 50% CuAl

In this subsection, the composition 50% Cu + 50% CuAl was analysed. The deposition of the wall comprised two wires, specifically CuAg and CuAl9Fe, with a total of twenty layers deposited on the selected wall, as illustrated in Figure 5.17.

Subsequently, three samples of the wall were analysed using mechanical characterisation techniques. As presented in Table 5.6, the welding parameters for the material

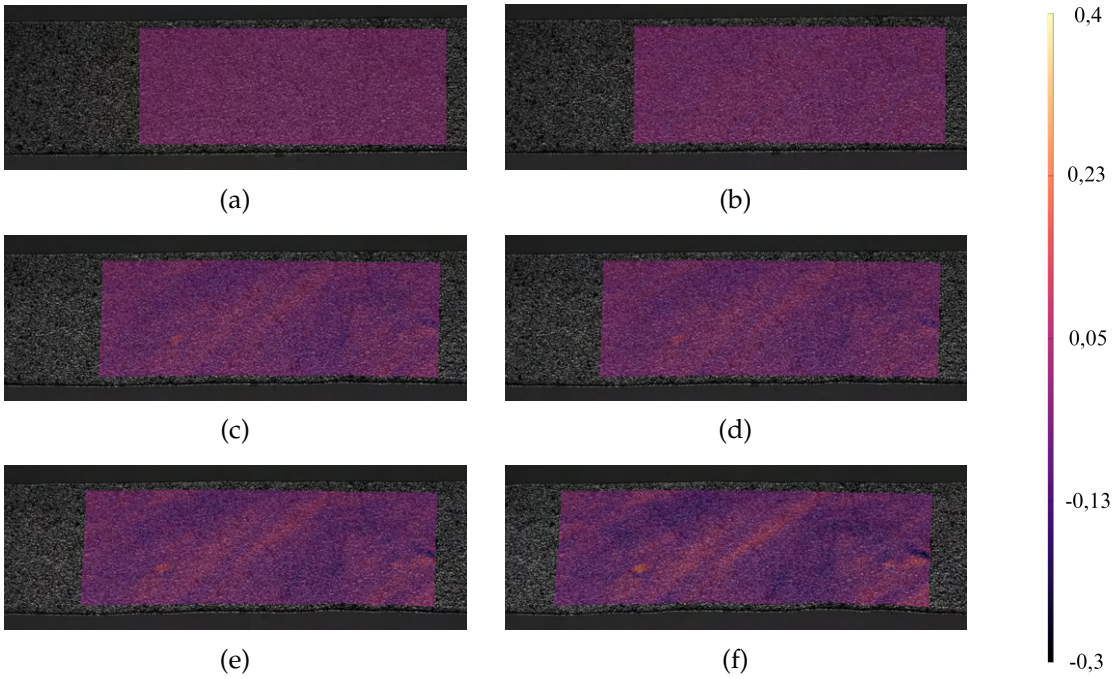

Figure 5.16: Global strain fields in the xy direction, ε_{xy}, for the 75%Cu–25%CuAl specimen under increasing tensile loads: (a) 971 N, (b) 1402 N, (c) 1838 N, (d) 2175 N, (e) 2240 N, (f) 1574 N.

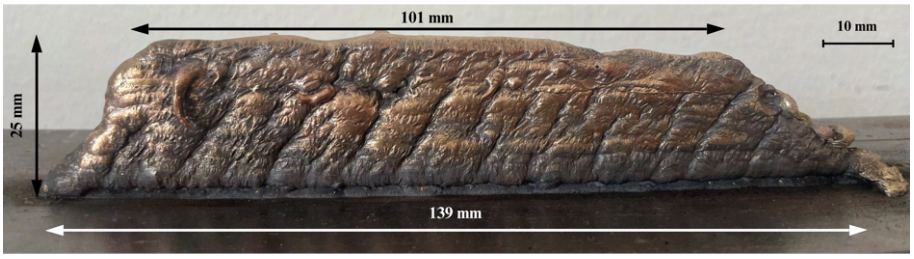

Figure 5.17: WAAM wall made of 50% Cu + 50% CuAl.

composition of 50% Cu + 50% CuAl are exhibited. The component was fabricated using the GTAW process. The travel speed and wire feed speeds were both set to 100 mm/min and 875 mm/min, respectively, for all layers. The pure Argon was utilised at a flow rate of 15–20 l/min. The process current was set to a range of 150 A, and the interpass temperature was set to a range of 250-350 °C.

Figure 5.18 illustrates the microhardness profiles of the 50% Cu + 50% CuAl samples. The average hardness of the 50% Cu + 50% CuAl layers is 83 HV. The 50% Cu + 50% CuAl based composite displays a U-shaped profile, characterised by elevated hardness at the extremities (base and apex) and diminished hardness in the medial region. This lower hardness region may be attributed to the accumulation of heat, resulting from the high wire feed speed and low travel speed. This elevated interpass temperature has been shown to promote grain growth, consequently resulting in reduced hardness measurements. Alternatively, the observed phenomenon may be attributable to microstructural

Table 5.6: Process parameters for the deposition of 50% Cu + 50% CuAl layers using GMAW in WAAM.

Process	GTAW
Travel speed	100 mm/min
Wire feed speed	875 mm/min
Cu wire feed speed	437,5 mm/min
CuAl wire feed speed	437,5 mm/min
Current	150 A
Shielding gas	Pure Ar
Shielding gas flow rate	15-20 l/min
Interpass temperature	250-350 ℃

heterogeneity within the central region, resulting from localised segregation or variation in effective mixing processes.

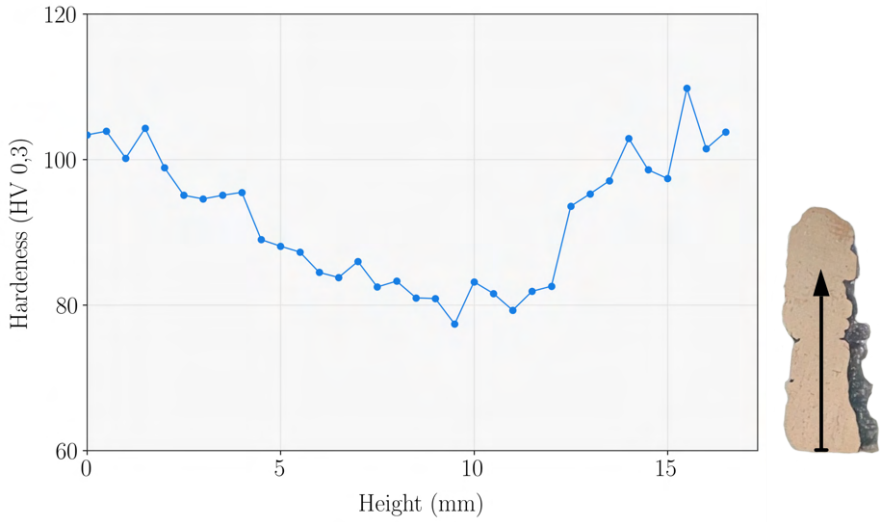

Figure 5.18: Hardness measurements taken from the substrate to the last deposited layer of the FGM crossection of the 50% Cu + 50% CuAl sample.

As shown in Figure 5.19, the stress-strain curves for the alloy with a 50% Cu + 50% CuAl composition are displayed. A substantial enhancement in mechanical strength is observed when compared to compositions with reduced aluminium content, attaining maximum values in excess of 500 MPa. This behaviour demonstrates the potent reinforcement effect associated with augmenting the proportion of CuAl within the microstructure. The three samples tested (Sample VIII, Sample IX and Sample X) have demonstrated consistent overall behaviour, albeit with minor disparities in stress levels at elevated levels of deformation. Curves VIII and X demonstrate analogous results, with marginally elevated stresses, while Sample IX exhibits comparatively diminished values. This variation can be attributed to microstructural heterogeneities inherent in the WAAM process, but the dispersion is clearly smaller than that observed for the 75% Cu + 25% CuAl alloy. Overall, these results confirm that the 50% Cu - 50% CuAl alloy combines high mechanical strength with good

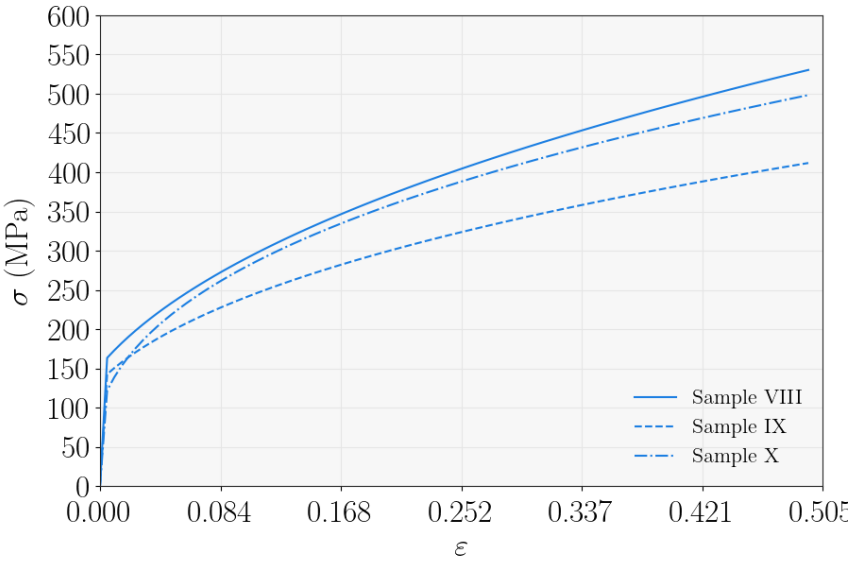

Figure 5.19: Strain-stress curves for all the 50% Cu + 50% CuAl specimens.

repeatability between samples, standing out as a promising composition for structural applications where the relationship between strength and ductility plays a critical role.

The DIC results for the horizontal displacements in the x direction, $U[mm]$, for the 50% Cu + 50% CuAl specimen are illustrated. In the initial stages of the process ((a) – (c)), the field displays a uniform and gradual distribution, indicative of homogeneous deformation. The initiation of displacement gradients, which become more precipitous as the loads increase ((d) – (f)), is particularly evident at the specimen's extremities, suggesting the occurrence of localised strain accumulation. In the stages proximate to fracture ((g) – (h)), a marked concentration of dislocation is observed in the lower central zone, accompanied by field asymmetry. This suggests the onset of plastic instability and crack propagation. The findings indicate that the equiatomic alloy exhibits remarkable deformation capacity at elevated load levels. However, the fracture of the materials occurs in a localised and abrupt manner, a characteristic that is typical of WAAM processed materials that are subject to microstructural heterogeneities.

The DIC results for the vertical displacements in the y direction, $V[mm]$, for the 50% Cu + 50% CuAl specimen. In the initial stages ((a) – (c)), displacements are negligible and relatively uniformly distributed, reflecting the elastic response. As the loads increase from higher levels ((d) and (f)), a marked increase in the magnitude of transverse displacements becomes evident. The presence of asymmetries becomes more pronounced in the lower region of the specimen, a consequence of the Poisson effect and the accumulation of local strains. In conditions approaching rupture ((g) and (h)), pronounced concentrations of vertical displacement and loss of symmetry emerge, concomitant with the initiation of plastic instability and the propagation of failure. The maximum recorded value is approximately 0.35 mm, which is smaller than the longitudinal displacement. However, this is still sufficient to indicate that the microstructural heterogeneity introduced by the

Cu–CuAl composition significantly influences transverse deformation.

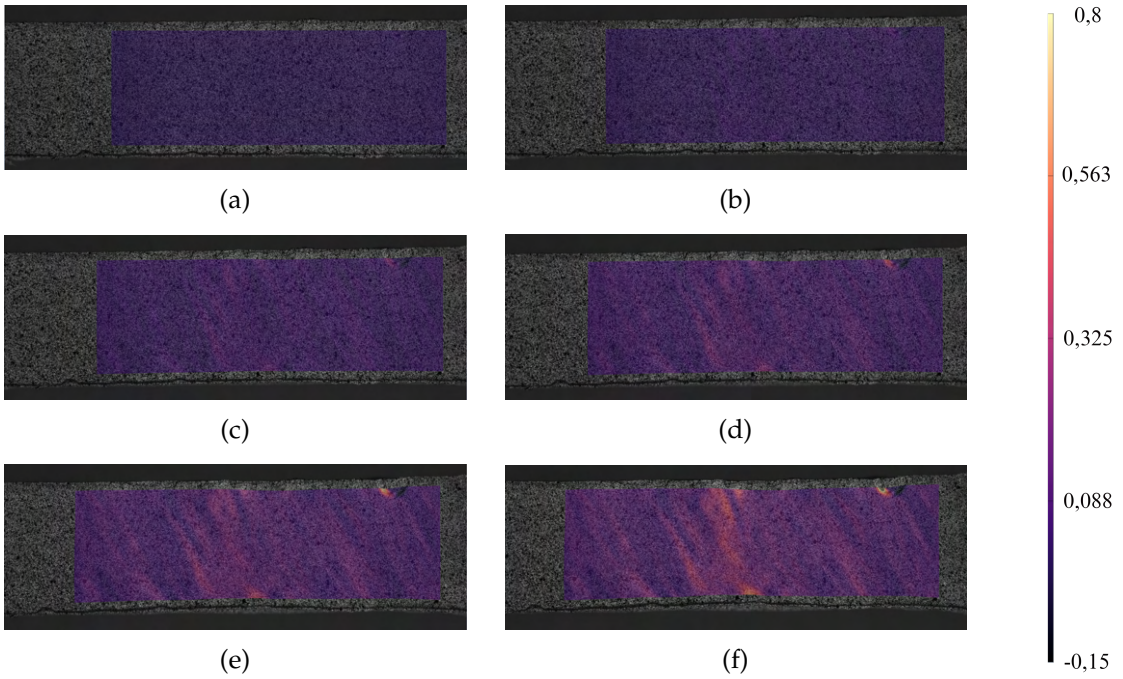

Figure 5.20: Global strain fields in the xx direction, ε_{xx}, for the 50% Cu + 50% CuAl specimen under increasing tensile loads: (a) 981 N, (b) 1787 N, (c) 2293 N, (d) 2579 N, (e) 2693 N, (f) 2153 N..

As shown in Figure 5.20, the global strain fields in the xx direction, denoted as ε_{xx}, for the 50% Cu + 50% CuAl specimen, are presented under increasing tensile loads. In the initial phases ((a) – (c)), strains are distributed relatively homogeneously and at low intensity, consistent with the elastic regime. As the intermediate loads ((d) and (e)) are initiated, the formation of diagonal bands of more intense deformation becomes apparent, thus indicating the onset of localised plasticity. As the load approaches its maximum capacity ((d) and (e)), these bands become more pronounced and highly localized, reaching values in excess of 0.8. This phenomenon is indicative of the occurrence of strong strain concentration and the onset of plastic instability. In the final stage (h), fracture propagation is observed, with a clear loss of continuity in the strain field. In comparison with pure copper, this alloy demonstrates a higher degree of localised deformation intensity, thereby validating the role of aluminium in diminishing the homogeneity of the mechanical response.

As observed in Figure 5.21, the global strain fields in the yy direction, denoted by ε_{yy}, for the 50% Cu + 50% CuAl specimen, are demonstrated as a function of increasing tensile loads. In the initial stages ((a) – (c)), deformations are minimal and uniform, suggesting a predominant elastic regime. From intermediate loads ((d) and (e)), diagonal patterns of transverse deformation form, aligned with the bands observed in the longitudinal direction. At load levels close to rupture ((f) and (g)), deformations become more intense and localised, reaching values close to –0.18, revealing significant transverse contraction

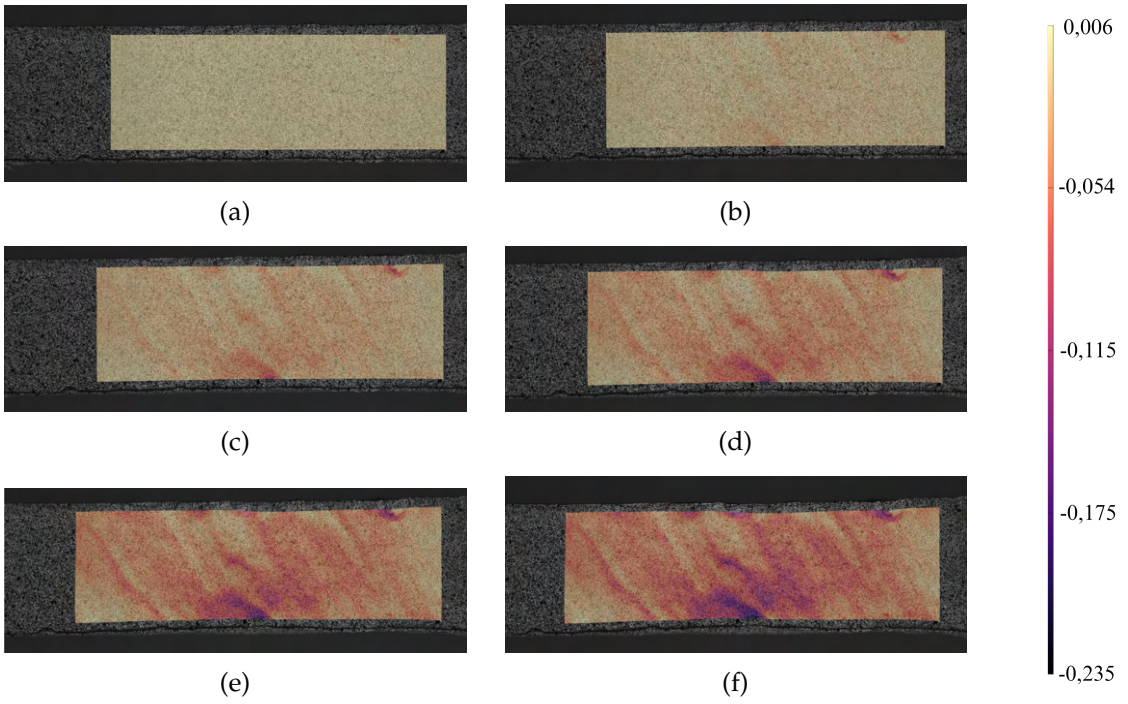

Figure 5.21: Global strain fields in the yy direction, ε_{yy}, for the 50% Cu + 50% CuAl specimen under increasing tensile loads: (a) 981 N, (b) 1787 N, (c) 2293 N, (d) 2579 N, (e) 2693 N, (f) 2153 N.

associated with the Poisson effect and the development of local instabilities. In the final stage (h), a clear loss of continuity in the deformation field is observed, indicating fracture propagation. In comparison with pure copper, this material demonstrates a higher degree of localized transverse deformations, thereby confirming the impact of aluminium in amplifying the heterogeneity of the mechanical response.

Figure 5.22 shows the global strain fields in the xy direction, denoted by ε_{xy}, for the 50% Cu + 50% CuAl specimen under increasing tensile loads. In the initial stages ((a) – (c)), the shear strains are practically homogeneous and of low intensity, consistent with an elastic response. As the intermediate loads ((d) and (e)) are initiated, the formation of regions characterised by substantial ε_{xy} variation begins to emerge. These regions exhibit diagonal patterns, which are indicative of shear bands. At levels approaching the maximum load ((f) and (g)), these bands become more intense and localised, reaching values close to 0.08. This indicates the intensification of plastic flow and the occurrence of instabilities. In the final stage (h), fracture propagation is observed, accompanied by a strong concentration of shear strains in the failure zone. In comparison with pure copper, the 50-50 alloy demonstrates a more heterogeneous response, thereby confirming the effect of aluminium in increasing anisotropy and intensifying strain localization.

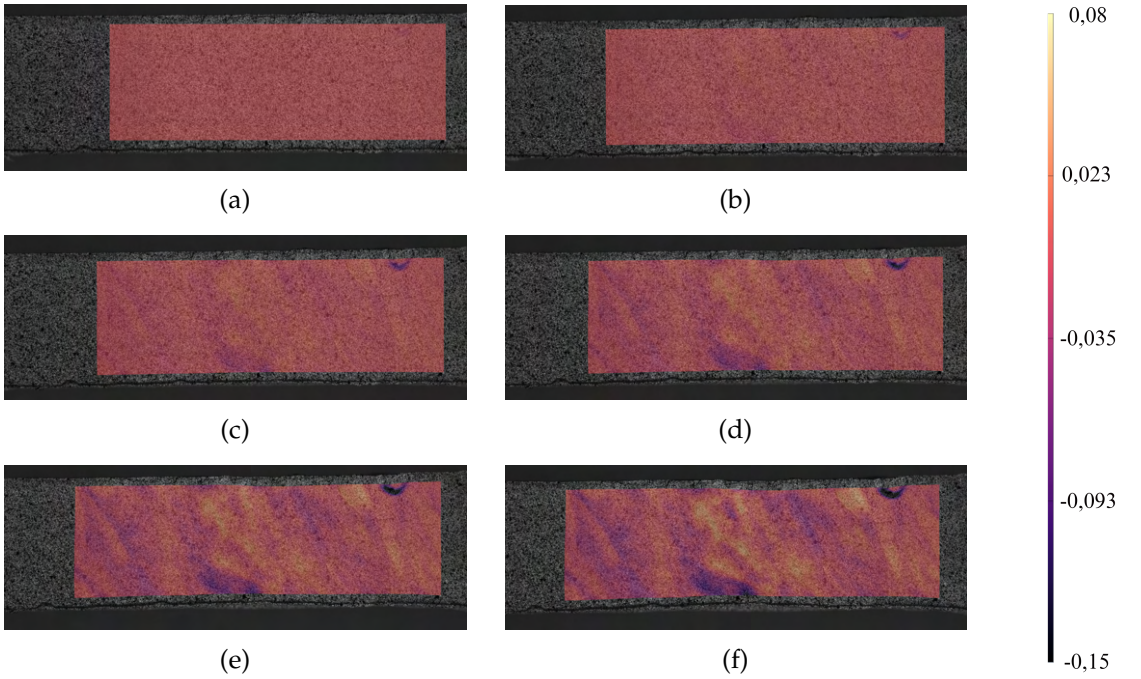

Figure 5.22: Global strain fields in the xy direction, ε_{xy}, for the 50% Cu + 50% CuAl specimen under increasing tensile loads: (a) 981 N, (b) 1787 N, (c) 2293 N, (d) 2579 N, (e) 2693 N, (f) 2153 N.

5.3.4 25% Cu + 75% CuAl

In this subsection, the composition 25% Cu + 75% CuAl was analysed. The deposition of the wall comprised two wires, specifically CuAg and CuAl9Fe, with a total of twenty layers deposited on the selected wall, as illustrated in Figure 5.23.

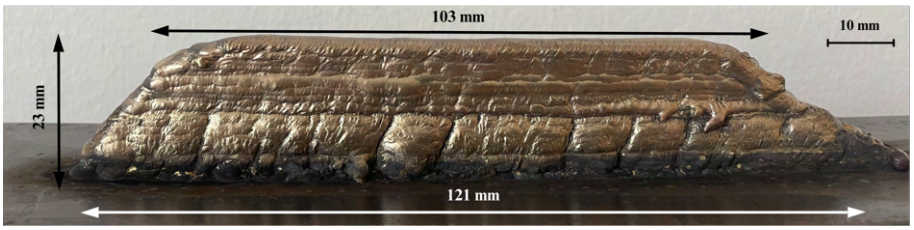

Figure 5.23: WAAM wall made of 25% Cu + 75% CuAl.

Subsequently, three samples were subjected to mechanical characterisation. The welding parameters for the 25% Cu + 75% CuAl composition are summarised in Table 5.7. The component was manufactured using the Gas Tungsten Arc Welding (GTAW) process. For all layers, the travel speed and wire feed speed were maintained at 100 mm/min and 875 mm/min, respectively. Pure argon shielding gas was employed at a flow rate of 15–20L/min. The process current was set to approximately 150A, and the interpass temperature was controlled within the range of 250–350°C.

Figure 5.24 illustrates the microhardness profiles of the 25% Cu + 75% CuAl samples. The average hardness of the 25% Cu + 75% CuAl layers is 99 HV. This hardness profile

Table 5.7: Process parameters for the deposition of 25% Cu + 75% CuAl layers using GMAW in WAAM.

Process	GTAW
Travel speed	100 mm/min
Wire feed speed	875 mm/min
Cu wire feed speed	218,75 mm/min
CuAl wire feed speed	656,25 mm/min
Current	150 A
Shielding gas	Pure Ar
Shielding gas flow rate	15-20 l/min
Interpass temperature	250-350 ℃

displays a distinct behaviour in comparison to that exhibited by the more copper-rich compositions. The area adjacent to the substrate exhibits elevated hardness levels (125-128 HV), attributable to the initial rapid cooling process applied to the substrate. As the measurement increases from 0 to 5 mm, a gradual decrease in hardness values is observed. However, between 85 and 95 HV, the values demonstrate notable stability, exhibiting only minor fluctuations. It is evident that an increase in the CuAl fraction is generally accompanied by an increase in overall hardness. The mixture of 25% Cu + 75% CuAl demonstrates a more stable hardness profile in comparison to other compositions that are more abundant in Cu. Subsequent to the initial decline, there is an absence of significant, abrupt variations. The thermal conductivity of CuAl, which is lower than that of Cu, helps to maintain more uniform thermal cycles throughout the height of the material, thereby reducing significant microstructural differences between the layers.

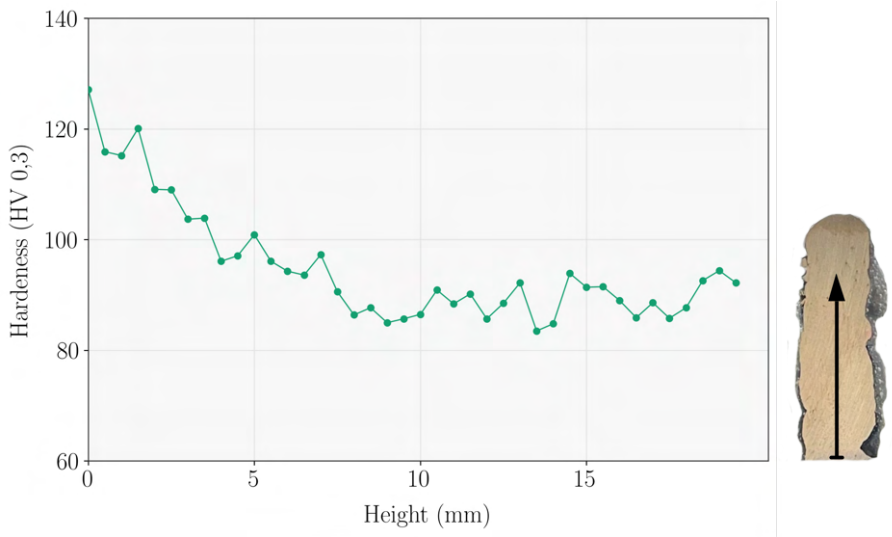

Figure 5.24: Hardness measurements taken from the substrate to the last deposited layer of the FGM crossection of the 25% Cu + 75% CuAl sample.

Figure 5.25 illustrates the stress-strain curves obtained for the 25% Cu + 75% CuAl composition. It is evident that augmenting the aluminium content results in a substantial

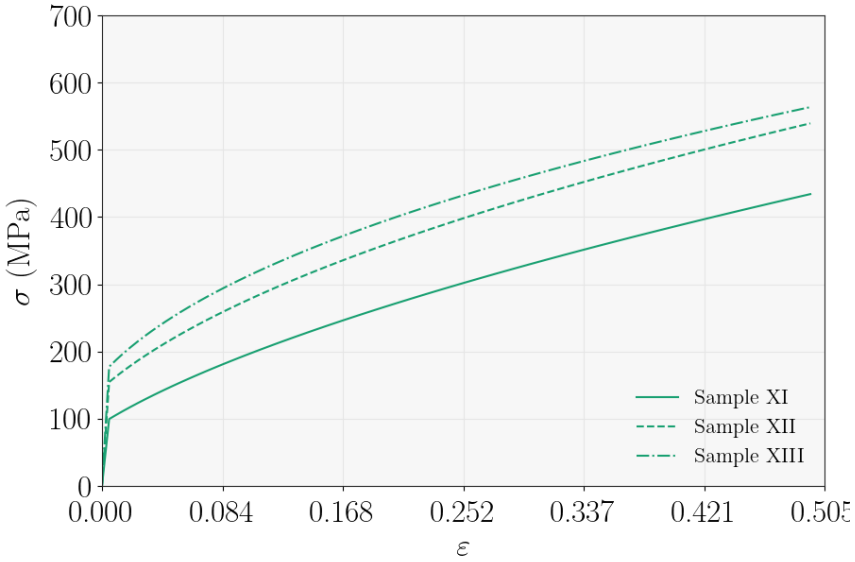

Figure 5.25: Strain-stress curves for all the 25% Cu + 75% CuAl specimens.

enhancement of mechanical strength, with stress values surpassing 500 MPa at strains approaching 0.5. This behaviour is indicative of the hardening effect associated with the higher CuAl fraction, which promotes the formation of more resistant microstructures. The three samples analysed (Sample XI, Sample XII and Sample XIII) exhibited comparable profiles, though with distinct variations in stress magnitude. Samples XII and XIII demonstrate a close proximity in their stress levels, with a marginal increase in Sample XII, while Sample XI exhibits a lower response, approximately 400 MPa. This dispersion is attributable to microstructural variations that are characteristic of the WAAM process, thereby underscoring the significance of meticulous regulation of the deposition parameters. The investigation revealed that the 25% Cu-75% CuAl alloy exhibited a consistent trend of augmented strength with the incorporation of CuAl, though this was accompanied by a notable dispersion among the samples. This outcome underscores the alloy's promise for high mechanical stress applications, while underscoring the necessity to refine the process to ensure enhanced homogeneity and reproducibility.

The DIC results for the horizontal displacements in the x direction, $U[mm]$, for the 25% Cu + 75% CuAl specimen. In the initial stages of the process ((a) – (c)), displacements are reduced and homogeneous, characteristics of the elastic regime. As the load increases ((d) and (f)), the displacement increases concomitantly, reaching values greater than 4 mm, and is distributed relatively uniformly throughout the working cross-section. At higher levels ((g) and (h)), in proximity to the maximum load (3184 N), steeper gradients emerge, accompanied by a localised concentration of displacements in the lower region of the specimen. This phenomenon is indicative of the onset of plastic instability and subsequent fracture propagation. The maximum recorded value, which approaches 5.7 mm, serves to confirm the high deformation capacity of the alloy, which is able to combine high strength with good ductility.

The DIC results for the horizontal displacements in the y direction, $V[mm]$, for the 25% Cu + 75% CuAl specimen. In the first stages of the process ((a) – (c)), displacements are minimal and essentially homogeneous, indicative of the elastic regime. As the middle loads (d) and (f)) are approached, the displacement field begins to manifest asymmetries, particularly in the lower region, with values that exceed –0.3 mm. At loads approaching rupture ((g) and (h)), a pronounced concentration of vertical displacements is evident, reaching a minimum of approximately –0.55 mm, accompanied by diagonal patterns indicative of plastic instability. In the final stage, a clear loss of continuity in the field is observed, associated with fracture propagation. The outcomes of this study demonstrate that, while the alloy displays elevated levels of strength, transverse deformation becomes more localised and critical, in contrast to the more homogeneous behaviour exhibited by pure copper.

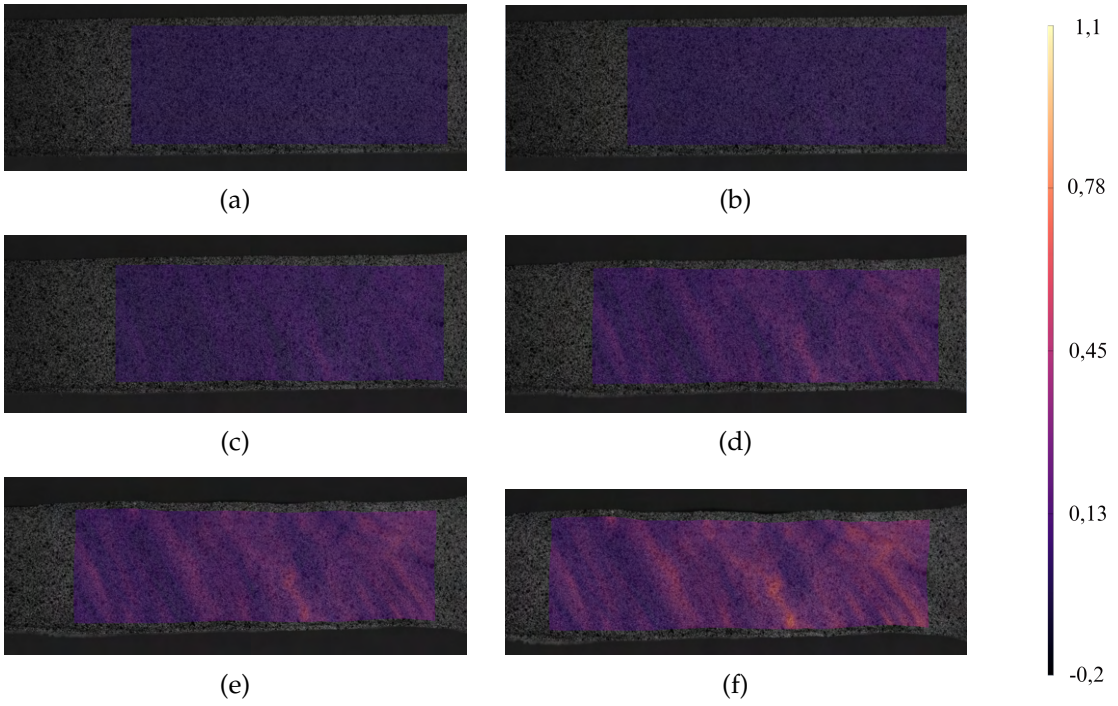

Figure 5.26: Global strain fields in the xx direction, ε_{xx}, for the 25% Cu + 75% CuAl specimen under increasing tensile loads: (a) 1114 N, (b) 1951 N, (c) 2549 N, (d) 3053 N, (e) 3188 N, (f) 1974 N.

Figure 5.26 shows the global strain fields in the xx direction, ε_{xx}, for the 25% Cu + 75% CuAl specimen under increasing tensile loads. In the initial stages of the process ((a) – (c)), the strains are homogeneous and of low magnitude, consistent with the elastic regime. As the load increases ((d) and (f)), the formation of diagonal bands of deformation becomes evident, thereby indicating the onset of localized plasticization. As the applied load approaches the maximum capacity (g), the deformations intensify, reaching values greater than 1.0 and concentrating in specific regions that evolve into well-defined shear bands. In the final stage (h), fracture propagation is observed, evidenced by the clear loss of

continuity in the deformation field. In comparison to pure copper and the equiatomic alloy, sample 25–75 demonstrates increased localized deformation intensity. This observation is indicative of the effect of the higher CuAl content, which serves to intensify heterogeneity and thereby favour the formation of critical failure zones.

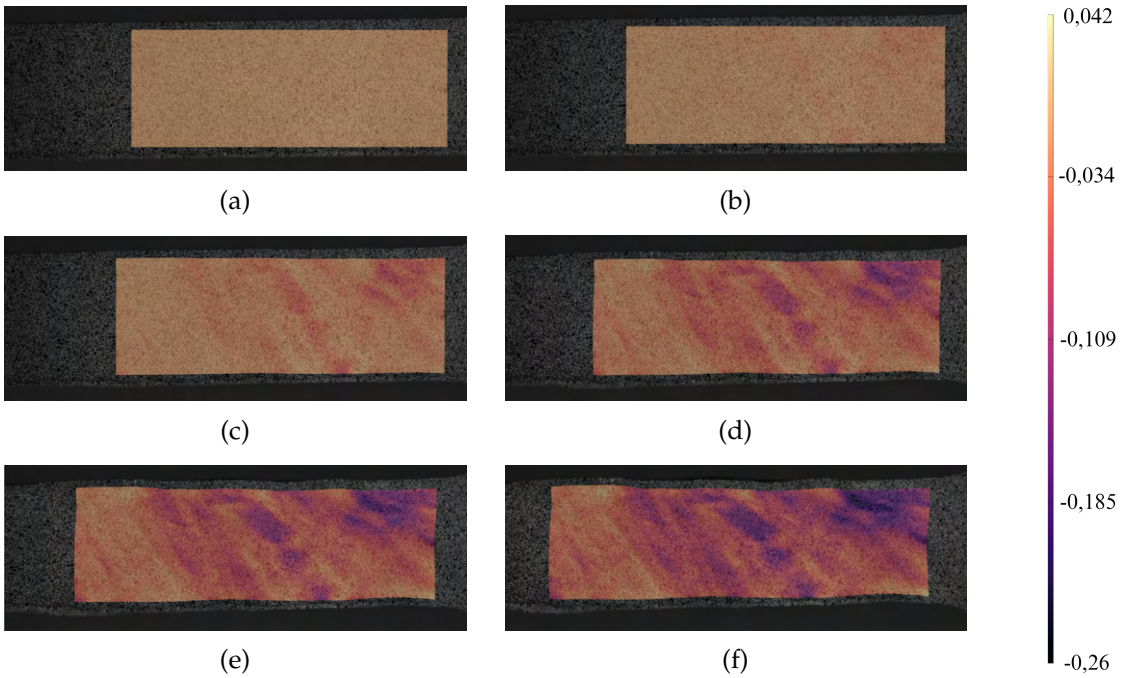

Figure 5.27: Global strain fields in the yy direction, ε_{yy}, for the 25% Cu + 75% CuAl specimen under increasing tensile loads: (a) 1114 N, (b) 1951 N, (c) 2549 N, (d) 3053 N, (e) 3188 N, (f) 1974 N.

Figure 5.27 shows the global strain fields in the yy direction, ε_{yy}, for the 25% Cu + 75% CuAl specimen under increasing tensile loads. In the initial stages ((a) – (c)), the deformations are low-intensity and homogeneously distributed, representing the elastic regime. As the load increases ((d) and (f)), diagonal patterns of transverse contraction begin to form, reflecting the intensification of the Poisson effect and the onset of plastic instability. At higher levels ((g) and (h)), the deformations become more intense and heterogeneous, reaching minimum values close to –0.26, accompanied by the concentration of instability zones that evolve towards fracture. In comparison with pure copper, the 25–75 alloy demonstrates a heightened propensity for localised transverse deformations, thereby validating the impact of the elevated CuAl content in enhancing mechanical anisotropy and diminishing the homogeneity of the structural response.

Figure 5.28 shows the global strain fields in the xy direction, ε_{xy}, for the 25% Cu + 75% CuAl specimen under increasing tensile loads. In the initial stages ((a) – (c)), shear strains are low-intensity and relatively uniformly distributed, consistent with the elastic regime. As the load increases ((d) and (f)), characteristic diagonal patterns of shear bands begin to emerge, indicating the intensification of plastic flow. As the load approaches its maximum capacity, the bands become more pronounced and localised, reaching values

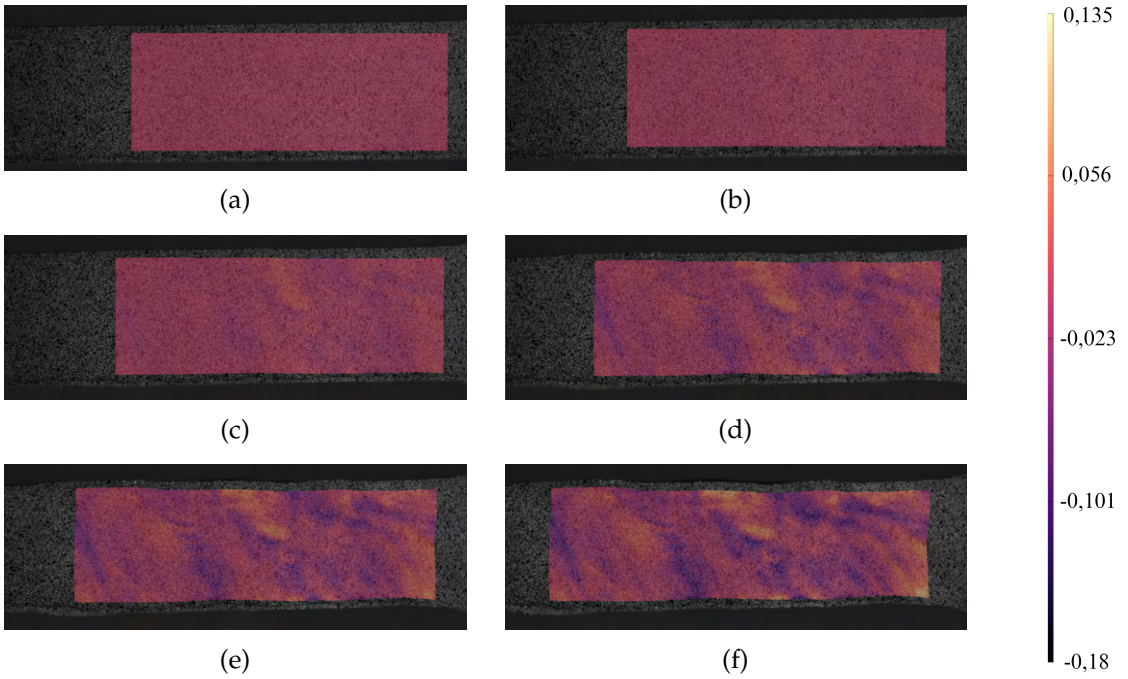

Figure 5.28: Global strain fields in the xy direction, ε_{xy}, for the 25% Cu + 75% CuAl specimen under increasing tensile loads: (a) 1114 N, (b) 1951 N, (c) 2549 N, (d) 3053 N, (e) 3188 N, (f) 1974 N.

of approximately 0.13, indicating a significant concentration of strains. In the final stage (h), fracture propagation is observed, accompanied by high heterogeneity in the shear field. In comparison with compositions that exhibit a lower CuAl content, alloy 25–75 demonstrates a heightened propensity for localized shear strains, thereby confirming the effect of aluminium in intensifying anisotropy and plastic instability.

5.3.5 0% Cu + 100% CuAl

This subsection examines the composition of 0% Cu + 100% CuAl. The wall was deposited with one wire (CuAl9Fe). Twenty-seven layers were deposited on the wall shown in Figure 5.29.

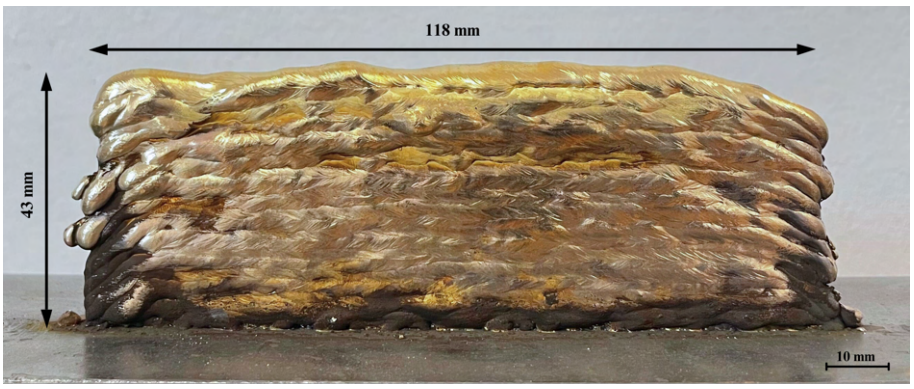

Figure 5.29: WAAM wall made of 100% CuAl.

Four samples of the wall were prepared for mechanical characterisation. As demonstrated in Table 5.8, the welding parameters for the material composition of 100% CuAl are presented. The GMAW process was employed in the fabrication of the component. The travel speed and wire feed speeds were both set to 300 mm/min and 380 mm/min, respectively, for all layers. The pure Argon was utilised at a flow rate of 15–20 l/min. The process voltage was set to a range of 19 to 20 V, and the interpass temperature was set to a range of 100-150 ℃.

Table 5.8: Process parameters for the deposition of 100% CuAl layers using GMAW in WAAM.

Process	GMAW
Travel speed	300 mm/min
Wire feed speed	From 380 mm/min to 400 mn/min
Voltage	19-20 V
Shielding gas	Pure Ar
Shielding gas flow rate	15 -20 l/min
Interpass temperature	100-150 ℃

Figure 5.30 illustrates the microhardness profiles of the 0% Cu + 100% CuAl samples. The average hardness of the CuAl layers is 138 HV. This hardness profile demonstrates a notably stable and elevated behaviour in comparison to all other compositions. It is evident that CuAl naturally exhibits a higher degree of hardness in comparison to Cu. This phenomenon can be attributed to the solid solution hardening of the aluminium, in conjunction with the potential presence of intermetallic phases. The hardness profile has been found to be the most stable of all the compositions analysed, as it is characterised by the absence of sharp drops or sudden recoveries. The low thermal conductivity of CuAl contributes to homogeneous thermal cycles during deposition, thereby reducing significant microstructural variations over time.

As illustrated in Figure 5.31, the stress-strain curves obtained for the 100% CuAl material are presented. This composite demonstrates the highest mechanical strength of all the compositions analysed, reaching values close to 900 MPa for deformations of approximately 0.5. This response lends further credence to the hypothesis that the high CuAl fraction plays a pivotal role in enhancing the hardness and load-bearing capacity of the material. The four samples tested (Sample I.1, Sample I.2, Sample II.1 and Sample II.2) demonstrate a striking degree of consistency in their behaviour, with the curves practically overlapping throughout the entire deformation range. The low dispersion observed between the samples indicates two things. Firstly, it demonstrates the reproducibility of the WAAM process when manufacturing this particular composition. Secondly, it indicates the inherent structural stability of the 100% CuAl alloy. A discernible advancement is evident in comparative analyses of alloys with reduced aluminium content. Pure copper demonstrated strengths of approximately 250-300 MPa, while the pure CuAl alloy exhibited strengths exceeding 800 MPa, thereby substantiating the favourable

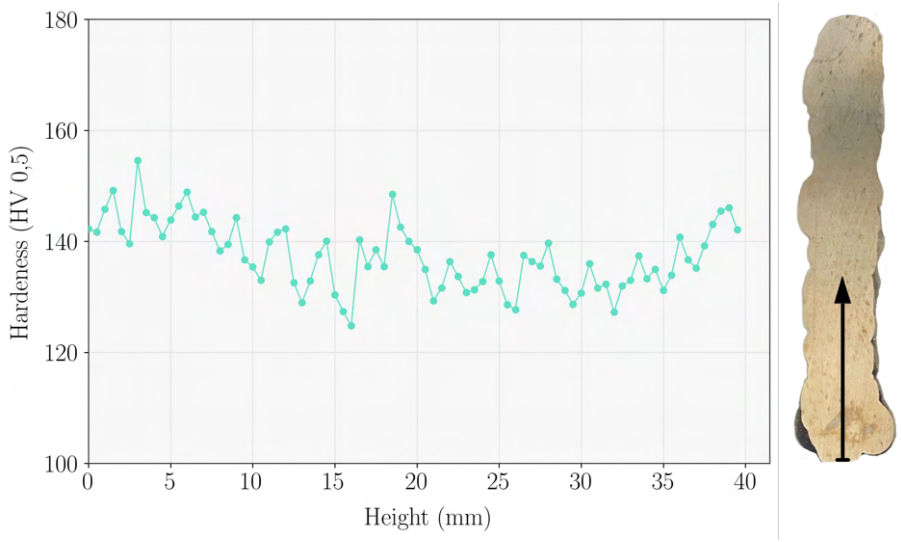

Figure 5.30: Hardness measurements taken from the substrate to the last deposited layer of the FGM crossection of the CuAl sample.

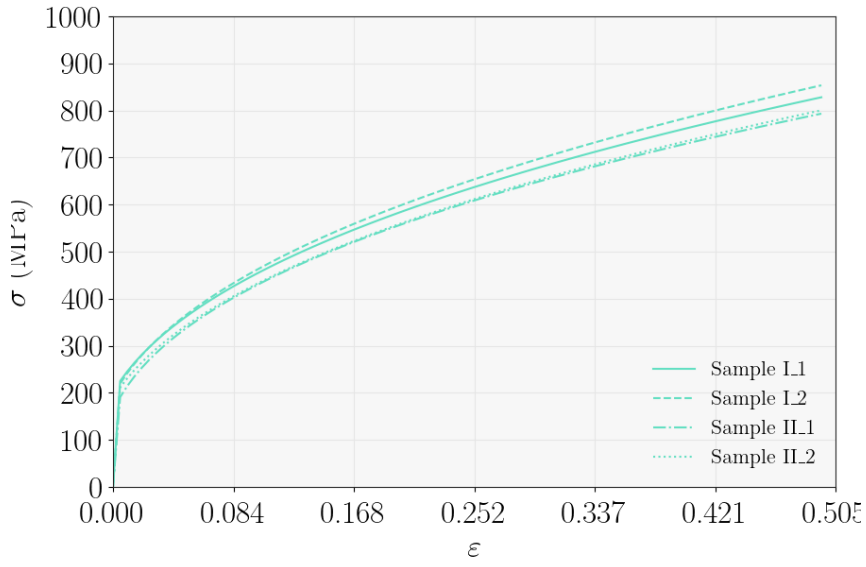

Figure 5.31: Strain-stress curves for all the 0% Cu + 100% CuAl specimens.

correlation between the CuAl fraction and enhanced mechanical strength. These results emphasise the potential of this composition for highly demanding structural applications where high strength is a determining requirement.

The DIC results for the horizontal displacements in the x direction, $U[mm]$, for the 100% CuAl specimen. In the initial stages ((a) – (c)), the dislocations are small and homogeneous, indicating stable elastic behaviour. As the load increases ((d) and (f)), a gradual intensification of the dislocation is observed, exceeding 2.5 mm, and is evenly distributed throughout the specimen's cross-section. At the highest levels ((g) and (h)), in proximity to the maximum load (5024 N), the displacement attains values close to 3.7 mm, exhibiting relative homogeneity until the final stages. In contrast to the observations

made in mixed alloys, where there is a strong tendency for the formation of asymmetric localisations and gradients, pure CuAl presents a more stable and continuous dislocation distribution, revealing good structural cohesion and resistance to the early development of local instabilities.

The DIC results for the horizontal displacements in the y direction, $V[mm]$, for the 100% CuAl specimen. In the initial stages ((a) – (c)), displacements are minimal and homogeneous, characteristics of the elastic regime. As the load increases ((d) and (f)), gentle gradients emerge, primarily in the lower region, with displacements reaching values close to –0.5 mm. At higher load levels ((g) and (h)), close to the maximum load (5024 N), the vertical contraction zones intensify, with minimum values close to –0.75 mm. Despite this intensification, the distribution remains relatively uniform, without abrupt localised concentrations as observed in mixed alloys. This behaviour underscores the capacity of pure CuAl to endure substantial loads while maintaining optimal structural integrity, thereby validating its enhanced strength and diminished propensity for premature development of transverse plastic instabilities when contrasted with intermediate Cu–CuAl alloys.

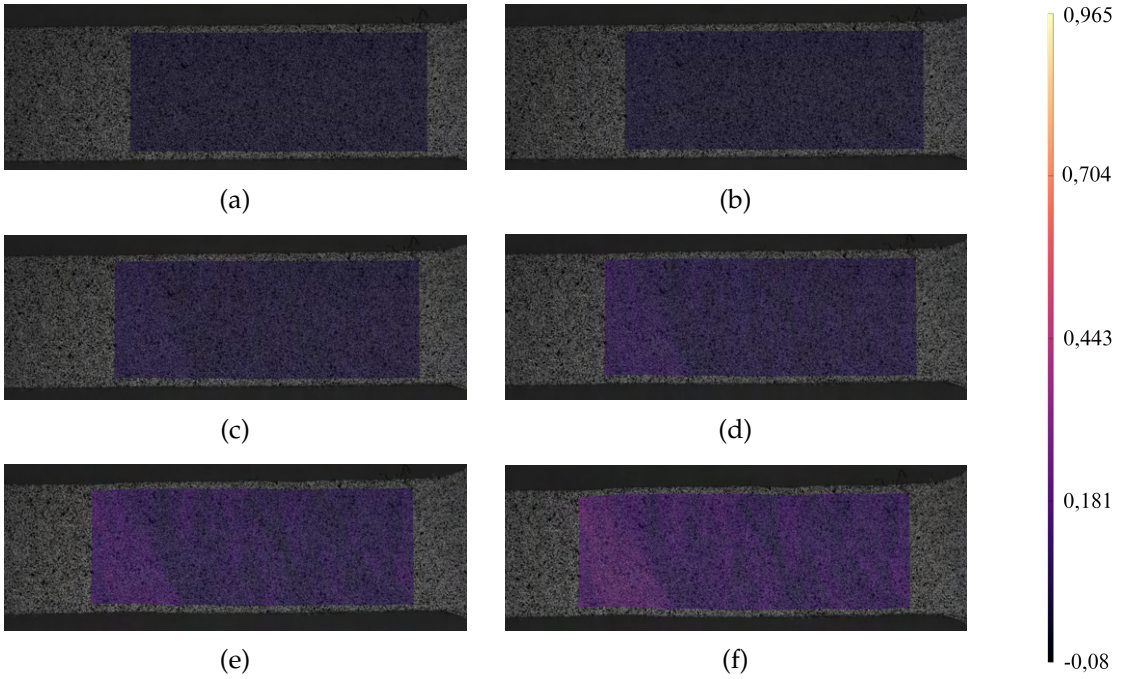

Figure 5.32: Global strain fields in the xx direction, ε_{xx}, for the 0% Cu + 100% CuAl specimen under increasing tensile loads: (a) 1444 N, (b) 2970 N, (c) 4009 N, (d) 4769 N, (e) 5031 N, (f) 4531 N.

Figure 5.32 shows the global strain fields in the xx direction, ε_{xx}, for the 100% CuAl specimen under increasing tensile loads. In the initial stages ((a) – (c)), strains are low and homogeneously distributed, consistent with the elastic regime. As the load increases ((d) - (f)), smooth, still relatively uniform strain gradients appear, reflecting the onset of plasticization. As the load increases ((g) and (h)), the strain values approach 1.0 at the

maximum load (5024 N). This is due to the fact that, at higher loads, strains become more intense and are concentrated in specific regions of the specimen's cross-section. This behaviour demonstrates that, although pure CuAl exhibits high strength, zones of localized deformation also form in advanced stages, associated with the onset of plastic instability and imminent fracture. In comparison to intermediate alloys, pure CuAl exhibits more homogeneous behaviour in the initial stages; however, it develops localized areas of greater intensity when subjected to extreme loads.

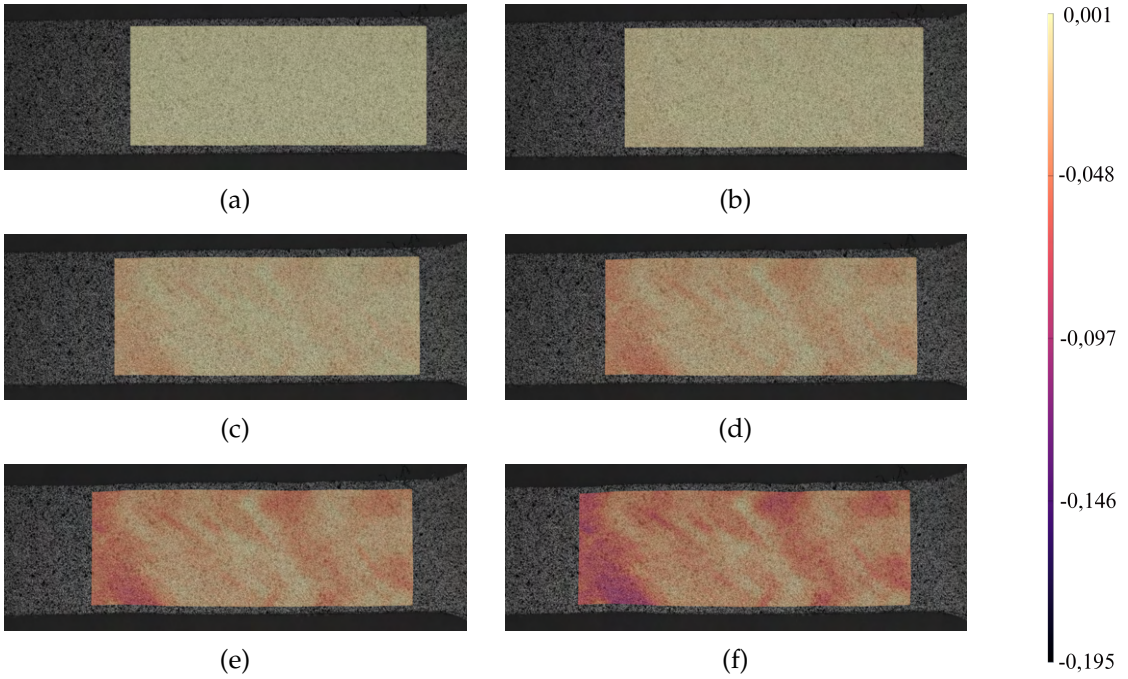

Figure 5.33: Global strain fields in the yy direction, ε_{yy}, for the 0% Cu + 100% CuAl specimen under increasing tensile loads: (a) 1444 N, (b) 2970 N, (c) 4009 N, (d) 4769 N, (e) 5031 N, (f) 4531 N.

Figure 5.33 shows the global strain fields in the yy direction, ε_{yy}, for the 100% CuAl specimen under increasing tensile loads. In the initial stages ((a) – (c)), transverse strains are minimal and uniform, indicating the elastic regime. From intermediate loads ((d) - (f)) onwards, diagonal patterns of transverse contraction emerge, associated with the Poisson effect and the onset of localized plasticity. At higher levels ((g) and (h)), strains reach values close to –0.20, and the distribution is heterogeneous with the formation of inclined bands that anticipate the fracture trajectory. In comparison to intermediate alloys, pure CuAl demonstrates more uniform behaviour in the initial stages but exhibits greater localized contraction intensity in later stages. This confirms the role of aluminium in amplifying the material's stiffness and mechanical anisotropy.

Figure 5.34 shows the global strain fields in the xy direction, ε_{xy}, for the 100% CuAl specimen under increasing tensile loads. In the initial stages ((a) – (c)), the shear field is practically zero and homogeneous, as would be expected in the elastic regime. As the load increases ((d) - (f)), diagonal shear gradients emerge, concomitant with the development

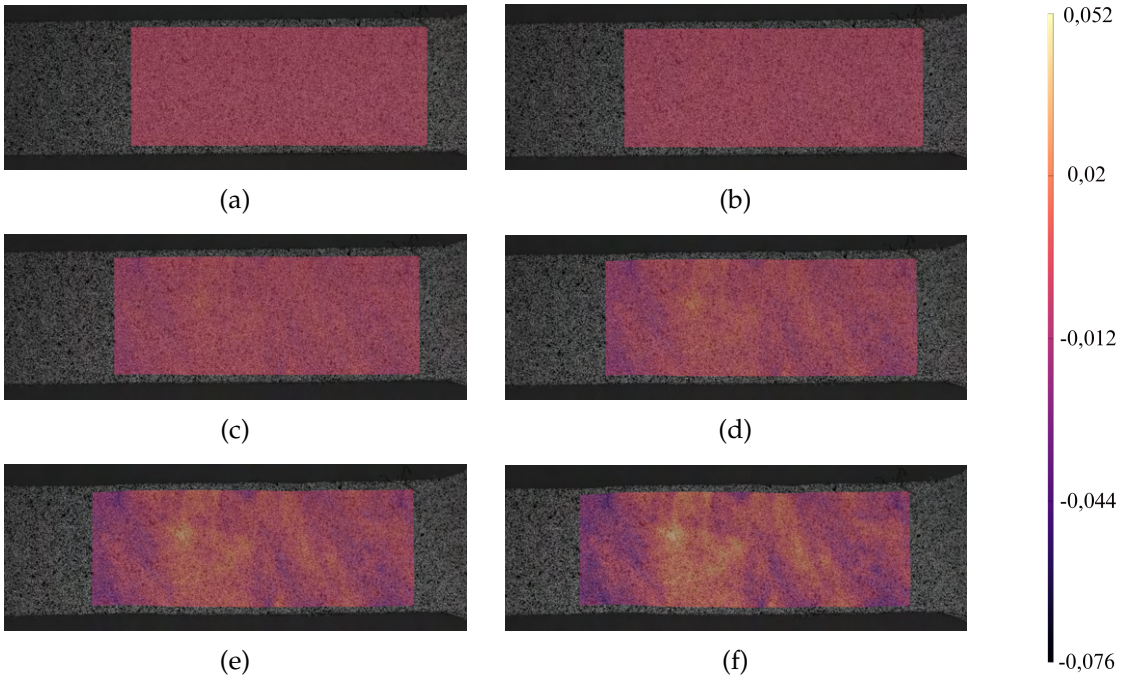

Figure 5.34: Global strain fields in the xy direction, ε_{xy}, for the 0% Cu + 100% CuAl specimen under increasing tensile loads: (a) 1444 N, (b) 2970 N, (c) 4009 N, (d) 4769 N, (e) 5031 N, (f) 4531 N.

of nonuniform deformations and the preferential alignment of plastic bands. In the final stages ((g) and (h)), close to the maximum load (5024 N), localised regions of greater shear intensity are observed, reaching values close to –0.07, indicating the formation of critical shear bands that precede fracture. In comparison with alloys that contain a lower proportion of CuAl, this material demonstrates more stable behaviour during the initial stages. However, it exhibits a more pronounced increase in localised concentration in the advanced plastic regime. This observation is indicative of its high strength, but also its increased propensity to nucleate shear instabilities prior to rupture.

5.3.6 Material properties

As each material composition is subject to different welding parameters, Table 5.9 presents a summary of the travel speed, wire feed speed, current and number of layers for each wall.

A thorough examination of the data presented in Table 5.9, coupled with a meticulous analysis of the interpass temperature, unveils three distinct thermal regimes. The interpass temperature of 80-100°Cis observed to occur at the lowest level for 100% Cu, while a range of 100-150°Cis identified as the intermediate temperature for 100% CuAl. Notably, the interpass temperature of 250-350°Cis identified as the highest for mixtures of both materials, namely Cu and CuAl. The deposition of mixtures of the two materials necessitated an elevated interlayer temperature in comparison to that required for the deposition of 100%

Table 5.9: Process parameters for different Cu–CuAl compositions in WAAM fabrication.

Compositions	Travel speed [mm/min]	Wire feed speed [mm/min]	Interpass temperature [$^{\circ}C$]	Nr of layers
100% Cu + 0% CuAl	450	500	80-100	27
75% Cu + 25% CuAl	95	712	250-350	19
50% Cu + 50% CuAl	100	875	250-350	20
25% Cu + 75% CuAl	100	875	250-350	20
0% Cu + 100% CuAl	300	400	100-150	27

material, in order to achieve interlayer cohesion.

It is evident from the data presented in the table that there is a direct correlation between travel speed and wire feed speed. When the wire feed is set to a higher level (875 mm/min), the travel speed is reduced to a lower setting of 100 mm/min. When the travel speed is elevated (450 mm/min at 100% Cu; 300 mm/min at 100% CuAl), the wire feed is reduced (500-400 mm/min). This adjustment facilitates the maintenance of a stable melt bath for the deposition of each material. It is evident that an increase in material deposition should result in an increase in travel speed, and conversely, a decrease in material deposition should result in a decrease in travel speed.

As illustrated in the table, an additional correlation exists between interpass temperature, wire feed speed and travel speed. It has been demonstrated that when the interpass temperature is higher, there is an increase in wire feed speed, but a decrease in travel speed. The underlying principle pertains to the observation that augmenting the deposition per unit length, characterised by elevated wire feed speed and diminished travel speed, results in enhanced heat retention within the designated section.

It has been demonstrated that an elevated CuAl fraction necessitates a reduced travel speed and augmented heat control to circumvent defects. However, this approach still affords a diminished interpass when compared to the mixtures, given the reduced deposited volume.

Intermediate mixtures are the most thermally critical, since the greater the heat input and the higher the accumulated temperature, the more stringent the parameters must be to avoid overheating and distortion.

As illustrated in Figure 5.35, the profiles of all material compositions, ranging from the substrate to the uppermost point of the cross-section, are delineated. As illustrated by the 100% Cu data (black line), this particular hardness profile is characterised by the lowest values, with an initial peak of 80 HV, subsequently decreasing to 40-50 HV across the majority of the cross-section. This 100% Cu profile displays a significant degree of variation in its vertical dimension, suggesting the presence of distinct zones characterised by varying microstructures. Such variations are likely attributable to the high levels of heat dissipation experienced, in addition to the potential presence of grain heterogeneity. The dark blue line (75% Cu - 25% CuAl) demonstrates a relatively stable profile of 100 HV, with a decline to 70-80 HV. This initial constant hardness profile demonstrates

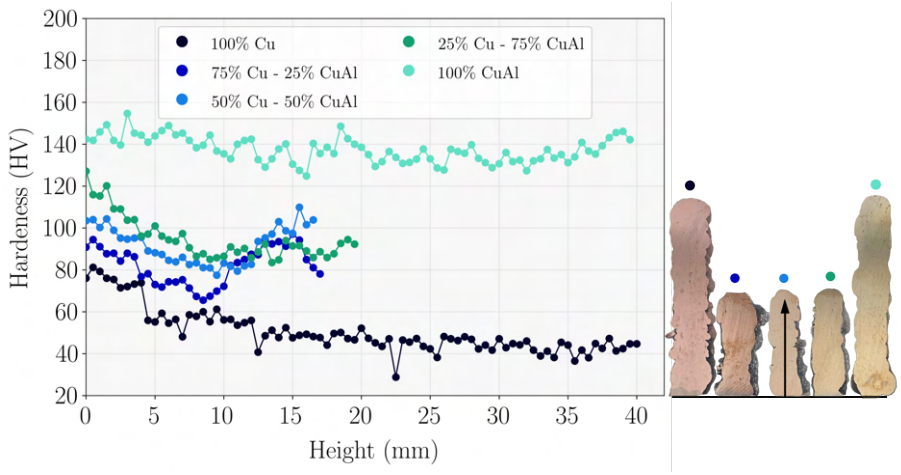

Figure 5.35: Hardness measurements taken from the substrate to the last deposited layer of the crossection of all material compositions.

microstructural uniformity following the initial deposition. It is evident that the material composition under scrutiny in this study exhibits a higher hardness profile in comparison with 100% Cu. This observation can be attributed to two primary factors: firstly, the reduced thermal conductivity and, secondly, the potential refinement of grains. The hardness profile of the 50% Cu + 50%CuAl composition material (light blue) commences with hardness measurements of 100-110 HV, exhibiting a decline to 90 HV, accompanied by substantial fluctuations. These fluctuations are indicative of variations in heat or the presence of zones with heterogeneous microstructures, which may be attributable to the elevated interpass temperature of 250-350 ℃. The material composition 25% Cu + 75% CuAl (dark green) demonstrates a more stable profile, initially at around 120 HV, but then maintaining 110-130 HV throughout the cross-section. This smaller variation suggests that the welding process was more controlled and the microstructure more uniform. The green line (100% CuAl) is the material with the highest hardness (140-150 HV) and is very stable throughout the entire cross-section. This finding suggests that the material possesses a homogeneous and resilient microstructure, characterised by minimal heat dissipation and effective interlayer bonding. In all Cu-rich compositions, a precipitous decline in hardness is evident after the initial few millimetres. This phenomenon may be attributed to the distinct solidification properties of the constituent layers. The initial layers, due to their rapid dissipation of heat to the substrate, undergo a swift solidification process, resulting in the formation of a finer (and consequently harder) microstructure. In contrast, the upper layers exhibit a slower rate of solidification, leading to the formation of thicker grains and a concomitant reduction in hardness. In CuAl-rich compositions, the hardness remains more uniform because the material retains more heat from the start, thereby reducing the thermal gradient between layers. In the context of CuAl-rich alloys, the maintenance of a homogeneous microstructure and constant properties is contingent upon the control of the heat of deposition and the reduction of thermal conductivity.

As illustrated in Figure 5.36, the response in eddy currents, measured over distance,

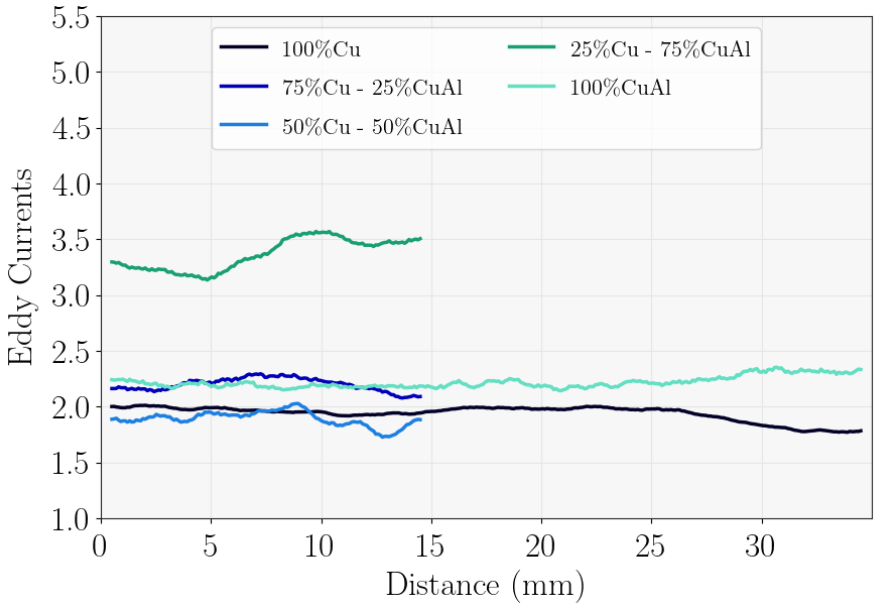

Figure 5.36: Eddy currents measurements taken from the substrate to the last deposited layer of the crossection of all material compositions.

for different Cu-CuAl compositions produced by WAAM is demonstrated. It is evident that pure copper (100% Cu) demonstrates relatively stable values, approaching 2.0, and maintains a consistent trajectory throughout the observed period. A similar behaviour is observed for the 75% Cu + 25% CuAl and 50% Cu + 50% CuAl alloys, albeit with minor fluctuations, also around 2.0. Conversely, the compositions with a higher aluminium fraction demonstrate substantially different responses: the 25% Cu + 75% CuAl alloy shows higher values, with an average of approximately 3.3 and more pronounced variations, while the 100% CuAl alloy reaches values close to 2.3-2.4, also showing a tendency to increase with increasing distance. The results obtained demonstrate that the chemical composition exerts a direct influence on the electromagnetic response, with increasing CuAl content resulting in higher eddy current intensities. This behaviour is associated with the differences in electrical conductivity and microstructure introduced by the variation in composition, providing relevant information for non-destructive characterisation and quality control in components produced by WAAM.

Figure 5.37 shows the load (N)–displacement (mm) curves for each material composition obtained from the tensile tests. An analysis of the load-displacement curves reveals that the 100% Cu material exhibits the lowest maximum load (1.8 kN) and moderate displacement (6 mm), while the 100% CuAl material demonstrates the highest maximum load (5.5 kN) and relatively high displacement (6.4 mm). The material compositions of the two mixed materials demonstrate an intermediate but non-linear behaviour. An examination of the maximum load reveals a direct correlation between the percentage of CuAl and the maximum load value; as the percentage of CuAl increases, the maximum load value concomitantly rises. However, it should be noted that the maximum displacement

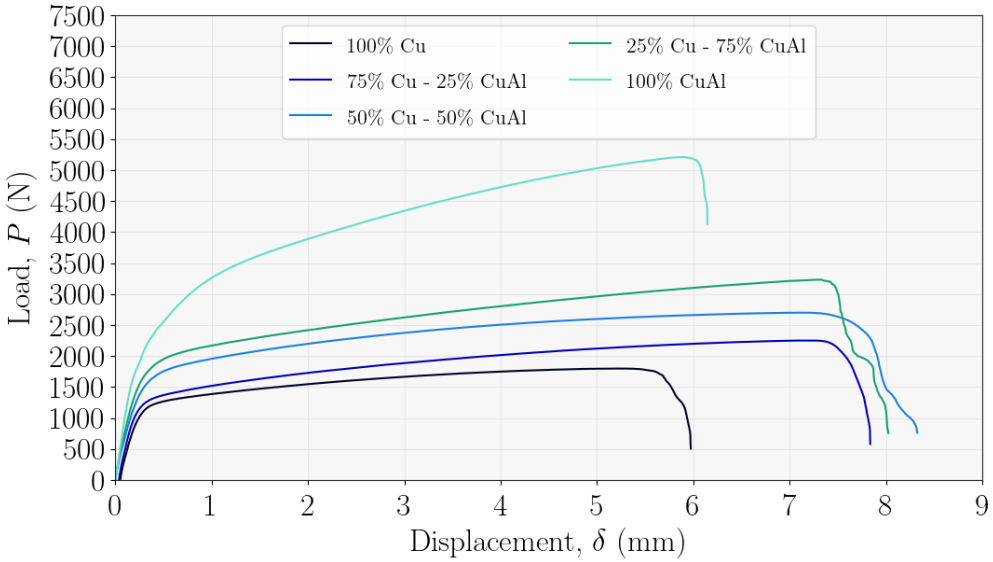

Figure 5.37: Load-displacement curves for all the material compositions specimens.

value is not linear for all material compositions.

Table 5.10: Summary of maximum load, displacement at fracture, and average hardness for different Cu–CuAl compositions.

Composition	Max. load (N)	Max. Displacement (mm)	Avg. hardness (HV)
100% Cu	1799	6.0	52
75% Cu + 25% CuAl	2251	7.8	79
50% Cu + 50% CuAl	2419	5.0	83
25% Cu + 75% CuAl	3232	8.0	99
0% Cu + 100% CuAl	5507	6.4	138

As illustrated in Table 5.10, the maximum load, maximum displacement and average hardness for all material compositions are summarised. It can be concluded that increasing maximum load and hardness is evident in the CuAl fraction. Pure copper demonstrates the lowest mechanical performance (1799 N, 52 HV), indicative of its high ductility but low strength. In contrast, pure CuAl exhibits the highest values (5507 N, 138 HV), thereby demonstrating the significant contribution of aluminium to enhanced strength. Intermediate compositions manifest distinctive behaviours: the 50%Cu + 50%CuAl alloy exhibits comparatively elevated hardness (83 HV) but diminished fracture displacement (5.0 mm), indicating enhanced brittleness. The 25% Cu + 75% CuAl alloy has been shown to achieve a high maximum load (3232 N) and greater displacement (8.0 mm), thus presenting the optimal compromise between strength and ductility. The 75% Cu + 25% CuAl alloy also exhibited good deformability (7.8 mm) with a moderate increase in strength (2251 N). In summary, the results confirm that the progressive addition of CuAl increases hardness and mechanical strength, but maximum ductility is achieved at intermediate compositions, especially for 25% Cu + 75% CuAl. These findings are consistent with the displacement and strain maps obtained by DIC, which revealed greater homogeneity in

pure copper and greater localization in aluminium-rich alloys.

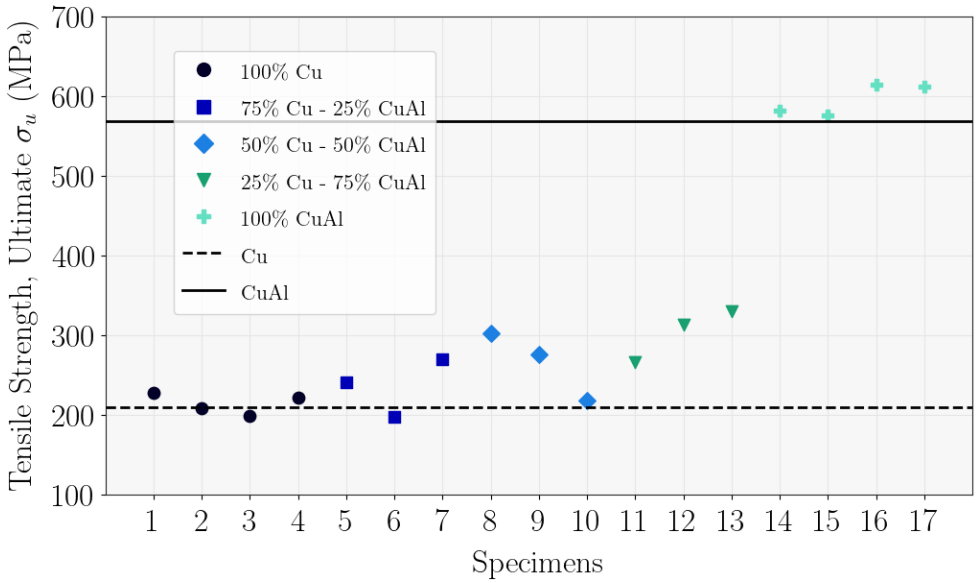

Figure 5.38: Graph of the ultimate tensile strength [MPa], σ_u, of all material compositions.

As demonstrated in Figure 5.38, the graph illustrates the ultimate tensile strength, denoted by σ_u in MPa, for all material compositions. The graph demonstrates a progressive increase in ultimate tensile strength as the Cu content decreases and as the CuAl content increases. The mean values are consistently below the reference lines for pure Cu (dashed black line) and pure CuAl (solid black line). This is to be expected, given that these materials are manufactured by WAAM with different microstructures and defects from commercial materials. The 100% Cu material exhibits the lowest measured value of shear modulus, with a range of 180-220 MPa, falling below the established reference value. The material composition, 75% Cu + 25% CuAl, demonstrates a marginal increase in comparison to 100% Cu (180-270 MPa). The addition of CuAl has been demonstrated to enhance tensile strength. In the case of the intermediate material composition (50% Cu + 50% CuAl), the value of the von Mises stress tensor, designated here as σ_u, is approximately 200-300 MPa. This is in close proximity to the Cu reference line, indicating that the benefit derived from the CuAl addition compensates for the losses incurred due to overheating. For the composition material 25% Cu + 75% CuAl, the shear modulus values are approximately 270-340 MPa. Finally, the 100% CuAl material exhibited values of 570-620 MPa for σ_u. However, these values were well below the reference value, likely attributable to the presence of internal defects characteristic of WAAM.

Figure 5.39 illustrates the yield strength values of the different Cu–CuAl alloy compositions produced by WAAM. The yield strength of the 100% Cu alloy exhibits a range of values from 130 to 155 MPa. As the CuAl content is increased, the yield strength is concomitantly increased, with values ranging between 130 and 170 MPa for the 75% Cu + 25% CuAl alloy. For the 50% Cu + 50% CuAl composition, yield strength values range from 130 to 210 MPa, demonstrating greater dispersion. The 25% Cu + 75% CuAl

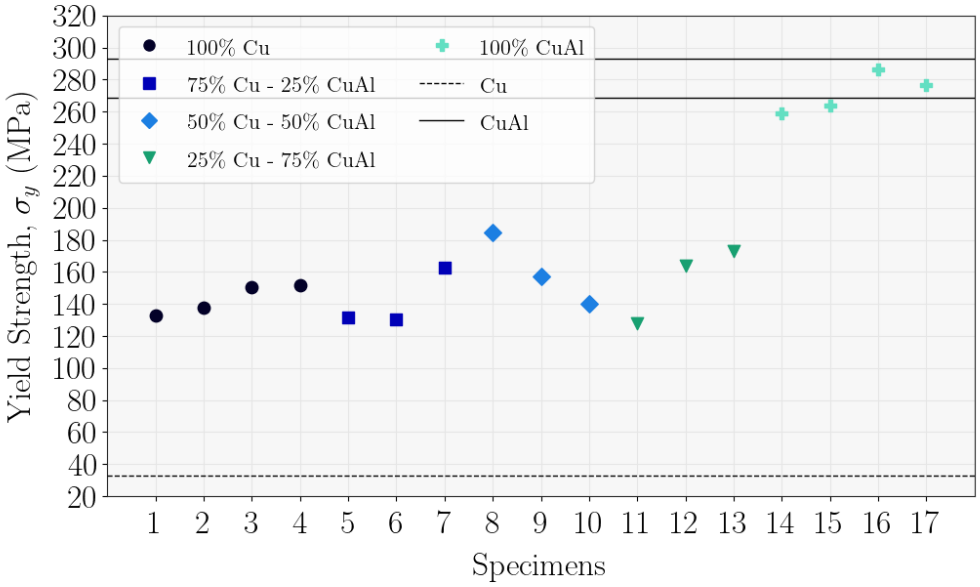

Figure 5.39: Graph of the Yield Strength [MPa], σ_y, of all material compositions.

alloy presents values between 130 and 180 MPa. For the 100% CuAl material, the yield strength increases significantly, with values ranging from 270 to 295 MPa. The graph also demonstrates that all alloys manufactured by WAAM exhibit lower yield strength values than the reference lines for Cu and CuAl materials (indicated by dashed black and solid black horizontal lines, respectively). The results obtained demonstrate the impact of internal defects and microstructures, introduced by the additive manufacturing process, in reducing the mechanical properties of the alloys when compared to their commercial counterparts.

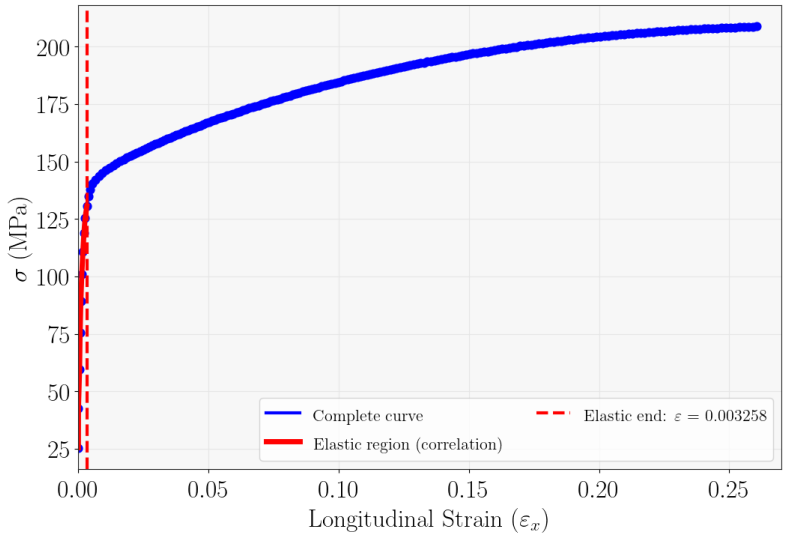

Figure 5.40: Stress-Strain curve of a 100% Cu specimen (specimen 2).

Figure 5.40 shows the relationship between stress (σ) and longitudinal deformation (ϵ)

in a material undergoing a tensile test. The blue curve shows the material's full response from when the load is first applied to when the maximum deformation is reached. The elastic region, indicated by red colouring, signifies the initial range in which deformation is directly proportional to stress in accordance with Hooke's law. In other words, the material reverts to its original shape once the load is released. The dashed red line in the figure indicates the yield point, marked by a deformation of 0.003258. Beyond this point, the material begins to deform plastically and the deformation becomes permanent. This graph is essential for understanding mechanical properties such as modulus of elasticity, yield strength and how the material behaves under stress. It enables analysis of the challenges faced and the resistance of the material during load application.

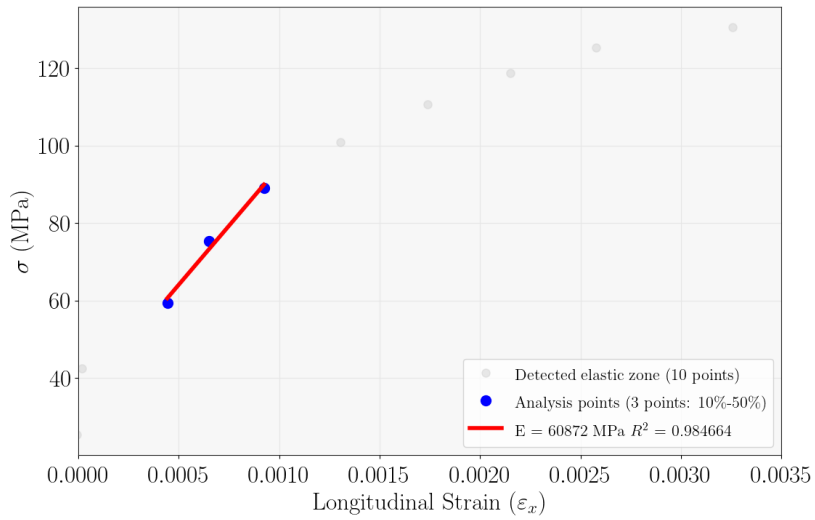

Figure 5.41: E determination from elastic analysis of a 100% Cu specimen (specimen 2).

Figure 5.41 presents a detailed representation of a material's elastic zone, illustrating the relationship between stress and longitudinal strain. The blue dots highlight the values analysed in the elastic region (corresponding to 10–50% of the elastic response), and the red line shows the linear fit obtained, indicating the found elastic modulus: E = 60.9 GPa. The resulting equation demonstrates excellent linearity, with a correlation coefficient ofR^2 = 0.984664. The legend shows that ten points were detected in the elastic zone, three of which were used for a more detailed analysis. This graph is crucial for precisely characterising the material's elastic behaviour and subsequently determining the Young's modulus value.

Figure 5.42 demonstrates the relationship between transverse strain (ϵ_y) and longitudinal strain (ϵ_x) within the elastic zone of the material. The green points represent analysed data from 10% to 50% of the elastic response, while the green line indicates the linear fit used to calculate Poisson's ratio. This results in a value of ν = 0.5172 for the ratio, with an R^2 value of 0.997137 indicating excellent linear correlation. The caption states that ten points were identified within the elastic zone, three of which were selected for analysis to

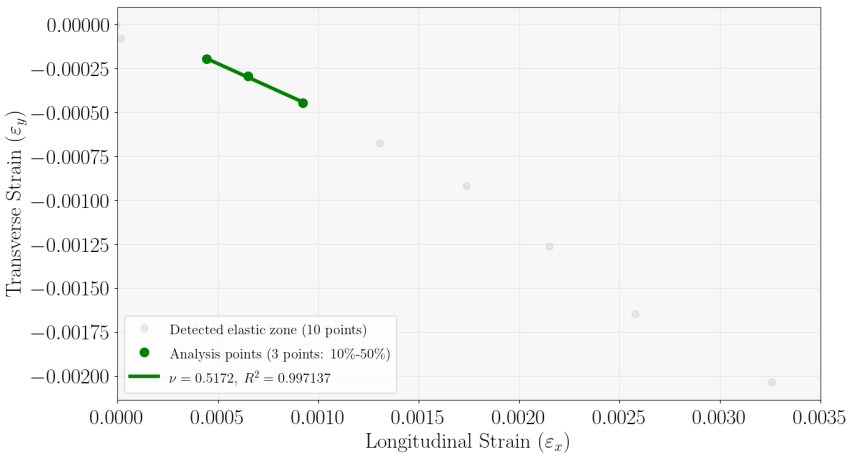

Figure 5.42: ν determination from elastic analysis of a 100% Cu specimen (specimen 2).

determine the presented value. This graph is pivotal in characterising Poisson's ratio, a crucial metric in analysing the mechanical behaviour of materials. It quantifies the extent to which a material deforms transversely when subjected to longitudinal stress.

Table 5.11: Measured Poisson's ratio and Young's modulus for each specimen.

Specimens	**Poisson's ratio ν**	**Young's modulus E (GPa)**
1	0,382	20,2
2	0,574	19,8
3	0,084	31,5
4	0,675	27,4
5	0,126	21,6
6	0,327	24,8
7	0,377	30,7
8	0,410	45,1
9	0,443	19,8
10	0,386	23,9
11	0,198	23,4
12	0,369	27,4
13	0,507	22,9
14	0,328	108,3
15	0,334	87,5
16	0,233	75,9
17	0,263	71,8

Table 5.11 presents the measured values of Poisson's ratio (ν) and Young's modulus (E, in GPa) for 17 different specimens. A wide variation is observed in both parameters, reflecting compositional and microstructural differences between the specimens. Experimental values for ν range from 0.084 to 0.675, while for E they range from 19.8 to 108.3 GPa. Compared to typical values for copper alloys, where Young's modulus is generally between 97-130 GPa and Poisson's ratio is close to 0.33-0.36, some samples present much

lower results, which may indicate the presence of discontinuities, porosity, or other non-ideal structural effects in the analyzed specimens. These results can be complemented and justified by microstructural analyses or considerations regarding materials processing.

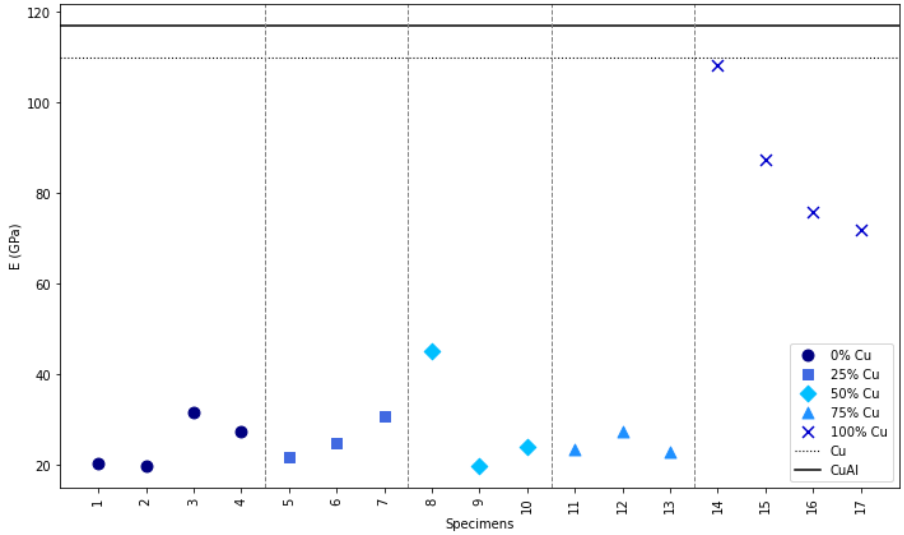

Figure 5.43: Comparison of E for different copper percentages.

Figure 5.43 displays the elastic modulus (E, in GPa) values of various specimens with different percentages of copper (Cu), identified by markers and distinct colours for each composition: The following concentrations of copper are represented: 0%, 25%, 50%, 75%, and 100%. Samples with a composition of 100% copper have been observed to exhibit significantly higher moduli, with values that exceed 70 GPa. In contrast, alloys with lower copper contents have been found to demonstrate substantially lower moduli, ranging from approximately 20 to 45 GPa. Horizontal lines demarcate reference values for pure copper and CuAl materials, thus facilitating comparison of experimental and theoretical results. Overall, there is considerable variation in elastic modulus as a function of copper percentage, reflecting the significant influence of composition on material stiffness, as evidenced by the clustering and scattering of points for each group of specimens.

Figure 5.44 presents the values of Poisson's ratio (ν) for various specimens, which have been grouped according to the percentage of copper (Cu) contained within each alloy. Distinctive markers are utilised to distinguish between the various composition groups. The following concentrations of copper are represented: 0%, 25%, 50%, 75%, and 100%. A significant dispersion of v values is noted, especially for samples with 0% and 25% Cu, ranging from approximately 0.08 to 0.67. Samples containing 100% copper exhibited closer values, falling below the theoretical value for pure Cu (horizontal line). This observation may be indicative of experimental or microstructural variations. In general, an observed tendency for the Poisson ratio, denoted by ν, to decrease with increasing copper content is evident, with occasional fluctuations observed in intermediate alloys. These fluctuations can be attributed to the complex influence of chemical composition on the mechanical properties of materials.

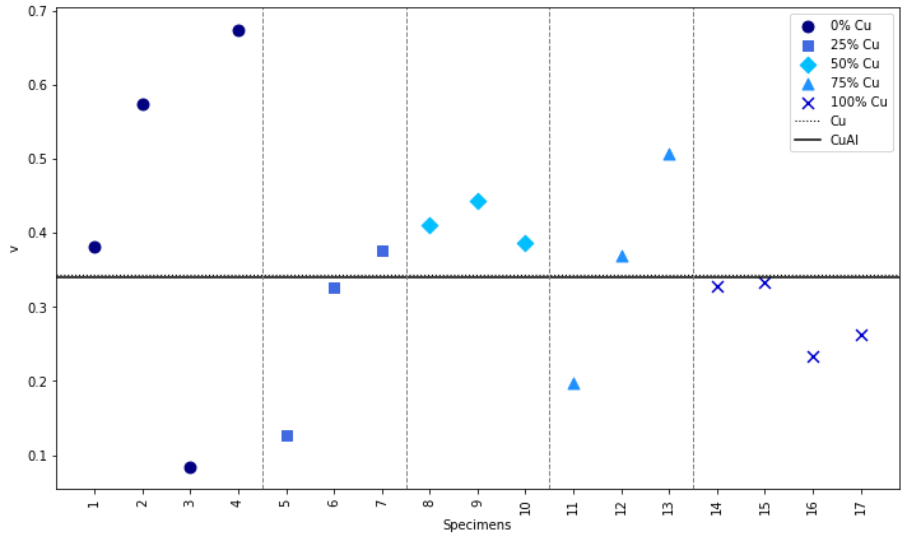

Figure 5.44: Comparison of ν for different copper percentages.

5.4 Conclusion

A library of material compositions and mechanical properties was created to evaluate all the different Cu and CuAl alloy compositions produced. Seventeen samples comprising various combinations of Cu and CuAl were studied. These samples were produced using WAAM with GMAW and GTAW. Each specimen was characterised using hardness measurements, eddy currents and DIC-based tensile testing. Examining the hardness measurements for all the material compositions revealed that the higher the CuAl content, the higher the hardness value. Examining the load-displacement curve revealed that the higher the CuAl content, the greater the maximum load. However, the maximum displacement for each material composition varies, and there is no correlation with changes in the percentages of Cu and CuAl. Ultimate tensile strength analysis showed that the higher the CuAl content, the higher the value of σ_u. The material displays an initial phase of linear behaviour, where deformation is proportional to stress, according to Hooke's law. The modulus of elasticity, alternatively termed Young's modulus, was calculated at approximately $E = 60.9$ GPa, indicating elevated levels of stiffness. The elastic zone was confirmed by a strong linear correlation ($R^2 = 0.985$), with points demonstrating the material's ability to recover its shape after moderate loads. Furthermore, the relationship between transverse and longitudinal strains resulted in a Poisson's ratio of 0.5172, indicating that the material undergoes lateral contraction upon stretching.

6

Cu-CuAl alloy FGM stepwise

6.1 Introduction

This chapter describes the study of Cu-CuAl alloy FGM stepwise with abrupt transition zone. This chapter begins with a finite element analysis of the tests to be developed. Next, a description of the experimental tests carried out on the specimens is given, explaining the tensile test procedure, the DIC procedure, the calibration process, the maximum force, the noise evaluation and the results. Finally, two inverse identifications are performed using VFM, one using synthetic images and the other using full-field data.

6.2 Finite element analysis

Once the AM wall has been fabricated, it is necessary to design the FGM specimens. A finite element model was created which underwent several changes in configuration and geometry to investigate the best configuration and geometry for the specimen. The use of FEA to determine the best geometry to adopt aims to validate a proposed design and ensure that test performance is as planned. FEA allows a virtual approach to optimising the design of a prototype and/or mechanical test, without wasting time and resources compared to traditional tests and error methods of developing physical prototypes. The FE model was created with ANSYS Mechanical APDL v24.2. First, it was decided that the specimen should be as rectangular as possible to maximise the spatial resolution of the camera. It was then determined that the geometry should have two opposing notches to ensure that the fracture of the specimen occurred in the area where the field of view of the camera was defined. The height of the specimen was defined as the maximum dimension of the AM wall after machining. The width of the specimen was defined based on the fact that we wanted enough space in this dimension to have the transition zone and the copper zone separated from the copper-aluminium zone without any mixing. The width of the sample was also related to the pixel size (mm/pixel) and the magnification of the camera used. For a magnification defined by the characteristics of the camera, a larger specimen width would result in a larger speckle size and vice versa. As a larger speckle

size is ultimately more difficult to pattern, the best approach would be to use a larger specimen width.

To solve this static analysis problem, the following code-writing process was followed:

- First, several parameters of the model were defined, such as the length (L=54 mm), width (W=25 mm) and thickness (T=1 mm) of the specimen, as well as the radius (R=3mm) of the notches. In this specimen, the FGM transition zone was determined to be 3mm, as illustrated in Figure 4.18;
- Then the properties of the materials were defined, such as Young's modulus (E), Poisson's ratio (ν), tangent modulus (E_t) and yield stress (Y_s). The distribution of these properties is constant, with each material exhibiting a single value. However, a linear variation in the properties of Young's modulus, Poisson's ratio and yield stress is observed in the transition zone between the two materials, while a constant value is recorded for tangent modulus. As illustrated in Figure 6.1, the distribution of the parameters is depicted alongside the values of the ends;

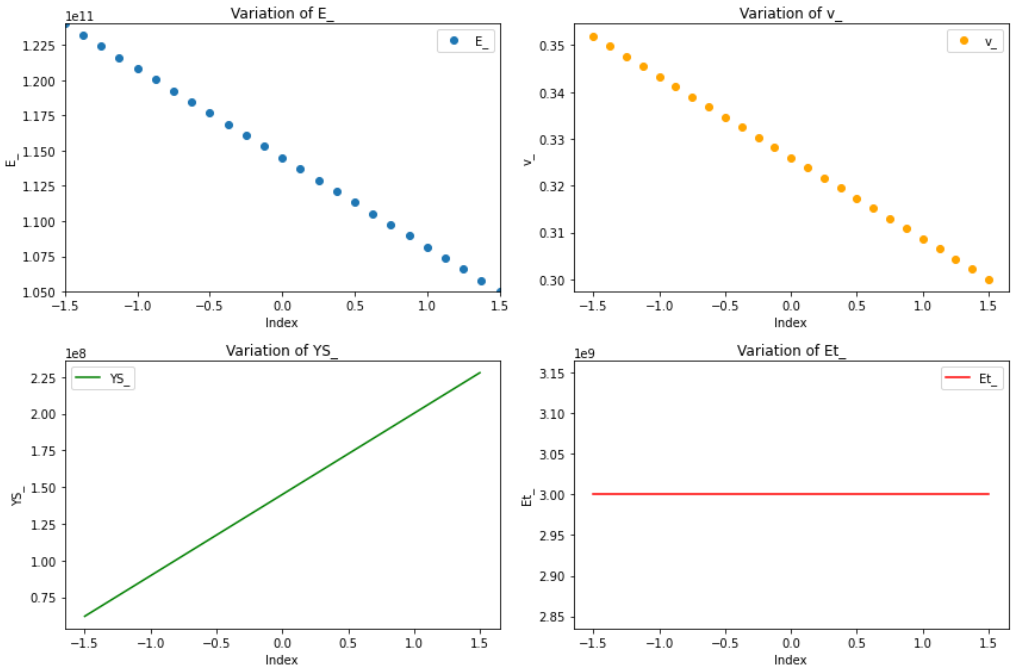

Figure 6.1: Distribution of the parameters E, ν, Y_s and E_t for the distribution zone of the Cu-CuAl alloy FGM stepwise without preheating (Transition zone equal to 3 mm).

- To define the mesh, was specified the element size as 0.5 mm and the desired displacement in the y-direction as Uy=1mm. The size of the element was determined based on a mesh convergence study and the maximum number of elements permitted for a student version of Ansys;
- The element type PLANE182 and PLANE183 have specific key options. These include a quadrilateral element shape, plane stress with thickness element behavior,

and pure displacement element formulation;

- Real constants were defined for the cross-section properties of the element with a specimen thickness of 1 mm;
- The model was assigned with material properties for Young's modulus and Poisson's ratio for both materials. Bilinear isotropic hardening was used with either von Mises or Hill plasticity as the model material;
- Geometry is defined using keypoints, arcs, and areas. Material properties are then associated with specific areas. Figure 6.2 shows the assignment of areas for material 1 (blue) and material 2 (purple), copper and CuAl alloy respectively;

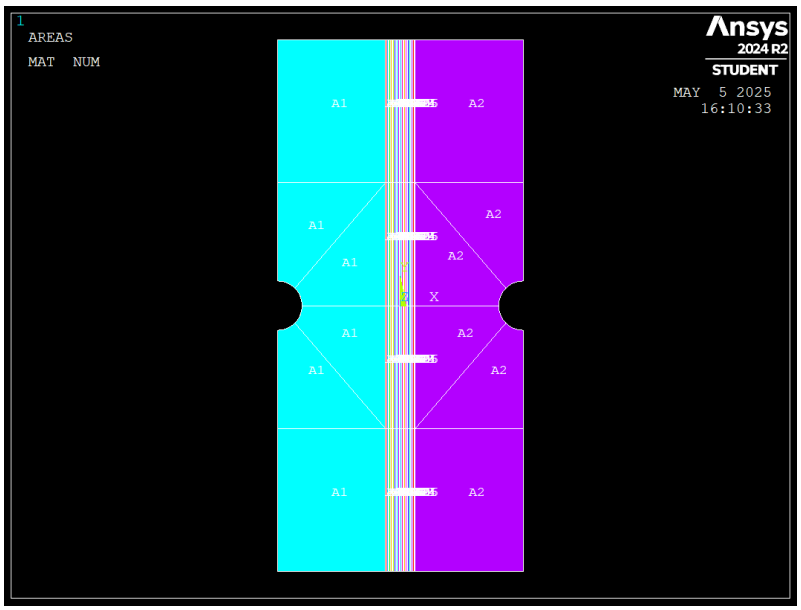

Figure 6.2: Cu-CuAl alloy FGM stepwise (transition zone equal to 3 mm) scheme for attributing the two materials to the defined areas: 1 (blue)- Copper and 2(purple)- CuAl alloy.

- This step involves meshing and merging. Meshing is determined by the size and shape of the elements. Figure 6.3 shows the mesh with its 86800 elements;
- The solution is executed using static analysis. The boundary conditions are defined as a displacement in y on the free surface of the test piece and an embedding on the opposite surface, with no displacement in x or y. The model's boundary conditions are illustrated in Figure 6.4.

Figure 6.5 shows the nodal solution of the specimen in the x-component of the displacement in Ansys. This plot shows that displacements on the x-axis are almost non-existent, which is consistent with the boundary conditions applied in the model. In a tensile test the displacements will be on the y-axis. However, slight bending of the specimen may be observed due to the materials exhibiting distinct yield stresses.

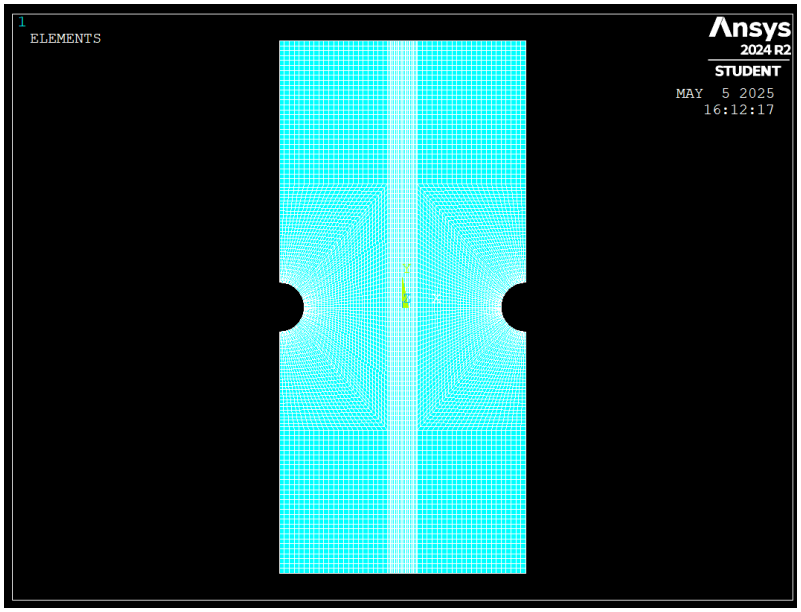

Figure 6.3: Meshing of Cu-CuAl alloy FGM stepwise (transition zone equal to 3 mm) specimen used for the Ansys model.

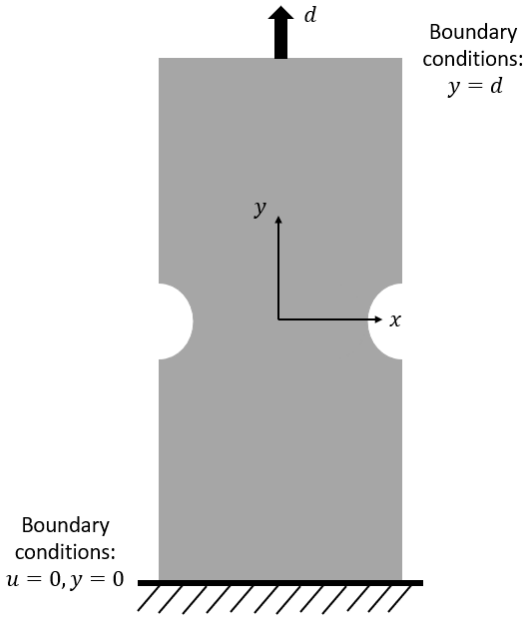

Figure 6.4: Schematic of tensile test.

Figure 6.6 shows the nodal solution of the specimen in the y-component of the displacement in Ansys. The nodal solution refers to the solution values for each node of the finite element mesh. From this plot we can see that the maximum displacement occurs on the top surface. Therefore, the failure of the specimen will occur in the centre. The y displacements are consistent with the direction of test performance.

Figure 6.7 shows the stress distribution of the x-component of the FGM specimen. Based on the results, it can be concluded that there is a higher level of stress concentration

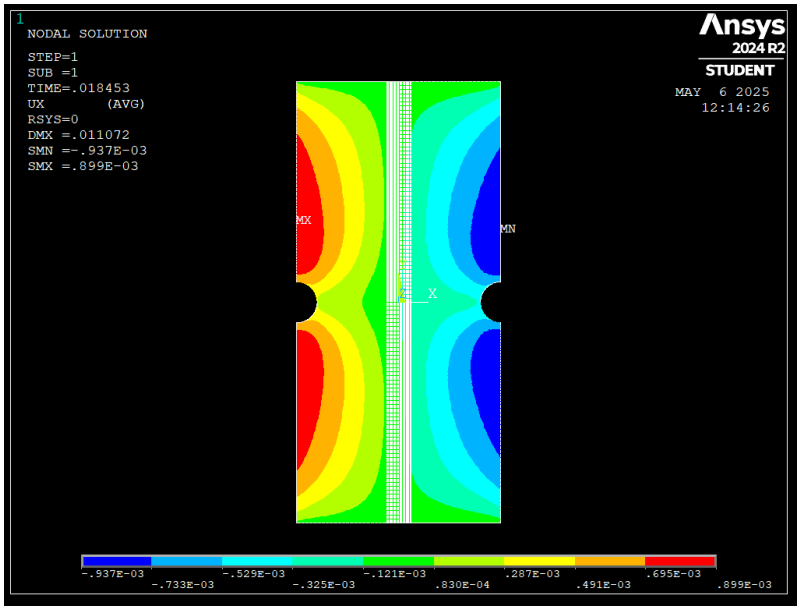

Figure 6.5: Cu-CuAl alloy FGM stepwise (transition zone equal to 3 mm) specimen DOF Solution: X-Component of displacement on nodal solution in ANSYS.

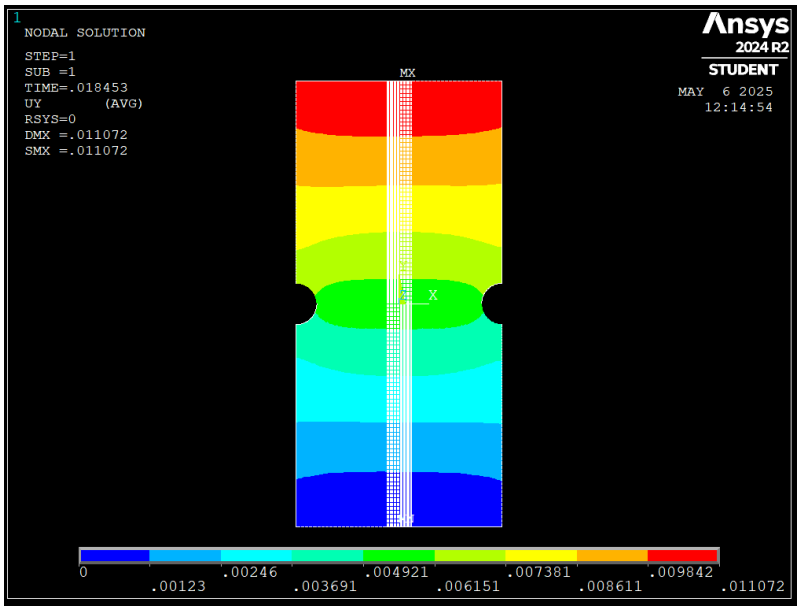

Figure 6.6: Cu-CuAl alloy FGM stepwise (transition zone equal to 3 mm) specimen DOF Solution: Y-Component of displacement on nodal solution in ANSYS.

in the notch area, making it more susceptible to fracture. The gripper area of the tensile test is also subject to high levels of stress concentration.

Figure 6.8 shows the stress distribution of the y-component of the FGM specimen. Stress distribution refers to the variation in stress values, in this case in the y component. The stress distribution shows that in this analysis the maximum normal stress will be in the centre of the notch of the copper material, so it is in this area that the material will frature first. According to the stress component graph, the copper material will be the

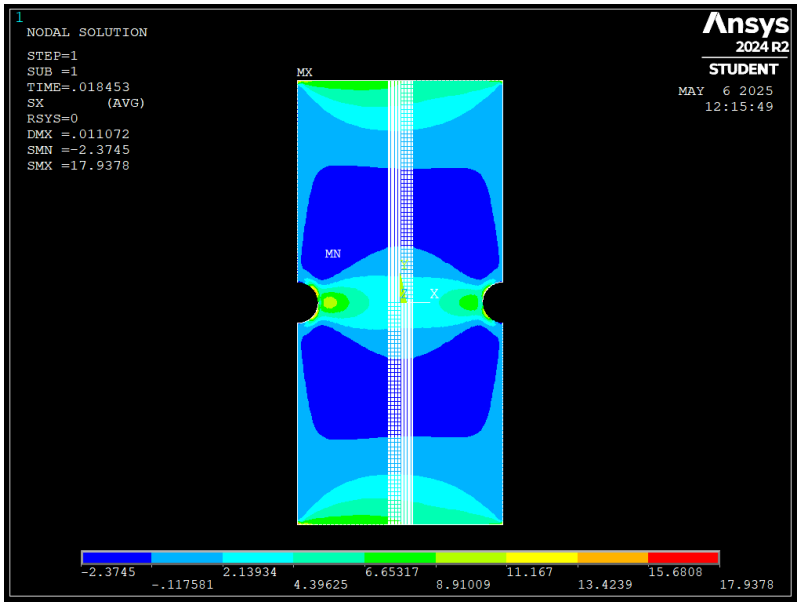

Figure 6.7: Contour plot of distribution of X-component of stress for Cu-CuAl alloy FGM stepwise (transition zone equal to 3 mm) specimen.

first to fracture because it has the lowest yield stress. The CuAl alloy material's notch area also exhibits a high stress concentration zone.

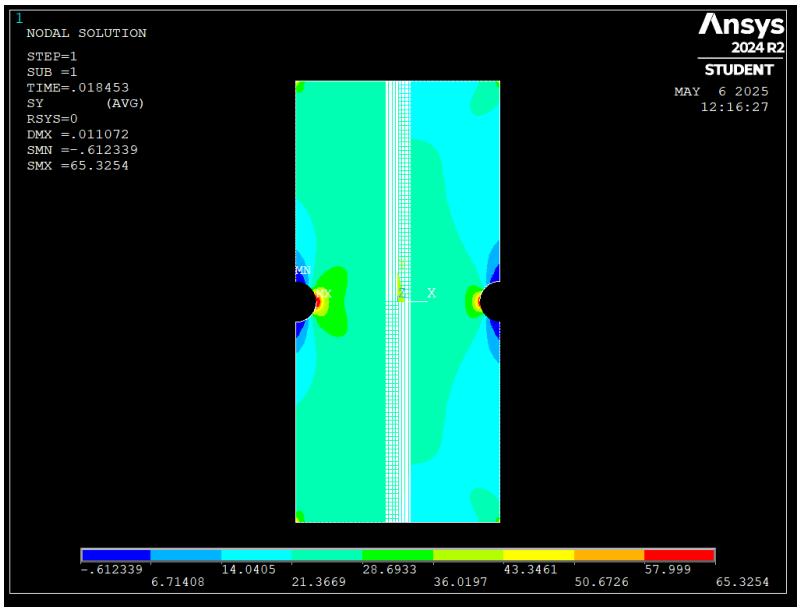

Figure 6.8: Contour plot of distribution of Y-component of stress for Cu-CuAl alloy FGM stepwise (transition zone equal to 3 mm) specimen.

As anticipated, the analysis of the results yielded the identification of the highest stress concentration zone in the area of the notches. The experimental findings indicate that the copper side of the specimen exhibits both the maximum and minimum normal stresses. It is evident from the findings that the copper side is the primary locus of deformation, and that the specimen will fracture at this location. Figure 6.9 shows the elastic strain

distribution of the x-component of the FGM specimen.

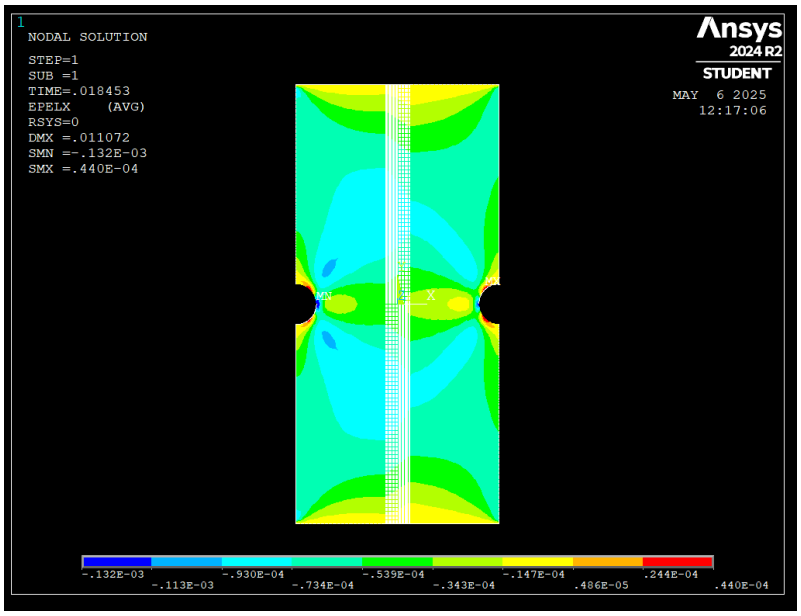

Figure 6.9: Contour plot of distribution of X-component of elastic strain for Cu-CuAl alloy FGM stepwise (transition zone equal to 3 mm) specimen.

Figure 6.10 shows the elastic strain distribution of the y-component of the FGM specimen.

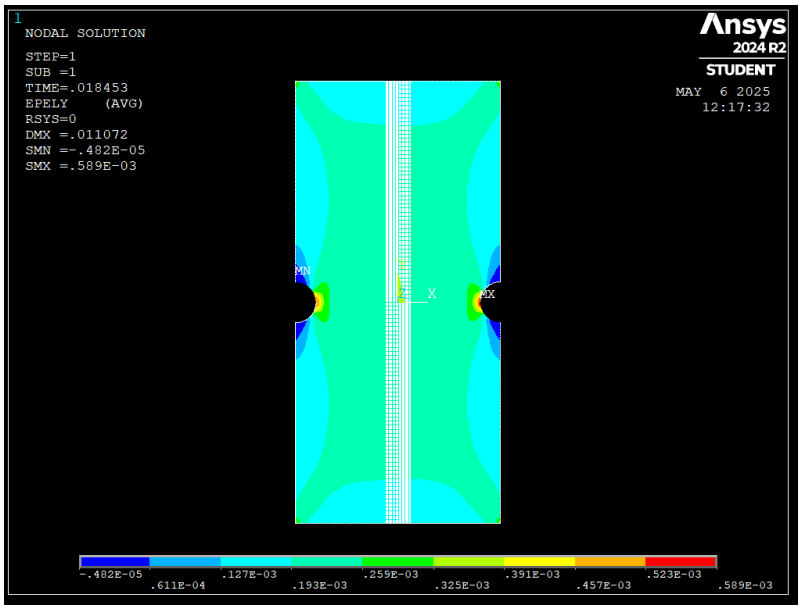

Figure 6.10: Contour plot of distribution of Y-component of elastic strain for Cu-CuAl alloy FGM stepwise (transition zone equal to 3 mm) specimen.

In a tensile test, the elastic strain is observed as the initial linear portion of the stress-strain curve. As indicated by the extant literature, the Young's modulus of copper is 110 GPa, while that of the CuAl alloy is 117 GPa. It has been observed that the maximum

elastic strain value is exhibited by the notch in the CuAl alloy material, as this has a lower Young's modulus value, and therefore deforms first. This statement serves to corroborate the data presented in Figure 6.9 and Figure 6.10.

6.3 Tensile tests with Digital Image Correlation

Four samples of Cu-CuAl alloy FGM were tested to validate the geometry decided in Chapter 4. The four test pieces are made up of a pre-test test piece, as explained in Section 4.4.2, in which there was no pre-heating of the copper layers. This pretest was used as a test specimen to test the setup. There are three more identical specimens, where the copper layers underwent preheating. These experimental tests aimed to identify the challenges and errors that require improvement. The dimensions of these samples are the same as the 316L stainless steel samples shown in the Figure 4.30. The field of view (FOV) of this study is represented by the green dashed area and has dimensions of 57X30 mm. Figure 6.11 displays one of the four specimens, each made of two distinct materials as can be seen.

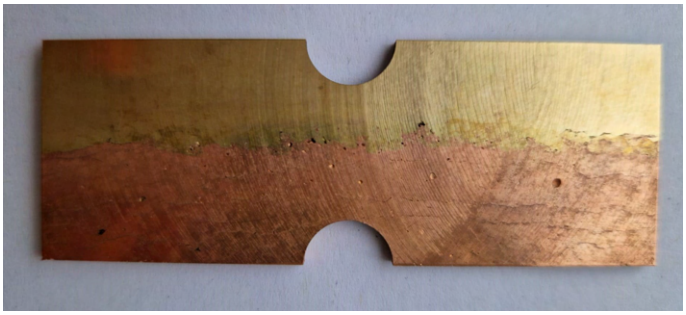

Figure 6.11: Cu-CuAl alloy FGM stepwise specimen.

6.3.1 Tensile test procedure

The study employed tensile test procedures similar to those used in 316L stainless steel tests. The Instron 5569 electromechanical test machine with a 50 kN load cell was also used. The specimens were vertically aligned and secured in the grips, and subjected to a displacement rate of 1.5 mm/min during the tensile tests. Two Blackfly 8.9MPx cameras acquired images using stereo DIC, one pointing towards the specimen and the other at an angle. The cameras were adjusted to optimize spatial resolution on the sample. They were mounted on 105mm lenses (Sigma 105mm f/2.8 EX DG Macro Lens, Sigma Corporation, Aizu, Japan) and a sensor array. Two polarisers were placed on both lenses to filter the light, and two LED lights were used to illuminate the specimens. This experimental setup is shown in Figure 6.12.

The system depicted in Figure 6.12 is connected to the MatchID trigger box, which, in turn, is connected to a desktop computer. The MatchID trigger box is custom hardware used to synchronize the two cameras with precise timing and provides analog output

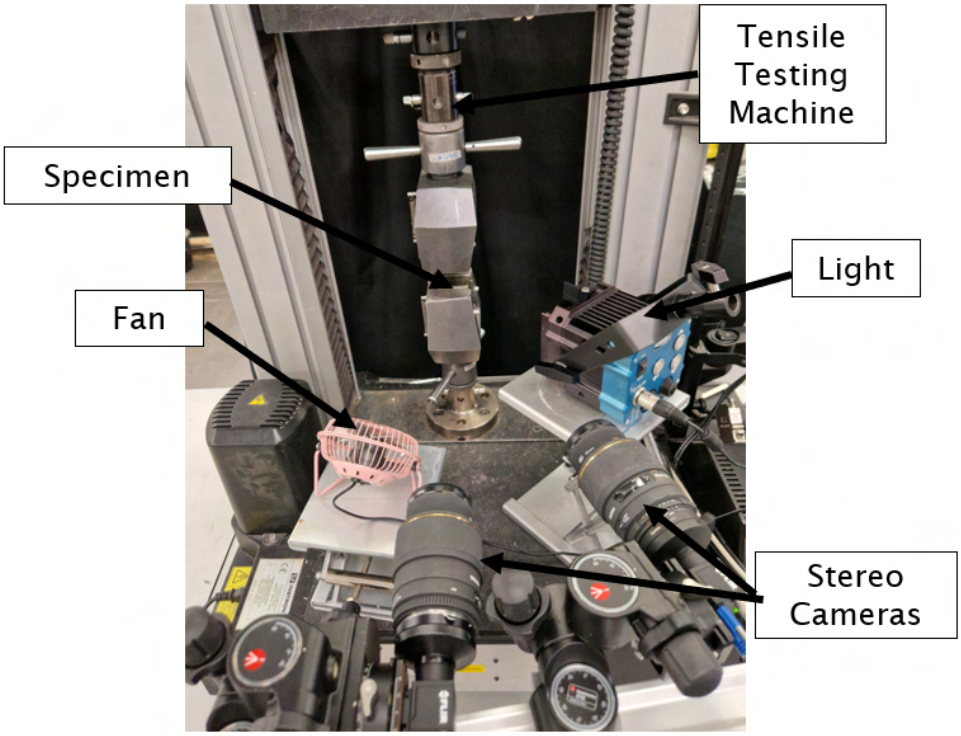

Figure 6.12: Experimental setup for stereo-DIC test on Cu-CuAl alloy FGM stepwise specimen.

for experimental feedback, such as force cell and displacements. Section 4.6.2 presents a schematic of the tensile test with DIC test system that was used for tests with FGM specimens. Table 6.1 presents the main characteristics employed in the stereo-DIC tensile tests of FGM specimens.

Table 6.1: Stereo-DIC settings for the tensile test of FGM specimens stepwise.

DIC setting	**Specification**
Electromechanical test machine	Instron 5569
CMOS Cameras	Blackfly 8.9MPx
Lens	Sigma 105mm f/2.8 EX DG Macro Lens
Stereo angle	21,04 °
Patterning technique	Airbrush
DIC technique	Stereo correlation
DIC software	MatchID, version 2024.1

6.3.2 Digital image correlation method procedure

The Digital Image Correlation (DIC) system was utilised to measure surface deformations in the analysed samples during tensile testing. A DIC software is necessary for capturing and analysing images of samples. The software utilises algorithms to track pixel patterns

and calculate surface deformations as these patterns change over time. High-resolution and high-frame-rate cameras are required to capture detailed images of samples during testing. The stereo system with two cameras was used to analyze the sample surface in this study. Adequate illumination is crucial to ensure sufficient contrast in the captured images for analysis using the DIC software. The speckle pattern plays a critical role in the DIC system, requiring a high-contrast pattern on the sample visible to the cameras and remaining undistorted during testing. These markings act as reference points for the DIC software to compute deformations, as explained in the section on speckle patterns. The experimental setup should be arranged with care to ensure that the cameras capture the entire surface of the sample without creating shadow areas during the tensile test. Table 6.2 lists the default DIC parameters for analyzing the FGM stepwise samples.

Table 6.2: DIC parameters for the tensile test of FGM specimens stepwise.

DIC Parameter	**Specification**
General DIC Settings	
Technique Used	2D Digital Image Correlation
Camera Resolution	16bit, 5320 × 4600 pixels
Pixel to mm conversion	0.004
Average Speckle Size	11 pixels
Subset Size	41 pixels
Step Size	2 pixels
Shape Function	Quadratic
Interpolation Function	Bicubic Spline
Correlation Criterion	ZNSSD
Prefiltering	Gaussian (Kernel size = 5)
Strain Settings	
Strain Window	55 data points
Virtual Strain Gauge (VSG)	149 pixels
Strain Interpolation Function	Bilinear Quadrilateral (Q4)
Strain Tensor	Hencky

After calibration, approximately 20 still images were captured. The Digital Image Correlation (DIC) technique necessitates a static reference image to compare with subsequent images to determine displacements and deformations during the test. Like many experimental methods, DIC is susceptible to experimental noise, also known as random error, which can affect the accuracy of results. This noise primarily stems from the camera acquisition process, introducing random variations in the gray level values of captured images. Image acquisition noise can influence measured coordinates and derived quantities during the DIC process. To mitigate this, multiple images can be averaged. Averaging is straightforward for the reference DIC image, typically obtained under no load conditions. Multiple static images of the test sample can be captured and averaged to generate an approximately noiseless reference image. However, creating similar noiseless deformed

images is a more complex task. It is important to be cautious about potential effects, such as creep. In the 4 samples, an aperture of 16 was used in both cameras. An illumination intensity of 64% was defined in the lamp used. A different exposure time was used for each test as the speckle pattern is different for each specimen. For the pre-test an exposure time of 33000 μs was used, for sample 1 an exposure time of 34000 μs, for sample 2 an exposure time of 22000 μs and for sample 3 an exposure time of 21000 μs. Because the camera's high spatial resolution does not provide much temporal resolution, the images were taken at 0.5 Hz.

6.3.3 Calibration process

The system setup needed calibration to evaluate the specimen geometry through captured images. The process involved determining the image parameters of each camera, as well as their relative position and orientation to one another. The camera calibration process should be repeated whenever the camera is relocated or when any of the settings are altered, such as focus or aperture. Calibration requires capturing images of the calibration target from different viewing angles. The calibration target is recommended to be similar in size to the specimen to be measured and placed in the same position as the specimen. Multiple images of the calibration target must be recorded at different angles and inclinations at the specimen position during calibration. Camera calibration is the procedure of determining the parameters between a lens and an image sensor of an imaging camera. The purpose of stereo DIC calibration is to determine the intrinsic camera parameters, such as image scale, focal length, image centre and lens distortion, as well as the extrinsic parameters of the stereo DIC system, such as stereo angle, distance between the cameras and distance from the cameras to the object. These parameters are used to correct lens distortion, measure object size, and determine camera location in the scene. The process of calibration comprised the following steps:

- The initial stage involved selecting a calibration target that is appropriately sized, either equal to or slightly smaller than the sample FOV.
- The following step involves creating a workspace for performing the calibration. The workspace must be spacious enough to hold, rotate, tilt, and translate the calibration target if required. For this particular task, a 9X12 2.50 mm calibration target was utilized.
- The next step is to adjust the lighting to ensure uniform contrast across the entire calibration target, without any glare in any direction or angle used by the calibration target. These settings must be consistent in both cameras for stereo DIC. The calibration target used in the calibration process for the four DIC tests is shown in Figure 4.31. Foi o mesmo calibration target usado para os provetes de 316L stainless steel.

- Image acquisition is carried out to ensure well-extracted resources throughout the optical system. The number of calibration images required or appropriate depends on the calibration target and the DIC software. The most suitable value for the number of images to error ratio is 150-200 images. Quality images are more important than a large number of images.

- All points in all images must be extracted. To validate the imposed settings, point detection must be performed on each image using image processing. A minimum of 80 points and a black and white threshold of 40 were used for point detection.

- The following step is to review the calibration results. Subsequently, examine the rejected images to determine if there was an apparent reason for the failure. It is crucial to confirm whether the accepted images that remain still occupy the working field of view of the optical system. Lastly, verify that the features extracted from the accepted images are accurate.

- Lastly, the calibration parameters are checked. The values of the calibration parameters are compared with the equivalent physical values. These parameters can include image centre, lens focal length, angles and the distance of two cameras. The results are shown in Figure 6.13.

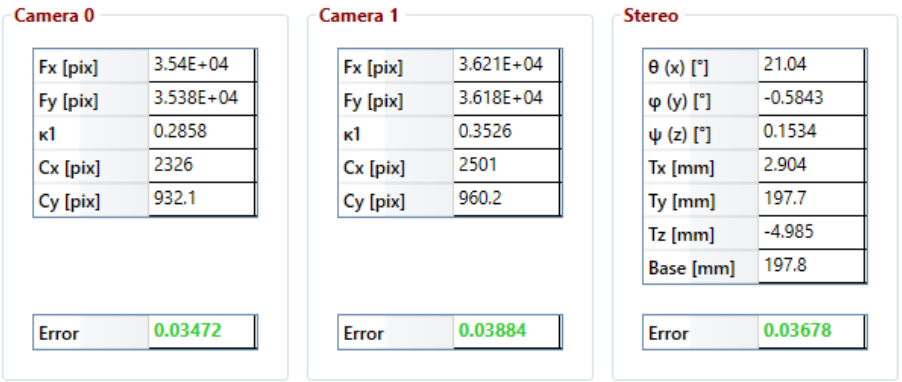

Figure 6.13: Calibration results of FGM samples.

The cameras have determined intrinsic properties, which include F_x, the focal length in the x-direction, F_y, the focal length in the y-direction, C_x, the principal point x-coordinate, C_y, the principal point y-coordinate, and K_1, the first-order radial distortion in the case of the radial/tangential distortion model. The extrinsic parameters of the stereo system include θ, the stereo angle around the x-axis; ϕ, the stereo angle around the y-axis; ϕ, the stereo angle around the z-axis; T_x [mm], the camera distance in the x-direction; T_y [mm], the camera distance in the y-direction; and T_z [mm], the camera distance in the z-direction.

6.3.4 Maximum Force

Four samples, including a pre-test sample and three samples made of the same material and geometry, were tested until failure. The maximum forces of the four specimens were very similar despite the different compositions of the two materials. Figure 6.14 illustrates the varying maximum forces of the four samples.

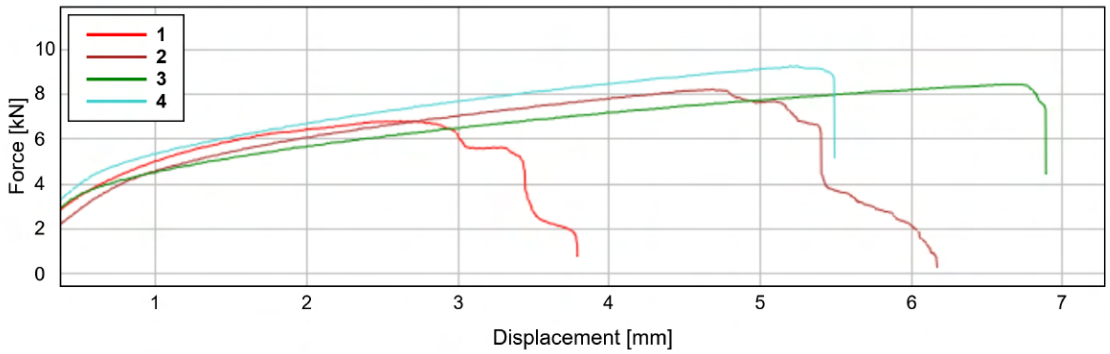

Figure 6.14: Maximum force until failure for the 4 specimens tested of FGM.

The graph compares the displacement in millimeters to the force required to be exerted on the specimens in kilonewtons. It displays four distinct curves: Curve 1 represents the pre-test specimen, while curves 2, 3, and 4 represent FGM specimens 1, 2, and 3. It is worth noting that the pre-test specimen exhibits different behavior from the others, as it did not undergo preheating between the two materials. It can be concluded that a specimen without preheating will fail earlier than a specimen with preheating for the same force value. The other three samples exhibit similar behavior, but the difference is due to the varying material content in the samples.

6.3.5 Noise evaluation

Before carrying out the DIC tensile test, it is essential to check the quality of the recorded images and evaluate the noise levels. 20 static images were captured before the start of the test, these images were then averaged to eliminate the noise, the static noise for each camera was calculated using MatchID. The quality of the captured images must be checked and their noise level assessed before the DIC test is performed. It was found that the noise was 0.01387 of the dynamic range for the sample-aligned camera. MatchID was used to calculate the average spot size for each sample. The lowest spot size obtained with an airbrush was approximately 6,6 pixels. Standard deviation of the selected DIC field variable gives the noise floor of the field variable. The grey level histogram for each pixel is shown in Figure 6.15.

Histograms should show good contrast, with different pixel intensities clearly distinguishable, and should cover all ranges of pixel intensities present in the image. Saturation at the extremes of the histogram should be avoided. An excess of pixels at one or both ends of the histogram may indicate a loss of information in areas of extremely high or

Figure 6.15: Gray level histogram for each pixel.

extremely low brightness in the image. By analysing the histogram, it can be concluded that this is a well-balanced and representative distribution of intensities among the pixels of the image.

6.3.6 Results

The process of analyzing the results is similar to that already conveyed in section 4.6.2. In these results, only 2 specimens will be shown, the pre-test, as it is different from the others. And only one of the three remaining specimens will be shown, as they are all very similar, and their results are identical. The first step is to define the ROI of the analysis. There is no need to analyse the entire FOV as the area further away from the notches shows similar behaviour.

The workflow carried out in these tests was as follows:

- Stereo MatchID was used to process the images captured during the test.
- First, it is necessary to load a reference image taken before the start of the test. It is also necessary to select the deformed images from the test that we want to analyse.
- It is then necessary to load two files acquired during the tensile test, the calibration parameters file generated by MatchID Calibration and the acquisition data file generated by the MatchID Grabber.
- The next step is to define the ROI (region of interest). The ROI is defined to show the area of the notch and some of the uniform area of the sample.
- The next step is to change the default settings, such as step and subset size.
- Finally, correlation can be performed by calculating the strains from the displacements recorded by the images during the test.

In this segment the results of the pre-test are shown. The horizontal displacements show that the x-axis displacement occurs according to the loading, from left to right, so the results are as expected. Displacements in z, the W component of the stress test, can be measured through the use of stereo DIC. It can be seen that there are practically no displacements, which is consistent with the test performed.

Figure 6.16 shows 4 frames of the tensile test for global strain fields in the xx direction. It can be seen that the layers of the Cu-Al alloy material are the first to show some deformation during the test, mainly in the notch area.

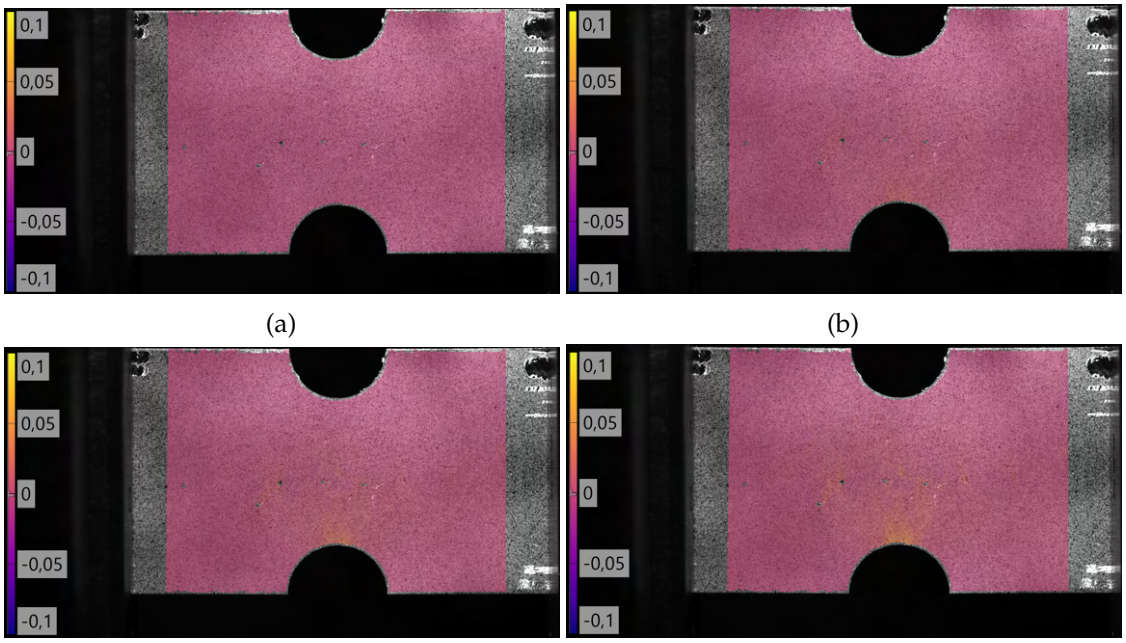

(a) (b)

(c) (d)

Figure 6.16: Global strain fields for specimen in the xx direction, ε_{xx}, for pretest Cu-CuAl alloy FGM stepwise specimen: (a) 0KN, (b) 3KN, (c) 4KN and (d) 5KN.

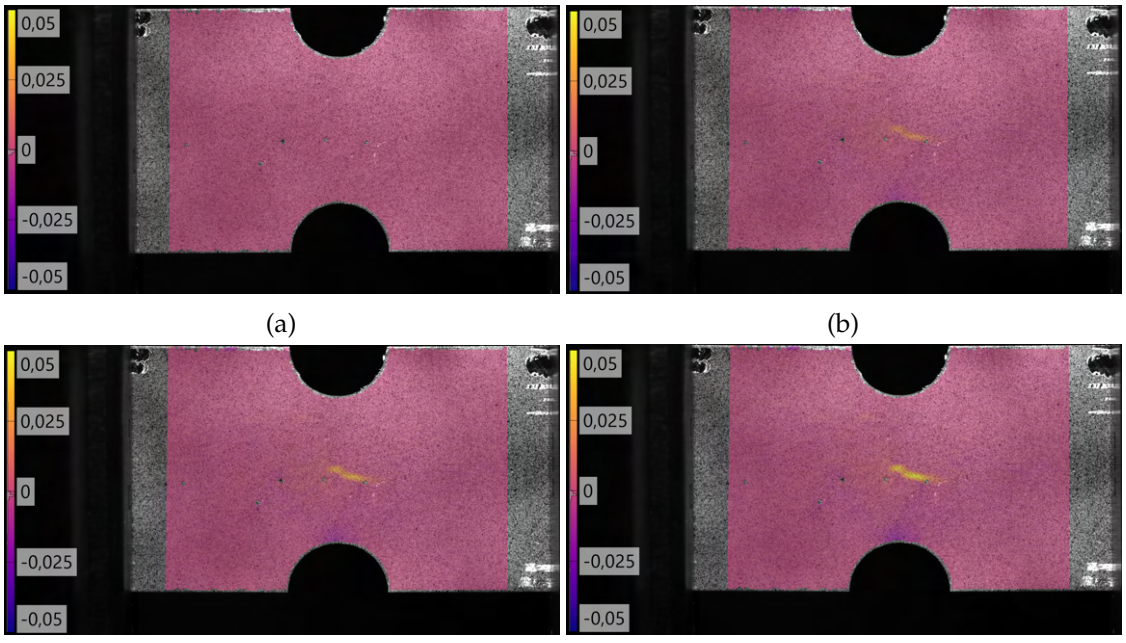

(a) (b)

(c) (d)

Figure 6.17: Global strain fields for specimen in the yy direction, ε_{yy}, for pretest Cu-CuAl alloy FGM stepwise specimen: (a) 0KN, (b) 4KN, (c) 4.5KN and (d) 5KN.

Figure 6.17 shows 4 frames of the stress test for the global strain fields in the yy direction. These maps show the area where the test piece will fracture, the transition zone from one material to the other, since this area has not had preheating, it becomes a brittle area.

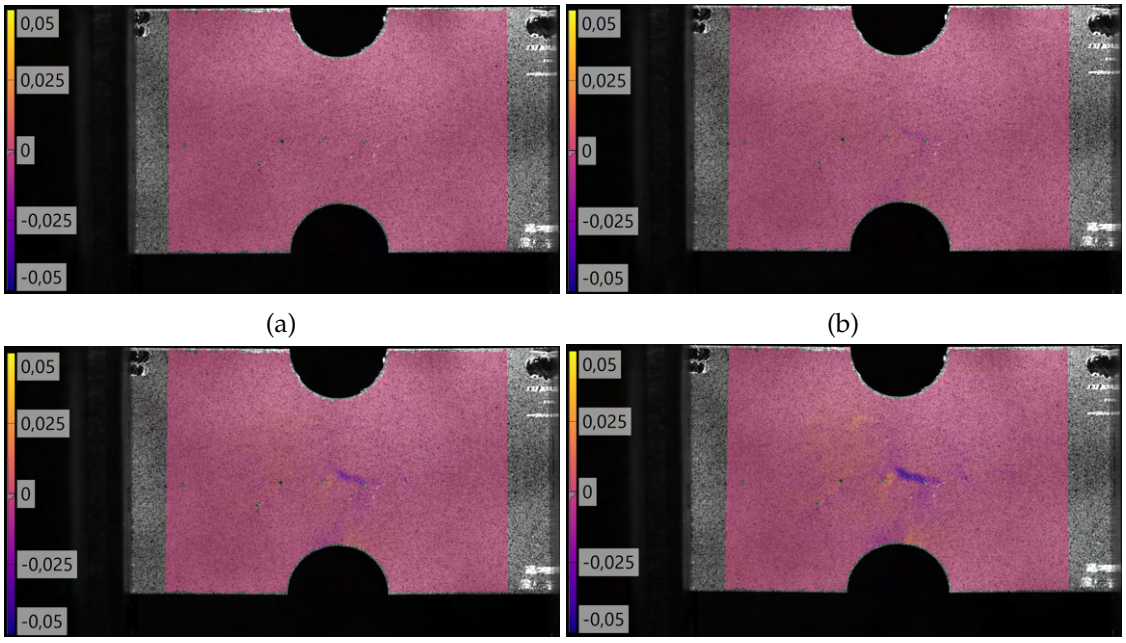

Figure 6.18: Global strain fields for specimen in the xy direction, ε_{xy}, for pretest Cu-CuAl alloy FGM stepwise specimen: (a) 0KN, (b) 4KN, (c) 4.5KN and (d) 5KN.

Figure 6.18 shows 4 frames of the stress test for the global strain fields in the xy direction. In these maps it is possible to verify that the central zone (transition zone), which is in purple, is the area where the specimen will fracture. It is also possible to observe that the CuAl layers are in the process of deformation.

The results of one of the specimens are presented in this segment of the report. The displacements in the xx direction demonstrate what is expected, that the displacement occurs from right to left, which is the direction of the load applied in the test. The frames of the W-component, the displacements in the z direction. It is only possible to determine these displacements because the stereo DIC technique was used. The results show that there are practically no displacements in the z direction, as would be expected in a test running in the xx direction.

Figure 6.19 shows 6 frames taken during the test to measure the global strain in the xx direction. It can be seen that in frame (c) the CuAl alloy is the first material to deform. In frame (d) we can see that the copper layers start to deform. In frame (f) it can be seen that the deformation of the specimen is greater in the CuAl alloy layers than in the copper layers.

Figure 6.20 shows the global strain fields for the specimens in the yy direction. The 6 frames chosen show that there is a little bending of the specimen over time, since the

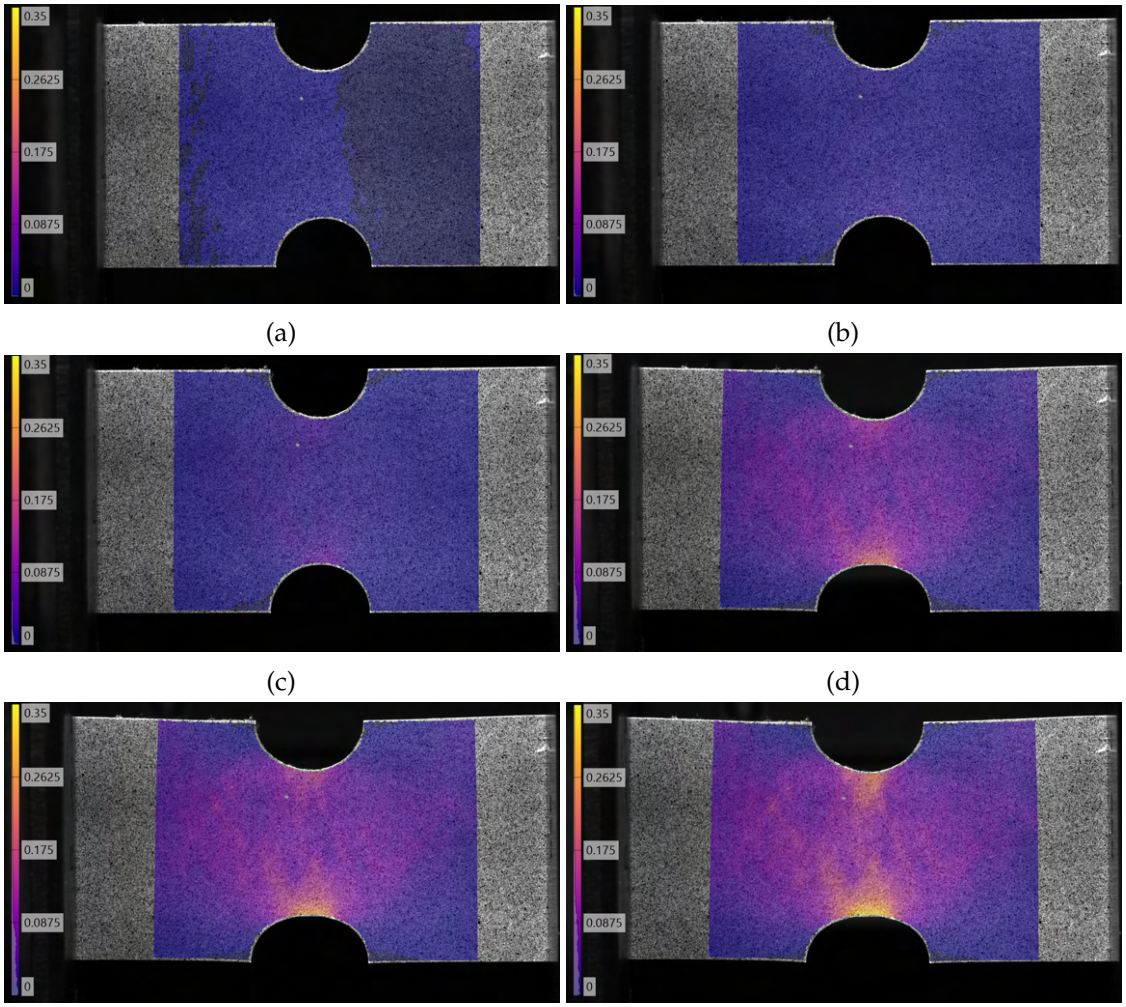

Figure 6.19: Global strain fields for specimen in the xx direction, ε_{xx}, for pretest Cu-CuAl alloy FGM stepwise specimen: (a) 0KN, (b) 1KN, (c) 2KN, (d) 2.5KN, (e) 3.5KN and (f) 4KN.

CuAl layers show deformation before the copper layers.

Figure 6.21 shows 6 frames taken during the test to measure the global strain in the xy direction. In these frames it is possible to observe the areas of the specimen where fracture will occur (darker areas) and which area will fracture first (the densest area).

6.4 Inverse identification through synthetic data by Virtual fields method

The FGM specimens are heterogeneous materials, it is not possible to use the VFM module of the MatchID software to perform the reverse identification of these specimens. The data used in this inverse identification comes from the finite element analysis in Section 6.2. The first step of inverse identification by VFM is to identify the FE nodes and element

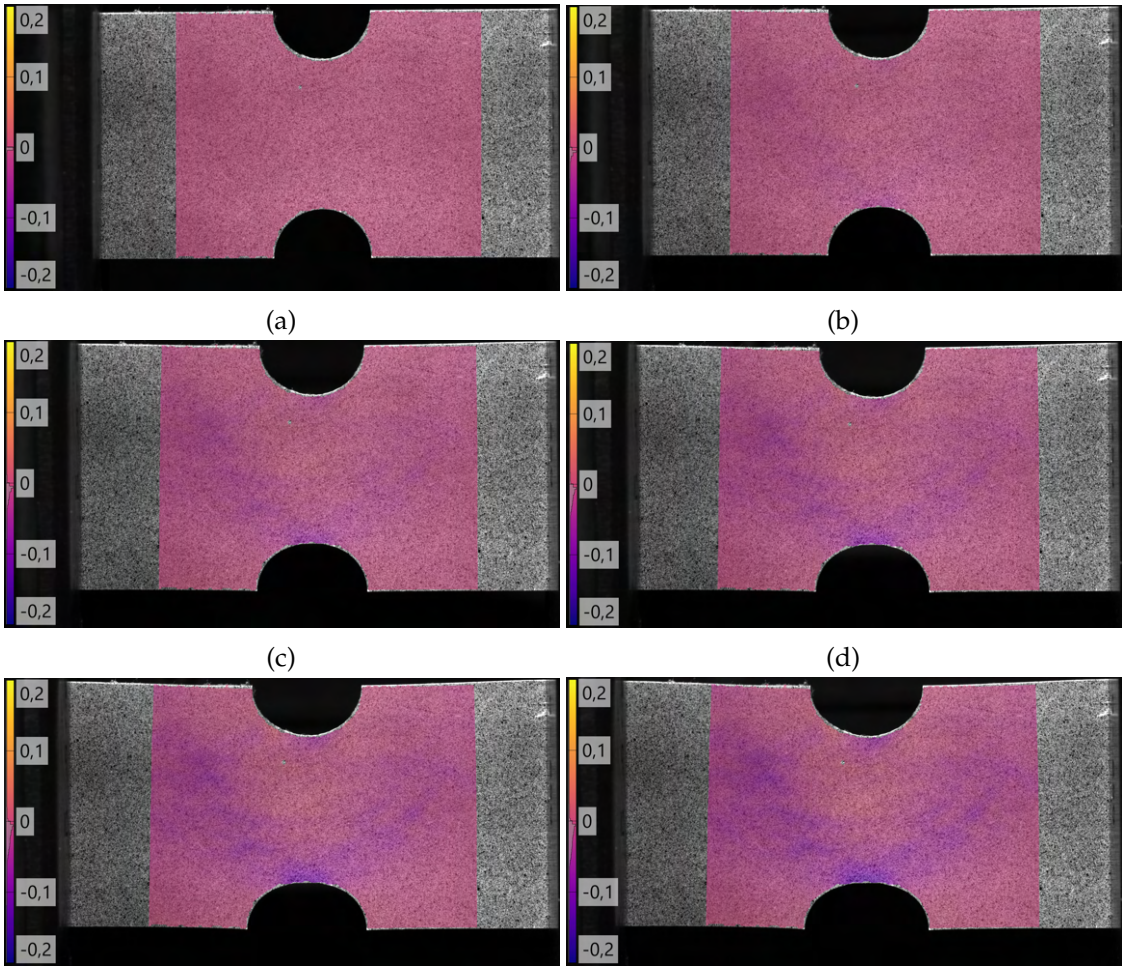

Figure 6.20: Global strain fields for specimen in the yy direction, ε_{yy}, for pretest Cu-CuAl alloy FGM stepwise specimen: (a) 0KN, (b) 5.6KN, (c) 6.7KN, (d) 7KN, (e) 7.7KN and (f) 8.2KN.

centroids. In this FEA, quadrilateral elements were used, so in each element there are 4 nodes. Figure 6.22 shows the element nodes and their centroids.

The next step is to create a regular grid across the entire specimen. Figure 6.23 displays FE nodes, centroid elements, and the created regular grid.

The next step is to identify the boundary nodes. Here all nodes belonging to the ends of the specimen are identified. Figure 6.24 shows all the nodes identified in the specimen and the nodes identified at the ends.

The next step is to identify the boundary nodes. Here all nodes belonging to the ends of the specimen are identified. Figure 6.24 shows all the nodes identified in the specimen and the nodes identified at the ends.

Then, a regular grid data was determined from the date from Figure 6.25. Therefore, Figure 6.26 shows regular grid data without nan values.

Finally, from the regular grid of Figure 6.26 it was possible to define data with a regular

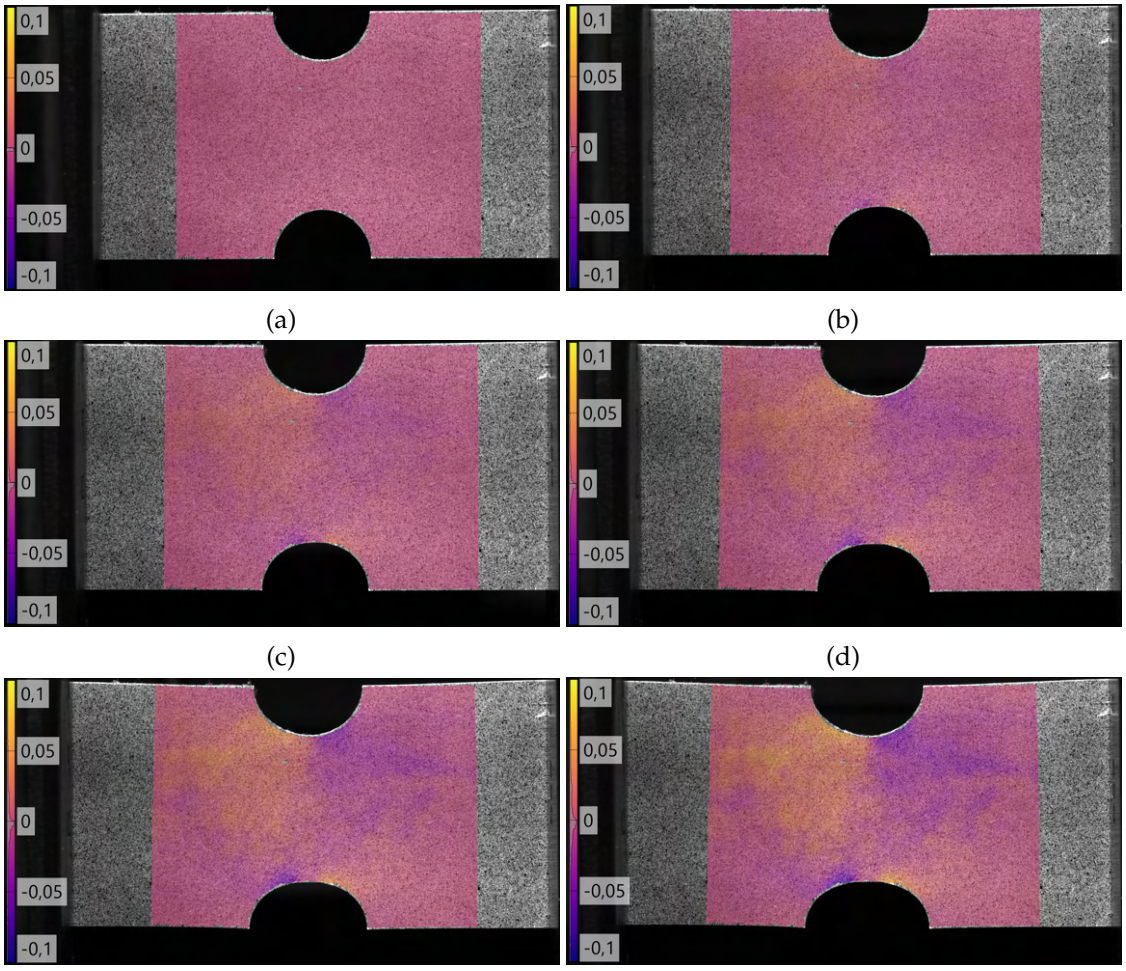

Figure 6.21: Global strain fields for specimen in the xy direction, ε_{xy}, for pretest Cu-CuAl alloy FGM stepwise specimen: (a) 0KN, (b) 5.5KN, (c) 6KN, (d) 7KN, (e) 7.6KN and (f) 8.2KN.

grid with possible nan values to implement VFM.

The Poisson's ratio results (Table 6.3) obtained for the Cu, CuAl, and Cu-CuAl FGM samples show values of 0.0894 for pure copper, 0.3920 for the CuAl alloy, and 0.2407 for the gradient material. While the value for Cu is below the typical range for metals (typically between 0.2 and 0.5, with the typical value for copper being around 0.33), the value obtained for CuAl is within this range, indicating good transverse ductility for the alloy. The mean value of the FGMs, located between the extremes of the two constituents, confirms the effect of the functional gradient by combining distinct mechanical properties, thereby providing a gradual transition of stiffness and ductility across the sample. The proximity between the mean and median values across all regions serves to reinforce the homogeneity of the results and the reliability of the numerical simulation.

Table 6.4 presents the mean Young's modulus values for Cu (50.745 GPa), CuAl (115.149 GPa), and the functional gradient material Cu-CuAl (82.947 GPa), obtained by finite

Figure 6.22: FE Nodes and Element Centroids.

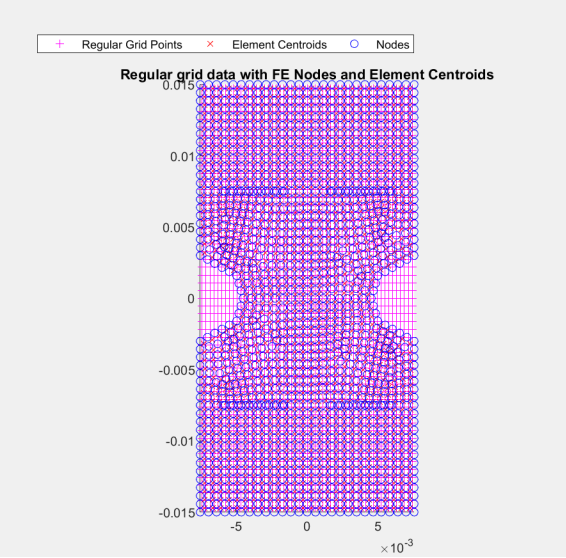

Figure 6.23: Regular grid data with FE Nodes and Element Centroids.

element analysis. By way of comparison, typical reference values for the Young's modulus of pure copper are around 110 GPa, while for the CuAl alloy it is usually close to 117 GPa. The discrepancy observed in the copper data can be ascribed to the mesh refinement in the model, which has a direct impact on the accuracy of the results, and to the consideration of specific material characteristics, such as microstructural heterogeneities or particular operating conditions. In order to enhance the correspondence between the simulated values and the reference values, it is recommended to increase the mesh refinement, particularly in regions exhibiting significant variations. Moreover, the application of model calibration with experimental data and the execution of sensitivity analyses to adjust critical material parameters are advised. These strategies facilitate enhanced fidelity in the representation of the material's actual behaviour without compromising

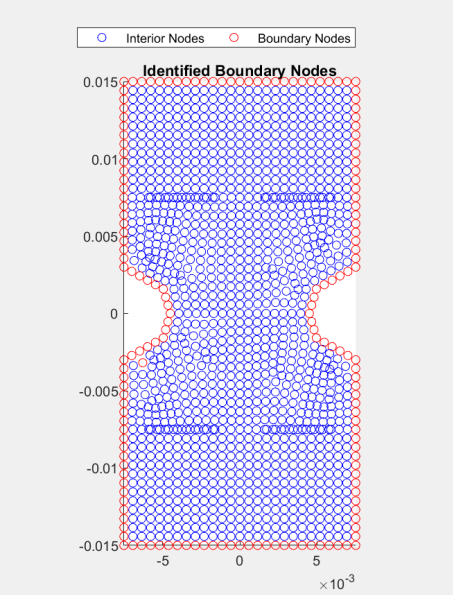

Figure 6.24: Identified Boundary Nodes.

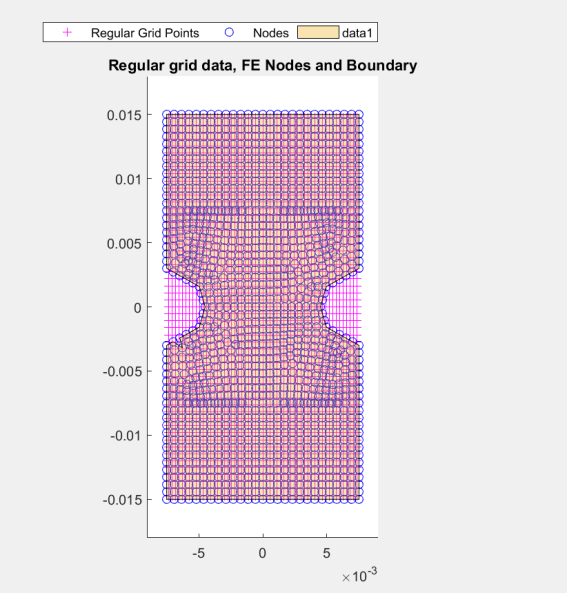

Figure 6.25: Regular grid data, FE Nodes and Boundary.

the model's robustness.

6.5 Inverse identification through full-field data by Virtual Fields Method

The Python code that has been implemented performs the experimental evaluation of the elastic properties (Young's modulus and Poisson's ratio) using the VFM directly from the experimental data of displacement (u, v) and force associated with time frames of a mechanical tensile test.

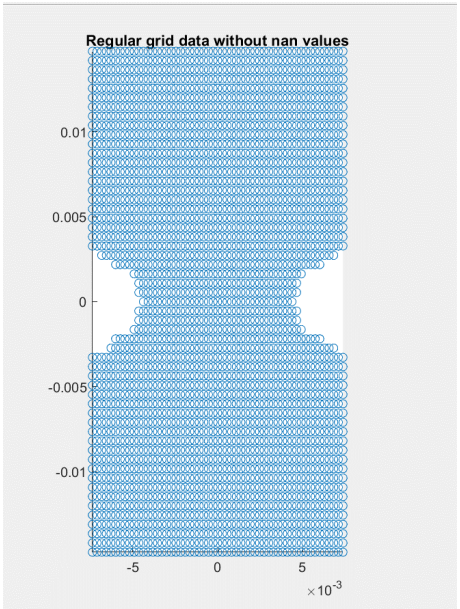

Figure 6.26: Regular grid data without nan values.

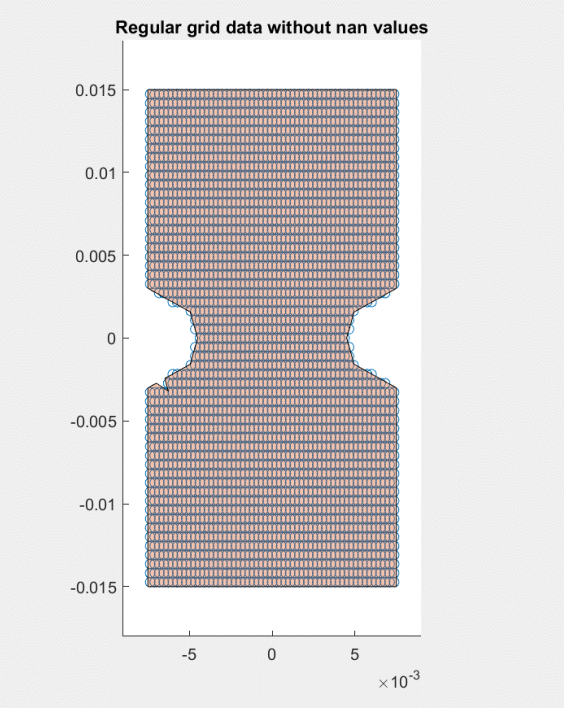

Figure 6.27: Regular grid data without nan values.

6.5.1 Code Organization and Data Structure

The implementation is organised around predefined configurations for different samples, where each configuration specifies:

- The input directories designated for displacement and coordinate fields are contained within folders labelled "u", "v", "ε_{xx}", "ε_{yy}", "x pic" and "y pic";

Table 6.3: Mean and median of Poisson coefficient for Cu-CuAl alloy FGMs stepwise specimens through finite element analysis.

	FEA
ν Cu (mean)	0,0894
ν Cu (median)	0,0894
ν CuAl (mean)	0,3920
ν CuAl (median)	0,3920
ν (mean)	0,2407
ν (median)	0,2407

Table 6.4: Mean of Young's module for Cu-CuAl alloy FGMs stepwise specimens through finite element analysis.

	FEA
E Cu (mean)	50,745 GPa
E CuAl (mean)	115,149 GPa
E (mean)	82,947 GPa

- File containing the force signal (force applied per frame);
- The following scale parameters are to be employed in order to convert pixel values to physical units (mm);
- The maximum number of frames to be processed, the standardisation of file names, and the use of suffixes for the identification of relevant files.

6.5.2 Data Location and Reading

The code locates the CSV files corresponding to the displacements, identifies their partner x and y coordinate files, and, when available, the experimentally derived stress fields. In instances where these are not present, the code employs the numerical derivative of the displacements to calculate the deformations, thereby ensuring flexibility in dealing with disparate levels of experimental data.

6.5.3 Region of Interest

In order to ensure the quality of the results, the code defines a spatial mask (ROI) that eliminates marginal areas affected by noise or discontinuities, based on relative edges in the coordinate domain. This procedure is undertaken to ensure that only reliable and representative data are used in the calculation of the method's integrals. The ROI used was 60% of the specimen.

6.5.4 Virtual Fields

The virtual fields implemented in the code are homogeneous uniform virtual deformation fields associated with uniaxial extension in the tensile direction. Denoting (x, y) the spatial coordinates, the virtual displacement fields u^* and the respective virtual deformations ε^* are defined by:

$$\text{Cu:} \quad \begin{cases} u_1^* = x \\ u_2^* = 0 \end{cases} \quad \text{and} \quad \begin{cases} \varepsilon_{11}^* = 1 \\ \varepsilon_{22}^* = 0 \\ \varepsilon_{12}^* = 0 \end{cases} \quad \text{CuAl:} \quad \begin{cases} u_1^* = -x \\ u_2^* = 0 \end{cases} \quad \text{and} \quad \begin{cases} \varepsilon_{11}^* = 1 \\ \varepsilon_{22}^* = 0 \\ \varepsilon_{12}^* = 0 \end{cases} \tag{6.1}$$

6.5.5 Constitutive Law

The constitutive law employed in the code is Hooke's law of isotropic linear elasticity in a plane state, which is appropriate for situations involving small displacements and deformations. This law describes the relationship between stresses and strains in materials using Young's modulus (E) and Poisson's ratio (ν).

The constitutive law used in matrix notation for the plane stress state is:

$$\begin{bmatrix} \sigma_{xx} \\ \sigma_{yy} \\ \sigma_{xy} \end{bmatrix} = \frac{E}{1-\nu^2} \begin{bmatrix} 1 & \nu & 0 \\ \nu & 1 & 0 \\ 0 & 0 & \frac{1-\nu}{2} \end{bmatrix} \begin{bmatrix} \varepsilon_{xx} \\ \varepsilon_{yy} \\ 2\varepsilon_{xy} \end{bmatrix} \tag{6.2}$$

This law is applied in the code, either directly or indirectly, by integrating the experimentally obtained (or numerically derived) deformation fields to calculate E and ν using the VFM methodology.

6.5.6 Calculation of Young's Modulus and Poisson's Ratio by VFM

At the core of the code, the calculation of Young's modulus (E) and Poisson's ratio (ν) uses the Virtual Field Method, which involves directly applying the Virtual Work Principle to linear, elastic, isotropic materials. The implemented procedure is detailed below:

For each test frame, the experimental deformation fields ε_{yy} and ε_{xx} are integrated into the Region of Interest (ROI):

$$S_{xx} = \int_A \varepsilon_{xx}\, dA \qquad S_{yy} = \int_A \varepsilon_{yy}\, dA \tag{6.3}$$

In the code, these integrals are calculated as discrete sums over the nodes of the mesh:

$$S_{xx} \approx \sum_{i,j} \varepsilon_{xx}^{(i,j)}\, \Delta x\, \Delta y \qquad S_{yy} \approx \sum_{i,j} \varepsilon_{yy}^{(i,j)}\, \Delta x\, \Delta y \tag{6.4}$$

Poisson's ratio is obtained from the ratio of the means of the integrated fields:

$$\nu = -\frac{\varepsilon_{yy}}{\varepsilon_{xx}} \tag{6.5}$$

This calculation is justified by the fact that Poisson's ratio expresses the relationship between axial (x) and transverse (y) deformations under uniaxial tension. The negative sign reflects typical transverse contraction behaviour.

Considering the equilibrium of virtual works and a linear elastic constitutive law, the following expression is used to calculate Young's modulus:

$$E = \frac{F \cdot L_x \left(1 - \nu^2\right)}{t \left(S_{xx} + \nu S_{yy}\right)} \tag{6.6}$$

Where: F is the applied force measured experimentally; L_x is the length of the region of interest in the loading direction (maximum x change); t is the thickness of the sample; S_{xx} and S_{yy} are the integrals of the deformations in the principal and transverse directions.

This expression is derived directly from the Virtual Work Principle, in which the external virtual work (given by the force applied to the virtual displacement) is equal to the internal virtual work (associated with the measured deformation fields) when the homogeneous virtual field is considered. The code performs these calculations for each frame, separating the 'top' and 'bottom' regions of the sample (e.g. Cu and CuAl). This makes it possible to analyse different layers or materials. All results are validated for data quality, stored and summarised into medians within the elastic zone of the curve. These steps faithfully translate VFM theory into an automated computational workflow, providing elastic parameters directly from experimental DIC and force data.

6.5.7 Frame Processing and Region Separation

In order to facilitate more precise characterisation, the code divides the sample into two primary regions, designated "top" (Cu) and "bottom" (CuAl), and undertakes independent calculations for these regions, taking into account specific masks within the ROI. This strategy facilitates the discernment of discrepancies in elastic behaviour between the composite layers. Furthermore, the processing is performed frame by frame to track the evolution of mechanical properties throughout the test, with the results stored in a CSV file for subsequent analysis.

6.5.8 Computational Robustness and Error Handling

During calculations, the code implements treatments to:

- Check data consistency, such as the existence of folders/files.
- Handle possible numerical errors, such as divisions by near zero and non-finite numbers (NaN, infinities).
- Exclude invalid tables from the overall statistical analysis.
- Summarize statistics based on the median, focusing on the elastic deformation zone (limit defined to avoid interference from plastic effects).

This implementation results in a robust automated tool for experimental elastic characterisation, utilising VFM principles directly on data obtained by field measurement techniques, with flexibility for partial data absence and the ability to discriminate between sample regions.

Table 6.5: Mean and median of Poisson coefficient for Cu-CuAl alloy FGMs stepwise specimens through engineering data.

	Specimen 1	**Specimen 2**	**Specimen 3**
ν Cu (mean)	0,2520	0,2864	0,3664
ν Cu (median)	0,2781	0,3385	0,4590
ν CuAl (mean)	0,3374	0,2979	0,4139
ν CuAl (median)	0,3991	0,3721	0,4631
ν (mean)	0,3055	0,2838	0,3853
ν (median)	0,3413	0,3520	0,4602

As illustrated in Table 6.5, the mean and median Poisson's ratio values for Cu and CuAl in three distinct specimens have been determined using experimental engineering data. The values for copper range from 0.2520 to 0.3664 (mean), progressively approaching the reference value of 0.343 for this material, while for CuAl, the mean values range from 0.2979 to 0.4139, also close to the reference value of 0.34 for the alloy. The medians demonstrate a comparable trend, thus indicating the reliability of the experimental results and underscoring the inherent variations between the diverse samples. The experimental values obtained in this study demonstrate a strong correlation with the existing literature, contradicting the significantly lower results obtained through numerical analysis, as previously observed. The importance of validating simulation models through reliable practical tests is reinforced by this study.

Figure 6.28 presents the engineering stress-strain curves obtained for Samples I, II and III. This type of graph is employed to illustrate the material response to applied tensile loading, whereby engineering stress (force per unit area) is plotted on the vertical axis and engineering strain (deformation per unit length) on the horizontal axis. The engineering stress was calculated from the applied force measured directly by the tensile testing machine, using the initial cross-sectional area of each specimen. The engineering strain was determined from the recorded displacement during the test, which was then normalized by the initial gauge length. The length measurement was performed by measuring the displacement of the machine's crossbar. The resulting curves highlight the typical elastic-plastic behaviour of the material, with clear differences in yield strength, strain hardening, and ultimate tensile strength among the three specimens.

As illustrated in Table 6.6, the primary parameters derived from the tensile tests conducted on the three samples are succinctly summarised. The initial gauge length L_0 is found to be consistent across the specimens, ranging from 30 to 32 millimetres. The quantity of data points that were documented was measured and recorded, that is

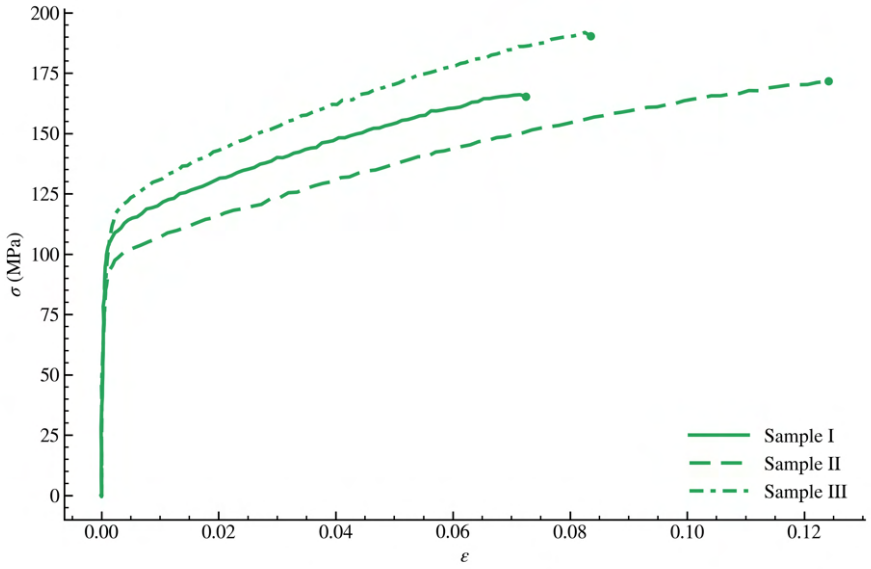

Figure 6.28: Engineering stress-strain curve for the Cu-CuAl alloy FGM stepwise specimens.

Table 6.6: Summary of tensile test engineering parameters and Young's modulus for the three Cu-CuAl alloy FGM stepwise specimens.

Sample	**Number of points**	L_0 **(mm)**	**Young's modulus** E **(GPa)**
Sample I	149	31	84.9
Sample II	118	30	68.5
Sample III	138	32	81.3

indicative of the resolution of the acquisition during the testing phase. The calculated Young's modulus values demonstrate some variation between the samples. Sample II exhibits the lowest stiffness (around 68.2GPa). The samples I and III present higher values (85 GPa and 81.3GPa). These differences are indicative of slight variations in the specimens' elastic behaviour. It is important to note that the Young's modulus reported here was calculated from the slope of the linear elastic region of the engineering stress–strain curve. For the sake of reference, it should be noted that typical literature values are approximately 124 GPa for pure copper and 105 GPa for CuAl alloys, which are higher than the experimental results obtained in this study. This discrepancy may be attributed to experimental factors, such as specimen geometry, testing conditions, or measurement resolution.

The Figure 6.29 represents the stress-strain curves of the three samples that were tested, thereby highlighting the mechanical behaviour of the materials during the DIC tensile test. The vertical axis denotes the stress, measured in MPa, while the horizontal axis indicates the deformation, illustrating a continuous evolution as the load increases. The initial curves demonstrate a rapid rise, which characterises the elastic region. This is followed by a transition to the plastic regime, where the material progressively hardens until reaching

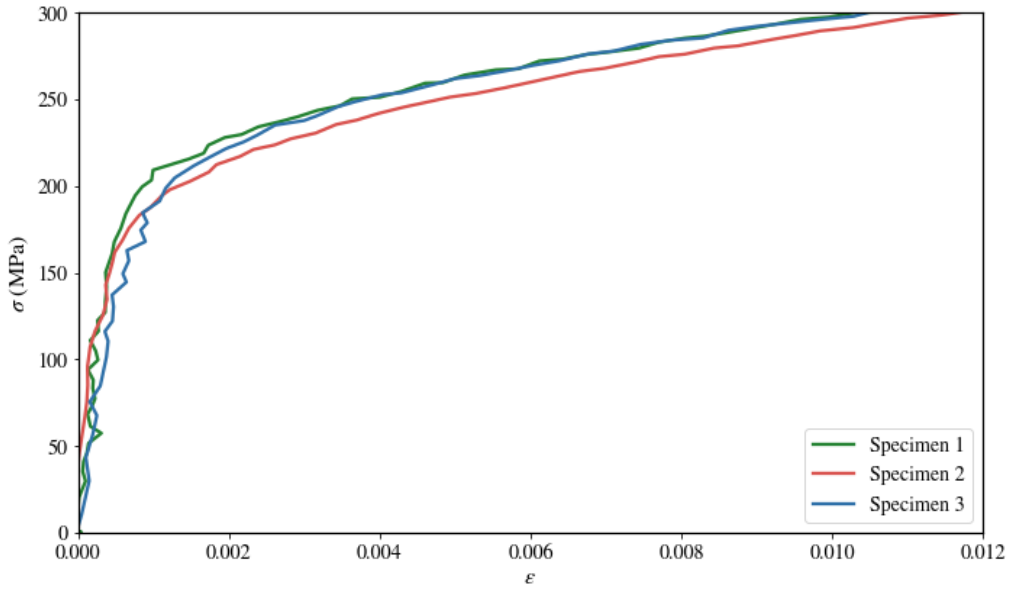

Figure 6.29: DIC stress-strain curve for the Cu-CuAl alloy FGM stepwise specimens.

values close to 300 MPa. Discrete differences between the specimens are indicative of structural variations or minor uncertainties in the experimental process. However, the high resolution of the DIC method, when coupled with the test, enables the accurate analysis of these discrepancies.

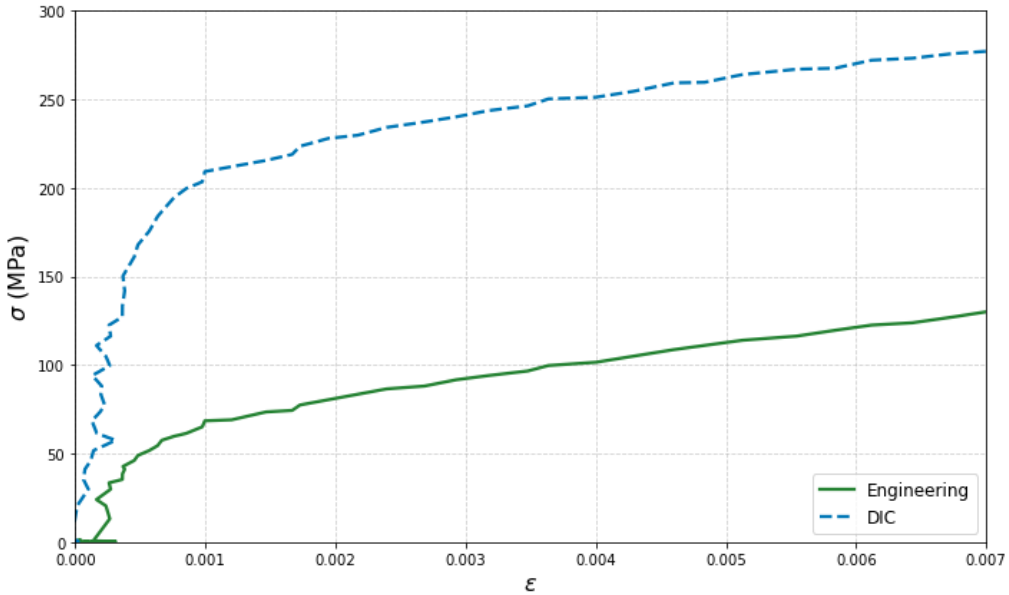

Figure 6.30: Comparison between stress strain curves for Cu-CuAl FGM stepwise specimen 1.

Figure 6.30 presents a direct comparison between the stress-strain curves obtained by the traditional engineering method and the DIC method. As is evident in the figure, the DIC curve (blue line) demonstrates markedly elevated stress values for equivalent strains

in comparison to the engineering curve (green line). This discrepancy can be attributed to the methodology employed in measuring the strain. Specifically, the engineering method utilises a global strain measurement based on initial extension, whereas the Digital Image Correlation (DIC) method captures local, real strain. It is noteworthy that the DIC approach typically yields higher strain measurements due to its ability to detect local concentrations and the material's evolution during the testing process. The comparison demonstrates the significance of DIC for conducting detailed and realistic analyses of the mechanical behaviour of materials, thereby emphasising the limitations of conventional engineering measurements.

Table 6.7: Mean of Poisson coefficient for Cu-CuAl alloy FGMs stepwise specimens through DIC data.

	Specimen 1	**Specimen 2**	**Specimen 3**
ν Cu (mean)	0,4900	0,2032	0,2032
ν CuAl (mean)	0,4038	0,1566	0,1128
ν (mean)	0,4469	0,1799	0,2394

Table 6.7 shows the mean of Poisson coefficient for Cu-CuAl alloy FGMs stepwise specimens through DIC data. The mean values of the Poisson's ratio for the Cu-CuAl alloy specimens indicate that the Cu region presents results that are relatively close to the expected reference value (0.343), especially for Specimen 1 and, to a lesser extent, for Specimen 3. However, for the CuAl region, the mean values are systematically lower than the reference value (0.34), particularly for Specimens 2 and 3. This suggests that there may be factors influencing the measurement, such as local heterogeneities in the material, limitations in the region of interest considered, or experimental variations. These disparities underscore the necessity of conducting a distinct evaluation of the mechanical properties in each region of the functional gradient material to ensure comprehensive characterisation. It is evident that adjustments to the calculation method and refinement in the selection of the analysed region can contribute to a better approximation of the measured values to the actual reference values.

Table 6.8: Mean and median of Young Modulus for Cu-CuAl alloy FGMs stepwise specimens through DIC data.

	Specimen 1	**Specimen 2**	**Specimen 3**
E Cu (mean)	61.337	37.277	87.011
E CuAl (mean)	124.284	141.115	111.501
E (mean)	93.662	89.196	99.256

Table 6.8 displays the mean Young's modulus values for copper and CuAl, as determined by the DIC method on three specimens. This facilitates a comparison with the reference values of 110 GPa for copper and 117 GPa for CuAl. It is evident from the

experimental results for Cu that the values are substantially below the reference value, ranging from 37,277 GPa to 87,011 GPa. In the case of CuAl, the values approach and even slightly exceed the reference parameter, ranging from 111,501 GPa to 141,115 GPa. These variations suggest that the specimen manufacturing processes or specific characteristics of the DIC measurement can significantly influence the obtained elastic modulus. This highlights the importance of experimental considerations and applied operations in the effective characterisation of the mechanical properties of materials.

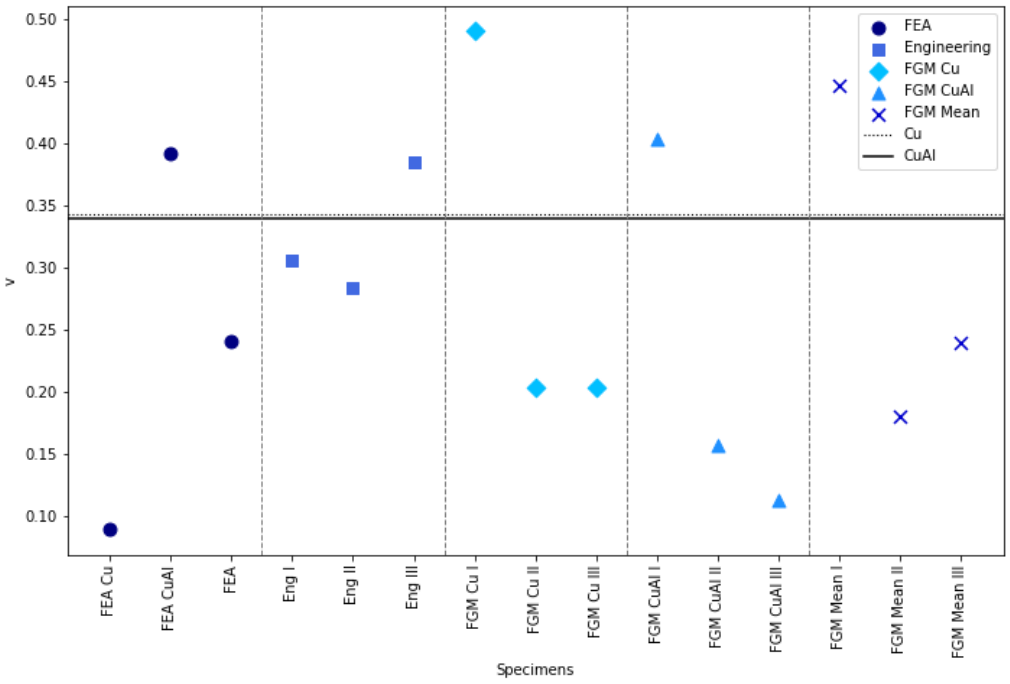

Figure 6.31: Comparison of ν from FEA, engineering and DIC values.

Figure 6.31 illustrates that the value of "v" (presumably Poisson's ratio) varies considerably between the various groups of materials and methodologies that were examined. FEA specimens manifest a distribution of values across two discrete regions, while engineering specimens demonstrate a modest and more consistent growth trend across the various tests. Conversely, FGM Cu, notably FGM CuAl and FGM Mean, exhibited lower values compared to the Cu and CuAl references, accompanied by significant dispersion. This finding suggests that functional gradients can induce properties that are, on occasion, inferior to those exhibited by pure metals. This finding suggests a strong influence of composition and manufacturing process on the observed behaviour of FGM materials. It is indicated that optimising these parameters may be essential to achieving the desired properties.

Figure 6.32 presents the elastic modulus values (E) (in GPa) for various specimens categorised into experimental groups: The following materials are to be considered: FEA, Engineering, FGM Cu, FGM CuAl, and FGM Mean. Along the x-axis, each specimen is identified, with the groups visually separated by dotted vertical lines, facilitating

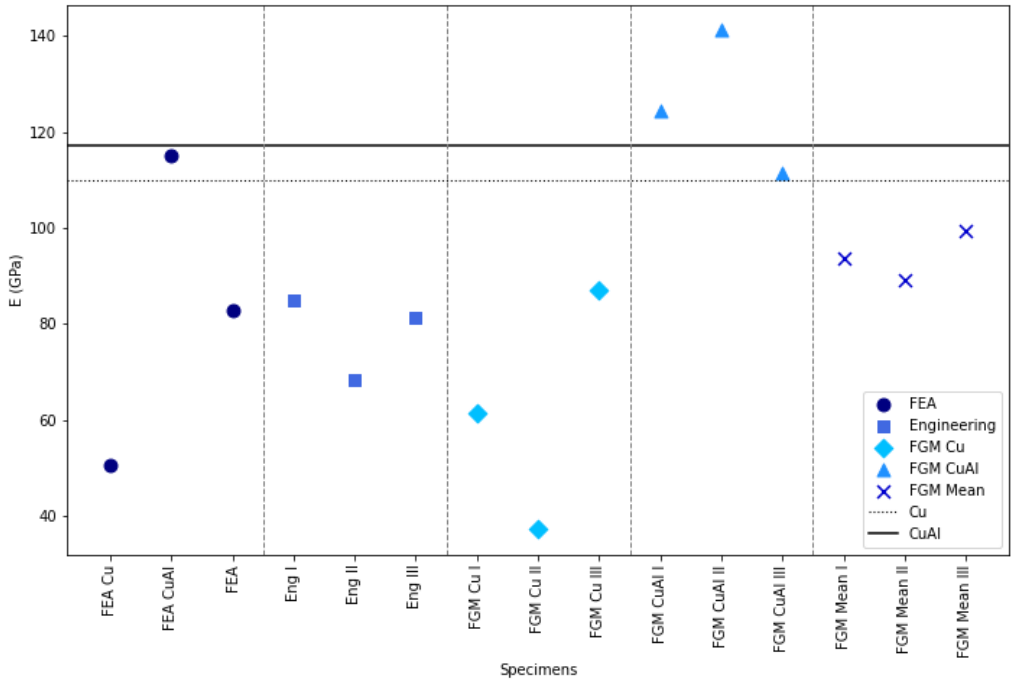

Figure 6.32: Comparison of E from FEA, engineering and DIC values.

distinction between families. The specimens in the FGM CuAl group demonstrate the highest E values, distinctly exceeding those of the other groups. The FEA and Engineering groups exhibit intermediate values, while the FGM Mean group approaches lower values. Horizontal lines serve as references for the moduli of pure Cu and CuAl, thus enabling a direct comparison of the results obtained with the materials and processes tested with the values of the reference metals. This highlights the relative efficiency of FGMs compared to traditional materials. The legend provides clear identification of the markers and colours for each group, thereby establishing a clear link between the data series and their respective samples or methodologies.

6.6 Conclusion

This chapter opened with an examination of the tests to be created using the finite element method. Subsequently, a comprehensive account of the experimental tests conducted on the specimens was provided, including the tensile test procedure, the DIC process, calibration, maximum force, noise evaluation and the corresponding results. Finally, two reverse identifications were conducted using the VFM method: one with synthetic data and the other with full-field data. The mechanical properties of the Cu-CuAl composite material in FGMs were evaluated by different methods, showing significant variations. FEA demonstrated average Poisson's ratios of 0.089 for copper and 0.392 for CuAl, with an overall mean value of 0.241. In contrast, experimental engineering data indicated Poisson's ratios for copper ranging from 0.252 to 0.366 and for CuAl between 0.297 and

0.414. The results obtained by DIC revealed more variable values, with copper ranging from 0.203 to 0.490 and CuAl between 0.112 and 0.403, suggesting local heterogeneities. With regard to Young's modulus, FEA indicated average values of 50.7 GPa for copper and 115.1 GPa for CuAl, while tensile tests yielded values between 68.5 and 84.9 GPa for the samples. The DIC method revealed higher values, reaching 141.1 GPa for CuAl, and overall average values between 89.2 and 99.3 GPa. These discrepancies underscore the potential limitations of FEA in capturing certain properties, while experimental methods offer a more comprehensive depiction of microstructural and regional variations. In order to ensure reliable material performance, it is recommended that analytical models be validated with experimental data, taking advantage of the spatial detail provided by DIC. This integrated approach is imperative for the optimised development of Cu-CuAl FGMs in engineering applications.

7

Cu-CuAl alloy FGM continuous

7.1 Introduction

This chapter delineates the study of Cu-CuAl alloy FGM with a continuous transition zone. The present chapter will proceed with a finite element analysis of the tests. In the following section, a detailed description of the experimental tests conducted on the specimens is provided. This description encompasses the tensile test procedure, the DIC method, the calibration process, the maximum force evaluation, the noise analysis, and the resulting outcomes. In conclusion, two reverse identifications will be conducted using VFM, with one employing synthetic images and the other utilising full-field data.

7.2 Finite element analysis

As outlined in Section 6.2, a finite element model was constructed in this section. FEA enables a virtual approach to the optimisation of the design of a digital twin and/or mechanical test, without compromising the downtime and resources typically associated with traditional test and error methods of developing physical prototypes. The FE model was created with the use of ANSYS Mechanical APDL v25.2. In this model, the geometry employed was identical to that utilised in Section 6.2. In accordance with the approach outlined in Section 6.2 the following code writing process was adopted in order to facilitate the resolution of the static analysis problem under consideration:

- Initially, the model parameters were specified, including the length of the specimen (L = 54 mm), width (W = 25 mm), and thickness (T = 1 mm), along with the notch radius (R = 3 mm), as illustrated in Figure 4.20;
- Subsequently, the material properties were specified, namely Young's modulus, Poisson's ratio, tangent modulus, and yield stress. The spatial distribution follows that shown in Figure 6.1, with a transition zone measuring 7 mm;
- The finite element mesh was generated with an element size of 0.5 mm, and the prescribed displacement in the y-direction was set to $U_y = 1mm$. The selected

element size resulted from a mesh convergence study while also considering the maximum number of elements allowed in the student version of Ansys;

- It is worth noting that the element types PLANE182 and PLANE183 include specific key options. In this study, the selected settings were: (i) a quadrilateral element shape; (ii) plane stress with thickness behaviour; and (iii) a pure displacement element formulation;

- The cross-sectional properties of the elements were defined through the specification of real constants, with the specimen thickness set to 1 mm;

- The model was assigned material properties for Young's modulus and Poisson's ratio for both materials. Bilinear isotropic hardening was adopted, combined with either von Mises or Hill yield criteria, to simulate the plastic behaviour of the material under investigation;

- The specimen geometry was defined using keypoints, arcs, and areas, with material properties subsequently assigned to the corresponding regions. As shown in Figure 7.1, the material distribution comprises material 1 (blue) and material 2 (purple), representing copper and a CuAl alloy, respectively. In this configuration, the transition zone spans approximately one-third of the specimen's total width;

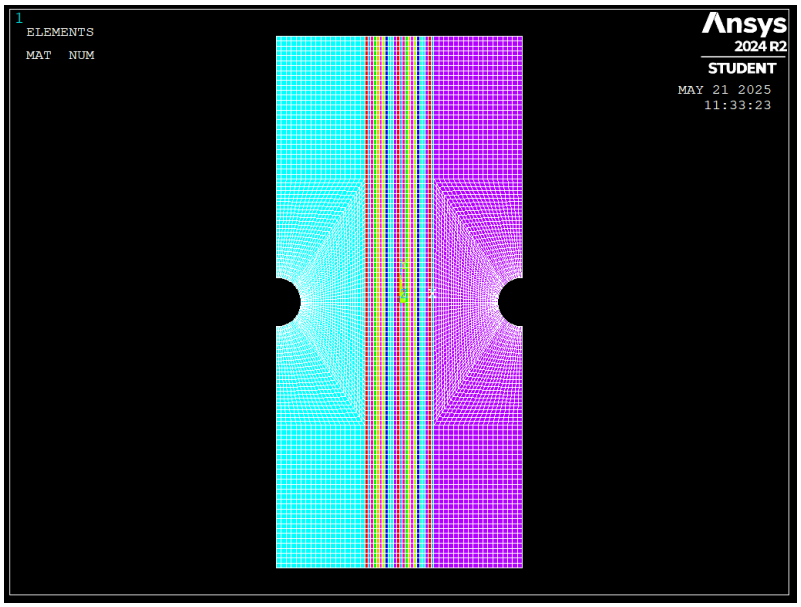

Figure 7.1: Cu-CuAl alloy FGM continuous (transition zone equal to 7 mm) scheme for attributing the two FGM materials to the defined areas: 1 (blue)- Copper and 2(purple)-CuAl alloy.

- This stage comprises the meshing and merging operations. The mesh configuration depends on the selected element size and shape. Figure 7.2 presents the resulting mesh, consisting of 86 800 elements;

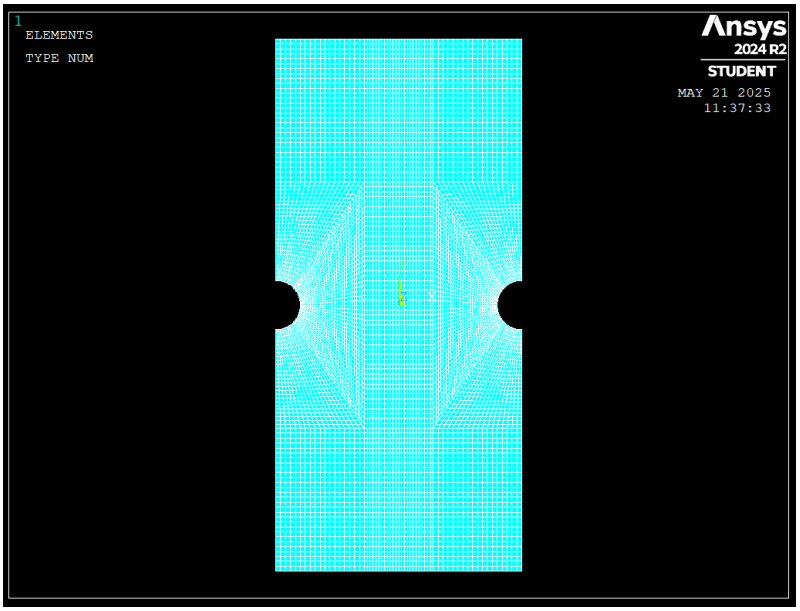

Figure 7.2: Meshing of Cu-CuAl alloy FGM continuous (transition zone equal to 7 mm) specimen used for the Ansys model.

- The solution was carried out through static analysis. The boundary conditions were defined as follows: (i) a prescribed displacement in the y-direction on the free surface of the specimen, and (ii) a fixed support on the opposite surface, constraining displacements in both the x and y directions.

Figure 7.3 presents the nodal solution for the x-component of the displacement in Ansys. The specimen exhibits behaviour consistent with that observed for the Cu–CuAl FGM stepwise configuration. Therefore, it can be inferred that variations in the transition zone do not influence the displacement in the x-direction.

Figure 7.4 presents the nodal solution for the y-component of the displacement in Ansys. The specimen exhibits behaviour similar to that of the Cu–CuAl FGM stepwise configuration. Consequently, it can be concluded that variations in the transition zone do not affect the displacement in the x-direction.

Figure 7.5 presents the stress distribution for the x-component of the FGM specimen. A comparative analysis between the Cu–CuAl FGM stepwise and continuous configurations indicates that increasing the transition zone width results in higher stress levels, particularly in the vicinity of the notch region within the copper material.

Figure 7.6 presents the stress distribution for the y-component of the FGM specimen. A comparative analysis between the stepwise and continuous Cu–CuAl configurations shows that an enlarged transition zone leads to increased stress levels, particularly in the notch region within the CuAl alloy section.

Consistent with the behaviour observed in the Cu–CuAl alloy FGM stepwise specimen, the continuous configuration also exhibits the highest stress concentrations in the notch regions. The results indicate that the copper side of the specimen experiences both

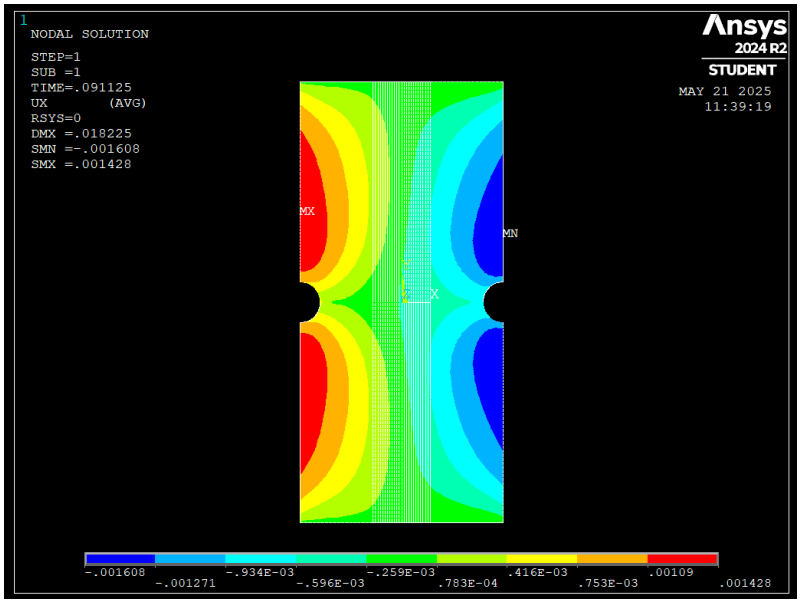

Figure 7.3: Cu-CuAl alloy FGM continuous (transition zone equal to 7 mm) specimen DOF Solution: X-Component of displacement on nodal solution in ANSYS.

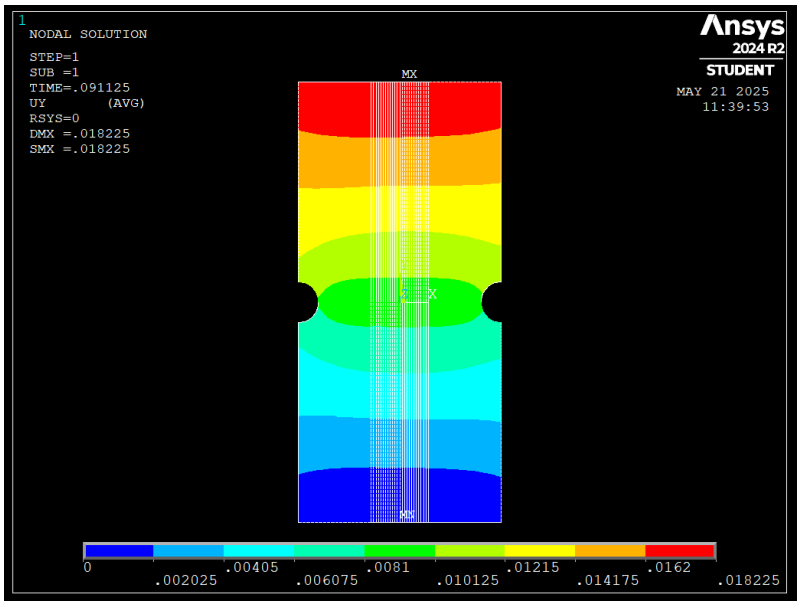

Figure 7.4: Cu-CuAl alloy FGM continuous (transition zone equal to 7 mm) specimen DOF Solution: Y-Component of displacement on nodal solution in ANSYS.

the maximum and minimum normal stresses, confirming it as the primary locus of deformation and the most likely site for fracture initiation. Figure 7.7 presents the elastic strain distribution for the x-component of the FGM specimen. For the Cu–CuAl alloy FGM continuous configuration with a 7 mm transition zone, the strain distribution closely resembles that of the Cu–CuAl alloy FGM stepwise configuration with a 3 mm transition zone.

Figure 7.8 presents the elastic strain distribution for the y-component of the FGM

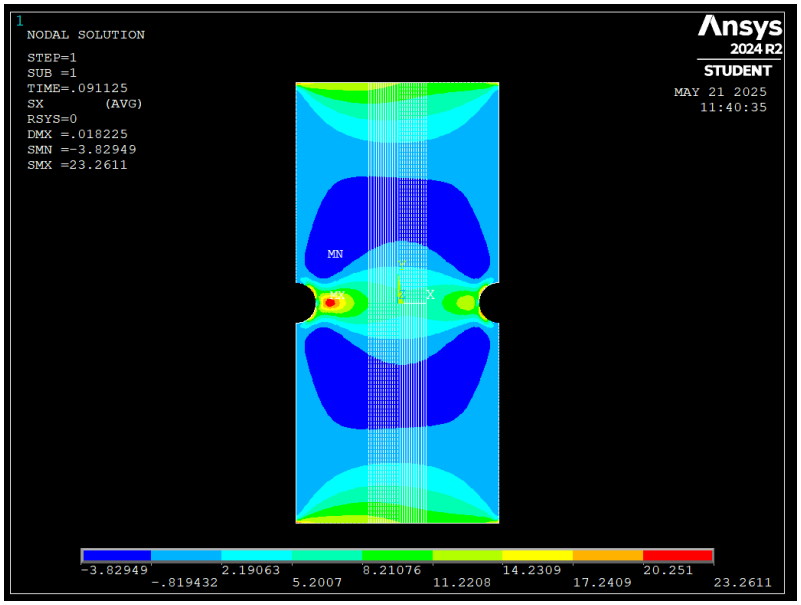

Figure 7.5: Contour plot of distribution of X-component of stress for Cu-CuAl alloy FGM continuous (transition zone equal to 7 mm) specimen.

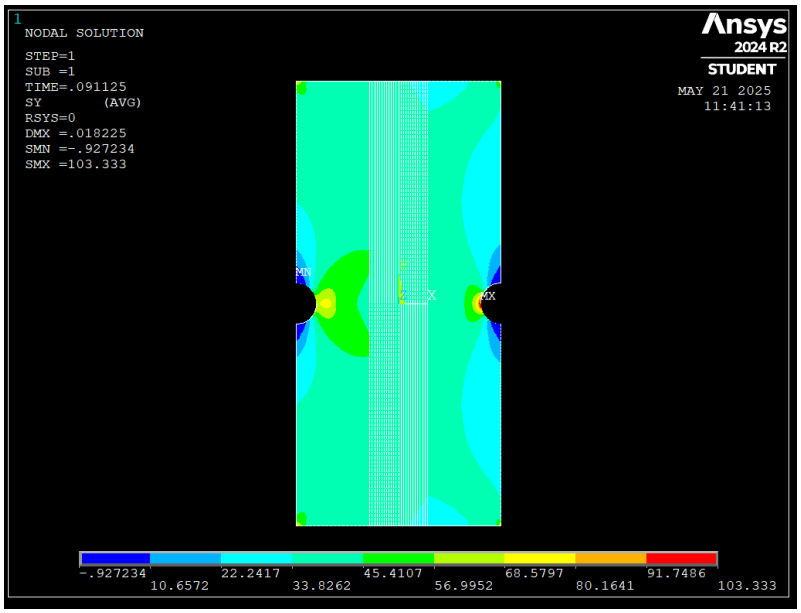

Figure 7.6: Contour plot of distribution of Y-component of stress for Cu-CuAl alloy FGM continuous (transition zone equal to 7 mm) specimen.

specimen. For the continuous Cu–CuAl configuration with a 7 mm transition zone, the strain distribution closely matches that of the stepwise Cu–CuAl configuration with a 3 mm transition zone.

In a tensile test, the elastic strain corresponds to the initial linear portion of the stress–strain curve. Literature reports a Young's modulus of 124 GPa for copper and a lower value of 105 GPa for the CuAl alloy. Consequently, the highest elastic strain is observed at the notch in the CuAl alloy, which undergoes deformation first due to its

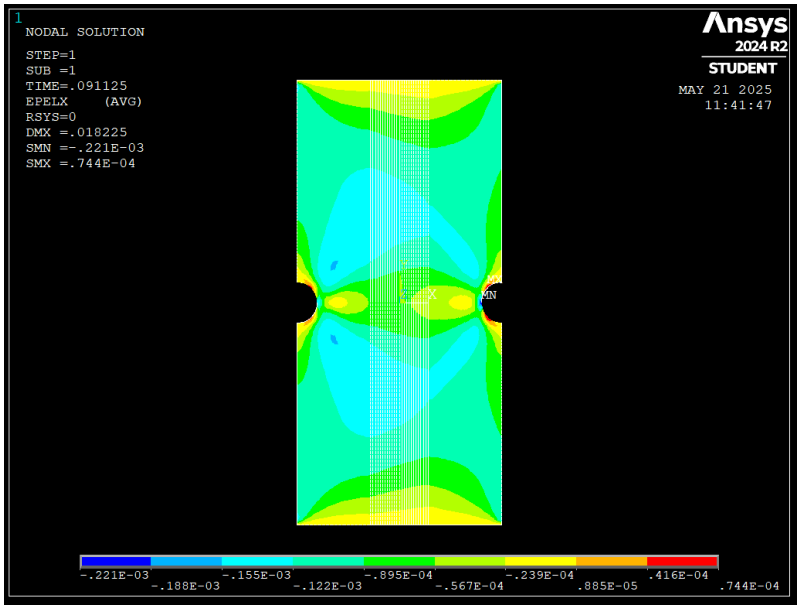

Figure 7.7: Contour plot of distribution of X-component of elastic strain for Cu-CuAl alloy FGM continuous (transition zone equal to 7 mm) specimen.

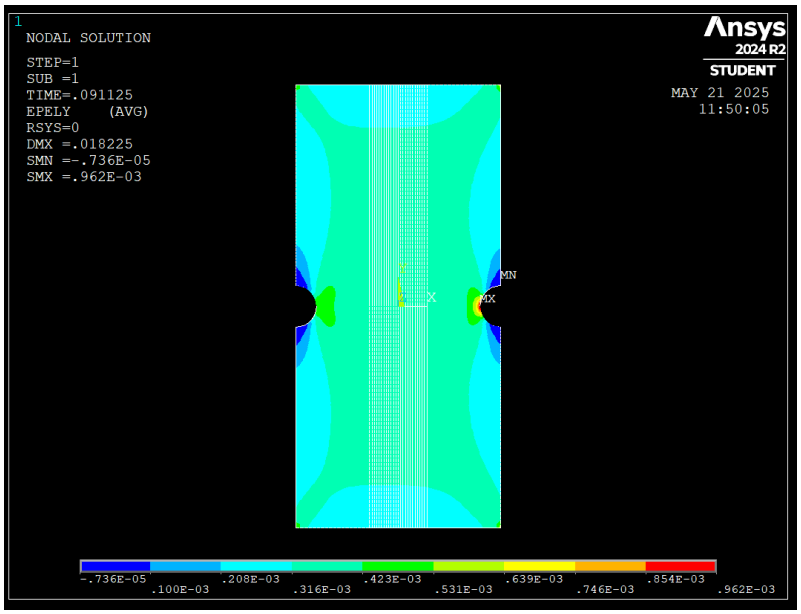

Figure 7.8: Contour plot of distribution of Y-component of elastic strain for Cu-CuAl alloy FGM continuous (transition zone equal to 7 mm) specimen.

lower stiffness. This observation corroborates the results shown in Figures 7.7 and 7.8.

7.3 Tensile tests with Digital Image Correlation

In this section, the Cu-CuAl alloy FGM specimens will be tested with a continuous gradient. In order to achieve this objective, a detailed description will be provided of the testing process that was employed. This will include a description of the materials that were

used, the camera that was utilised for the purpose of capturing the process. Finally, the maximum force that was measured will be presented. The discussion will also address the results of the study. A total of six samples of the Cu-CuAl alloy FGM were subjected to rigorous testing to analyse the geometry that had been determined in Chapter 4. The six test pieces are composed of a pre-test piece that was utilised to verify the configuration. The dimensions of these samples are equivalent to those of the 316L stainless steel samples and the Cu-CuAl alloy FGM stepwise. The field of view (FOV) is 25 mm width and 30 mm height. Figure 7.9 presented illustrates one of the five samples.

Figure 7.9: Cu-CuAl alloy FGM continuous specimen.

7.3.1 Tensile test procedure

The study employed tensile test procedures similar to those used in Cu-CuAl alloy FGM stepwise tests. The Step Lab EA05 electromechanical test machine with a 15 kN load cell was also used. The specimens were vertically aligned and secured in the grips, and subjected to a displacement rate of 1.5 mm/min during the tensile tests. One Manta G-1236 camera acquired images using 2D DIC, pointing towards the specimen. The camera was adjusted to optimize spatial resolution on the sample. It was assembled on AF Micro-Nikkor 200mm f/4D IF-ED lense and a extension ring of 25 mm. Two green LED lights were placed in the setup. When observing the quantum efficiency of the camera, it was found that green LED illumination maximised the sensor's response to green light, thereby increasing the signal-to-noise ratio. This experimental setup is shown in Figure 7.10.

Table 7.1 presents the main characteristics employed in the stereo-DIC tensile tests of FGM specimens.

7.3.2 Performance Analysis

Following the execution of tensile tests employing the coupled DIC technique, the ensuing analysis is to be conducted using MatchID software. Prior to the processing of the images, a precise selection of the DIC parameters was made using MatchID's performance analysis module. This module has been found to be of particular utility in applications that seek to measure high strain gradients. To this end, a reference point was utilised in proximity to the copper notch, the material exhibiting the most significant deformations, and midway

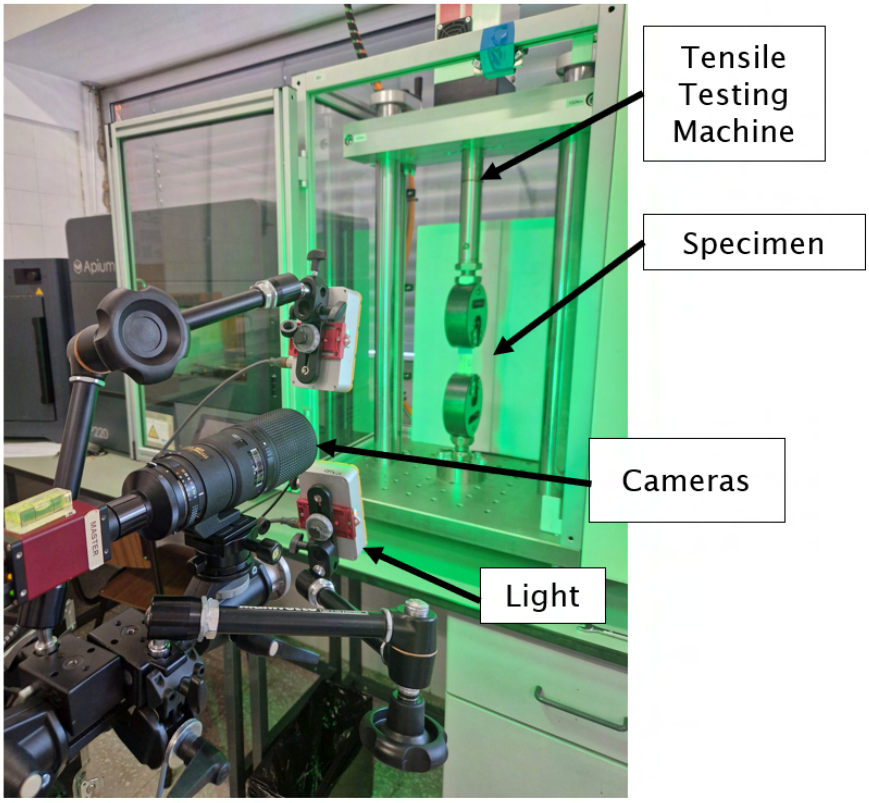

Figure 7.10: Experimental setup for DIC test on Cu-CuAl alloy FGM continuous specimen.

Table 7.1: 2D-DIC settings for the tensile test of FGM specimens continuous.

DIC setting	**Specification**
Electromechanical test machine	Step Lab EA05
CMOS Cameras	Manta G-1236
Lens	AF Micro-Nikkor 200mm f/4D IF-ED
Patterning technique	Spray painting
Extension ring	25m
DIC technique	2D DIC
DIC software	MatchID, version 2025.2

between the two notches, where the stress concentration is maximal. As illustrated in Figure 7.11, the reference point has been located on the specimen.

A reference image was selected, as well as an image prior to the commencement of the test and a deformed image, which was selected during the deformation of both materials, but before any fracture occurred in the specimen. Additionally, a static image was selected, captured at the moment the specimen was positioned within the designated setup, devoid of any external loading forces.

Upon rigorous examination of the graph and its various points (Figure 7.12), it becomes possible to draw several conclusions. The quadratic shape function was selected for its superior ability to smooth the signal when compared with the affline function. The VSG

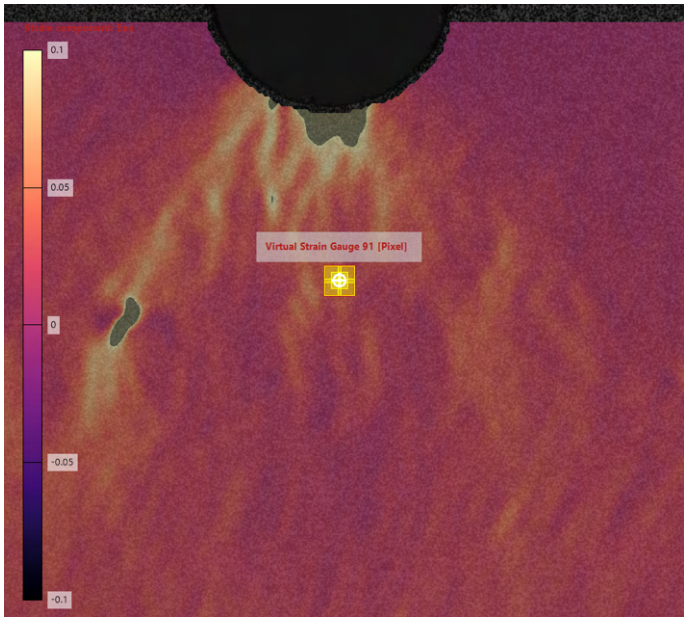

Figure 7.11: Graphic performance analysis of the strain component signal (E_{xx}).

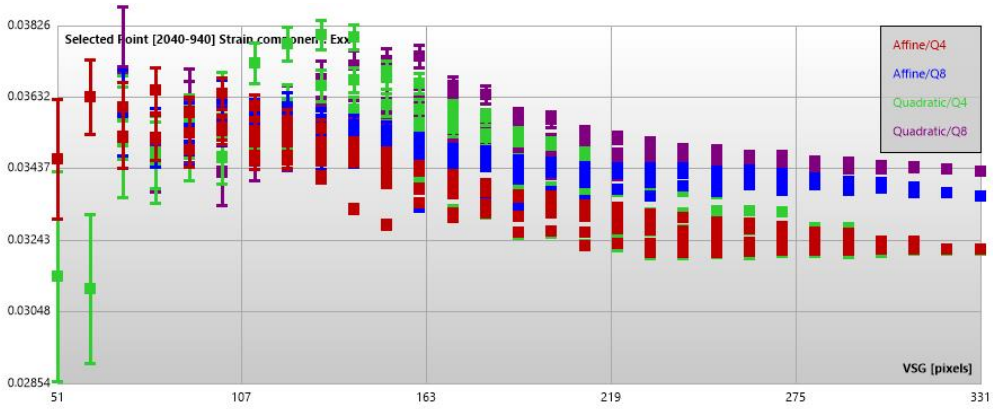

Figure 7.12: Graphic performance analysis of the signal in relation to virtual strain gauge (pixels).

(virtual strain gauge) from 51 to 81 presents a highly dispersed set of values, while the VSG from 91 to 111 appears to represent a satisfactory compromise. The VSG from 121 to 131 exhibits a convergence of values, leading to a smoothing effect. It is evident that an increase in the VSG results in enhanced spatial resolution, concurrently accompanied by a reduction in signal resolution. This, in turn, leads to an augmentation in data smoothing. Therefore, it is imperative to minimise the VSG to avoid compromising the spatial resolution of the test. Consequently, a VSG of 91 was selected. For a VSG of 91, the difference between the highest and lowest signal points is approximately 5%, which is negligible. Consequently, a value that falls midway between the highest and lowest signals was selected. The PA target settings selected for the analysis were as follows:

- Subset size: min 31, max 131,increments 10

- Step size: 10
- Shape function: quadractic
- Strain window: min 3, max 31, increments 10
- Polynomial order: bilinear Q4 and biquadratic Q8
- Tensor: Green-Lagrange
- Virtual strain gauge: 91

7.3.3 Digital image correlation (DIC) method procedure

The Digital Image Correlation (DIC) system was employed to measure surface deformations in the analysed samples during tensile testing. The utilisation of a DIC software is imperative for the capture and analysis of images of samples. The software utilises algorithms to track pixel patterns and calculate surface deformations as these patterns change over time. In order to capture images of samples with optimal detail, it is necessary to utilise high-resolution and high-frame-rate cameras during the testing process. The stereo system, equipped with two cameras, was utilised in this study to analyse the sample surface. It is imperative to ensure adequate illumination to facilitate the generation of sufficient contrast in the captured images for subsequent analysis using the DIC software. The speckle pattern plays a critical role in the DIC system, requiring a high-contrast pattern on the sample that is visible to the cameras and remains undistorted during testing. These markings function as reference points for the DIC software to compute deformations, as elucidated in the section on speckle patterns. The experimental setup must be meticulously arranged to guarantee that the cameras capture the entire surface of the sample without generating shadow areas during the tensile test. Table 7.2 lists the default DIC parameters for analysing FGM specimens continuous samples.

The Digital Image Correlation (DIC) technique requires a static reference image to be established for the purpose of comparison with subsequent images, with the objective of determining displacements and deformations during the test. As with many experimental methods, DIC is susceptible to experimental noise, also known as random error, which has the capacity to affect the accuracy of results. This noise is primarily attributable to the camera acquisition process, which introduces random variations in the grey level values of captured images. It has been demonstrated that image acquisition noise has the capacity to exert an influence on measured coordinates and derived quantities during the process of digital image correlation (DIC). In order to mitigate this issue, it is possible to average multiple images. The content of the enhanced text must be as close as possible to the source text, and the addition of further aspects must be avoided at all costs. The calculation of the mean is a relatively simple process for the reference DIC image, which is generally obtained under conditions of no load. It is imperative to employ language that is clear, concise, and objective, eschewing biased or emotional language. It is possible to capture

Table 7.2: DIC parameters for the tensile test of FGM specimens continuous.

DIC Parameter	Specification
General DIC Settings	
Technique Used	2D Digital Image Correlation
Camera Resolution	12bit, 4112 × 3008 pixels
Pixel to mm conversion	0.004864
Average Speckle Size	8 pixels
Subset Size	51 pixels
Step Size	10 pixels
Shape Function	Quadratic
Interpolation Function	Bicubic Spline
Correlation Criterion	ZNSSD
Prefiltering	Gaussian (Kernel size = 5)
Strain Settings	
Strain Window	5 data points
Virtual Strain Gauge (VSG)	91 pixels
Strain Interpolation Function	Bilinear Quadrilateral (Q4)
Strain Tensor	Green-Lagrange

multiple static images of the test sample and then calculate the mean of these images in order to generate an image with minimal noise. However, the creation of analogous noiseless deformed images is a more intricate process. It is imperative to exercise caution with regard to potential effects, including creep. In the four samples examined, an aperture of 11 was employed in the camera. An exposure time of 80000 μs was considered.

7.3.4 Maximum Force

Six samples, including a pre-test sample and five samples made of the same material and geometry, were tested until failure. The maximum forces of the six specimens were very different for all FGMs specimens. Figure 7.13 illustrates the varying maximum forces of the six samples.

The graph compares the displacement in millimeters to the force required to be exerted on the specimens in kilonewtons. It displays six distinct curves: Curve 1 represents the pre-test specimen, while curves 2, 3, 4, 5 and 6 represent FGM specimens 1, 2, 3, 4 and 5. The majority of the curves exhibited the customary behaviour associated with a tensile test, characterised by an initial linear region and an elastic phase. It is evident that all the curves demonstrate a maximum point (maximum load peak), followed by a descending region where the sample continues to deform, but the load decreases due to necking. Ultimately, fracture occurs. The pretest curve demonstrates that the specimen was subjected to a maximum stress load of approximately 8,000 N. Subsequently, the claws exhibited slippage on the specimen, thereby indicating the presence of the stable zone. It is noteworthy that the specimen in question was composed of 100% CuAl. The

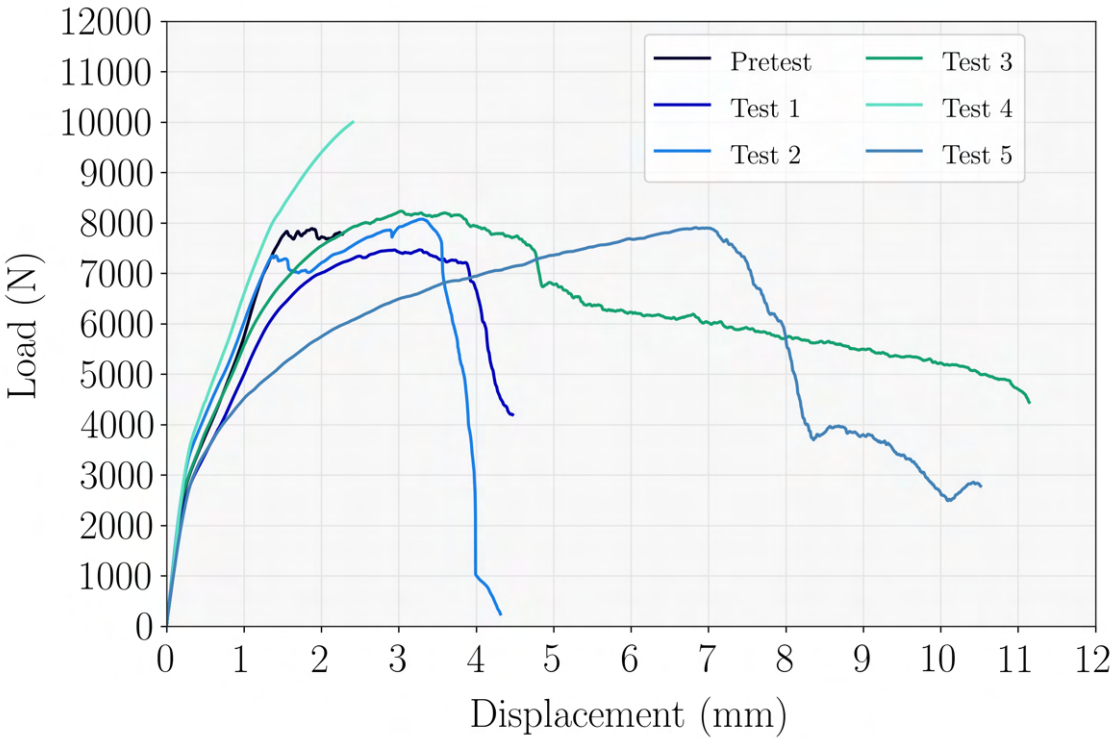

Figure 7.13: Maximum force until failure for the 5 specimens tested of FGM.

pre-test specimen was made of 100% CuAl because this is the material with the highest hardness. The curves for test 1 and 2 demonstrate a comparable tendency, exhibiting a maximum force of 7000 to 8000 N and an early fracture in comparison to the other specimens (displacement up to 4-5 mm). This suggests that they exhibited a reduced ductile behaviour. The curve for test 3 demonstrates a maximum force greater than 8000N, yet a greater displacement before fracture (approximately 5mm). In curve 4, the specimen did not fracture because it reached the machine's dynamic limit of 10kN. The curve of test 5 demonstrates a maximum force of 8000N, and the greatest displacement before fracture (7mm), indicating enhanced ductility, despite the strength not being the highest.

7.3.5 Noise evaluation

Prior to conducting the DIC tensile test, it is imperative to ascertain the quality of the recorded images and to undertake a comprehensive evaluation of the noise levels. Prior to the commencement of the test, some static images were captured. These images were then subjected to averaging in order to eliminate noise. The static noise for each camera was calculated using MatchID. Prior to conducting the DIC test, it is imperative to meticulously evaluate the quality of the captured images and to accurately ascertain their noise levels. It was determined that the noise exhibited a dynamic range of ... for the sample-aligned camera and ... for the angled camera. These values are within the typical range for a machine vision camera. MatchID was utilised to calculate the mean spot size for each sample. The lowest spot size that could be obtained with a spray painting

was approximately ... pixels. The standard deviation of the selected DIC field variable provides an indication of the noise floor of the field variable. The grey level histogram for each pixel is shown in Figure 7.14.

Figure 7.14: Gray level histogram for each pixel.

Histograms should exhibit adequate contrast, with divergent pixel intensities clearly distinguishable, and should encompass all extant ranges of pixel intensities present in the image. It is imperative to avoid saturation at the extremes of the histogram. An excess of pixels at one or both extremes of the histogram may signify a loss of information in areas of the image characterised by extremely high or extremely low brightness. The highest concentration of pixels is observed to be between 20 and 70 grey levels. The occurrence of the peak at a value of approximately 50 indicates that the image is predominantly characterised by dark tones, with medium and low tones being the most prevalent.

7.3.6 Results

The subsequent analysis of the results is analogous to that previously delineated in Chapter 6. In the ensuing results, a single specimen will be exhibited, designated as 'test 3', on account of the marked similarity between the specimens and the uniformity of their results. The initial step in this process is to define the return on investment (ROI) of the analysis. It is not necessary to analyse the entire FOV, since the area further away from the notches displays comparable behaviour. The workflow carried out in these tests was as follows:

- The images captured during the test were processed using 2D MatchID;
- Firstly, it is imperative to load a reference image captured prior to the commencement of the test. In addition, it is imperative to select the deformed images from the test that are to be analysed;
- It is then necessary to load two files that were acquired during the tensile test. These are the calibration parameters file, which was generated by MatchID Calibration, and the acquisition data file, which was generated by the MatchID Grabber;
- The subsequent stage in this process is to define the ROI (region of interest). The ROI is defined to show the area of the notch and some of the uniform area of the sample;
- The subsequent stage of the process is to modify the default settings, including parameters such as step and subset size;

- Finally, the possibility exists to perform correlation by calculating the strains from the displacements recorded by the images during the test.

The results of one of the specimens are presented in this segment of the report. The observed movements in the x direction are consistent with the anticipated outcomes, indicating a movement from right to left, which aligns with the direction of the load applied during the experimental procedure.

As demonstrated in Figure 7.15, six frames were captured during the test to assess global deformation in the xx direction. (a) illustrates an initial phase of the mechanical test, characterised by a force of 0 KN and negligible deformation. As demonstrated in Figure (b), the CuAl alloy is the primary material that undergoes deformation. At this stage of the test, the initial loading appears, where small concentrations of deformations begin to appear. As demonstrated in tables (c) and (d), the copper layers begin to deform. The distribution of deformation becomes more heterogeneous, with greater deformation in the Cu layers. As demonstrated in tables (e) and (f), it is evident that the deformation of the sample is more pronounced in the Cu layers compared to the CuAl layers. This phenomenon is indicative of the onset of plastic localisation and striation, which occurs prior to the fracture. The ϵ_{xx} deformation fields demonstrate the enhanced ductile behaviour of copper, which exhibits a propensity to distribute deformations more effectively. In contrast, CuAl exhibits a tendency to be more resistant and to manifest more localised deformations. The behaviour exhibited in this figure aligns with the load-displacement curve depicted in Figure 7.13 (Test curve 3).

Figure 7.16 shows the global strain fields for the specimens in the yy direction. The 6 frames chosen show that there is a little bending of the specimen over time, since the Cu layers show deformation higher the CuAl layers. As the load is applied in the x direction, there is almost no deformation in the y direction. (a) shows the initial state without significant deformation. In image (b) it is possible to observe an initial loading with the beginning of deformation concentration in the Cu layers. These deformation gradients by "steps" show the heterogeneity of the specimen. (c) and (d) show an intermediate evolution, where deformations intensify in specific regions of the specimen, zones where fractures will occur. (e) and (f) show high loads, indicating the beginning of necking. (a) illustrate the initial state and the absence of any significant deformation. As illustrated in image (b), the initial loading process is evident, with the beginning of deformation observed in the Cu layers. The observed gradients of deformation by "steps" are indicative of the heterogeneity exhibited by the specimen. (c) and (d) illustrate an intermediate phase of evolution, during which deformations intensify in specific regions of the specimen, i.e., areas where fracture is expected. (e) and (f) demonstrate elevated loads, thus indicating the commencement of necking.

As illustrated in Figure 7.17, six frames were captured during the test to assess the global strain in the xy direction. It is evident that the Cu region is the primary region of deformation. The initial stage (a) displays a virtually uniform deformation field,

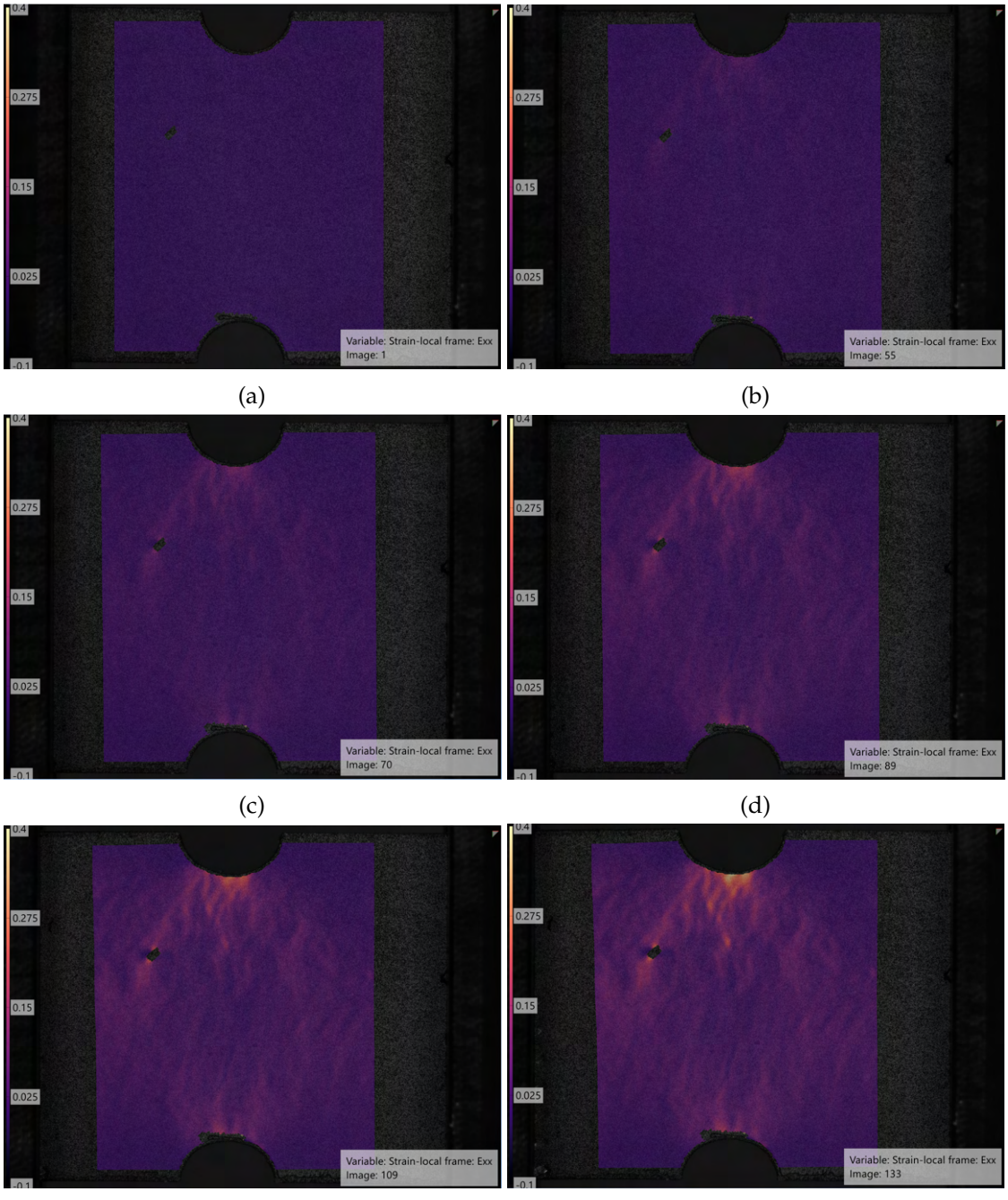

(a) (b)

(c) (d)

(e) (f)

Figure 7.15: Global strain fields for specimen in the xx direction, ε_{xx}, for Cu-CuAl alloy FGM continuous specimen: (a) 0KN, (b) 3.3KN, (c) 4.2KN, (d) 5.5KN, (e) 6.7KN and (f) 8KN.

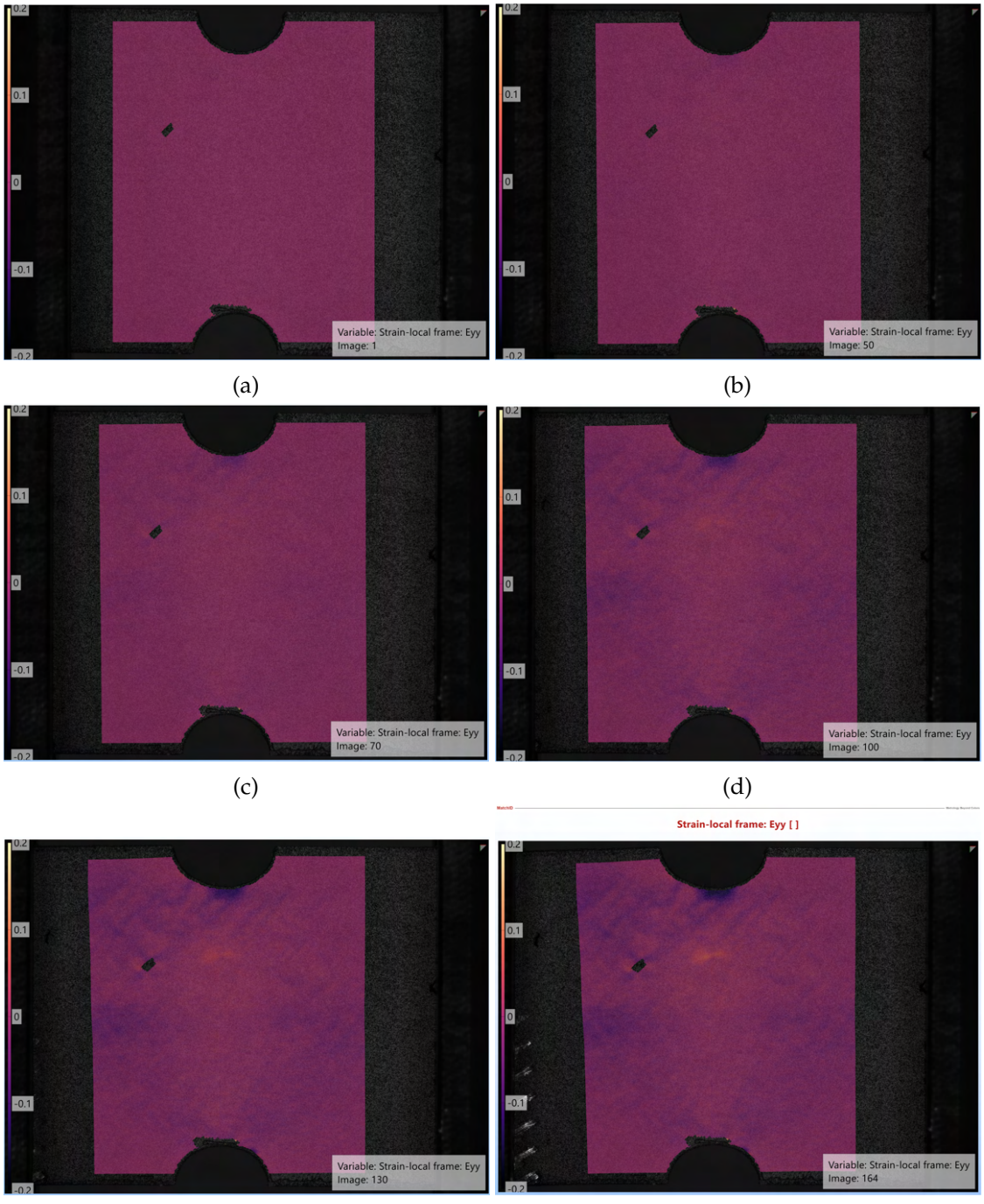

(a) (b)

(c) (d)

(e) (f)

Figure 7.16: Global strain fields for specimen in the yy direction, ε_{yy}, for Cu-CuAl alloy FGM continuous specimen: (a) 0KN, (b) 3.2KN, (c) 4.2KN, (d) 6.5KN, (e) 8KN and (f) 8.2KN.

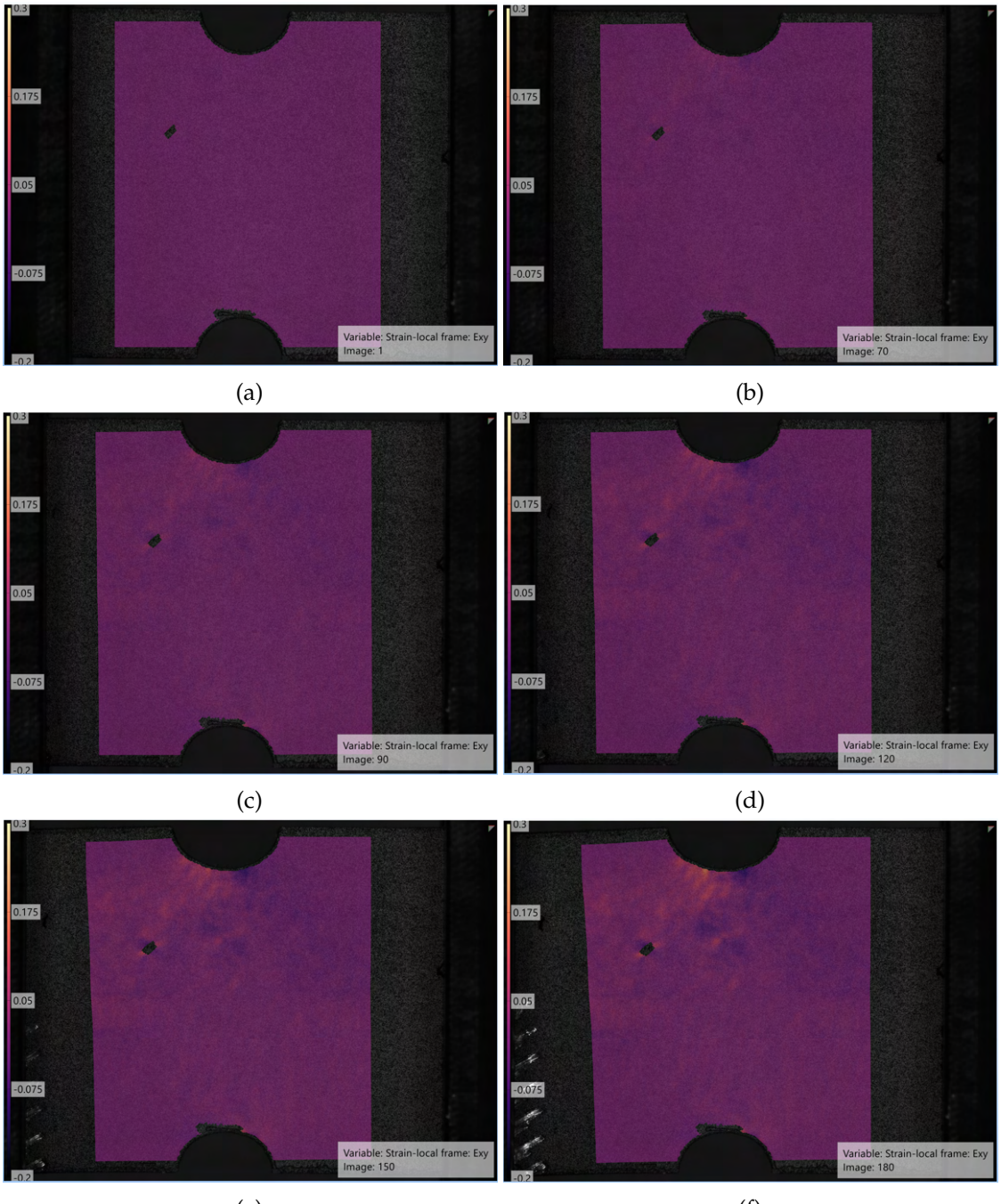

(a) (b)

(c) (d)

(e) (f)

Figure 7.17: Global strain fields for specimen in the xy direction, ε_{xy}, for Cu-CuAl alloy FGM specimen: (a) 0KN, (b) 4.2KN, (c) 5.5KN, (d) 7.5KN, (e) 7.8KN and (f) 8.2KN.

exhibiting no strain. (b) illustrates the initiation of the load application, exhibiting minor local deformation concentrations. (d) and (e) illustrate a concentration of positive (light-coloured zone) and negative (dark-coloured zone) deformations, indicating the probability of fracture in this zone. As illustrated in Figure (f), the maximum load prior to fracture is evident, accompanied by a substantial accumulation of localised deformation prior to failure.

7.4 Inverse identification through synthetic data by Virtual Fields Method

In this section, the inverse identification of the Cu-CuAl FGMs specimens will be carried out stepwise through synthetic images by VFM.

Table 7.3: Mean and median of Poisson coefficient for Cu-CuAl alloy FGMs continuous specimens through finite element analysis.

	FEA
ν Cu (mean)	0,9954
ν Cu (median)	0,9954
ν CuAl (mean)	1,2937
ν CuAl (median)	1,2937
ν (mean)	1,1446
ν (median)	1,1446

Table 7.3 shows that the Poisson's ratios obtained for the continuous Cu, CuAl, and FGM Cu-CuAl samples were 0.9954, 1.2937, and 1.1446, respectively. These values significantly exceed the typical range for metals, which is typically from 0.2 to 0.5. Despite this, the mean and median values are found to be highly similar across each group, suggesting a relatively homogeneous distribution of the finite element simulation results. This internal consistency in the data indicates that, despite the high absolute value, the model response for each analysed region was stable.

Table 7.4: Mean of Young's module for Cu-CuAl alloy FGMs continuous specimens through finite element analysis.

	FEA
E Cu (mean)	69,181 GPa
E CuAl (mean)	89,593 GPa
E (mean)	79,387 GPa

The Young's modulus values (Table 7.4) obtained by finite element analysis for Cu (69.181 GPa), CuAl (89.593 GPa), and the Cu-CuAl FGM (79.387 GPa) are lower than the reference values, which are typically 110 GPa for Cu and 117 GPa for CuAl. This

discrepancy may be attributable to the degree of mesh refinement in the simulation, the definition of the material properties, or even modelled microstructural effects. In order to approximate the numerical results to the real values, it is recommended to increase the mesh refinement and calibrate the model parameters with experimental data, thus optimising the fidelity of the finite element analysis.

7.5 Inverse identification through full-field data by Virtual Fields Method

In this section, the inverse identification of the Cu-CuAl FGMs specimens will be carried out stepwise through full-field data by VFM.

Table 7.5: Mean and median of Poisson coefficient for Cu-CuAl alloy FGMs continuous specimens through engineering data.

	Specimen 1	**Specimen 2**	**Specimen 3**
ν Cu (mean)	0,0155	0,1573	0,1333
ν Cu (median)	0,0826	0,1381	0,1789
νCuAl (mean)	0,2387	0,3750	0,2716
ν CuAl (median)	0,3040	0,3762	0,3227
ν (mean)	0,1821	0,2839	0,1980
ν (median)	0,2757	0,2478	0,2379

As demonstrated in Table 7.5, the mean and median values of Poisson's ratio obtained through experimental analysis for copper in the continuous samples are significantly below the anticipated reference value of 0,343 for this material, particularly in the first specimen, where a mean value of only 0,0155 is observed. For CuAl, the Poisson's ratios range from 0,2387 to 0,3750 (mean), closer to the reference value of 0,34 for the alloy, although showing some dispersion between the different samples. This discrepancy is indicative of not only the influence of the specific microstructural characteristics of the samples and the experimental conditions, but also possible limitations in the characterisation method. This underscores the necessity for meticulous analysis when interpreting the mechanical properties of graded functional materials, particularly in continuous geometries.

Figure 7.18 demonstrates the engineering stress-strain curves for Samples I, II and III, which were obtained under continuous loading conditions. As was the case in the preceding instance (see Figure 6.28), the curves represent the material response to tensile loading, with engineering stress plotted against engineering strain. In comparison with the stepwise test, the continuous curves demonstrate more uniform profiles and consistent strain hardening behaviour, thus eliminating the interruptions or local fluctuations that are associated with the incremental loading procedure. Nevertheless, both approaches reveal the same general trends: Sample III exhibited the highest degree of strength, Sample II demonstrated an intermediate response, and Sample I exhibited the lowest degree of

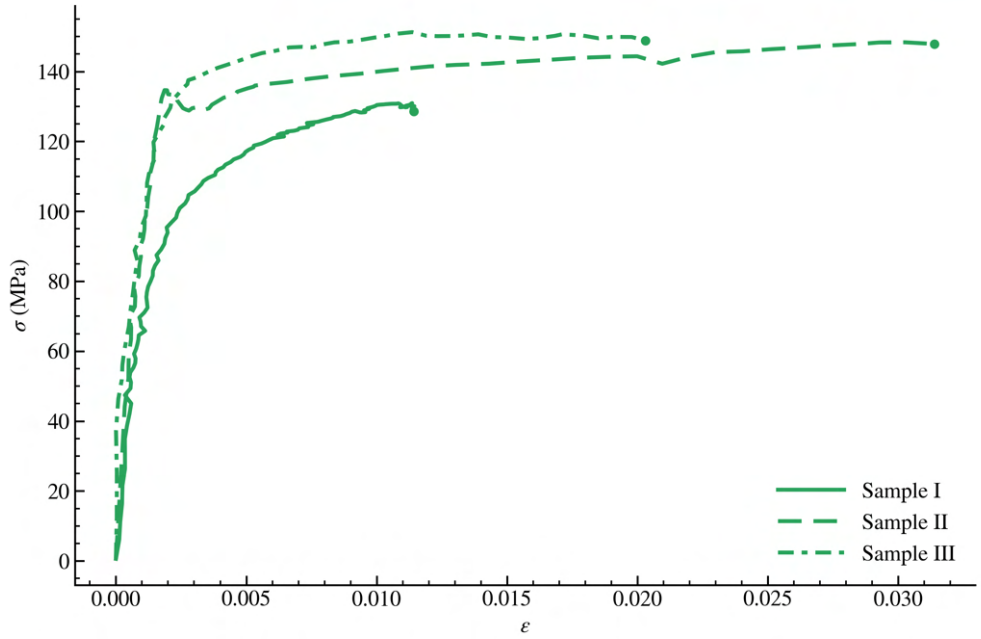

Figure 7.18: Engineering stress-strain curve for the Cu-CuAl alloy FGM continuous specimens.

strength. The comparison between the two testing methods highlights that, while stepwise loading can introduce minor instabilities in the recorded curves, the overall mechanical behaviour and ranking of the samples remain consistent.

Table 7.6: Summary of tensile test engineering parameters and Young's modulus for the three Cu-CuAl alloy FGM continuous specimens.

Sample	**Number of points**	L_0 **(mm)**	**Young's modulus** E **(GPa)**
Sample I	176	33	54,1
Sample II	100	25	72,4
Sample III	225	22	63,9

Table 7.6 provides a summary of the primary engineering parameters and Young's modulus derived from the continuous tensile tests conducted on the three Cu–CuAl FGM specimens. The initial gauge lengths (L_0) range from 22 to 33 mm, with a corresponding variation in the number of recorded points, reflecting the divergent acquisition conditions of each test. The calculated Young's modulus values are lower than the expected literature values for pure Cu (124 GPa) and CuAl alloys (105 GPa), ranging from 54.1 to 72.4 GPa. In comparison with the results obtained from the stepwise tests (see Table 6.6 for details), the continuous tests consistently yield systematically lower stiffness values. This discrepancy can be ascribed to the disparate testing methodologies employed: the stepwise procedure has the capacity to artificially augment the apparent modulus due to relaxation effects between loading steps, whereas the continuous method captures a more uniform elastic response that may be more indicative of the actual material behaviour. Notwithstanding

these discrepancies, both approaches demonstrate consistent relative trends across the three samples, with Sample II exhibiting the highest stiffness and Sample I the lowest.

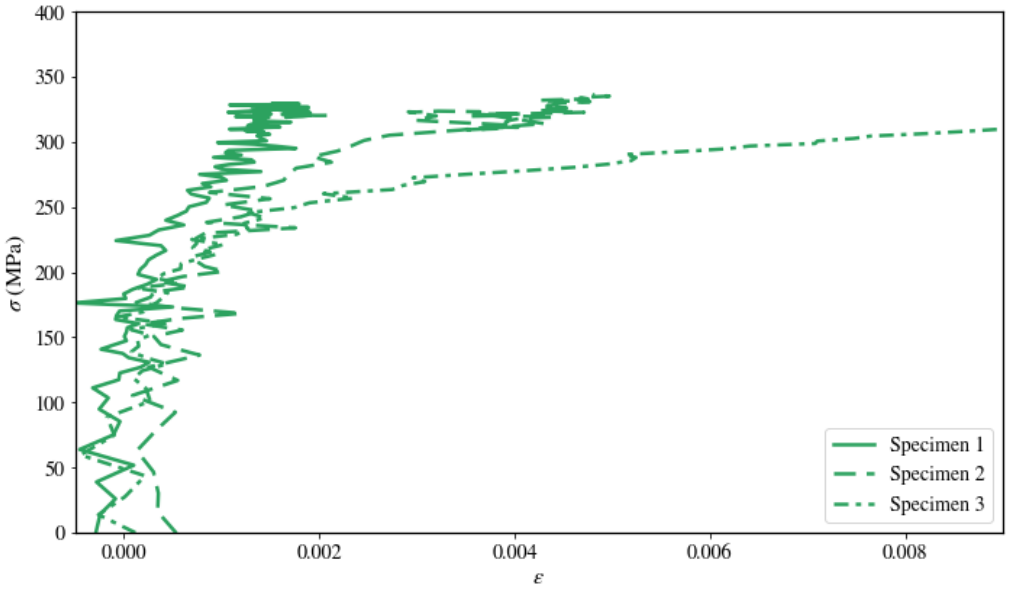

Figure 7.19: DIC stress-strain curve for the Cu-CuAl alloy FGM continuous specimens.

Figure 7.19 displays a stress-strain graph, with three curves representing tests on different specimens. The mechanical behaviour of each specimen can be evaluated based on the relationship between σ (stress) and ϵ (strain) throughout the test. Each curve illustrates a distinct response to load application, but none of them exhibits a perfectly smooth and continuous path. This lack of uniformity can be attributed to several experimental and material factors, including noise in the data from the DIC acquisition process, small geometric imperfections in the specimens or surface preparation, and fluctuations in the clamping or load application, as well as natural microscopic variations in the material itself. Furthermore, oscillations may be generated due to slippage in the grips that occurred during the test. This can result in the graph displaying "jumps" or irregularities rather than a smooth and continuous curve. Consequently, these characteristics are indicative not only of the intrinsic response of the material itself but also of the limitations and sources of variation of the experimental test.

Figure 7.20 displays a stress-strain graph, which compares two distinct measurement methods: a curve designated "Engineering" (presumably obtained by traditional strain gage) and a curve labelled "DIC" (obtained by Digital Image Correlation). The vertical axis is employed to denote stress values. It is evident that the DIC curve attains considerably higher stress levels and more accurately reflects the material's hardening and yielding stages in comparison to the Engineering curve, which exhibits lower stress values and an earlier plateau stabilisation. This type of graph is notable for its ability to both highlight the differences between strain measurement methods and illustrate the gain in local precision provided by DIC in analysing the mechanical behaviour of materials.

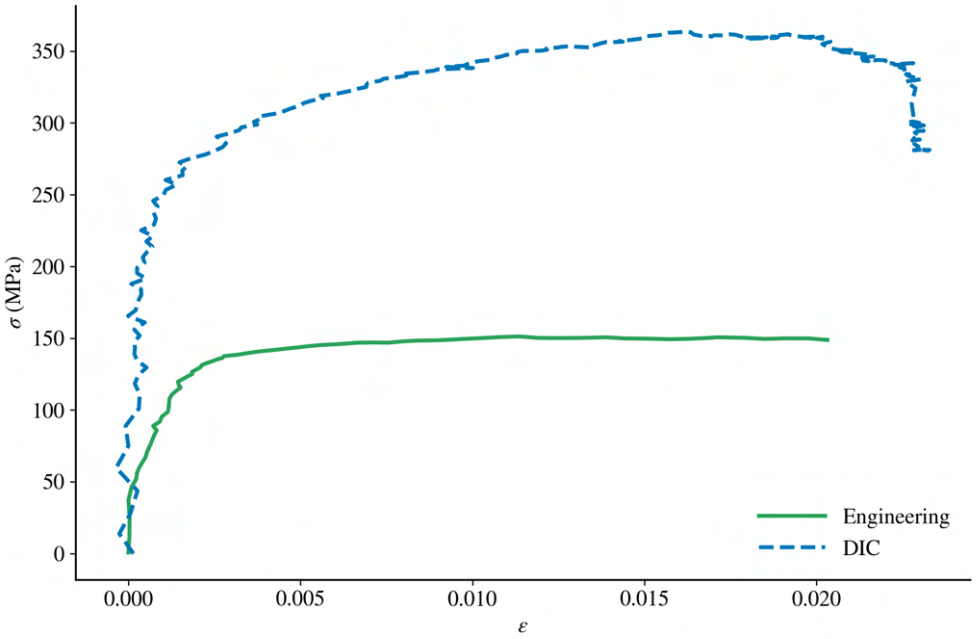

Figure 7.20: Comparison between stress strain curves for Cu-CuAl FGM continuous specimen 3.

Table 7.7: Mean of Poisson coefficient for Cu-CuAl alloy FGMs continuous specimens through DIC data.

	Specimen 1	**Specimen 2**	**Specimen 3**
ν Cu (mean)	0,2323	0,2047	0,1177
ν CuAl (mean)	0,4839	0,2453	0,1190
ν (mean)	0,3581	0,2250	0,2250

Table 7.7 presents the mean average of the Poisson's ratio values for continuous Cu-CuAl alloy specimens obtained from Digital Image Correlation (DIC) data. In the three specimens analysed, the values for copper range from 0,1177 to 0,2323, while for CuAl they range from 0,1190 to 0,4839, with overall averages for each specimen between 0,1184 and 0,3581. It is noteworthy that, in contrast to the reference values utilized for these materials (0,343 for Cu and 0,34 for CuAl), only the CuAl specimen 1 demonstrates a significant deviation from the anticipated values. The remaining results, encompassing both copper and the alloy, are considerably lower than the expected values. This behaviour serves to reinforce the impact of experimental variations, microstructure and the DIC analysis method in the characterisation of the properties of continuous FGMs. It has been demonstrated that experimental values do not always follow theoretical parameters and, as such, a critical analysis of the results obtained is required.

Table 7.8 presents the mean Young's modulus values for Cu and CuAl in continuous specimens, as determined via DIC. For copper, the results range from 72,232 GPa to 96,642 GPa, while for CuAl, the values range from 86,672 GPa to 102,580 GPa, with overall

Table 7.8: Mean and median of Young Modulus for Cu-CuAl alloy FGMs continuous specimens through DIC data.

	Specimen 1	**Specimen 2**	**Specimen 3**
E Cu (mean)	96.642	72.232	86.146
E CuAl (mean)	102.580	86.672	87.377
E (mean)	99.611	79.452	86.762

averages for specimens between 79,452 GPa and 99,611 GPa. A comparison of these results with the reference values of 110 GPa for Cu and 117 GPa for CuAl demonstrates that the experimentally measured properties are lower than expected for both materials. This deviation may be attributable to various factors, including the processing conditions of the materials, the microstructural heterogeneity of the FGMs, or the inherent characteristics of the DIC technique employed. The data, taken as a whole, demonstrate that, despite the fact that the elastic properties obtained for continuous specimens approximate the theoretical parameters, these properties fall below the reference values cited in the extant literature. This finding suggests a necessity for caution when interpreting the results in the context of advanced materials engineering.

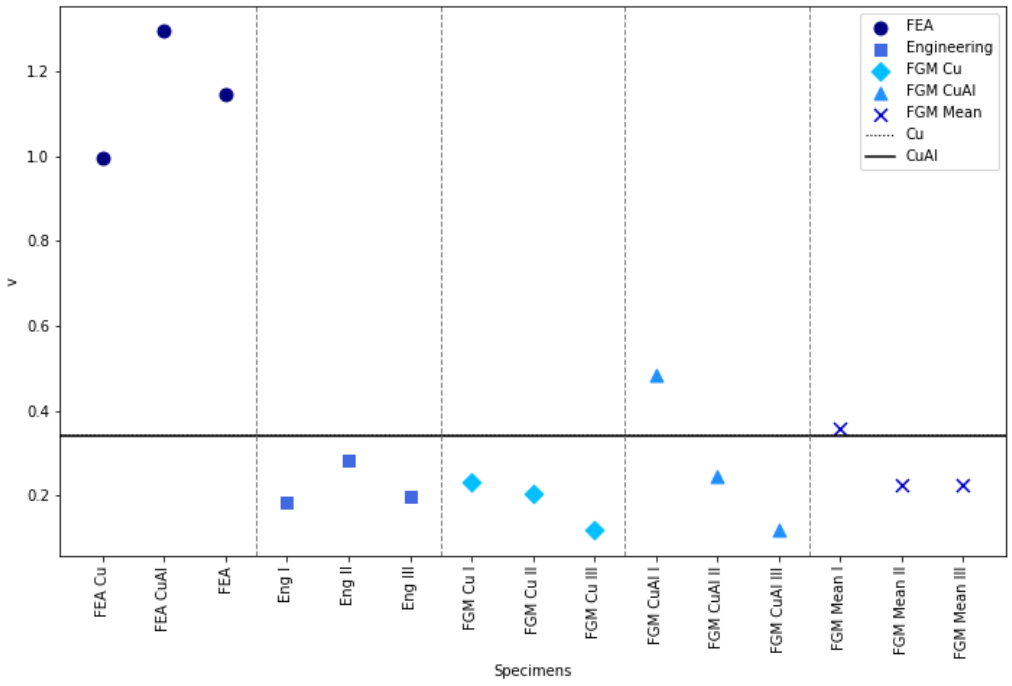

Figure 7.21: Comparison of ν from FEA, engineering and DIC values.

Figure 7.21 illustrates the variation of the ν parameter (which may be the modulus of elasticity or Poisson's ratio, in GPa) for different specimen types, divided into experimental groups. The following materials are to be considered: FEA, Engineering, FGM Cu, FGM CuAl, and FGM Mean. It is evident that the highest ν values are exhibited by the FEA group, as indicated by the dark circular markers, which distinctly differentiate this group from all

other groups. The values obtained for the Engineering group are notably lower, ranging from 0,2 to 0,3, and exhibit a relatively stable distribution across its various specimens. The FGM Cu and FGM CuAl specimens present intermediate values, with moderate dispersion and a tendency toward lower values as one moves from FGM Cu to FGM CuAl. In conclusion, the ν values for the FGM Mean specimens are systematically among the lowest of all groups. This finding suggests that the material's functional gradient results in a marked decrease in this parameter compared to the other approaches. The presence of the dotted vertical lines facilitates the visual separation of each experimental family along the specimen axis, thereby rendering the clear differentiation between the responses of the various materials and processes more evident. The graph demonstrates both the substantial disparities amongst the families and the correlation between the utilisation of FGM, notably in medium and CuAl-rich compositions, and reduced v values when compared to those of FEA and Engineering. This finding signifies the influence of functional grading on the mechanical properties that are obtained.

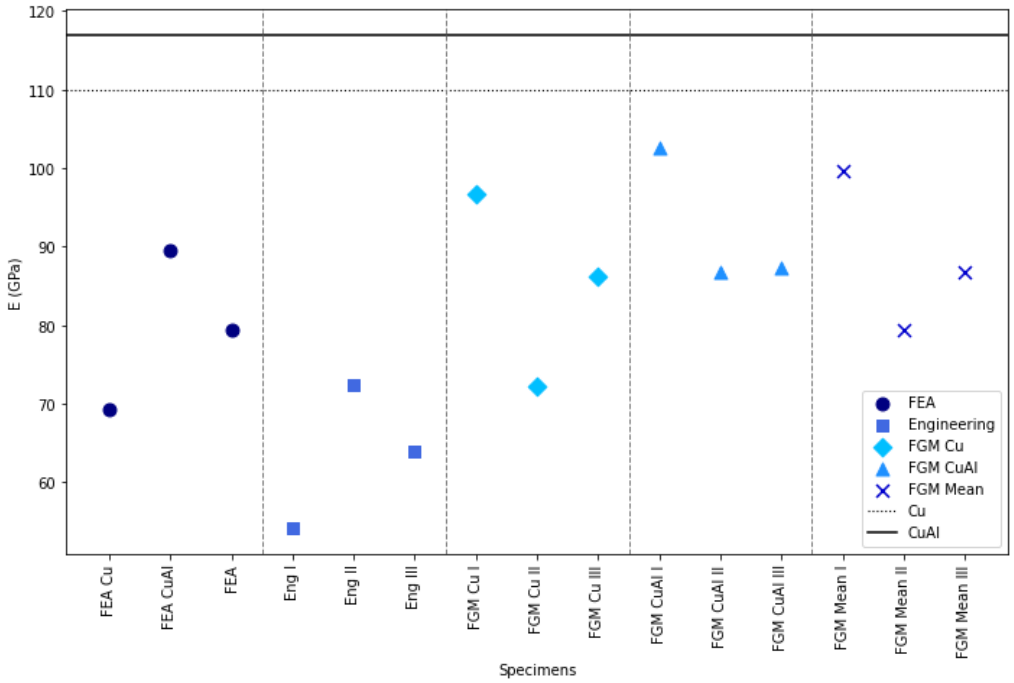

Figure 7.22: Comparison of E from FEA, engineering and DIC values.

The Figure 7.22 presents the elastic modulus (E) values of the various test materials, categorised by group (FEA, Engineering, FGM Cu, FGM CuAl, and FGM Mean). It is evident that the E values vary considerably between the groups. The specimens in the FEA group present values between 75 and 90 GPa, while those in the Engineering group have lower values, ranging from approximately 55 to 73 GPa. In the case of FGM Cu and FGM CuAl, a wide dispersion is observed, reaching values above 100 GPa for FGM CuAl, approaching the reference line for pure metals. The FGM Mean group reveals intermediate and slightly increasing values. The horizontal lines demarcate reference

values for Cu and CuAl, thus facilitating direct comparison of the sample results with the base materials. The presence of dashed vertical lines serves to accentuate the visual separation between the families, thereby highlighting the distinct trends observed for each experimental procedure or material formulation that was tested.

7.6 Conclusion

This chapter begins with an analysis of tests to be developed using the finite element method. Next, a detailed description of the experimental tests carried out on the specimens is presented, covering the tensile test procedure, the DIC process, maximum force, noise assessment and the respective results. Finally, two inverse identifications will be carried out using the VFM method: one with synthetic data and the other with full field data. The experimental determination of Poisson's ratio, employing both conventional methods and DIC analysis, yielded values that are in close agreement with the anticipated values for metals. The range of these values extends from 0.0155 to 0.4839, with the Cu and CuAl phases exhibiting distinct values within this range. This indicates that the lateral deformation of the material is within the standard parameters for these metals, taking into account the inherent local heterogeneities present within the functional gradient. Conversely, FEA yielded unfeasible values for Poisson's ratio, exceeding the physical limit of 0.5. This suggests that the numerical modelling for continuous specimens requires refinement, potentially through adjusting material parameters, boundary conditions, or the modelling approach itself. With regard to Young's modulus, the varying methodologies employed also demonstrate significant variability. FEA indicated average values for copper of approximately 69.18 GPa and for CuAl of 89.59 GPa. These values are reasonably consistent with the properties of known metals, but there is a tendency to underestimate the overall average value measured by experimental techniques. Tensile tests indicate lower values, ranging from 54.1 GPa to 72.4 GPa. These findings are indicative of the effects of actual test conditions, potential defects in the material, and the influence of internal microstructures. The DIC method, which facilitates detailed spatial analysis, yielded the highest values, with averages reaching 99.6 GPa. This finding underscores the significance of local resolution in capturing stiffer regions of the material. The observed discrepancies between the methods indicate that accurate characterisation of FGMs necessitates a multifaceted approach, integrating experimental data with numerical simulations. The experimental validation of computational models is of crucial importance in ensuring that predictions accurately reflect the physical reality of the material, especially given its heterogeneous nature and functional gradient. The employment of DIC facilitates the quantification of local mechanical properties, aiding in the identification of critical zones that could influence final performance.

8

Conclusions and future work

8.1 Summary and conclusions

The main conclusions of the entire work are outlined in this chapter.

FGM production through WAAM:

- The Chapter 4 details the materials and parameters that have been selected for the fabrication of Cu-CuAl FGMs using the WAAM process. The focus of this study was materials such as pure copper, copper-silver alloys, aluminium, and copper-aluminium alloys, with specific MIG and TIG welding parameters. CuAg wire deposited by MIG had a better surface finish and fewer defects than the Cu wire electrolytic deposited by MIG or TIG;
- Aluminum alloys must be deposited by alternating current (AC), however the walls show a poor surface finish and little cohesion between layers;
- The results show that Cu and Al have very different thermal conductivity coefficients (K) and melting temperatures (Tf), which contributes to their metallurgical incompatibility. In this way, Cu and CuAl alloys were combined into a FGM that showed better metallurgical compatibility;
- The Cu and CuAl materials show better cohesion between the deposited layers and better metallurgical compatibility. Mixing these two wires through twin-wire and arc additive manufacturing (T-WAAM) shows promising results;
- The production of FGM walls occurred in two configurations: stepwise gradient and continuous gradient. This highlights the importance of preheating the Cu layers to improve the cohesion between Cu and CuAl, expanding the transition zone in the FGM;
- This study demonstrated the feasibility of using WAAM in the production of FGMs.

FGM material characterization:

- The material was characterised by means of hardness tests and eddy current measurements, which revealed clear transitions between Cu and CuAl, thus confirming the efficacy of the method for identifying material interfaces;
- The findings demonstrate that preheating the layers prior to the deposition of subsequent materials enhances the material transition zone in the FGM, accompanied by a modest decline in the mean hardness of the copper and CuAl layers. Furthermore, the integration of an intermediate layer comprising 50% Cu and 50% CuAl between the copper and CuAl alloy zones results in the formation of the largest observed transition zone, thereby indicating a more gradual blending of mechanical properties throughout the specimen height. These findings indicate that both preheating and intermediate layer deposition are effective strategies for adjusting the hardness profile and gradually optimizing material properties in the context of FGM design;
- The eddy current measurement results demonstrate the efficacy of this technique in identifying transition zones and electrical conductivity variations in Cu and CuAl materials. In all samples analysed, a clear change in the signal was observed as the probe crossed the interface between the copper and the CuAl alloy, thus confirming the significant difference in electrical properties between the two regions. Furthermore, it was determined that the preheated and continuously graded samples exhibited smoother transitions in the signal profile, indicating enhanced microstructural homogenization and improved continuity between layers. Consequently, it is determined that eddy current measurements are an effective tool for the non-destructive characterisation of uniformity and property transitions in functionally graded Cu-CuAl materials.

Library of material compositions and mechanical properties:

- It was observed that increasing the aluminium content resulted in a progressive increase in hardness (from approximately 50 HV in Cu to approximately 150 HV in CuAl) and mechanical strength, although this was accompanied by greater microstructural heterogeneity;
- Copper-rich alloys exhibited enhanced ductility and homogeneous deformation. In contrast, alloys with higher aluminium content demonstrated superior strength, but also greater vulnerability to plastic instability and localised fractures;
- Among the intermediate compositions, the 25% Cu–75% CuAl alloy was distinguished by its optimal balance between strength (3.2 kN) and ductility (8 mm);
- Despite the positive trends observed, it was noted that all results fell below the values reported for equivalent commercial alloys. This finding serves to demonstrate the inherent defects of the WAAM process, including porosity, lack of fusion, and steep thermal gradients;

- DIC characterisation was found to be essential for comprehending the local evolution of deformations and the formation of shear bands, thus enabling the correlation of the microstructure with the mechanical response;
- A detailed analysis of the initial linear region of the stress-strain curve was conducted, enabling the precise calculation of the elastic modulus ($R^2 = 0.98$), with a resultant Young's modulus of $E = 60.9$ GPa. The calculated Poisson's ratio ($\nu = 0.517$) confirms robust linearity between 10% and 50% of the elastic range, thus validating the methodology used to extract the fundamental elastic parameters;
- The outcomes of this study corroborate the viability of Cu–CuAl alloys produced by WAAM for structural and functional applications. However, the necessity to optimise deposition parameters and apply post-process thermal or mechanical treatments to reduce defects and improve performance in comparison to industrial standards is highlighted.

Experimental tests with digital image correlation:

- Preheating the copper layers before deposition of the copper-aluminum alloy layers provides cohesion between the two materials;
- It is possible to observe that the CuAl alloy layers are the first to deform;
- However, the copper layers are the first to fracture;
- It is possible to successfully couple the DIC technique with experimental tensile tests;
- Conclusions drawn from experimental tests of the specific FGM of the Cu-CuAl alloy;
- The findings reveal substantial discrepancies between the numerical (FEA) and experimental methods, particularly with regard to the Poisson's ratio values. It is imperative to make adjustments to the parameters and boundary conditions of the FEA simulations in order to achieve a more accurate representation of real behaviour;
- The combination of numerical modelling and experimental validation is essential to correctly characterise materials with a functional gradient;
- The DIC method revealed significant local variations, reflecting the heterogeneity of the Cu-CuAl FGM. These variations indicate that different regions of the specimen have different mechanical parameters, associated with the non-uniform distribution of the Cu and CuAl phases. This ability to capture spatial differences demonstrates the potential of DIC to identify critical zones that can influence the overall performance of the material.

8.2 Innovative aspects

The innovative aspects of this thesis include the following:

- This study focused on the production of FGM with Cu and CuAl alloy using the WAAM technique.
- The present study investigated the feasibility of utilising the full-field technique of digital image correlation (DIC) to conduct experimental tensile tests on Cu-CuAl alloy specimens.
- The inverse identification of materials produced by WAAM with copper and aluminium was performed.

8.3 Future research

There are aspects of this study that have the potential to be developed at a future date:

- Change the functionality gradient of the Cu-CuAl FGM alloys, as an exponential gradient;
- The process of FGM production utilising Twin Waam (2 wires) starting with 100% Cu + 0% CuAl layers, transitioning to 0% Cu + 100% CuAl layers, which varied gradually;
- The inverse identification through VFM of the FGm samples produced by WAAM, as well as the samples produced for library material compositions, has the potential to be deepened and further detailed.

8.4 Future applications

The materials that were studied and the WAAM technique show potential for use in different industries in the future, such as:

- The WAAM process can have several applications in different industries. WAAM allows you to deposit any shape and use less material to make it. This not only makes manufacturing more cost-effective, but also makes the parts manufacturing process more environmentally friendly, using less material than conventional methods. This AM process can be implemented in industry when the intention is to produce on a smaller scale. The combination of high deposition rates, low material and equipment costs, and good structural integrity makes Wire and Arc Additive Manufacturing a suitable candidate for replacing the current method of manufacturing from solid billets or large forgings, particularly in the case of low and medium complexity parts. When considered in comparison to conventional machining, WAAM demonstrates

significant potential for reducing material consumption, decreasing reliance on large and costly forgings, and enhancing design flexibility, while also reducing lead time for both new and legacy parts.

- Copper can have various applications such as in the aerospace, automotive, and electrical sectors, due to its high thermal and electrical conductivity. CuAl has excellent resistance to corrosion, which is why it is widely used in fossil fuel pipelines, as well as in shipbuilding coatings. Copper based alloys are commonly used in seawater systems for applications such as heat exchangers, pumps, valves, pipes, fittings. Depending on the application and the requirement for mechanical properties, CuNi alloys (e.g. CuNi10Fe1Mn) or nickel aluminium bronzes can be used.

- A possible application is the aeronautical industry. Aluminum is the most used material in the construction of aircraft. However, it is rarely used as pure aluminum, but rather as various alloys, with copper as the main component of the alloys. Aluminum alloy with silicon, manganese, magnesium and zinc are also used. Copper, like aluminum, is an essential component of an aircraft as it has many unique properties. Firstly, copper is an excellent electrical and thermal conductor. At the same time, copper is incredibly durable and resistant to corrosion. This metal was, is and will be used in the aeronautical industry, as there is no other substitute with similar properties. WAAM deposition rates are sufficiently high to enable large parts to be deposited in reasonable timescales.

Bibliography

[1] R. Mahamood and E. Akinlabi. *Functionally Graded Materials*. Springer International Publishing AG, Switzerland, 2017. ISBN: 9783319537559 (cit. on pp. 1, 37, 38, 40).

[2] M. Feischl et al. *Quasi-optimal convergence rates for adaptive boundary element methods with data approximation. Part II: Hyper-singular integral equation*. Vol. 44. 2015, pp. 153–176. ISBN: 9780080969862 (cit. on p. 1).

[3] M. Naebe and K. Shirvanimoghaddam. "Functionally graded materials: A review of fabrication and properties". In: *Applied Materials Today* 5 (2016), pp. 223–245. ISSN: 23529407. DOI: 10.1016/j.apmt.2016.10.001 (cit. on pp. 1, 2, 37).

[4] Y. W. Chung. *Introduction to materials science and engineering*. 2006, pp. 1–291. ISBN: 9781420009057 (cit. on p. 1).

[5] V. Bhavar et al. "A Review on Functionally Gradient Materials and Their Applications". In: *IOP Conference Series: Materials Science and Engineering* 229.1 (2017), p. 012021 (cit. on p. 1).

[6] G. Knoppers et al. "The reality of functionally graded material products". In: *Proceedings of the Solid Freeform Fabrication Symposium* (2004), pp. 38–43 (cit. on p. 1).

[7] A. O. Ghaziani, R. Soheilifard, and S. Kowsar. "The effect of functionally graded materials on bone remodeling around osseointegrated trans-femoral prostheses". In: *Journal of the Mechanical Behavior of Biomedical Materials* 118.December 2020 (2021), p. 104426. ISSN: 18780180. DOI: 10.1016/j.jmbbm.2021.104426 (cit. on p. 1).

[8] M. Huang et al. "Bioinspired design of dental multilayers". In: *Journal of Materials Science: Materials in Medicine* 18.1 (2007), pp. 57–64. ISSN: 09574530. DOI: 10.1007/s10856-006-0662-0 (cit. on p. 1).

[9] H. A. Bruck, J. J. Evans, and M. L. Peterson. "The role of mechanics in biological and biologically inspired materials". In: *Experimental Mechanics* 42.4 (2002), pp. 361–371. ISSN: 0014-4851. DOI: 10.1007/bf02412140 (cit. on pp. 1, 36, 40).

[10] S. Askarinejad et al. "Fracture and mixed-mode resistance curve behavior of bamboo". In: *Mechanics Research Communications* 78 (2016), pp. 79–85. ISSN: 00936413. DOI: 10.1016/j.mechrescom.2016.02.001 (cit. on p. 1).

[11] Z. Liu et al. "Functional gradients and heterogeneities in biological materials: Design principles, functions, and bioinspired applications". In: *Progress in Materials Science* 88 (2017), pp. 467–498. DOI: 10.1016/j.pmatsci.2017.04.013 (cit. on pp. 1, 2, 33).

[12] W. E. Frazier. "Metal additive manufacturing: A review". In: *J. Mater. Eng. Perform.* 23.6 (2014), pp. 1917–1928 (cit. on p. 1).

[13] J. L. Bartlett et al. "Prediction of microstructural defects in additive manufacturing from powder bed quality using digital image correlation". In: *Materials Science and Engineering: A* 794 (2020), p. 140002 (cit. on p. 1).

[14] Z. A. Mierzejewska. "Effect of Laser Energy Density, Internal Porosity and Heat Treatment on Mechanical Behavior of Biomedical Ti6Al4V Alloy Obtained with DMLS Technology". In: *Materials* 12.14 (2019). ISSN: 1996-1944. DOI: 10.3390/ma12142331 (cit. on p. 1).

[15] J. Torok et al. "Monitoring of the Impacts of Used Materials for Resulting Attributes of an Electric Motor Created via Additive Technology". In: *TEM Journal* 9 (2020-05), pp. 826–830. DOI: 10.18421/TEM92-54 (cit. on p. 1).

[16] Y. Balit, E. Charkaluk, and A. Constantinescu. "Digital image correlation for microstructural analysis of deformation pattern in additively manufactured 316L thin walls". In: *Addit. Manuf.* 31.May 2019 (2020), p. 100862 (cit. on p. 1).

[17] "Additive manufacturing: scientific and technological challenges, market uptake and opportunities". In: *Materials Today* 21.1 (2018), pp. 22–37. ISSN: 1369-7021. DOI: https://doi.org/10.1016/j.mattod.2017.07.001 (cit. on p. 2).

[18] Z.-C. Fang et al. "Review on residual stress in selective laser melting additive manufacturing of alloy parts". In: *Optics & Laser Technology* 129 (2020), p. 106283 (cit. on p. 2).

[19] A. Razavykia et al. "An Overview of Additive Manufacturing Technologies—A Review to Technical Synthesis in Numerical Study of Selective Laser Melting". In: *Materials* 13.17 (2020), p. 3895 (cit. on p. 2).

[20] R. Mahamood and E. Akinlabi. *Functionally Graded Materials 1996*. 1997. ISBN: 9783319537559 (cit. on pp. 2, 39, 40).

[21] J. Wang et al. "Characterization of wire arc additively manufactured titanium aluminide functionally graded material: Microstructure, mechanical properties and oxidation behaviour". In: *Materials Science and Engineering A* 734.May (2018), pp. 110–119. ISSN: 09215093. DOI: 10.1016/j.msea.2018.07.097 (cit. on pp. 2, 8, 9, 11).

[22] C. Shen et al. "Fabrication of Fe-FeAl Functionally Graded Material Using the Wire-Arc Additive Manufacturing Process". In: *Metallurgical and Materials Transactions B: Process Metallurgy and Materials Processing Science* 47.1 (2015), pp. 763–772. ISSN: 10735615. DOI: 10.1007/s11663-015-0509-5 (cit. on pp. 2, 8, 9, 20, 21).

[23] C. Shen et al. "Effect of the post-production heat treatment on phase evolution in the Fe3Ni-FeNi functionally graded material: An in-situ neutron diffraction study". In: *Intermetallics* 129 (2021) (cit. on pp. 2, 8, 9, 11).

[24] Z. Zeng et al. "Wire and arc additive manufacturing of a Ni-rich NiTi shape memory alloy: Microstructure and mechanical properties". In: *Additive Manufacturing* 32 (2020), p. 101051. DOI: 10.1016/j.addma.2020.101051 (cit. on pp. 2, 8, 9, 12, 20, 21, 25).

[25] B. Dong et al. "Fabrication of Copper-Rich Cu-Al Alloy Using the Wire-Arc Additive Manufacturing Process". In: *Metallurgical and Materials Transactions B: Process Metallurgy and Materials Processing Science* 48.6 (2017), pp. 3143–3151. ISSN: 10735615. DOI: 10.1007/s11663-017-1071-0 (cit. on p. 2).

[26] S. Chandrasekaran, S. Hari, and M. Amirthalingam. "Wire arc additive manufacturing of functionally graded material for marine risers". In: *Materials Science and Engineering A* 792.May (2020), p. 139530. ISSN: 09215093. DOI: 10.1016/j.msea.2020.139530 (cit. on pp. 2, 9, 16, 19–21).

[27] T. A. Rodrigues et al. "Steel-copper functionally graded material produced by twin-wire and arc additive manufacturing (T-WAAM)". In: *Materials & Design* 213 (2022), p. 110270. ISSN: 02641275. DOI: 10.1016/j.matdes.2021.110270 (cit. on pp. 2, 9, 13, 20, 21).

[28] F. Pierron and M. Grediac. *The virtual fields method: Extracting constitutive mechanical parameters from full-field deformation measurements*. Vol. 9781461418. Springer, 2012, pp. 1–517. ISBN: 9781461418245 (cit. on pp. 2, 4, 30).

[29] M. Grédiac, F. Hild, and A. Pineau. John Wiley & Sons, Ltd, 2013. ISBN: 9781118578469. DOI: 10.1002/9781118578469.ch8 (cit. on p. 3).

[30] M. Sutton, J.-J. Orteu, and H. Schreier. *Image Correlation for Shape, Motion and Deformation Measurements. Basic Concepts, Theory and Applications*. 2009-01. ISBN: 978-0-387-78746-6. DOI: 10.1007/978-0-387-78747-3 (cit. on p. 3).

[31] M. Grédiac and F. Hild. *Full-Field Measurements and Identification in Solid Mechanics*. John Wiley and Sons, 2012 (cit. on p. 3).

[32] P. Rastogi and E. Hack. *Optical Methods for Solid Mechanics: A Full-Field Approach*. John Wiley and Sons, 2012, p. 432 (cit. on p. 3).

[33] G. Cloud. *Optical methods of engineering analysis*. Cambridge University Press, New York, 1995 (cit. on p. 3).

[34] C. Sciammarella and F. Sciammarella. *Experimental Mechanics of Solids*. John Wiley and Sons, 2012, p. 776 (cit. on p. 3).

[35] F. Lagattu, J. Brillaud, and M.-C. Lafarie-Frenot. "High strain gradient measurements by using digital image correlation technique". In: *Materials Characterization* 53.1 (2004), pp. 17–28 (cit. on p. 3).

[36] D. Dang et al. "Inverse identification of early- and latewood hydric properties using full-field measurements". In: *Wood Material Science & Engineering* 13.1 (2018), pp. 50–63 (cit. on p. 3).

[37] J. Pereira et al. "On the identification of earlywood and latewood radial elastic modulus of Pinus pinaster by digital image correlation: A parametric analysis". In: *The Journal of Strain Analysis for Engineering Design* 53.8 (2018), pp. 566–574 (cit. on pp. 3, 42).

[38] K. Samadian, S. Hertelé, and W. De Waele. "Measurement of CTOD along a surface crack by means of digital image correlation". In: *Eng. Fract. Mech.* 205 (2019), pp. 470–485 (cit. on p. 3).

[39] R. Cappello et al. "Experimental determination of mode I fracture parameters in orthotropic materials by means of Digital Image Correlation". In: *Theoretical and Applied Fracture Mechanics* 108 (2020), p. 102663 (cit. on p. 3).

[40] A. Majano-Majano et al. "Measuring the Cohesive Law in Mode I Loading of Eucalyptus globulus". In: *Materials* 12.1 (2019) (cit. on p. 3).

[41] A. Majano-Majano et al. "Experimental Evaluation of Mode II fracture Properties of Eucalyptus globulus L." In: *Materials* 13.3 (2020) (cit. on p. 3).

[42] J. Oliveira et al. "Direct evaluation of mixed mode I+II cohesive laws of wood by coupling MMB test with DIC". In: *Materials* 14.2 (2021) (cit. on p. 3).

[43] J. V. Blitterswyk, L. Fletcher, and F. Pierron. "Image-Based Inertial Impact Test for Composite Interlaminar Tensile Properties". In: *J. Dyn. Behav. Mater.* (2018) (cit. on p. 3).

[44] L. Fletcher and F. Pierron. "An Image-Based Inertial Impact (IBII) Test for Tungsten Carbide Cermets". In: *Journal of Dynamic Behavior of Materials* 4.4 (2018), pp. 481–504 (cit. on pp. 3, 43, 47).

[45] L. Fletcher, J. Van-Blitterswyk, and F. Pierron. "A Novel Image-Based Inertial Impact Test (IBII) for the Transverse Properties of Composites at High Strain Rates". In: *J. Dyn. Behav. Mater.* (2019) (cit. on p. 3).

[46] P. Kuhn et al. "Determination of the crack resistance curve for intralaminar fiber tensile failure mode in polymer composites under high rate loading". In: *Compos. Struct.* 204 (2018), pp. 276–287 (cit. on p. 3).

[47] G. Catalanotti et al. "High strain rate characterisation of intralaminar fracture toughness of GFRPs for longitudinal tension and compression failure". In: *Compos. Struct.* 240 (2020), p. 112068 (cit. on p. 3).

[48] J. Xavier, J. Pereira, and A. de Jesus. "Characterisation of steel components under monotonic loading by means of image-based methods". In: *Opt. Lasers Eng.* 53 (2014), pp. 142–151 (cit. on p. 3).

[49] E. Hack, G. Lampeas, and E. Patterson. "An evaluation of a protocol for the validation of computational solid mechanics models". In: *The Journal of Strain Analysis for Engineering Design* 51.1 (2016), pp. 5–13 (cit. on p. 3).

[50] L. Felipe-Sesé et al. "A Validation Approach for Quasistatic Numerical/Experimental Indentation Analysis in Soft Materials Using 3D Digital Image Correlation". In: *Materials* 10.7 (2017) (cit. on p. 3).

[51] J. Xavier et al. "Characterisation of the bending stiffness components of MDF panels from full-field slope measurements". In: *Wood Science and Technology* 47 (2013), pp. 423–441. DOI: 10.1007/s00226-012-0507-6 (cit. on p. 3).

[52] J. Xavier and F. Pierron. "Measuring orthotropic bending stiffness components of Pinus pinaster by the virtual fields method". In: *The Journal of Strain Analysis for Engineering Design* 53.8 (2018), pp. 556–565 (cit. on pp. 3, 21).

[53] F. Pierron and M. Grédiac. "Towards Material Testing 2.0. A review of test design for identification of constitutive parameters from full-field measurements". In: *Strain* 57.1 (2021). DOI: 10.1111/str.12370 (cit. on pp. 3, 21).

[54] J. Aquino et al. "Design of heterogeneous mechanical tests: Numerical methodology and experimental validation". In: *Strain* 55.4 (2019), e12313 (cit. on p. 3).

[55] A. Jain, J. A. Bollinger, and T. M. Truskett. "Perspective: Inverse methods for material design". In: *arXiv e-prints*, arXiv:1405.4060 (2014-05), arXiv:1405.4060. DOI: 10.48550/arXiv.1405.4060. eprint: 1405.4060 (cit. on p. 3).

[56] T. Uhl. "The inverse identification problem and its technical application". In: *Archive of Applied Mechanics* 77 (2007-05), pp. 325–337. DOI: 10.1007/s00419-006-0086-9 (cit. on p. 4).

[57] J. M. Martins, S. Thuillier, and A. Andrade-Campos. "Identification of Material Parameters for Plasticity Models: A Comparative Study on the Finite Element Model Updating and the Virtual Fields Method". In: *AIP Conference Proceedings*. Vol. 1960. 1. AIP Publishing, 2018, p. 060006. DOI: 10.1063/1.5034900 (cit. on p. 4).

[58] S. J. Subramanian. "The Eigenfunction Virtual Fields Method". In: *Conference Proceedings of the Society for Experimental Mechanics Series* 3.March (2014), pp. 35–42. DOI: 10.1007/978-3-319-00768-7_6 (cit. on pp. 4, 26).

[59] N. Nayakanti and S. J. Subramanian. "Computation of elastic constants of functionally graded materials using Eigenfunction Virtual Fields Method". In: *ASME International Mechanical Engineering Congress and Exposition, Proceedings (IMECE)* 9.November 2013 (2013). DOI: 10.1115/IMECE2013-64584 (cit. on pp. 4, 25, 26).

[60] T. A. Rodrigues et al. "Current status and perspectives on wire and arc additive manufacturing (WAAM)". In: *Materials* 12.7 (2019) (cit. on pp. 8, 33).

[61] C. Shen et al. "In-depth study of the mechanical properties for Fe3Al based iron aluminide fabricated using the wire-arc additive manufacturing process". In: *Materials Science and Engineering: A* 669 (2016), pp. 118–126. ISSN: 0921-5093. DOI: 10.1016/j.msea.2016.05.047. URL: https://www.sciencedirect.com/science/article/pii/S0921509316305548 (cit. on pp. 8–10, 20, 21).

[62] Y. Ma et al. "Effect of interpass temperature on in-situ alloying and additive manufacturing of titanium aluminides using gas tungsten arc welding". In: *Additive Manufacturing* 8 (2015), pp. 71–77. ISSN: 2214-8604. DOI: 10.1016/j.addma.2015.08.001 (cit. on pp. 8, 9, 11).

[63] Y. Ma et al. "The effect of location on the microstructure and mechanical properties of titanium aluminides produced by additive layer manufacturing using in-situ alloying and gas tungsten arc welding". In: *Materials Science and Engineering: A* 631 (2015), pp. 230–240. ISSN: 0921-5093. DOI: 10.1016/j.msea.2015.02.051 (cit. on pp. 8, 9, 11, 19–21).

[64] L. Yu et al. "Microstructures and mechanical properties of NiTi shape memory alloys fabricated by wire arc additive manufacturing". In: *Journal of Alloys and Compounds* 892 (2022), p. 162193. ISSN: 0925-8388. DOI: 10.1016/j.jallcom.2021.162193 (cit. on pp. 8, 9, 12, 20, 21).

[65] Y. Dong et al. "Fabrication of Copper Rich Cu-Al Alloy Using the Wire Arc Additive Manufacturing Process". In: *Materials* (2017), pp. 1–14 (cit. on pp. 8, 9, 12, 20, 21, 50).

[66] C. Shen et al. "Thermal induced phase evolution of Fe-Fe3Ni functionally graded material fabricated using the wire-arc additive manufacturing process: An in-situ neutron diffraction study". In: *Journal of Alloys and Compounds* 826 (2020), p. 154097. ISSN: 0925-8388. DOI: 10.1016/j.jallcom.2020.154097 (cit. on pp. 9, 10, 20, 21).

[67] C. Shen et al. "Fabrication of FeNi intermetallic using the wire-arc additive manufacturing process: A feasibility and neutron diffraction phase characterization study". In: *Journal of Manufacturing Processes* 57 (2020), pp. 691–699. ISSN: 1526-6125. DOI: 10.1016/j.jmapro.2020.07.027 (cit. on pp. 9, 10, 20, 21).

[68] G. Marinelli et al. "Functionally graded structures of refractory metals by wire arc additive manufacturing". In: *Science and Technology of Welding and Joining* 24.5 (2019), pp. 495–503. ISSN: 17432936. DOI: 10.1080/13621718.2019.1586162 (cit. on pp. 9, 12, 19, 21, 25).

[69] J. Zhang et al. "In-situ heat treatment wire arc additive manufacturing of Inconel625-HSLA steel functionally graded material". In: *Materials Letters* 330 (2023). DOI: 10.1016/j.matlet.2022.133326 (cit. on pp. 9, 13, 14, 25).

[70] J. Zhang et al. "Effect of Electromagnetic Stirring Frequency on Inconel625-High Strength Low Alloy Steel Functionally Graded Material Fabricated by Wire Arc Additive Manufacturing". In: *Journal of Materials Engineering and Performance* 31.12 (2022), pp. 9703–9713. DOI: 10.1007/s11665-022-07008-8 (cit. on pp. 9, 13).

[71] J. Zhang et al. "Effect of synchronous electromagnetic stirring on Laves phase morphology and mechanical property of Inconel625-HSLA steel functionally graded material fabricated by wire arc additive manufacturing". In: *Materials Letters* 316 (2022). DOI: 10.1016/j.matlet.2022.132015 (cit. on pp. 9, 13).

[72] J. Zhang et al. "Transition Strategy Optimization of Inconel625-HSLA Steel Functionally Graded Material Fabricated by Wire Arc Additive Manufacturing". In: *Metals and Materials International* (2022). DOI: 10.1007/s12540-022-01247-z (cit. on pp. 9, 13, 14).

[73] J. Han et al. "Microstructure and mechanical properties of a novel functionally graded material from Ti6Al4V to Inconel 625 fabricated by dual wire + arc additive manufacturing". In: *Journal of Alloys and Compounds* 903 (2022). DOI: 10.1016/j.jallcom.2022.163981. URL: https://www.scopus.com/inward/record.uri?eid=2-s2.0-85123750797&doi=10.1016%2fj.jallcom.2022.163981&partnerID=40&md5=967acc0c3a61a64269de2c59558ff979 (cit. on pp. 9, 14).

[74] X. Chen et al. "A functionally graded material from TC4 to 316L stainless steel fabricated by double-wire + arc additive manufacturing". In: *Materials Letters* 300 (2021). DOI: 10.1016/j.matlet.2021.130141. URL: https://www.scopus.com/inward/record.uri?eid=2-s2.0-85107273776&doi=10.1016%2fj.matlet.2021.130141&partnerID=40&md5=3a76fdc41552675d10b0a689e18a30ac (cit. on pp. 9, 14).

[75] M. R. Ahsan et al. "Microstructures and mechanical behavior of the bimetallic additively-manufactured structure (BAMS) of austenitic stainless steel and Inconel 625". In: *Journal of Materials Science and Technology* 74 (2021), pp. 176–188. ISSN: 10050302. DOI: 10.1016/j.jmst.2020.10.001 (cit. on pp. 9, 15, 19, 21).

[76] R. Sasikumar et al. "Wire arc additive manufacturing of functionally graded material with SS 316L and IN625: Microstructural and mechanical perspectives". In: *CIRP Journal of Manufacturing Science and Technology* 38 (2022), pp. 230–242. DOI: 10.1016/j.cirpj.2022.05.005 (cit. on p. 9).

[77] T. Rodrigues et al. "Wire and arc additive manufacturing of 316L stainless steel/Inconel 625 functionally graded material: Development and characterization". In: *Journal of Materials Research and Technology* 21 (2022), pp. 237–251. DOI: 10.1016/j.jmrt.2022.08.169 (cit. on p. 9).

[78] X. Yu et al. "Effect of composition gradient design on microstructure and mechanical properties of dual-wire plasma arc additively manufactured 316L/IN625 functionally graded materials". In: *Materials Chemistry and Physics* 307 (2023), p. 128121. ISSN: 0254-0584. DOI: https://doi.org/10.1016/j.matchemphys.2023.128121 (cit. on pp. 9, 15, 25).

[79] T. Li et al. "Fabrication and characterization of stainless steel 308 L / Inconel 625 functionally graded material with continuous change in composition by dual-wire arc additive manufacturing". In: *Journal of Alloys and Compounds* 915 (2022). DOI: 10.1016/j.jallcom.2022.165398 (cit. on pp. 9, 15).

[80] T. Li et al. "Strengthening the functionally graded material of stainless steel 308L and Inconel 625 by local Nb alloying". In: *Materials Letters* 331 (2023). DOI: 10.1016/j.matlet.2022.133499. URL: https://www.scopus.com/inward/record.uri?eid=2-s2.0-85141915537&doi=10.1016%2fj.matlet.2022.133499&partnerID=40&md5=6c8be4f301231f3d34df5151e3e36655 (cit. on pp. 9, 15, 16).

[81] T. Li et al. "Effect of Different Wire Feeding Strategies on the Preparation of Functionally Graded Materials by Dual-Wire Arc Additive Manufacturing". In: *Metallurgical and Materials Transactions B: Process Metallurgy and Materials Processing Science* 54.1 (2023), pp. 43–49. DOI: 10.1007/s11663-022-02690-4. URL: https://www.scopus.com/inward/record.uri?eid=2-s2.0-85143225210&doi=10.1007%2fs11663-022-02690-4&partnerID=40&md5=5bdb3facbfce6fbede2236899d7f1d70 (cit. on pp. 9, 15, 16).

[82] T. Li et al. "Hot cracking during the fabrication of Inconel 625/stainless steel 308 L functionally graded material by dual-wire arc additive manufacturing". In: *Journal of Manufacturing Processes* 82 (2022), pp. 461–473. DOI: 10.1016/j.jmapro.2022.08.018. URL: https://www.scopus.com/inward/record.uri?eid=2-s2.0-85135874676&doi=10.1016%2fj.jmapro.2022.08.018&partnerID=40&md5=d5e77adfb81d38ea4873b368e677c45a (cit. on pp. 9, 15).

[83] S.-W. Yoo, C.-M. Lee, and D.-H. Kim. "Effect of Functionally Graded Material (FGM) Interlayer in Metal Additive Manufacturing of Inconel-Stainless Bimetallic Structure by Laser Melting Deposition and Wire Arc Additive Manufacturing (WAAM)". In: *Materials* 16.2 (2023). DOI: 10.3390/ma16020535. URL: https://www.scopus.com/inward/record.uri?eid=2-s2.0-85146532679&doi=10.3390%2fma16020535&partnerID=40&md5=a4619f27bc442a859c57c8296c78459c (cit. on pp. 9, 16).

[84] S. Chandrasekaran, S. Hari, and M. Amirthalingam. "Functionally graded materials for marine risers by additive manufacturing for high-temperature applications: Experimental investigations". In: *Structures* 35 (2022), pp. 931–938. DOI: 10.1016/j.istruc.2021.12.004 (cit. on p. 9).

[85] M. R. Ahsan et al. "Heat-treatment effects on a bimetallic additively-manufactured structure (BAMS) of the low-carbon steel and austenitic-stainless steel". In: *Additive Manufacturing* 32 (2020), pp. 1–25. ISSN: 22148604. DOI: 10.1016/j.addma.2020.101036 (cit. on pp. 9, 17, 19–21).

[86] Y. Ayan and N. Kahraman. "Fabrication and characterization of functionally graded material structure containing two dissimilar steels (ER70S-6 and 308LSi) by wire arc additive manufacturing". In: *Materials Today Communications* 33 (2022) (cit. on pp. 9, 17, 22).

[87] A. Rajesh Kannan et al. "Process-microstructural features for tailoring fatigue strength of wire arc additive manufactured functionally graded material of SS904L and Hastelloy C-276". In: *Materials Letters* 274 (2020) (cit. on pp. 9, 17).

[88] T. Senthil et al. "Pitting corrosion studies on functionally graded Inconel 825-SS316L wall manufactured by wire arc additive manufacturing". In: *Engineering Research Express* 4.3 (2022) (cit. on p. 9).

[89] T. Senthil et al. "Mechanical and microstructural characterization of functionally graded Inconel 825 - SS316L fabricated using wire arc additive manufacturing". In: *Journal of Materials Research and Technology* 15 (2021), pp. 661–669 (cit. on p. 9).

[90] Y. Lu, E. Shevtshenko, and Y. Wang. "Physics-based compressive sensing to enable digital twins of additive manufacturing processes". In: *Journal of Computing and Information Science in Engineering* 21.3 (2021). DOI: 10.1115/1.4050377 (cit. on p. 9).

[91] M. El-Husseiny et al. "Fabrication of Bimetallic High-Strength Low-Alloy Steel/Si-Bronze Functionally Graded Materials Using Wire Arc Additive Manufacturing". In: *Journal of Manufacturing and Materials Processing* 7 (2023-07), p. 138. DOI: 10.3390/jmmp7040138 (cit. on pp. 9, 18).

[92] M. Singh, R. Singh, and D. Gupta. "Investigation of Frictional Deformation on Mechanical and Metallurgical Properties of Ni-based Functionally Graded Materials Developed by Wire and Arc Additive Manufacturing". In: *Journal of Materials Engineering and Performance* 34 (2024-01). DOI: 10.1007/s11665-024-09136-9 (cit. on pp. 9, 18).

[93] A. Thirugnanasambandam, M. K. Subramaniyan, and M. Hariharan. "Characterization of Functionally Graded Material (Stainless Steel 347/308L) Fabricated through Wire and Arc Additive Manufacturing: Microstructure and Mechanical Perspectives". In: *steel research international* 95.8 (2024), p. 2300881. DOI: https://doi.org/10.1002/srin.202300881 (cit. on pp. 9, 18).

[94] U. Reisgen, R. Sharma, and L. Oster. "Plasma multiwire technology with alternating wire feed for tailor-made material properties in wire and arc additive manufacturing". In: *Metals* 9.7 (2019). DOI: 10.3390/met9070745 (cit. on p. 19).

[95] Y. Watanabe et al. "Micro-hardness Measurements to Evaluate Composition Gradients in Metal-Based Functionally Graded Materials". In: *International Journal of Materials Research* 92.1 (2001), pp. 53–57 (cit. on pp. 19, 21).

[96] S. Vijay and S. R. Ch. "A comparative investigation of hardness and compression strength of Nickel coated B4C reinforced 601AC/201AC selective layered functionally graded materials". In: *Materials Research Express* 7.1 (2019). ISSN: 20531591 (cit. on pp. 19, 21).

[97] J. Zhang et al. "Microstructure and properties of functionally graded materials Ti6Al4V/TiC fabricated by direct laser deposition". In: *Rapid Prototyping Journal* 24.4 (2018), pp. 677–687. ISSN: 13552546. DOI: 10.1108/RPJ-12-2016-0215 (cit. on pp. 19, 21).

[98] S. C. Ferreira et al. "Corrosion behaviour of Al/Al3Ti and Al/Al3Zr functionally graded materials produced by centrifugal solid-particle method: Influence of the intermetallics volume fraction". In: *Corrosion Science* 53.6 (2011), pp. 2058–2065. ISSN: 0010938X. DOI: 10.1016/j.corsci.2011.02.010 (cit. on pp. 20, 21).

[99] P. J. Withers et al. "X-ray computed tomography". In: *Nature Reviews Methods Primers* 1.1 (2021), p. 18. ISSN: 2662-8449. DOI: 10.1038/s43586-021-00015-4 (cit. on pp. 20, 21).

[100] Y. Hangai et al. "Fabrication and compression properties of functionally graded foam with uniform pore structures consisting of dissimilar A1050 and A6061 aluminum alloys". In: *Materials Science and Engineering A* 613 (2014), pp. 163–170. ISSN: 09215093. DOI: 10.1016/j.msea.2014.06.039 (cit. on pp. 20, 21).

[101] Y. Hangai et al. "Nondestructive observation of pore structure deformation behavior of functionally graded aluminum foam by X-ray computed tomography". In: *Materials Science and Engineering A* 556 (2012), pp. 678–684. ISSN: 09215093. DOI: 10.1016/j.msea.2012.07.047 (cit. on pp. 20, 21).

[102] ASTM E8. "ASTM E8/E8M standard test methods for tension testing of metallic materials 1". In: *Annual Book of ASTM Standards 4* 1 (2010), pp. 1–27. DOI: 10.1520/E0008 (cit. on p. 20).

[103] F. Pierron. "Material Testing 2.0: A brief review". In: *Strain* 59.3 (2023). DOI: https://doi.org/10.1111/str.12434 (cit. on pp. 21, 23).

[104] J. Martins, A. Andrade-Campos, and S. Thuillier. "Comparison of inverse identification strategies for constitutive mechanical models using full-field measurements". In: *International Journal of Mechanical Sciences* 145 (2018), pp. 330–345. ISSN: 0020-7403. DOI: 10.1016/j.ijmecsci.2018.07.013 (cit. on pp. 21, 23).

[105] J. Xavier et al. "Novel experimental approach for longitudinal-radial stiffness characterisation of clear wood by a single test". In: *Holzforschung* 61.5 (2007), pp. 573–581 (cit. on p. 21).

[106] P. Badoniya, M. Srivastava, and P. K. Jain. "Tailoring microstructure for enhanced mechanical and wear performance of wire arc additively manufactured SS 316 L: Role of interlayer cooling time". In: *Materials Today Communications* 46 (2025). DOI: 10.1016/j.mtcomm.2025.112612 (cit. on p. 22).

[107] Y. Kabaldin et al. "Microstructure, Phase Composition, and Mechanical Properties of a Layered Bimetallic Composite ER70S-6-ER309LSI Obtained by the WAAM Method". In: *Metals* 13.5 (2023). DOI: 10.3390/met13050851 (cit. on p. 22).

[108] S. A. Shalnova et al. "Effect of recycled powder content on the structure and mechanical properties of Ti-6Al-4V alloy produced by direct energy deposition". In: *Journal of Alloys and Compounds* 893 (2022). DOI: 10.1016/j.jallcom.2021.162264 (cit. on p. 22).

[109] P. Badoniya et al. "Microstructural refinement and strengthening of wire arc additively manufactured construction grade low carbon steel through heat treatment". In: *Structures* 68 (2024). DOI: 10.1016/j.istruc.2024.107153 (cit. on p. 22).

[110] M. Madhu et al. "Optimizing post-deposition heat treatment in hot wire TIG manufactured Ni-based superalloy 740H". In: *Sadhana - Academy Proceedings in Engineering Sciences* 50.2 (2025). DOI: 10.1007/s12046-025-02689-y (cit. on p. 22).

[111] Y. Geng et al. "Investigation of Microstructure and Fracture Mechanism of Al-5.0Mg Alloys Fabricated by Wire Arc Additive Manufacturing". In: *Journal of Materials Engineering and Performance* 30.10 (2021), pp. 7406 –7416. DOI: 10.1007/s11665-021-05973-0 (cit. on p. 22).

[112] K. Teja et al. "Optimization of mechanical properties of wire arc additive manufactured specimens using grey-based Taguchi method". In: *Journal of Critical Reviews* 7.9 (2020), pp. 808 –817. DOI: 10.31838/jcr.07.09.153 (cit. on p. 22).

[113] A. Astarita et al. "Microstructure and mechanical properties of specimens produced using the wire-arc additive manufacturing process". In: *Proceedings of the Institution of Mechanical Engineers, Part C: Journal of Mechanical Engineering Science* 235.10 (2021), pp. 1788 –1798. DOI: 10.1177/0954406219883324 (cit. on p. 22).

[114] C. Schneider-Maunoury et al. "An application of differential injection to fabricate functionally graded Ti-Nb alloys using DED-CLAD ® process". In: *Journal of Materials Processing Technology* 268 (2019), pp. 171–180. DOI: 10.1016/j.jmatprotec.2019.01.018 (cit. on p. 22).

[115] C. Shen et al. "The influence of post-production heat treatment on the multi-directional properties of nickel-aluminum bronze alloy fabricated using wire-arc additive manufacturing process". In: *Additive Manufacturing* 23 (2018), pp. 411 –421. DOI: 10.1016/j.addma.2018.08.008 (cit. on p. 22).

[116] M. Gushchina et al. "Multilayer composite Ti-6Al-4 V/Cp-Ti alloy produced by laser direct energy deposition". In: *International Journal of Advanced Manufacturing Technology* 124.3-4 (2023), pp. 907–918. DOI: 10.1007/s00170-022-10521-8 (cit. on p. 22).

[117] V. Semenchuk et al. "Structure organisation of bimetallic elements of functional products printed from aluminium-manganese bronze and steel by Wire-Arc additive technology". In: *Russian Physics Journal* 67.11 (2024), pp. 1969 –1975. DOI: 10.1007/s11182-024-03334-7 (cit. on p. 22).

[118] D. Smith et al. "Mechanical Properties of Cobalt Chromium Alloy Manufactured by Direct Energy Deposition Technology". In: *Journal of Thermal Spray Technology* 34.2 (2025), pp. 674 –689. DOI: 10.1007/s11666-024-01913-1 (cit. on p. 22).

[119] J. Wang et al. "Arc Additively Manufactured 5356 Aluminum Alloy with Cable-Type Welding Wire: Microstructure and Mechanical Properties". In: *Journal of Materials Engineering and Performance* 30.10 (2021), pp. 7472 –7478. DOI: 10.1007/s11665-021-05905-y (cit. on p. 22).

[120] T. Lai et al. "Enhancing corrosion resistance and mechanical properties of laser-direct energy deposited 316 stainless steel via W addition". In: *Corrosion Science* 231 (2024). DOI: 10.1016/j.corsci.2024.111960 (cit. on p. 22).

[121] J. Fu et al. "A VFM-based identification method for anisotropic thermal-mechanical properties of sheet metals using the digital image correlation and infrared thermography assisted heterogeneous test". In: *Journal of Materials Processing Technology* 330 (2024). DOI: 10.1016/j.jmatprotec.2024.118490 (cit. on pp. 22, 23).

[122] J.-H. Kim et al. "Characterization of the post-necking strain hardening behavior using the virtual fields method". In: *International Journal of Solids and Structures* 50.24 (2013), pp. 3829 –3842. DOI: 10.1016/j.ijsolstr.2013.07.018 (cit. on p. 22).

[123] R. Bai et al. "Virtual field method for identifying elastic-plastic constitutive parameters of aluminum alloy laser welding considering kinematic hardening". In: *Optics and Lasers in Engineering* 110 (2018), pp. 122 –131. DOI: 10.1016/j.optlaseng.2018.05.017 (cit. on pp. 22, 24).

[124] E. Sakaridis et al. "Post-Necking full-field FEMU identification of anisotropic plasticity from flat notched tension experiments". In: *International Journal of Solids and Structures* 305 (2024). DOI: 10.1016/j.ijsolstr.2024.113076 (cit. on pp. 22, 23).

[125] S. Dutta and S. K. R. Narala. "Investigations on machining characteristics and chip morphology in turning Al-Mn (AM) alloy using finite element simulation". In: *Proceedings of the Institution of Mechanical Engineers, Part E: Journal of Process Mechanical Engineering* 235.5 (2021), 1608 – 1617. DOI: 10.1177/09544089211014027 (cit. on p. 22).

[126] W. Zhao et al. "An inverse-identification-based finite element simulation of orthogonal cutting tungsten carbide". In: *Journal of the Brazilian Society of Mechanical Sciences and Engineering* 41.2 (2019). DOI: 10.1007/s40430-019-1568-3 (cit. on p. 22).

[127] M. Gonçalves et al. "Key performance indicators for heterogeneous mechanical tests". In: *International Journal of Mechanical Sciences* 264 (2024). DOI: 10.1016/j.ijmecsci.2023.108821 (cit. on p. 23).

[128] N. Nazemi and F. Ghrib. "Strength Characteristics of Heat-Affected Zones in Welded Aluminum Connections". In: *Journal of Engineering Mechanics* 145.12 (2019). DOI: 10.1061/(ASCE)EM.1943-7889.0001647 (cit. on pp. 23–25).

[129] L. Fratini and G. Buffa. "CDRX modelling in friction stir welding of aluminium alloys". In: *International Journal of Machine Tools and Manufacture* 45.10 (2005), 1188 – 1194. DOI: 10.1016/j.ijmachtools.2004.12.001 (cit. on p. 23).

[130] C. Zhang et al. "A coupled electrical-thermal-mechanical modeling of gleeble tensile tests for ultra-high-strength (UHS) steel at a high temperature". In: *Metallurgical and Materials Transactions A: Physical Metallurgy and Materials Science* 41.9 (2010), 2304 – 2317. DOI: 10.1007/s11661-010-0310-7 (cit. on p. 23).

[131] Y. Zhang et al. "Enhancing the information-richness of sheet metal specimens for inverse identification of plastic anisotropy through strain fields". In: *International Journal of Mechanical Sciences* 214 (2022). DOI: 10.1016/j.ijmecsci.2021.106891 (cit. on p. 23).

[132] H. Tian et al. "The modified GTN model for fracture of nickel-based superalloys considering size effect and healing effect in pulsed current assisted deformation". In: *International Journal of Plasticity* 167 (2023). DOI: 10.1016/j.ijplas.2023.103656 (cit. on p. 23).

[133] J. Gelin and O. Ghouati. "The Inverse Approach for the Determination of Constitutive Equations in Metal Forming". In: *CIRP Annals - Manufacturing Technology* 44.1 (1995), 189 – 192. DOI: 10.1016/S0007-8506(07)62304-X (cit. on p. 23).

[134] Z. He, H. Zhu, and Y. Hu. "An improved shear modified GTN model for ductile fracture of aluminium alloys under different stress states and its parameters identification". In: *International Journal of Mechanical Sciences* 192 (2021). DOI: 10.1016/j.ijmecsci.2020.106081 (cit. on p. 23).

[135] S.-H. Yoon and C. Siviour. "The incremental Virtual Fields Method and prestretching method applied to rubbers under uniaxial medium-strain-rate loading". In: *Strain* 53.3 (2017). DOI: 10.1111/str.12225 (cit. on p. 23).

[136] P. Prates, M. Oliveira, and J. Fernandes. "Identification of material parameters for thin sheets from single biaxial tensile test using a sequential inverse identification strategy". In: *International Journal of Material Forming* 9.4 (2016), 547 – 571. DOI: 10.1007/s12289-015-1241-z (cit. on p. 23).

[137] K. Saranath and M. Ramji. "Local zone wise elastic and plastic properties of electron beam welded Ti-6Al-4V alloy using digital image correlation technique: A comparative study between uniform stress and virtual fields method". In: *Optics and Lasers in Engineering* 68 (2015), 222 – 234. DOI: 10.1016/j.optlaseng.2015.01.005 (cit. on p. 23).

[138] Y.-M. Jeong et al. "A Practical Inverse Identification of Johnson-Cook Parameters at Intermediate Strain Rates Using Split Hopkinson Pressure Bar Test". In: *Metals and Materials International* 30.8 (2024), pp. 2093 –2109. DOI: 10.1007/s12540-024-01636-6 (cit. on p. 23).

[139] Y. Coget et al. "Lateral ring compression test applied to a small caliber steel jacket: Identification of a constitutive model". In: *Defence Technology* 36 (2024), 133 – 148. DOI: 10.1016/j.dt.2023.11.001 (cit. on p. 23).

[140] A. Shahmirzaloo, M. Farahani, and M. Farhang. "Evaluation of local constitutive properties of Al2024 friction stir-welded joints using digital image correlation method". In: *Journal of Strain Analysis for Engineering Design* 56.7 (2021), pp. 419 –429. DOI: 10.1177/0309324720981201 (cit. on p. 23).

[141] A. K. Mishra and S. Chakraborty. "Inverse detection of constituent level elastic parameters of FRP composite panels with elastic boundaries using finite element model updating". In: *Ocean Engineering* 111 (2016), 358 – 368. DOI: 10.1016/j.oceaneng.2015.11.003 (cit. on p. 23).

[142] M. Hrairi et al. "Modeling the powder compaction process using the finite element method and inverse optimization". In: *International Journal of Advanced Manufacturing Technology* 56.5-8 (2011), 631 – 647. DOI: 10.1007/s00170-011-3211-z (cit. on p. 23).

[143] C. Kim et al. "Inhomogeneous flow stresses in FSW jointed aluminum alloy sheets inversely identified by FE-VFM". In: *International Journal of Mechanical Sciences* 245 (2023). DOI: 10.1016/j.ijmecsci.2022.108097 (cit. on pp. 23, 24).

[144] R. Bastos, P. A. Prates, and A. Andrade-Campos. "Material Parameter Identification of Elastoplastic Constitutive Models Using Machine Learning Approaches". In: *Key Engineering Materials* 926 (2022), pp. 321–328. DOI: 10.4028/p-8133r1 (cit. on p. 23).

[145] L. Liang et al. "Synergistic integration of deep neural networks and finite element method with applications of nonlinear large deformation biomechanics". In: *Computer Methods in Applied Mechanics and Engineering* 416 (2023). DOI: https://doi.org/10.1016/j.cma.2023.116347 (cit. on p. 23).

[146] Y. Fukui, N. Yamanaka, and K. Wakashima. "Stresses and strains in a thick-walled tube for functionally graded material under uniform thermal loading". In: *JSME International Journal, Series A: Mechanics and Material Engineering* 36.2 (1993), pp. 156–162. DOI: 10.1299/jsmea1993.36.2_156 (cit. on p. 23).

[147] M. Sutton et al. "Identification of heterogeneous constitutive parameters in a welded specimen: Uniform stress and virtual fields methods for material property estimation". In: *Experimental Mechanics* 48.4 (2008), pp. 451 –464. DOI: 10.1007/s11340-008-9132-6 (cit. on p. 24).

[148] G.-Q. Sun et al. "Numerical Simulation of Tension Properties for Al-Cu Alloy Friction Stir-Welded Joints with GTN Damage Model". In: *Journal of Materials Engineering and Performance* 24.11 (2015), pp. 4358 –4363. DOI: 10.1007/s11665-015-1715-7 (cit. on p. 24).

[149] J.-M. Kim et al. "Determination of strain rate dependence at intermediate strain rates using acceleration information". In: *International Journal of Impact Engineering* 173 (2023). DOI: 10.1016/j.ijimpeng.2022.104482 (cit. on p. 24).

[150] K. Saranath and M. Ramji. "Local zone wise elastic and plastic properties of electron beam welded Ti-6Al-4V alloy using digital image correlation technique: A comparative study between uniform stress and virtual fields method". In: *Optics and Lasers in Engineering* 68 (2015), pp. 222 –234. DOI: 10.1016/j.optlaseng.2015.01.005 (cit. on p. 24).

[151] A. Shahmirzaloo, M. Farahani, and M. Farhang. "Evaluation of local constitutive properties of Al2024 friction stir-welded joints using digital image correlation method". In: *Journal of Strain Analysis for Engineering Design* 56.7 (2021), 419 – 429. DOI: 10.1177/0309324720981201 (cit. on p. 24).

[152] S. Stutz, J. Cugnoni, and J. Botsis. "Studies of mode I delamination in monotonic and fatigue loading using FBG wavelength multiplexing and numerical analysis". In: *Composites Science and Technology* 71.4 (2011), pp. 443 –449. DOI: 10.1016/j.compscitech.2010.12.016 (cit. on pp. 24, 25).

[153] R. Chtourou et al. "Macro-modeling of the strength and failure of multi-layer multi-steel grade spot welds: Connector formulation, assembly model and identification procedure". In: *Thin-Walled Structures* 113 (2017), pp. 228 –239. DOI: 10.1016/j.tws.2017.01.023 (cit. on p. 24).

[154] J. Cognard et al. "On modelling the behaviour of a ductile adhesive under low temperatures". In: *International Journal of Adhesion and Adhesives* 47 (2013), pp. 46–56. DOI: 10.1016/j.ijadhadh.2013.09.024 (cit. on pp. 24, 25).

[155] E. Markiewicz, B. Langrand, and D. Notta-Cuvier. "A Review of Characterisation and Parameters Identification of Materials Constitutive and Damage Models: From Normalised Direct Approach to Most Advanced Inverse Problem Resolution". In: *International Journal of Impact Engineering* 110 (2017). Special Issue in Honor of Seventy Fifth Birthday of Professor N. K. Gupta, pp. 371–381. ISSN: 0734-743X. DOI: 10.1016/j.ijimpeng.2017.01.028 (cit. on pp. 24, 25).

[156] J. Cognard et al. "On modelling the behaviour of a ductile adhesive under low temperatures". In: *International Journal of Adhesion and Adhesives* 48 (2014), pp. 119–129. DOI: 10.1016/j.ijadhadh.2013.09.014 (cit. on pp. 24, 25).

[157] H. Jiang et al. "Identifying elasto-plastic damage coupling model of laser-welded aluminum alloy by virtual field method and digital image correlation". In: *Optics and Laser Technology* 129 (2020). DOI: 10.1016/j.optlastec.2020.106268 (cit. on pp. 24, 25, 30).

[158] N. Totaro. "Selective structural source identification". In: *Journal of Sound and Vibration* 420 (2018), pp. 114 –128. DOI: 10.1016/j.jsv.2018.01.037 (cit. on p. 24).

[159] M. Lezgy-Nazargah. "Fully coupled thermo-mechanical analysis of bi-directional FGM beams using NURBS isogeometric finite element approach". In: *Aerospace Science and Technology* 45 (2015), pp. 154–164. DOI: 10.1016/j.ast.2015.05.006 (cit. on p. 25).

[160] W. Hao, Y. Zhang, and Y. Yuan. "Eigenfunction virtual fields method for thermo-mechanical parameters identification of composite materials". In: *Polymer Testing* 50 (2016), pp. 224 –234. DOI: 10.1016/j.polymertesting.2016.01.016 (cit. on p. 25).

[161] N. Nigamaa and S. Subramanian. "Identification of orthotropic elastic constants using the Eigenfunction Virtual Fields Method". In: *International Journal of Solids and Structures* 51.2 (2014), pp. 295 –304. DOI: 10.1016/j.ijsolstr.2013.09.021 (cit. on p. 25).

[162] W. Hao et al. "Characterizing thermo-mechanical behavior of superalloy using the eigenfunction virtual fields method". In: *Advances in Engineering Software* 93 (2016), pp. 22 –29. DOI: 10.1016/j.advengsoft.2015.11.006 (cit. on p. 25).

[163] J. Ahn et al. "In-situ micro-tensile testing of AA2024-T3 fibre laser welds with digital image correlation as a function of welding speed". In: *International Journal of Lightweight Materials and Manufacture* 1 (3 2018-09), pp. 179–188. DOI: 10.1016/j.ijlmm.2018.07.003 (cit. on pp. 28, 30).

[164] W. Li et al. "Fabrication and characterization of a functionally graded material from Ti-6Al-4V to SS316 by laser metal deposition". In: *Addit. Manuf.* 14 (2017), pp. 95 –104 (cit. on pp. 28, 30).

[165] A. Kumar and S. K. Paul. "Restoration of ductility in hydrogen embrittled dual-phase (DP 780) steel by the electric pulse treatment". In: *Materials Science and Engineering: A* 847 (2022-07). DOI: 10.1016/j.msea.2022.143256 (cit. on p. 28).

[166] G. Sun et al. "On quasi-static behaviors of different joint methods for connecting carbon fiber reinforce plastic (CFRP) laminate and aluminum alloy". In: *Thin-Walled Structures* 164 (2021-07). DOI: 10.1016/j.tws.2021.107657 (cit. on p. 28).

[167] Y. Otani et al. "Microstructural origin of anisotropic tensile ductility of Al-Si alloy manufactured by laser powder bed fusion". In: *Scripta Materialia* 226 (2023-03). DOI: 10.1016/j.scriptamat.2022.115259 (cit. on pp. 28, 30).

[168] K. Omer, C. Butcher, and M. Worswick. "Characterization and application of a constitutive model for two 7000-series aluminum alloys subjected to hot forming". In: *International Journal of Mechanical Sciences* 165 (2020-01). DOI: 10.1016/j.ijmecsci.2019.105218 (cit. on p. 28).

[169] X. Zheng, H. Ghassemi-Armaki, and A. Srivastava. "Structural and microstructural influence on deformation and fracture of dual-phase steels". In: *Materials Science and Engineering: A* 774 (2020-02). DOI: 10.1016/j.msea.2020.138924 (cit. on p. 28).

[170] K. A. Kasvayee et al. "Microstructural strain distribution in ductile iron; comparison between finite element simulation and digital image correlation measurements". In: *Materials Science and Engineering: A* 655 (2016-02), pp. 27–35. DOI: 10.1016/j.msea.2015.12.056 (cit. on pp. 28, 30).

[171] K. A. Kasvayee et al. "Strain localization and crack formation effects on stress-strain response of ductile iron". In: *Materials Science and Engineering: A* 702 (2017-08), pp. 265–271. DOI: 10.1016/j.msea.2017.07.018 (cit. on pp. 28, 30).

[172] I. Janeiro, O. Hubert, and J. H. Schmitt. "In-situ strain induced martensitic transformation measurement and consequences for the modeling of medium Mn stainless steels mechanical behavior". In: *International Journal of Plasticity* 154 (2022-07). DOI: 10.1016/j.ijplas.2022.103248 (cit. on pp. 29, 30).

[173] C. Ren et al. "Effect of banded morphology and grain size on the tensile behavior of acicular ferrite in HSLA steel". In: *Materials Science and Engineering: A* 705 (2017-09), pp. 394–401. DOI: 10.1016/j.msea.2017.08.109 (cit. on pp. 29, 30).

[174] K. I. Kim et al. "Strain Analysis of Multi-Phase Steel Using In-Situ EBSD Tensile Testing and Digital Image Correlation". In: *Metals and Materials International* 28 (5 2022-05), pp. 1094–1104. DOI: 10.1007/s12540-021-01044-0 (cit. on pp. 29, 30).

[175] H. Gao et al. "Heterogeneous deformation behavior of hybrid manufactured TC11 titanium alloy via directed energy deposition". In: *Materials Science and Engineering: A* 867 (2023-03). DOI: 10.1016/j.msea.2023.144728 (cit. on pp. 29, 30).

[176] W. Ling et al. "In-situ investigation on tensile deformation and fracture behaviors of inhomogeneous microstructure during laser repair of Ti-6Al-4 V titanium alloy". In: *Engineering Fracture Mechanics* 291 (2023-10). DOI: 10.1016/j.engfracmech.2023.109538 (cit. on pp. 29, 30).

[177] S. Shen, B. He, and H. Wang. "Heterogeneous deformation behavior of hybrid manufactured high strength titanium alloy: Coordinate deformation and stress concentration". In: *Materials Science and Engineering: A* 849 (2022-08). DOI: 10.1016/j.msea.2022.143467 (cit. on pp. 29, 30).

[178] D. Shi et al. "On the tensile behaviors of 2D twill woven SiO2f/SiO2 composites at ambient and elevated temperatures: Mesoscale analysis and in situ experimental investigation". In: *Ceramics International* 47 (9 2021-05), pp. 12680–12694. DOI: 10.1016/j.ceramint.2021.01.128 (cit. on pp. 29, 30).

[179] E. S. Statnik et al. "The analysis of micro-scale deformation and fracture of carbonized elastomer-based composites by in situ SEM". In: *Molecules* 26 (3 2021-02). DOI: 10.3390/molecules26030587 (cit. on pp. 29, 30).

[180] P. Wang et al. "Effect of overlap distance on the microstructure and mechanical properties of in situ welded parts built by electron beam melting process". In: *Journal of Alloys and Compounds* 772 (2019), pp. 247–255 (cit. on pp. 29, 30).

[181] J. Marae Djouda et al. "Experimental approach for microscale mechanical characterization of polymeric structured materials obtained by additive manufacturing". In: *Polymer Testing* 89 (2020), p. 106634 (cit. on pp. 29, 30).

[182] Z. Hadjem-Hamouche et al. "In-situ experimental and numerical studies of the damage evolution and fracture in a Fe-TiB2 composite". In: *Materials Science and Engineering: A* 724 (2018-05), pp. 594–605. DOI: 10.1016/j.msea.2018.03.108 (cit. on pp. 29, 30).

[183] M. P. Moutrille et al. "Through-thickness strain field measurement in a composite/aluminium adhesive joint". In: *Composites Part A: Applied Science and Manufacturing* 40 (8 2009-08), pp. 985–996. DOI: 10.1016/j.compositesa.2008.04.018 (cit. on pp. 29, 30).

[184] G. Ben Salem et al. "Mechanical Behavior Characterization of a Stainless Steel Dissimilar Metal Weld Interface: In-situ Micro-Tensile Testing on Carburized Martensite and Austenite". In: *Experimental Mechanics* 60.8 (2020), pp. 1037–1053. DOI: 10.1007/s11340-020-00633-1 (cit. on pp. 29, 30).

[185] Y. Sun et al. "High plasticity achieved by spark plasma sintering method in aluminum matrix composites reinforced with Ti2AlC particles". In: *Materials Characterization* 177 (2021-07). DOI: 10.1016/j.matchar.2021.111204 (cit. on pp. 29, 30).

[186] J. Luo et al. "In-situ measurements of mechanical and volume change of LiCoO2 lithium-ion batteries during repeated charge–discharge cycling by using digital image correlation". In: *Measurement: Journal of the International Measurement Confederation* 94 (2016-12), pp. 759–770. DOI: 10.1016/j.measurement.2016.09.023 (cit. on pp. 29, 30).

[187] S. Kalnaus et al. "Strain distribution and failure mode of polymer separators for Li-ion batteries under biaxial loading". In: *Journal of Power Sources* 378 (2018-02), pp. 139–145. DOI: 10.1016/j.jpowsour.2017.12.029 (cit. on pp. 29, 30).

[188] A. S. Caro-Bretelle et al. "Effect of sample preservation on stress softening and permanent set of porcine skin". In: *Journal of Biomechanics* 48 (12 2015-09), pp. 3135–3141. DOI: 10.1016/j.jbiomech.2015.07.014 (cit. on pp. 29, 30).

[189] F. Pierron and M. Grédiac. "Towards Material Testing 2.0. A review of test design for identification of constitutive parameters from full-field measurements". In: *Strain* 57.1 (2021), e12370. DOI: 10.1111/str.12370 (cit. on p. 29).

[190] F. Pierron. "Material Testing 2.0: A brief review". In: *Strain* 59.3 (2023), e12434. DOI: 10.1111/str.12434 (cit. on pp. 30, 31).

[191] K. T. Kavanagh and R. W. Clough. "Finite element applications in the characterization of elastic solids". In: *International Journal of Solids and Structures* 7.1 (1971), pp. 11–23. DOI: 10.1016/0020-7683(71)90015-1 (cit. on p. 30).

[192] T. He, L. Liu, and A. Makeev. "Uncertainty analysis in composite material properties characterization using digital image correlation and finite element model updating". In: *Composite Structures* 184 (2018), pp. 337–351. DOI: 10.1016/j.compstruct.2017.10.009 (cit. on p. 30).

[193] D. Notta-Cuvier et al. "An innovative procedure for characterising a coupled elastoplastic damage model of behaviour using the Virtual Fields Method". In: *International Journal of Solids and Structures* 69-70 (2015-09), pp. 415–427. DOI: 10.1016/j.ijsolstr.2015.05.009 (cit. on p. 30).

[194] A. Mulliken and M. Boyce. "Mechanics of the rate-dependent elastic–plastic deformation of glassy polymers from low to high strain rates". In: *International Journal of Solids and Structures* 43.5 (2006), pp. 1331–1356. DOI: 10.1016/j.ijsolstr.2005.04.016 (cit. on p. 31).

[195] J. Henriques, J. Xavier, and A. Andrade-Campos. "Identification of Orthotropic Elastic Properties of Wood by a Synthetic Image Approach Based on Digital Image Correlation". In: *Materials* 15 (2022-01), p. 625. DOI: 10.3390/ma15020625 (cit. on p. 31).

[196] B. Lukić, D. Saletti, and P. Forquin. "Experimental study of the dynamic behaviour of High Performance Concrete (HPC) under tensile loading". In: *EPJ Web of Conferences* 183 (2018-01), p. 02043. DOI: 10.1051/epjconf/201818302043 (cit. on p. 31).

[197] R. Bigger et al. "A Good Practices Guide for Digital Image Correlation". In: 2018 (cit. on p. 31).

[198] M. Sutton, J.-J. Orteu, and H. Schreier. *Image Correlation for Shape, Motion and Deformation Measurements. Basic Concepts, Theory and Applications*. 2009-01. DOI: 10.1007/978-0-387-78747-3 (cit. on p. 31).

[199] International Organization for Standardization. *Additive Manufacturing – General Principles – Part 2: Overview of process categories and feedstock*. International Standard ISO 17296-2:2015. ISO, 2015 (cit. on pp. 32, 34).

[200] A. Dass and A. Moridi. "State of the Art in Directed Energy Deposition : From". In: *Coatings* (2019) (cit. on p. 32).

[201] W. O. Engineering. *Wire + Arc Additive Manufacturing (WAAM)*. https://www.youtube.com/watch?v=Au_zRPr1wr4&ab_channel=WorldOfEngineering. Accessed: 04/02/2021 (cit. on p. 32).

[202] P. Peyre et al. "Analytical and numerical modelling of the direct metal deposition laser process". In: *Journal of Physics D: Applied Physics* 41.2 (2008) (cit. on p. 33).

[203] E. Toyserkani, A. Khajepour, and S. Corbin. "3-D finite element modeling of laser cladding by powder injection: effects of laser pulse shaping on the process". In: *Opt. Lasers Eng.* 41.6 (2004), pp. 849–867 (cit. on p. 33).

[204] N. Shamsaei et al. "An overview of Direct Laser Deposition for additive manufacturing; Part II: Mechanical behavior, process parameter optimization and control". In: *Addit. Manuf.* 8 (2015), pp. 12–35 (cit. on p. 33).

[205] K. V. Wong and A. Hernandez. "A Review of Additive Manufacturing". In: *ISRN Mechanical Engineering* 2012 (2012), pp. 1–10 (cit. on p. 33).

[206] V. Bhavar et al. "A review on powder bed fusion technology of metal additive manufacturing". In: *Additive Manufacturing Handbook: Product Development for the Defense Industry* (2014), pp. 251–261 (cit. on pp. 33, 34).

[207] D. MORI. *New method of manufacturing using powder bed: Additive Manufacturing with Selective Laser Melting*. https://www.youtube.com/watch?v=te9OaSZ0kf8{&}ab{_}channel=DMGMORI. Accessed: 04/02/2021 (cit. on p. 33).

[208] M Shellabear and O Nyrhilä. "DMLS - Development History and State of the Art". In: *Lane 2004* (2004), pp. 1–12 (cit. on p. 34).

[209] Formlabs. *Introduction to Stereolithography*. https://www.youtube.com/watch?v=yW4EbCWaJHE{&}ab{_}channel=Formlabs. Accessed: 04/02/2021 (cit. on p. 34).

[210] N. Vidakis et al. "Sustainable additive manufacturing: Mechanical response of acrylonitrile-butadiene-styrene over multiple recycling processes". In: *Sustainability* 12.9 (2020), p. 3568 (cit. on p. 34).

[211] S. Concepts. *PolyJet Technology*. https://www.youtube.com/watch?v=Som3CddHfZE{&}feature=youtu.be{&}ab{_}channel=SolidConcepts. Accessed: 04/02/2021 (cit. on p. 34).

[212] M. P. Marketing. *ExOne Binder Jetting EN (3D Core & Mold Printing)*. https://www.youtube.com/watch?v=deA-7b3guT4{&}ab{_}channel=MovingPeopleMarketing. Accessed: 04/02/2021 (cit. on p. 34).

[213] K.-E. Aslani et al. "Quality Performance Evaluation of Thin Walled PLA 3D Printed Parts Using the Taguchi Method and Grey Relational Analysis". In: *J. Manuf. Mater. Process.* 4.2 (2020) (cit. on p. 34).

[214] M. Explanations. *Fused Filament Fabrication*. https://www.youtube.com/watch?v=GUbBjPN_Y_c&ab_channel=mechexplanations. Accessed: 04/02/2021 (cit. on p. 34).

[215] J. Kechagias. "An Experimental Investigation of the Surface Roughness of Parts Produced by LOM Process". In: *Rapid Prototyp. J.* 13 (2007-01), pp. 17–22 (cit. on p. 34).

[216] S. Kumaraguru. *LOM Process*. https://www.youtube.com/watch?v=Z1WNA6tdfWM{&}ab{_}channel=SenthilkumaranKumaraguru. Accessed: 04/02/2021 (cit. on p. 34).

[217] Y. Miyamoto and I. Shiota. *Functionally Graded Materials*. Elsevier, 1996 (cit. on pp. 35, 39, 40).

[218] M. Niino, T. Hirai, and R. Watanabe. "Functionally Graded Materials". In: *The Functionally Gradient Materials*. Vol. 13. Proceedings of the National Conference. Tokyo, Japan: Japan Society of Composite Materials, 1987, pp. 257–264 (cit. on pp. 35, 36).

[219] A. Kawasaki and R. Watanabe. "Concept and P/M fabrication of functionally gradient materials". In: *Ceramics International* 23.1 (1997), pp. 73–83. ISSN: 02728842. DOI: 10.1016/0272-8842(95)00143-3 (cit. on p. 35).

[220] S. Suresh and A. Mortensen. "Functionally graded metals and metal-ceramic composites: Part 2 Thermomechanical behaviour". In: *International Materials Reviews* 42.3 (1997), pp. 85–116. ISSN: 09506608. DOI: 10.1179/imr.1997.42.3.85 (cit. on p. 36).

[221] S. Amada et al. "Fiber texture and mechanical graded structure of bamboo". In: *Composites Part B: Engineering* 28.1-2 (1997), pp. 13–20. ISSN: 13598368. DOI: 10.1016/s1359-8368(96)00020-0 (cit. on p. 36).

[222] P. Kreuz, W. Arnold, and A. B. Kesel. "Acoustic microscopic analysis of the biological structure of insect wing membranes with emphasis on their waxy surface". In: *Annals of Biomedical Engineering* 29.12 (2001), pp. 1054–1058. ISSN: 00906964. DOI: 10.1114/1.1424921 (cit. on p. 36).

[223] A. Gupta and M. Talha. "Recent development in modeling and analysis of functionally graded materials and structures". In: *Progress in Aerospace Sciences* 79 (2015), pp. 1–14. ISSN: 03760421. DOI: 10.1016/j.paerosci.2015.07.001 (cit. on p. 36).

[224] T. Khan, N. Zhang, and A. Akram. "State of the art review of functionally graded materials". In: *2019 2nd International Conference on Computing, Mathematics and Engineering Technologies, iCoMET 2019* October (2019). DOI: 10.1109/ICOMET.2019.8673489 (cit. on pp. 36, 37).

[225] C. Zhang et al. "Additive manufacturing of functionally graded materials: A review". In: *Materials Science and Engineering A* 764 (2019), p. 138209. ISSN: 09215093. DOI: 10.1016/j.msea.2019.138209 (cit. on p. 37).

[226] K. L. Choy. "Chemical vapour deposition of coatings". In: *Progress in Materials Science* 48.2 (2003), pp. 57–170. ISSN: 00796425. DOI: 10.1016/S0079-6425(01)00009-3 (cit. on pp. 37, 38).

[227] K. Harsha. "Principles of Physical Vapor Deposition of Thin Films". In: *Elsevier* (2006), p. 1058. ISSN: 1098-6596. eprint: arXiv:1011.1669v3 (cit. on pp. 37, 38).

[228] M. Dorfman. "Thermal Spray Coatings". In: *Handbook of Environmental Degradation of Materials* (2005-12), pp. 405–422. DOI: 10.1016/B978-081551500-5.50022-7 (cit. on pp. 37, 38).

[229] Y. Song, G. Wei, and R. Xiong. "Structure and properties of PbO2-CeO2 anodes on stainless steel". In: *Electrochimica Acta* 52.24 (2007), pp. 7022–7027. ISSN: 00134686. DOI: 10.1016/j.electacta.2007.05.024 (cit. on pp. 37, 38).

[230] W. S. Ebhota, A. S. Karun, and F. L. Inambao. "Centrifugal casting technique baseline knowledge, applications, and processing parameters: Overview". In: *International Journal of Materials Research* 107.10 (2016), pp. 960–969. ISSN: 18625282. DOI: 10.3139/146.111423 (cit. on pp. 37, 38).

[231] Y. Watanabe et al. "A novel fabrication method for functionally graded materials under centrifugal force: The centrifugal mixed-powder method". In: *Materials* 2.4 (2009), pp. 2510–2525. ISSN: 19961944. DOI: 10.3390/ma2042510 (cit. on pp. 37, 38).

[232] A. Varma et al. "Combustion Synthesis of Advanced Materials: Principles and Applications". In: *Advances in Chemical Engineering*. Ed. by J. Wei. Vol. 24. Advances in Chemical Engineering. Academic Press, 1998, pp. 79–226 (cit. on pp. 37, 38).

[233] J. G. Yeo, Y. G. Jung, and S. C. Choi. "Design and microstructure of ZrO2/SUS316 functionally graded materials by tape casting". In: *Materials Letters* 37.6 (1998), pp. 304–311. ISSN: 0167577X. DOI: 10.1016/S0167-577X(98)00111-6 (cit. on pp. 37, 38).

[234] T. Katayama et al. "Fabrication of Al2O3-W functionally graded materials by slipcasting method". In: *IOP Conference Series: Materials Science and Engineering* 18.SYMPOSIUM 14 (2011), pp. 1–5. ISSN: 1757899X. DOI: 10.1088/1757-899X/18/20/202023 (cit. on pp. 37, 38).

[235] R. W. Schwartz, T. Schneller, and R. Waser. "Chemical solution deposition of electronic oxide films". In: *Comptes Rendus Chimie* 7.5 (2004), pp. 433–461. ISSN: 16310748. DOI: 10.1016/j.crci.2004.01.007 (cit. on pp. 37, 38).

[236] L. Besra and M. Liu. "A review on fundamentals and applications of electrophoretic deposition (EPD)". In: *Progress in Materials Science* 52.1 (2007), pp. 1–61. ISSN: 00796425. DOI: 10.1016/j.pmatsci.2006.07.001 (cit. on pp. 37, 38).

[237] J. M. Wilson and Y. C. Shin. "Microstructure and wear properties of laser-deposited functionally graded Inconel 690 reinforced with TiC". In: *Surface and Coatings Technology* 207 (2012), pp. 517–522. ISSN: 02578972. DOI: 10.1016/j.surfcoat.2012.07.058 (cit. on pp. 37, 38).

[238] J Fessler, A Nickel, and G Link. "Functional gradient metallic prototypes through shape deposition manufacturing". In: *Proceedings of the solid freeform fabrication symposium* (1997), pp. 521–528. URL: http://utwired.engr.utexas.edu/lff/symposium/proceedingsArchive/pubs/Manuscripts/1997/1997-61-Fessler.pdf (cit. on pp. 37, 38).

[239] W. J. Boettinger et al. "Solidification microstructures: recent developments, future directions". In: *Acta Materialia* 48.1 (2000), pp. 43–70. ISSN: 13596454. DOI: 10.1016/S1359-6454(99)00287-6 (cit. on pp. 37, 38).

[240] L. Drenchev, J. Sobczak, and N. Sobczak. "Sedimentation phenomenon and viscosity of water-SiC suspension under gravity conditions - A water model study for composites synthesis". In: *Colloids and Surfaces A: Physicochemical and Engineering Aspects* 197.1-3 (2002), pp. 203–211. ISSN: 09277757. DOI: 10.1016/S0927-7757(01)00893-7 (cit. on pp. 37, 38).

[241] R. Jedamzik, A. Neubrand, and J. Rödel. "Functionally graded materials by electrochemical processing and infiltration: Application to tungsten/copper composites". In: *Journal of Materials Science* 35.2 (2000), pp. 477–486. ISSN: 00222461. DOI: 10.1023/A:1004735904984 (cit. on pp. 37, 38).

[242] Z. Qiao et al. "Investigation of binderless WC-TiC-Cr3C2 hard materials prepared by spark plasma sintering (SPS)". In: *International Journal of Refractory Metals and Hard Materials* 38 (2013), pp. 7–14. ISSN: 02634368. DOI: 10.1016/j.ijrmhm.2012.12.002 (cit. on pp. 37, 38).

[243] T. P. Rajan, R. M. Pillai, and B. C. Pai. "Functionally graded Al-Al3Ni in situ intermetallic composites: Fabrication and microstructural characterization". In: *Journal of Alloys and Compounds* 453.1-2 (2008), pp. 2006–2009. ISSN: 09258388. DOI: 10.1016/j.jallcom.2006.11.181 (cit. on pp. 37, 38).

[244] M. M. Nemat-Alla et al. "Powder Metallurgical Fabrication and Microstructural Investigations of Aluminum/Steel Functionally Graded Material". In: *Materials Sciences and Applications* 02.12 (2011), pp. 1708–1718. ISSN: 2153-117X. DOI: 10.4236/msa.2011.212228 (cit. on pp. 37, 38).

[245] J. Yang, J. Yu, and Y. Huang. "Recent developments in gelcasting of ceramics". In: *Journal of the European Ceramic Society* 31.14 (2011), pp. 2569–2591. ISSN: 09552219. DOI: 10.1016/j.jeurceramsoc.2010.12.035 (cit. on p. 38).

[246] R. M. Mahamood et al. "Functionally graded material: An overview". In: *Lecture Notes in Engineering and Computer Science* 3.January 2016 (2012), pp. 1593–1597. ISSN: 20780958 (cit. on p. 39).

[247] M Ansari, E Jabari, and E Toyserkani. "Opportunities and challenges in additive manufacturing of functionally graded metallic materials via powder-fed laser directed energy deposition: A review". In: *Journal of Materials Processing Technology* 294 (2021). ISSN: 0924-0136. DOI: 10.1016/j.jmatprotec.2021.117117 (cit. on p. 39).

[248] S. A. C. P. M. et al. "A Review on Functionally Graded Materials". In: *The International Journal of Engineering and Science* 3.6 (2014), pp. 90–101. ISSN: 2319-1813 (cit. on pp. 39, 40).

[249] R. Mahamood et al. "Revolutionary Additive Manufacturing: An Overview". In: *Lasers in Engineering* 27 (2014-01), pp. 161–178 (cit. on p. 40).

[250] D. Sarathchandra, S. Kanmani Subbu, and N. Venkaiah. "Functionally graded materials and processing techniques: An art of review". In: *Materials Today: Proceedings* 5.10, Part 1 (2018). International Conference on Smart Engineering Materials (ICSEM 2016), October 20-22, 2016, pp. 21328–21334. ISSN: 2214-7853. DOI: 10.1016/j.matpr.2018.06.536. URL: https://www.sciencedirect.com/science/article/pii/S2214785318316699 (cit. on p. 40).

[251] S. A., S. R., and D. P. "Centrifugally Cast Functionally Graded Materials - A Review". In: *International Conference on Systems, Science, Control, Communication, Engineering and Technology*. CSSCCET 2016. 2010, pp. 68–73 (cit. on p. 40).

[252] E. C. Aifantis. "Gradient material mechanics: Perspectives and Prospects". In: *Acta Mechanica* 225.4-5 (2014), pp. 999–1012. ISSN: 00015970. DOI: 10.1007/s00707-013-1076-y (cit. on p. 40).

[253] M. Sutton, J.-J. Orteu, and H. Schreier. *Image correlation for shape, motion and deformation measurements: Basic concepts, theory and applications*. Springer, 2009 (cit. on p. 41).

[254] B. Pan et al. "Two-dimensional digital image correlation for in-plane displacement and strain measurement: a review". In: *Meas. Sci. Technol.* 20.6 (2009), p. 062001 (cit. on pp. 41, 42).

[255] B. Pan. "Digital image correlation for surface deformation measurement: Historical developments, recent advances and future goals". In: *Meas. Sci. Technol.* 29.8 (2018) (cit. on p. 41).

[256] D. Atkinson and T. Becker. "A 117 Line 2D Digital Image Correlation Code Written in MATLAB". In: *Remote Sens-Basel* 12.18 (2020) (cit. on p. 41).

[257] J.-J. Orteu. "3-D computer vision in experimental mechanics". In: *Opt. Lasers Eng.* 47.3 (2009), pp. 282–291 (cit. on p. 41).

[258] A. Buljac et al. "Digital Volume Correlation: Review of Progress and Challenges". In: *Exp. Mech.* 58.5 (2018), pp. 661–708 (cit. on p. 41).

[259] F. Hild and S. Roux. "Comparison of Local and Global Approaches to Digital Image Correlation". In: *Exp. Mech.* 52.9 (2012), pp. 1503–1519 (cit. on p. 42).

[260] Y. Su et al. "Fourier-based interpolation bias prediction in digital image correlation". In: *Optics Express* 23.15 (2015), pp. 19242–19260 (cit. on p. 42).

[261] *Correlated Solutions*. https://www.correlatedsolutions.com/. Accessed: 04/02/2021. 2021. URL: https://www.correlatedsolutions.com/ (visited on 2021-02-04) (cit. on p. 42).

[262] *GOM ARAMIS/GOM Correlate*. https://www.gom.com/en/products/3d-testing. Accessed: 04/02/2021. 2021. URL: https://www.gom.com/en/products/3d-testing (visited on 2021-02-04) (cit. on p. 42).

[263] *MatchID*. https://www.matchid.eu/Software.html. Accessed: 04/02/2021. 2021. URL: https://www.matchid.eu/Software.html (visited on 2021-02-04) (cit. on p. 42).

[264] *The Imetrum*. https://www.imetrum.com/company/the-imetrum-story/. Accessed: 04/02/2021. 2021. URL: https://www.imetrum.com/company/the-imetrum-story/ (visited on 2021-02-04) (cit. on p. 42).

[265] *EikoSim*. https://eikosim.com/en/use-cases/digital-image-correlation-lattice-structures/. Accessed: 04/02/2021. 2021. URL: https://eikosim.com/en/use-cases/digital-image-correlation-lattice-structures/ (visited on 2021-02-04) (cit. on p. 42).

[266] J. Blaber and B. A. B. Antoniou. "Ncorr: Open-Source 2D Digital Image Correlation Matlab Software". In: *Exp. Mech.* 55.6 (2015), pp. 1105–1122 (cit. on p. 42).

[267] D. Turner, P. Crozier, and P. Reu. *Digital Image Correlation Engine (DICe)*. 2015 (cit. on p. 42).

[268] S. Olufsen, M. Andersen, and E. Fagerholt. "μDIC: An open-source toolkit for digital image correlation". In: *SoftwareX* 11 (2020), p. 100391 (cit. on p. 42).

[269] D. Solav et al. "MultiDIC: An Open-Source Toolbox for Multi-View 3D Digital Image Correlation". In: *IEEE Access* 6 (2018), pp. 30520–30535 (cit. on p. 42).

[270] J. Pierré, J. Passieux, and J. Périé. "Finite Element Stereo Digital Image Correlation: Framework and Mechanical Regularization". In: *Exp. Mech.* 57 (2017), pp. 443–456 (cit. on p. 42).

[271] V. Belloni et al. "py2DIC: A New Free and Open Source Software for Displacement and Strain Measurements in the Field of Experimental Mechanics". In: *Exp. Mech.* 19.18 (2019), p. 3832 (cit. on p. 42).

[272] J. Réthoré. "UFreckles". Version v 2.0. In: (2018) (cit. on p. 42).

[273] R. Seghir, J. Witz, and S. Coudert. "YaDICs - digital image correlation 2/3D". In: (2015) (cit. on p. 42).

[274] K. Triconnet et al. "Parameter choice for optimized digital image correlation". In: *Opt. Lasers Eng.* 47.6 (2009), pp. 728–737 (cit. on p. 42).

[275] J. Xavier et al. "Stereovision measurements on evaluating the modulus of elasticity of wood by compression tests parallel to the grain". In: *Constr. Bulid. Mater.* 26.1 (2012), pp. 207–215 (cit. on p. 42).

[276] B. Wattrisse et al. "Analysis of strain localization during tensile tests by digital image correlation". In: *Exp. Mech.* 41.1 (2001), pp. 29–39 (cit. on p. 42).

[277] M. Grédiac et al. "The Virtual Fields Method for Extracting Constitutive Parameters From Full-Field Measurements: a Review". In: *Strain* 42.4 (2006), pp. 233–253 (cit. on p. 42).

[278] F. Pierron, M. Sutton, and V. Tiwari. "Ultra High Speed DIC and Virtual Fields Method Analysis of a Three Point Bending Impact Test on an Aluminium Bar". In: *Experimental Mechanics* 51.4 (2011), pp. 537–563 (cit. on p. 42).

[279] P. F. and G. M. *The Virtual Fields Method: Extracting Constitutive Mechanical Parameters from Full-field Deformation Measurements*. Springer New York, 2012 (cit. on pp. 44, 45).

[280] H. Zhu. "A Novel Methodology for High Strain Rate Testing Using Full-field Measurements and the Virtual Fields Haibin". PhD thesis. Université de Technologie de Troyes, 2015 (cit. on p. 47).

[281] P. Lykov, E. Safonov, and A. Akhmedianov. "Selective Laser Melting of Copper". In: *Materials Science Forum* 843 (2016-02), pp. 284–288. DOI: 10.4028/www.scientific.net/MSF.843.284 (cit. on p. 48).

[282] J. Baby and M. Amirthalingam. "Microstructural development during wire arc additive manufacturing of copper-based components". In: *Welding in the World* 64 (2020-01). DOI: 10.1007/s40194-019-00840-y (cit. on p. 49).

[283] M. Colopi et al. "Limits and solutions in processing pure Cu via selective laser melting using a high-power single-mode fiber laser". In: *The International Journal of Advanced Manufacturing Technology* 104 (2019-10). DOI: 10.1007/s00170-019-04015-3 (cit. on p. 49).

[284] P. S. Deshmukh et al. "Optimum strength and ductility of pure copper fabricated by Wire Arc Additive Manufacturing". In: *Manufacturing Letters* 33 (2022), pp. 24–28. DOI: 10.1016/j.mfglet.2022.06.005 (cit. on p. 49).

[285] C. Silbernagel et al. "Electrical resistivity of pure copper processed by medium-powered laser powder bed fusion additive manufacturing for use in electromagnetic applications". In: *Additive Manufacturing* 29 (2019), p. 100831. DOI: 10.1016/j.addma.2019.100831 (cit. on p. 49).

[286] T. Q. Tran et al. "3D Printing of Highly Pure Copper". In: *Metals* 9.7 (2019). DOI: 10.3390/met9070756 (cit. on p. 49).

[287] Matweb. *Copper (Cu)*. Accessed: 04/07/2025. URL: https://www.matweb.com/search/DataSheet.aspx?MatGUID=9aebe83845c04c1db5126fada6f76f7e (cit. on p. 49).

[288] J. Gu et al. "The effect of inter-layer cold working and post-deposition heat treatment on porosity in additively manufactured aluminum alloys". In: *Journal of Materials Processing Technology* 230 (2016), pp. 26–34. DOI: 10.1016/j.jmatprotec.2015.11.006 (cit. on p. 49).

[289] K. S. Derekar. "A review of wire arc additive manufacturing and advances in wire arc additive manufacturing of aluminium". In: *Materials Science and Technology* 34.8 (2018), pp. 895–916. DOI: 10.1080/02670836.2018.1455012 (cit. on p. 50).

[290] S. C. Altıparmak et al. "Challenges in additive manufacturing of high-strength aluminium alloys and current developments in hybrid additive manufacturing". In: *International Journal of Lightweight Materials and Manufacture* 4.2 (2021), pp. 246–261. DOI: 10.1016/j.ijlmm.2020.12.004 (cit. on p. 50).

[291] T. Hauser et al. "Porosity in wire arc additive manufacturing of aluminium alloys". In: *Additive Manufacturing* 41 (2021), p. 101993. DOI: 10.1016/j.addma.2021.101993 (cit. on p. 50).

[292] K. Vimal, M. Naveen Srinivas, and S. Rajak. "Wire arc additive manufacturing of aluminium alloys: A review". In: *Materials Today: Proceedings* 41 (2021). Advances in Minerals, Metals, Materials, Manufacturing and Modelling, pp. 1139–1145. DOI: 10.1016/j.matpr.2020.09.153 (cit. on p. 50).

[293] MatWeb. *Copper (CuAl)*. URL: https://www.matweb.com/search/DataSheet.aspx?MatGUID=218942d08d354d999f3f2142a8fa85fd (visited on 2025-07-04) (cit. on p. 51).

[294] DARTEC. *Copper - DRATEC Drahttechnik GmbH*. URL: https://dratec.de/kupfer/?lang=en (visited on 2025-07-04) (cit. on p. 51).

[295] N. Kozamernik, D. Bračun, and D. Klobčar. "WAAM system with interpass temperature control and forced cooling for near-net-shape printing of small metal components". In: *International journal of advanced manufacturing technology* 110.7/8 (2020), 1955–1968. DOI: 10.1007/s00170-020-05958-8 (cit. on p. 64).

[296] S. Szalai and G. Dogossy. "Speckle pattern optimization for DIC technologies". In: *Acta Technica Jaurinensis* 14 (2021-04). DOI: 10.14513/actatechjaur.00573 (cit. on p. 76).

[297] E. E. Gdoutos. "Digital Image Correlation (DIC)". In: *Experimental Mechanics: An Introduction*. Cham: Springer International Publishing, 2022, pp. 251–259. DOI: 10.1007/978-3-030-89466-5_12 (cit. on p. 81).